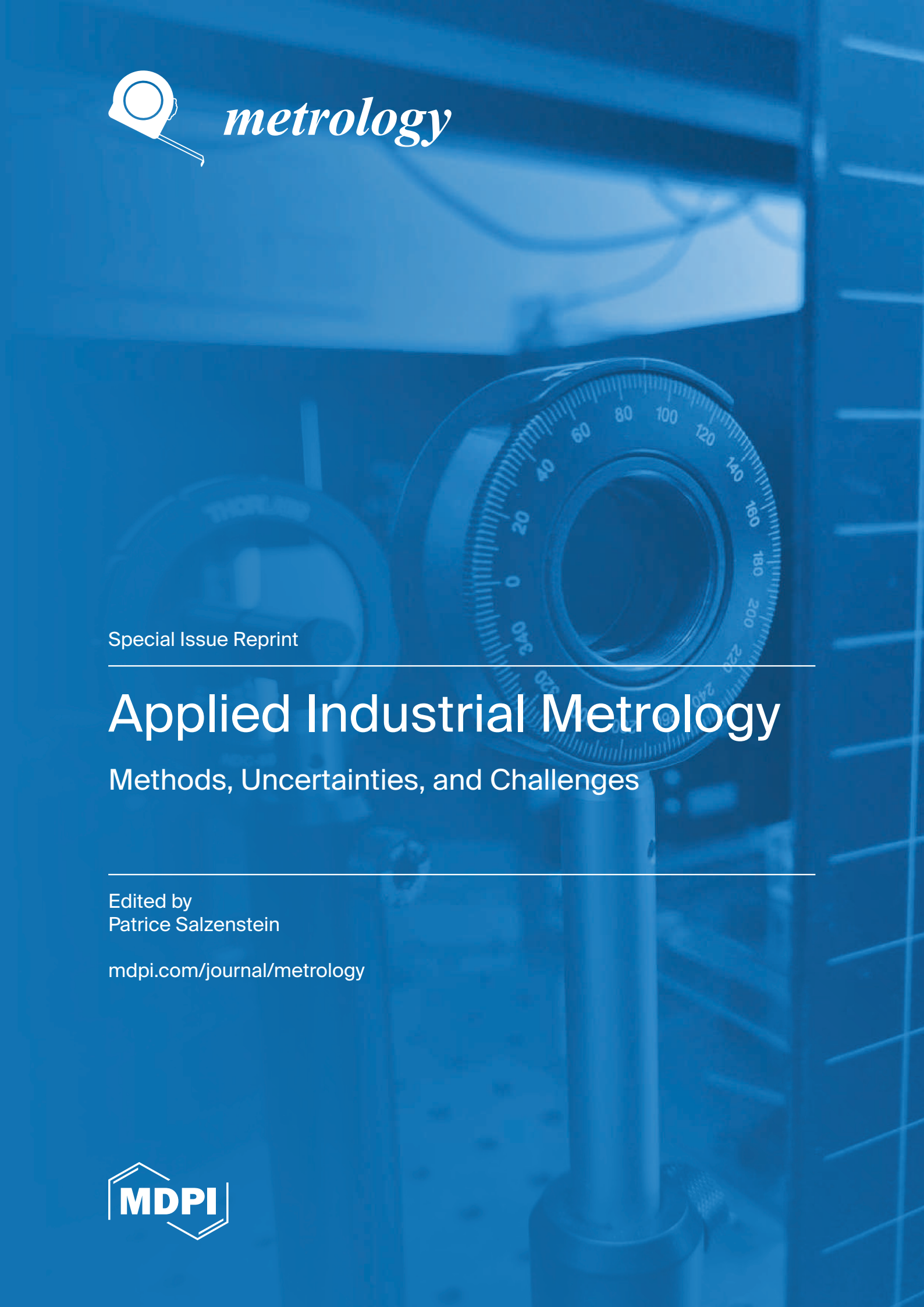
metrology



Special Issue Reprint

Applied Industrial Metrology

Methods, Uncertainties, and Challenges

Edited by
Patrice Salzenstein

mdpi.com/journal/metrology

MDPI

Applied Industrial Metrology: Methods, Uncertainties, and Challenges

Applied Industrial Metrology: Methods, Uncertainties, and Challenges

Guest Editor

Patrice Salzenstein

MDPI

Basel • Beijing • Wuhan • Barcelona • Belgrade • Novi Sad • Cluj • Manchester

Guest Editor
Patrice Salzenstein
Franche-Comté Electronique
Optique Sciences et
Technologies (FEMTO-ST)
Institute
Université Marie et Louis
Pasteur
Centre National de la
Recherche Scientifique
(CNRS)
Besançon
France

Editorial Office
MDPI AG
Grosspeteranlage 5
4052 Basel, Switzerland

This is a reprint of the Special Issue, published open access by the journal *Metrology* (ISSN), freely accessible at: https://www.mdpi.com/journal/metrology/special_issues/M6F97Y1E32.

For citation purposes, cite each article independently as indicated on the article page online and as indicated below:

Lastname, A.A.; Lastname, B.B. Article Title. *Journal Name* **Year**, *Volume Number*, Page Range.

ISBN 978-3-7258-9117-7 (Hbk)
ISBN 978-3-7258-9118-4 (PDF)
https://doi.org/10.3390/books978-3-7258-9118-4

Cover image courtesy of Patrice Salzenstein

© 2026 by the authors. Articles in this reprint are Open Access and distributed under the Creative Commons Attribution (CC BY) license. The reprint as a whole is distributed by MDPI under the terms and conditions of the Creative Commons Attribution-NonCommercial-NoDerivs (CC BY-NC-ND) license (https://creativecommons.org/licenses/by-nc-nd/4.0/).

Contents

About the Editor . . . . . **vii**

Preface . . . . . **ix**

Patrice Salzenstein
Closing Editorial: Applied Industrial Metrology: Methods, Uncertainties, and Challenges
Reprinted from: *Metrology* **2026**, *6*, 49, https://doi.org/10.3390/metrology6030049 . . . . . **1**

Anil Cetinkaya, Aliye Kartal Doğan, Erkan Danacı, Martin Hudlicka, Jar Grajciar, Osman Sibonjic, et al.
Interlaboratory Comparison of RF Power Measurements Made by Automatic Power Measurement Software
Reprinted from: *Metrology* **2026**, *6*, 47, https://doi.org/10.3390/metrology6030047 . . . . . **6**

Akira Ono
Dual-Mode Standardization of Emerging Material Specifications: Structuring Measurement-Based Information for Market Decision-Making
Reprinted from: *Metrology* **2026**, *6*, 36, https://doi.org/10.3390/metrology6020036 . . . . . **21**

Sulaiman Mohaidat, Mohammad Okour, Mutaz Al Fayad and Fadi Alsaleem
High-Frequency Coupled-Resonator CMUT with Stepped Cavity for Enhanced Sensitivity and Bandwidth in Acoustic Emission Detection
Reprinted from: *Metrology* **2026**, *6*, 29, https://doi.org/10.3390/metrology6020029 . . . . . **36**

Thet Pai Oo, Thipamas Phakaew, Muhammad Uzair, Prayoot Akkaraekthalin, Wutthinan Jeamsaksiri and Suramate Chalermwisutkul
A Cost-Effective Cylindrical Capacitive Sensor for Liquid Dielectric Characterization from 1 to 30 MHz
Reprinted from: *Metrology* **2026**, *6*, 23, https://doi.org/10.3390/metrology6020023 . . . . . **47**

Ara Abdulrahman, Gabriele Chinello, Revata Seneviratne, Kurt Rasmussen, Dennis van Putten and Pier Giorgio Spazzini
Interlaboratory Comparison of SI-Traceable Flow Metering Calibration Facilities with Gaseous Carbon Dioxide
Reprinted from: *Metrology* **2026**, *6*, 22, https://doi.org/10.3390/metrology6020022 . . . . . **66**

Miroslav Petrov, Grazia Lo Sciuto, Evgeni Tongov, Yavor Sofronov, Todor Todorov, Georgi Todorov, et al.
Geometrical Prediction of Copper-Coated Solid-Wire Deposition by Wire-Arc Additive Manufacturing Based on Artificial Neural Networks and Support Vector Machines
Reprinted from: *Metrology* **2026**, *6*, 18, https://doi.org/10.3390/metrology6010018 . . . . . **93**

Ionuț-Alin Dumitrache, Andrei George Totu, Ana-Maria Dumitrache and Mihai Vlăduț
Uncertainty Evaluation of CMM and Optical 3D Scanning in Centrifugal Rotor Inspection
Reprinted from: *Metrology* **2026**, *6*, 12, https://doi.org/10.3390/metrology6010012 . . . . . **121**

Bo Shi, Hongli Liu and Emanuele Zappa
A Flexible Wheel Alignment Measurement Method via APCS-SwinUnet and Point Cloud Registration
Reprinted from: *Metrology* **2026**, *6*, 4, https://doi.org/10.3390/metrology6010004 . . . . . **139**

Patrice Salzenstein, Thomas Y. Wu and Ekaterina Pavlyuchenko
The Critical Role of International Comparisons in Global Metrology System: An Overview
Reprinted from: *Metrology* **2025**, *5*, 74, https://doi.org/10.3390/metrology5040074 . . . . . **168**

About the Editor

Patrice Salzenstein

Patrice Salzenstein holds a PhD in Electronics from the University of Sciences and Technologies of Lille (USTL, 1996), a Master of Research degree (USTL, 1993), and an engineering degree from EUDIL, Lille (1993). Between 1996 and 2001, he worked in the Paris area at Thomson CSF LCR (now Thales TRT), Alcatel Alsthom Recherche, and the LCIE private research laboratories. From 2002 to early 2012, he managed a calibration laboratory specializing in phase noise and short-term frequency stability. Since 2001, he has been affiliated with the Centre National de la Recherche Scientifique (CNRS), a government-funded research organization under the authority of the French Ministry of Research, working at the FEMTO-ST Institute in Besançon. In 2010, one of his articles was highlighted in *Electronics Letters* for reporting, together with Czech and Swiss collaborators, the best frequency stability ever measured on a quartz crystal oscillator (2.5×10^{-14} at 5 MHz). From 2010 until recently, his research focused on optoelectronic resonators and oscillators for microwave photonics applications. He currently serves as the deputy head of the Phononics & Microscopy team in the Micro Nano Science & Systems Department (CNRS UMR 6174, FEMTO-ST), with an ongoing interest in uncertainty estimation. Dr. Salzenstein has contributed to more than 140 publications in peer-reviewed international journals and international conferences. He is Associate Editor for *Metrology*. He has more than 30 verified editor records and 100 verified peer reviews.

Preface

Industrial metrology is undergoing a profound transformation driven by advances in digital manufacturing, intelligent sensing, artificial intelligence, and increasingly stringent requirements for traceability and measurement uncertainty. As manufacturing systems become more autonomous and interconnected, reliable measurements are no longer limited to quality assurance but have become an essential component of process optimization, predictive maintenance, sustainability, and regulatory compliance. Consequently, applied industrial metrology continues to evolve by integrating innovative measurement techniques with rigorous uncertainty evaluation and internationally recognized standards.

The idea for this Special Issue, "Applied Industrial Metrology: Methods, Uncertainties, and Challenges", originated from my ongoing interest in uncertainty estimation and from my experience as an Associate Editor of *Metrology* and from coordinating previous Special Issues in *Micromachines*. It was conceived as a forum bringing together recent advances in applied industrial metrology while emphasizing traceability, measurement uncertainty, comparability, advanced sensing, digitalization, and standardization.

I sincerely thank the Editorial Board and Editorial Office of *Metrology* for their continuous institutional and logistical support, as well as all participating authors and their institutions for their valuable contributions. Special appreciation is extended to the peer reviewers, whose careful evaluations and constructive comments were essential to ensuring the scientific quality of this collection.

By bringing together complementary contributions within *Metrology*, this Special Issue highlights how metrology is evolving toward integrated, intelligent, and increasingly data-driven measurement systems supporting advanced manufacturing, Industry 4.0, sustainability, and international confidence in measurement results.

Patrice Salzenstein
Guest Editor

metrology

MDPI

Editorial

Closing Editorial: Applied Industrial Metrology: Methods, Uncertainties, and Challenges

Patrice Salzenstein

Centre National de la Recherche Scientifique (CNRS), Franche-Comté Electronique Optique Sciences et Technologies (FEMTO-ST) Institute, Université Marie et Louis Pasteur (UMLP), 15B Avenue des Montboucons, F-25030 Besançon, France; patrice.salzenstein@cnrs.fr

Abstract

This closing editorial summarizes and introduces the Special Issue, Applied Industrial Metrology: Methods, Uncertainties, and Challenges, highlighting recent advances in traceability, uncertainty evaluation, intelligent metrology, sensor technologies, flow measurement, and standardization. The collected contributions demonstrate how digitalization, artificial intelligence, and advanced sensing are transforming industrial measurement while reinforcing the enduring importance of measurement traceability, comparability, and uncertainty for reliable, sustainable industrial applications.

1. Introduction

Metrology provides the foundation for confidence in measurements, enabling scientific discovery, industrial innovation, international trade, and regulatory compliance. While the International System of Units (SI) ensures worldwide consistency and is based on international comparisons [1], industrial metrology [2–5] extends these principles into practical environments where measurement systems must operate under constraints related to cost, speed, robustness, traceability, and uncertainty [6]. As manufacturing technologies become increasingly digitalized and autonomous, the demand for reliable, traceable, and intelligent measurement solutions continues to grow.

The Special Issue, Applied Industrial Metrology: Methods, Uncertainties, and Challenges, was conceived to provide a forum for researchers and practitioners working at the interface between fundamental metrology and industrial applications. The objective was to highlight recent advances in measurement methods, uncertainty evaluation, calibration, traceability, sensor development, and data-driven metrology across diverse industrial sectors. This Special Issue presents nine high-quality contributions originating from different countries and covering a broad spectrum of industrial metrology topics. Together, these articles illustrate the diversity of modern measurement science, ranging from dimensional and optical metrology to flow metering, dielectric characterization, acoustic sensing, machine learning, and the standardization of emerging materials.

2. Overview of Published Articles

Although addressing different application domains, the contributions naturally cluster around several complementary themes that characterize current developments in industrial metrology.

2.1. Traceability, Standardization, and Measurement Comparability and Intercomparison

Reliable measurements depend not only on accurate instruments but also on internationally recognized traceability chains and harmonized measurement procedures [7,8]. The review article on international comparisons published at the beginning of this Special Issue highlights the fundamental role of the CIPM Mutual Recognition Arrangement in ensuring worldwide confidence in measurement capabilities. It emphasizes how international comparisons establish equivalence among national metrology institutes and support global trade, regulation, and scientific collaboration. Complementing this perspective, Ono proposes a novel framework for the dual-mode standardization of emerging material specifications. Rather than focusing solely on technical standards, the work integrates measurement-based information with market-oriented decision-making, illustrating how metrology can facilitate the industrial adoption of innovative materials while preserving comparability and reliability. This contribution demonstrates that standardization and traceability remain essential pillars for transferring measurement confidence from laboratories to industrial applications. Cetinkaya et al. present an interlaboratory comparison of RF power measurements using automatic measurement software across European metrology laboratories. Measurements at multiple frequencies and power levels were evaluated using GUM and Monte Carlo uncertainty methods. Results showed strong agreement, validating the software's reliability and suitability for accurate, consistent RF power comparisons.

2.2. Measurement Uncertainty and Industrial Verification

Quantifying measurement uncertainty remains one of the defining characteristics of modern metrology. Industrial users increasingly require uncertainty budgets that realistically reflect measurement conditions while remaining practical for routine inspection. This challenge is illustrated by the investigation of uncertainty associated with coordinate measuring machines (CMMs) and optical 3D scanning for centrifugal rotor inspection. By comparing tactile and optical approaches, the authors demonstrate how complementary measurement technologies can be evaluated within a common uncertainty framework, allowing informed decisions according to the functional requirements of complex industrial components. The emphasis on uncertainty evaluation reflects an important trend in industrial metrology: moving beyond measurement accuracy alone toward comprehensive confidence assessment.

2.3. Intelligent Metrology and Artificial Intelligence

Artificial intelligence is rapidly transforming industrial measurement systems by improving feature extraction, prediction, and process optimization. Two contributions exemplify this evolution. One article presents a flexible wheel alignment measurement method combining semantic segmentation based on APCS-SwinUnet with point-cloud registration to achieve low-cost three-dimensional measurements suitable for automotive applications. Another investigates the prediction of deposited bead geometry in wire-arc additive manufacturing using artificial neural networks and support vector machines [9]. Accurate prediction of deposited geometry contributes to improved process control, reduced waste, and enhanced manufacturing quality. These studies demonstrate how machine learning is becoming an integral component of industrial metrology, complementing traditional measurement science with advanced data analysis and predictive capabilities.

2.4. Advanced Sensors and Measurement Instrumentation

Industrial measurements increasingly rely on compact, robust, and application-specific sensing technologies capable of operating in challenging environments.

https://doi.org/10.3390/metrology6030049

A novel cylindrical capacitive sensor is introduced for characterizing the dielectric properties of liquids over the frequency range from 1 to 30 MHz. The proposed design offers a cost-effective alternative while maintaining satisfactory measurement performance, illustrating how sensor innovation can broaden access to reliable electrical characterization.

Another contribution presents a high-frequency coupled-resonator capacitive micromachined ultrasonic transducer (CMUT) designed for acoustic emission monitoring during additive manufacturing. By combining enhanced bandwidth and sensitivity with compact dimensions, the proposed sensor addresses the growing need for real-time structural health monitoring in advanced manufacturing processes.

Together, these papers illustrate the continuous development of measurement instrumentation that balances performance, affordability, and industrial applicability.

2.5. Flow Metrology and Sustainability

Accurate flow measurement plays a critical role in emerging energy and environmental technologies [10,11]. This is particularly true for carbon capture [12], utilization, and storage (CCUS), where reliable quantification of gaseous carbon dioxide is essential throughout the process chain [13].

The reported interlaboratory comparison of SI-traceable calibration facilities for gaseous CO_2 flow metering represents an important contribution to establishing international consistency in this strategically important field. By comparing calibration capabilities across laboratories, the study reinforces confidence in flow measurements supporting future low-carbon technologies.

This contribution illustrates the growing role of metrology in addressing global sustainability challenges. One additional challenge consists of measuring it for nanoparticles [14].

3. Emerging Trends and Future Perspectives

Several important trends emerge collectively from the contributions published in this Special Issue.

- First, industrial metrology is becoming increasingly data-driven [15]. Artificial intelligence, machine learning, and advanced computational methods are no longer peripheral tools but are progressively integrated into measurement systems themselves.
- Second, uncertainty evaluation continues to evolve beyond laboratory environments. Future developments will require uncertainty methodologies capable of supporting autonomous production systems, digital twins [16], and real-time decision making.
- Third, sensor innovation remains a key driver of industrial metrology [17]. Miniaturized, application-specific sensors with improved sensitivity and broader operating ranges will continue expanding measurement capabilities across manufacturing, materials science, and environmental monitoring.

Finally, traceability and standardization [18,19] remain indispensable despite rapid technological evolution. Whether measurements concern advanced materials, additive manufacturing, environmental monitoring, or intelligent production systems, confidence ultimately depends on internationally recognized measurement infrastructures.

These directions clearly illustrate that future industrial metrology will combine rigorous measurement science with digital technologies while maintaining the fundamental principles of traceability, comparability, and uncertainty evaluation.

4. Conclusions

The Special Issue Applied Industrial Metrology: Methods, Uncertainties, and Challenges, successfully brings together contributions illustrating both the diversity and the

https://doi.org/10.3390/metrology6030049

evolution of contemporary industrial measurement science. The published papers span topics ranging from international metrology infrastructure and standardization to intelligent sensing, additive manufacturing, dimensional metrology, dielectric characterization, flow measurement, and machine-learning-assisted measurement systems. Collectively, these contributions demonstrate that industrial metrology is undergoing significant transformation driven by digitalization, advanced sensing technologies, artificial intelligence, and increasing societal demands for sustainable and reliable industrial processes. At the same time, the Special Issue reaffirms that the fundamental principles of traceability, uncertainty evaluation, and international comparability remain central to all measurement activities.

I would like to express my sincere gratitude to all authors for submitting their valuable contributions, and to the reviewers for their careful evaluations and constructive comments.

It is hoped that the articles collected here will serve as useful references for researchers, engineers, and industrial practitioners, while stimulating further developments in applied industrial metrology and strengthening the links between measurement science and industrial innovation.

Funding: This research received no external funding.

Conflicts of Interest: The author declares no conflicts of interest.

List of Contributions:

1. Abdulrahman, A.; Chinello, G.; Seneviratne, R.; Rasmussen, K.; van Putten, D.; Spazzini, P.G. Interlaboratory Comparison of SI-Traceable Flow Metering Calibration Facilities with Gaseous Carbon Dioxide. *Metrology* **2026**, *6*, 22. https://doi.org/10.3390/metrology6020022.
2. Cetinkaya, A.; Dogan, A.K.; Danaci, E.; Hudlicka, M.; Grajciar, J.; Sibonjic, O.; Lippert, T.; Mortensen, S.; Prendergast, S.; Usydus, Ł.; et al. Interlaboratory Comparison of RF Power Measurements Made by Automatic Power Measurement Software. *Metrology* **2026**, *6*, 47. https://doi.org/10.3390/metrology6030047.
3. Dumitrache, I.-A.; Totu, A.G.; Dumitrache, A.-M.; Vlăduț, M. Uncertainty Evaluation of CMM and Optical 3D Scanning in Centrifugal Rotor Inspection. *Metrology* **2026**, *6*, 12. https://doi.org/10.3390/metrology6010012.
4. Mohaidat, S.; Okour, M.; Al Fayad, M.; Alsaleem, F. High-Frequency Coupled-Resonator CMUT with Stepped Cavity for Enhanced Sensitivity and Bandwidth in Acoustic Emission Detection. *Metrology* **2026**, *6*, 29. https://doi.org/10.3390/metrology6020029.
5. Ono, A. Dual-Mode Standardization of Emerging Material Specifications: Structuring Measurement-Based Information for Market Decision-Making. *Metrology* **2026**, *6*, 36. https://doi.org/10.3390/metrology6020036.
6. Oo, T.P.; Phakaew, T.; Uzair, M.; Akkaraekthalin, P.; Jeamsaksiri, W.; Chalermwisutkul, S. A Cost-Effective Cylindrical Capacitive Sensor for Liquid Dielectric Characterization from 1 to 30 MHz. *Metrology* **2026**, *6*, 23. https://doi.org/10.3390/metrology6020023.
7. Petrov, M.; Lo Sciuto, G.; Tongov, E.; Sofronov, Y.; Todorov, G.; Todorov, T.; Mishev, V.; Nikolov, A.; Petrov, K. Geometrical Prediction of Copper-Coated Solid-Wire Deposition by Wire-Arc Additive Manufacturing Based on Artificial Neural Networks and Support Vector Machines. *Metrology* **2026**, *6*, 18. https://doi.org/10.3390/metrology6010018.
8. Salzenstein, P.; Wu, T.Y.; Pavlyuchenko, E. The Critical Role of International Comparisons in Global Metrology System: An Overview. *Metrology* **2025**, *5*, 74. https://doi.org/10.3390/metrology5040074.
9. Shi, B.; Liu, H.; Zappa, E. A Flexible Wheel Alignment Measurement Method via APCS-SwinUnet and Point Cloud Registration. *Metrology* **2026**, *6*, 4. https://doi.org/10.3390/metrology6010004.

References

1. Wallard, A.J. The Organization of Metrology. In *Proceedings of the International School of Physics "Enrico Fermi"*; IOS Press: Amsterdam, The Netherlands, 2007; Volume 166, pp. 21–33. [CrossRef]

2. Placko, D. *Metrology in Industry: The Key for Quality*; Wiley: Hoboken, NJ, USA, 2010.
3. Gao, W.; Kim, S.W.; Bosse, H.; Haitjema, H.; Chen, Y.L.; Lu, X.D.; Knapp, W.; Weckenmann, A.; Estler, W.T.; Kunzmann, H. Measurement technologies for precision positioning. *CIRP Ann.* **2015**, *64*, 773–796. [CrossRef]
4. Oe, T.; Rigosi, A.F.; Kruskopf, M.; Wu, B.Y.; Lee, H.Y.; Yang, Y.; Elmquist, R.E.; Kaneko, N.H.; Jarrett, D.G. Comparison between NIST Graphene and AIST GaAs Quantized Hall Devices. *IEEE Trans. Instrum. Meas.* **2019**, *69*, 3103–3108. [CrossRef] [PubMed]
5. Milano, G.; Zheng, X.; Michieletti, F.; Leonetti, G.; Caballero, G.; Oztoprak, I.; Boarino, L.; Bozat, Ö.; Callegaro, L.; De Leo, N.; et al. A Quantum Resistance Memristor for an Intrinsically Traceable International System of Units Standard. *Nat. Nanotechnol.* **2025**, *20*, 1884–1890. [CrossRef] [PubMed]
6. *ISO/IEC 17025:2017*; ISO/IEC General Requirements for the Competence of Testing and Calibration Laboratories. International Organization for Standardization: Geneva, Switzerland, 2017.
7. Salsbury, J. Uncertainty Management versus Risk Management in Calibration. *NCSLI Meas.* **2010**, *5*, 60–67. [CrossRef]
8. Dobbert, M. A Guard-Band Strategy for Managing False-Accept Risk. *NCSLI Meas.* **2008**, *3*, 44–48. [CrossRef]
9. Mittal, M.K.; Biswas, J.C.; Yadav, A.S. Proficiency Testing in AC Power and Energy. *Mapan J. Metrol. Soc. India* **2009**, *24*, 41–66. [CrossRef]
10. Thorn, R.; Melling, A.; Kochner, H.; Haak, R.; Husain, Z.; Wass, D.; Wadlow, D.; Miller, H.; Eren, H.; Vaterlaus, H.-P.; et al. Flow Measurement. In *CRC Handbook of Electrical and Computer Engineering*, 3rd ed.; Webster, J.G., Ed.; CRC Press: Boca Raton, FL, USA, 2022; Chapter 9. [CrossRef]
11. Thorn, R.; Johansen, G.A.; Hjertaker, B.T. Three-Phase Flow Measurement in the Petroleum Industry. *Meas. Sci. Technol.* **2013**, *24*, 012003. [CrossRef]
12. Konopelko, L.; Kolobova, A.; Chubchenko, I.; Efremova, O.; Rozhnov, M.; Melnyk, D.; Kisel, S.; Levbarg, O.; Shpilnyi, S.; Yakubov, S.; et al. Key Comparison COOMET.QM-K120 "Carbon Dioxide in Air at Urban Level (480–800) μmol/mol". *Metrologia* **2023**, *60*, 08005. [CrossRef]
13. Liu, E.; Lu, X.; Wang, D. A Systematic Review of Carbon Capture, Utilization and Storage: Status, Progress and Challenges. *Energies* **2023**, *16*, 2865. [CrossRef]
14. Brosseau-Habert, N.; Lbadaoui-Darvas, M.; Devel, M.; Picaud, S. Coalescence of Two Carbonaceous Nanoparticles: A Steered Molecular Dynamics Study of the First Steps of the Soot Aggregate Formation. In Proceedings of the Abstract from EGU General Assembly 2025, Vienna, Austria, 27 April–2 May 2025. [CrossRef]
15. Schneider, L.-S.; Krauss, P.; Schiering, N.; Syben, C.; Schielein, R.; Maier, A. Data-Driven Modeling in Metrology—A Short Introduction, Current Developments and Future Perspectives. *tm—Tech. Mess.* **2024**, *91*, 480–503. [CrossRef]
16. Sajadieh, S.M.M.; Noh, S.D. From Simulation to Autonomy: Reviews of the Integration of Artificial Intelligence and Digital Twins. *Int. J. Precis. Eng. Manuf.-Green Technol.* **2025**, *12*, 1597–1628. [CrossRef]
17. Varshney, A.; Garg, N.; Nagla, K.S.; Nair, T.S.; Jaiswal, S.K.; Yadav, S.; Aswal, D.K. Challenges in Sensors Technology for Industry 4.0 for Futuristic Metrological Applications. *MAPAN* **2021**, *36*, 215–226. [CrossRef]
18. Aizenbud-Reshef, N.; Nolan, B.T.; Rubin, J.; Shaham-Gafni, Y. Model traceability. *IBM Syst. J.* **2006**, *45*, 515–526. [CrossRef]
19. Ellis, J.D.; Smith, S.T.; Hocken, R.J. Alignment uncertainties in ideal indentation styli. *Precis. Eng.* **2008**, *32*, 207–214. [CrossRef]

Disclaimer/Publisher's Note: The statements, opinions and data contained in all publications are solely those of the individual author(s) and contributor(s) and not of MDPI and/or the editor(s). MDPI and/or the editor(s) disclaim responsibility for any injury to people or property resulting from any ideas, methods, instructions or products referred to in the content.

https://doi.org/10.3390/metrology6030049

metrology

MDPI

Article

Interlaboratory Comparison of RF Power Measurements Made by Automatic Power Measurement Software

Anil Cetinkaya [1,2], Aliye Kartal Dogan [1,*], Erkan Danaci [1], Martin Hudlicka [3], Jan Grajciar [3], Osman Sibonjic [4], Torsten Lippert [5], Søren Mortensen [5], Sean Prendergast [6], Łukasz Usydus [7], Marko Berginc [8], Emre Çetin [9], Muhammed Cagri Kaya [10] and Halit Oğuztüzün [11]

[1] National Metrology Institute (UME), The Scientific and Technological Research Council of Türkiye (TÜBİTAK), 41470 Kocaeli, Türkiye; anil.cetinkaya@tubitak.gov.tr (A.C.); erkan.danaci@tubitak.gov.tr (E.D.)
[2] Department of Computer Engineering, Faculty of Engineering and Natural Sciences, Iskenderun Technical University, 31200 Hatay, Türkiye
[3] Czech Metrology Institute (CMI), Praha 10, CZ-10200 Prague, Czech Republic; martin.hudlicka@cmi.gov.cz (M.H.); jan.grajciar@cmi.gov.cz (J.G.)
[4] Institute of Metrology of Bosnia and Herzegovina (IMBIH), 71000 Sarajevo, Bosnia and Herzegovina; osman.sibonjic@met.gov.ba
[5] Trescal A/S, 8660 Silkeborg, Denmark; torsten.lippert@trescal.com (T.L.); soren.mortensen@trescal.com (S.M.)
[6] National Standards Authority of Ireland (NSAI), D09 A0E4 Dublin, Ireland; sean.prendergast@nsai.ie
[7] Central Office of Measures (GUM), 00-139 Warsaw, Poland; lukasz.usydus@gum.gov.pl
[8] Slovenian Institute of Quality and Metrology (SIQ), SI-1000 Ljubljana, Slovenia; marko.berginc@siq.si
[9] Spark Calibration Services Inc. (SPARK), 06530 Ankara, Türkiye; emre_cetin@sparkmeasure.com
[10] Department of Computer Science and Engineering, Chalmers University of Technology, SE-412 96 Gothenburg, Sweden; cagri.kaya@chalmers.se
[11] Department of Computer Engineering, Middle East Technical University, 06800 Ankara, Türkiye; oguztuzn@ceng.metu.edu.tr
* Correspondence: aliye.dogan@tubitak.gov.tr

Abstract

An interlaboratory comparison of RF power measurements using automatic power measurement software was carried out among partners of the European Partnership on Metrology project titled "Development of RF and microwave metrology capability II" (RFMicrowave2). The absolute RF power output of a travelling signal generator was measured at six frequencies between 2 GHz and 18 GHz and at three nominal power levels of −10 dBm, 0 dBm, and 10 dBm. Comparison results were evaluated in terms of comparison reference values, degrees of equivalence, and normalised errors. Uncertainty evaluations were performed using both the Guide to the Expression of Uncertainty in Measurement and Monte Carlo simulation methods. The results demonstrate an acceptable level of agreement among participating laboratories and confirm the applicability of automatic power measurement software for interlaboratory RF power comparisons.

Keywords: RF power measurement; interlaboratory comparison; automatic measurement; uncertainty evaluation; Monte Carlo simulation; metrology

1. Introduction

The integrity of the global metrology system is based fundamentally on international comparisons to achieve measurement accuracy, consistency, and trust [1]. Mostly administered by International Committee for Weights and Measures (CIPM) Mutual Recognition Arrangement (MRA), these comparisons provide National Metrology Institutes (NMIs) with the opportunity to show the equivalence of their national standards and validate their

Calibration Measurement Capabilities (CMCs). Therefore, interlaboratory comparisons allow institutions to ensure that their measurements are traceable to the International System of Units (SI) and ensure international recognition by reducing technical barriers. For example, in the RF and microwave domain, international comparisons have been carried out for quantities such as RF power and complex reflection coefficients, establishing the equivalence of national standards across participating institutes [2,3].

Reliable measurement of radio-frequency (RF) and microwave (MW) power is a fundamental requirement for calibration, testing, communications, electromagnetic compatibility (EMC), and a wide range of industrial and regulatory applications [4]. In RF and MW metrology, power is one of the core quantities underpinning traceability chains for related measurements such as attenuation and sensor calibration, and its reliable determination directly affects the quality of higher-level measurement and calibration services [5,6].

RF power calibration is often time-consuming because measurements are repeated over wide frequency and power ranges and require careful management of sensor behaviour, mismatch effects, and instrumental stability. For this reason, automated measurement software offers clear practical advantages by reducing operator dependence, improving repeatability, and enabling more systematic handling of uncertainty budgets [7]. These aspects are particularly relevant for developing laboratories aiming to establish robust and reproducible services for industrial stakeholders.

The evaluation of measurement uncertainty is equally important. The Guide to the Expression of Uncertainty in Measurement (GUM) provides the internationally accepted framework for uncertainty evaluation [8]. The Monte Carlo simulation (MCS) method described in Supplement S1 to the GUM provides a distribution-based alternative that is especially useful when linearisation assumptions are weak or when the output distribution deviates from normality [9]. In RF power transfer measurements, uncertainty contributions associated with mismatch, transfer stability, sensor characteristics, and measurement system configuration can strongly influence the reported results, making rigorous and comparable uncertainty treatment essential [5,6].

At the European level, these needs have motivated coordinated capability-building efforts for RF and MW metrology. The European Partnership on Metrology (EPM) project 22RPT04, "Development of RF and microwave metrology capability II" (RFMicrowave2), aims to improve measurement and research capability in RF and MW metrology, particularly in less experienced NMIs and DIs, and to strengthen future cooperation among European institutes and stakeholders. The project addresses several strategically important areas, including RF and MW power, attenuation, reflection and transmission measurements, antenna parameters, and electromagnetic field measurements, together with a unified approach to measurement uncertainty evaluation [10].

Within this framework, the project focuses on advanced measurement techniques for RF power and power-related quantities. Its objectives include developing traceable capabilities for attenuation and reflection/transmission measurements while establishing a harmonised approach to evaluating their uncertainties. In particular, automatic RF power measurement and uncertainty calculation with different methods is addressed within the framework of the RFMicrowave2 project. The goals of the task are to establish automated RF power measurement capability in participating laboratories, incorporate both traditional law of propagation (GUM-based) and Monte Carlo simulation (MCS) based uncertainty evaluation approaches into the software environment, and validate the established capabilities through an interlaboratory comparison of direct RF power measurement.

Our previous research has been focused systematically on digitalisation and automation of metrological processes, providing the foundational components for the current study. Initially, the "Internet of Measurement Things" (IoMT) architecture was proposed [11],

https://doi.org/10.3390/metrology6030047

establishing the communication and networking requirements for automated calibration in the Industry 4.0 era. Within this framework, the AutoRFPower software was specifically developed and introduced [12] as a specialised desktop application for automated RF power measurements, designed to ensure metrological rigour and flexibility; subsequent research [13] explored the potential of "Uncertainty Calculation as a Service" (UCaaS) through cloud-based microservices as a proof of concept, the present study focuses on the practical validation of the established AutoRFPower desktop tool. This paper demonstrates the software's performance in a large-scale interlaboratory comparison involving eight international partners, confirming its reliability as a standardised tool for high-precision RF power metrology.

This study, conducted within the framework of the 22RPT04 RFMicrowave2 project, presents an interlaboratory comparison of RF power measurements made by automatic power measurement software. The comparison was designed to assess the consistency of RF power measurements performed by different laboratories using a common travelling standard and to evaluate the applicability of automated measurement software in conjunction with both GUM-based and MCS-based uncertainty evaluation approaches. Eight laboratories participated in the comparison according to a technical protocol prepared by the National Metrology Institute (UME) of the Scientific and Technological Research Council of Türkiye (TÜBİTAK) and approved by all of the comparison participants.

Section 2 of this article presents a review of related work. Sections 3 and 4 describe the travelling standard used in the comparison and the measurement methodology, focusing on the automated workflow of the AutoRFPower software and the implementation of GUM-based and MCS-based uncertainty evaluations, respectively. The interlaboratory comparison results, including Comparison Reference Values (CRVs) and Degrees of Equivalence (DoEs), are presented in Section 5. Section 6 discusses the findings, the impact of automated tools on measurement harmony, and potential refinements. Finally, Section 7 concludes the paper with possible future directions.

2. Related Work

Evaluation of interlaboratory comparisons and attainment of measurement equivalence rely on established metrological principles and international guidelines. Salzenstein et al. [1] provide an overview of the global metrology infrastructure and emphasise the critical role of interlaboratory comparisons in validating CMCs. However, the metrology sector is undergoing a profound digital transformation in which the focus is shifting toward establishing robust e-infrastructures and digital quality frameworks. To this end, Neyezhmakov et al. [14] highlight that paving the way for digital transformation requires the development of metrological e-infrastructures and the digitalisation of calibration data to ensure seamless data exchange. Moreover, Verma [15] discusses the potential of cutting-edge technologies such as AI and Big Data in creating a digital quality infrastructure that enhances international trade and measurement reliability. In line with this trend, our work presents a specific case study utilising the AutoRFPower software to implement a digitalised and automated workflow for an interlaboratory comparison.

The mathematical model used to analyse the comparison data follows the procedures set forth by Cox [16]. In our study, we employed the weighted mean approach introduced in [16] when calculating CRVs. This process is automated using the AutoRFPower software. The used statistical framework is supported by other studies in the literature as well: Rukhin and Sedransk [17] provide a rigorous basis for using meta-analysis models in international key comparisons. By building these core stochastic ideas into the process, our automated method ensures that both the CRV and the related DoE come from a solid consensus value that reflects the different uncertainty levels of all participating laboratories.

https://doi.org/10.3390/metrology6030047

Reliability also depends heavily on how measurement uncertainty is handled in RF power metrology and sensor comparison. For example, Koepke et al. [18] advocate the use of advanced model-based approaches, such as hierarchical Bayesian models and MCS, to account for "dark uncertainty". Their work provides the theoretical foundation for the MCS methods that are integrated into our automated software environment. While they focus on the statistical rigour of mathematical models, our study bridges the gap between theory and practice by incorporating these models (both GUM-based and MCS-based) into an automated measurement framework. Thus, our method reduces operator dependence and improves the repeatability of results across different laboratory settings.

3. Travelling Standard and Measurement Conditions

The travelling standard, supplied by Trescal A/S, was an Agilent model 83640A signal generator with serial number 3250A00717. The signal generator operates in the frequency range from 10 MHz to 40 GHz and provides output power levels between -110 dBm and 15 dBm.

A total of eight laboratories participated in the interlaboratory comparison. Measurements were carried out under controlled environmental conditions, with temperatures maintained around (23 ± 2) °C and relative humidity around (45 ± 15) %rh. The participating laboratories and their environmental conditions are listed in Table 1.

Table 1. Laboratories participating in the interlaboratory comparison of RF power.

Country	Institute	Temperature (°C)	Humidity (%rh)
Bosnia and Herzegovina	Institute of Metrology of Bosnia and Herzegovina (IMBIH)	23 ± 2	50 ± 20
Czech Republic	Czech Metrology Institute (CMI)	23 ± 2	40 ± 10
Denmark	Trescal A/S	23 ± 1	45 ± 15
Ireland	National Standards Authority of Ireland (NSAI)	23 ± 2	45 ± 20
Poland	Central Office of Measures (GUM)	23.6	45.7
Slovenia	Slovenian Institute of Quality and Metrology (SIQ)	23 ± 2	50 ± 20
Türkiye	Spark Calibration Services Inc.	23 ± 2	50 ± 20
Türkiye	TÜBİTAK National Metrology Institute (TÜBİTAK UME)	23 ± 1	45 ± 15

Measurements were taken at six frequencies, namely, 2 GHz, 5 GHz, 8 GHz, 12 GHz, 15 GHz, and 18 GHz, and at nominal power levels of 10 dBm, 0 dBm, and -10 dBm. Each participating institute carried out the comparison measurements using its own measurement system, including a power meter, a power sensor and the proper adaptors.

Each participant measured the absolute RF power output of the travelling standard using the AutoRFPower software, which was used to manage the complete measurement workflow, including data acquisition and uncertainty evaluation. The software incorporates both Standing Wave Ratio (SWR) values provided by the manufacturer and complex reflection coefficient (RCC) values measured by selected laboratories.

For one participating laboratory, incompatibility issues prevented the use of AutoRFPower for direct data acquisition. In this case, measurement data were recorded using an alternative data logging approach. However, the recorded data were subsequently processed using the AutoRFPower software, particularly its uncertainty evaluation modules, in the same manner as for the other participants. Therefore, consistency in data processing and uncertainty evaluation was maintained across all laboratories.

https://doi.org/10.3390/metrology6030047

The SWR values represent a scalar description of the mismatch behaviour between the source and the power sensor and are typically provided by the manufacturer as part of the instrument specifications. In contrast, the RCC is a complex quantity describing both the magnitude and phase of the reflected signal, usually obtained from vector network analyser (VNA) measurements.

Prior to the comparison, the vector RCC of the adaptor connected to the signal generator to be used in the comparison as a travelling standard was measured by TÜBİTAK UME with the help of Spark Calibration Services Inc., Ankara, Türkiye (Spark) using a VNA-based vector reflection coefficient measurement technique [19]. The measured vector RCC values were shared with the comparison participants.

Using the complex reflection coefficient allows a more complete vector description of the mismatch interaction between the adaptor and the power sensor, which can improve the accuracy of mismatch corrections and uncertainty evaluation [20]. For this reason, both SWR-based and RCC-based approaches were considered in the software to assess their influence on the calculated RF power and associated measurement uncertainties.

4. Measurement Methodology and Evaluation

The circulation of the travelling standard was organised to follow a ring-style path. The circulation began in June 2024, and comparison measurements were completed in January 2025. Each laboratory had a week to carry out the measurements.

Each participant institute used the AutoRFPower software to measure the absolute RF power of the travelling standard against its own traceable reference standards, namely, power sensors and power meters. At each test point, the measurement was completed by taking at least 10 successive readings. Further details of this comparison are provided in the associated technical report [21].

Uncertainty evaluations were performed according to two different approaches included in the AutoRFPower software:

- the Guide to the Expression of Uncertainty in Measurement (GUM);
- Monte Carlo Simulation (MCS).

The MCS-based evaluation is implemented in the developed software following Supplement S1 to the Joint Committee for Guides in Metrology (JCGM) 101 [9]. Its application to RF power measurements was described and validated against a commercial Monte Carlo tool in [22]. In contrast to the law of propagation approach, in which every contribution is reduced to the equivalent standard uncertainty of a normal distribution, the MCS module assigns a probability density function (PDF) to each input quantity of the measurement model and propagates these PDFs through the model by repeated random sampling, so that the actual shape of each input distribution is retained in the output distribution [22].

The measurement model relates the power indicated by the sensor to the absolute output power of the travelling standard through the calibration factor of the standard power sensor, the (complex) forward transmission coefficient of the adaptor/attenuator where used, and the impedance-mismatch factor M between the source and the sensor [22]. For each measurement point, the input quantities were assigned PDFs according to their nature. The repeatability of the power readings, the calibration factor of the standard power sensor, the forward transmission coefficient of the adaptor/attenuator, and the magnitude and phase of the reflection coefficients were modelled with Gaussian (normal) PDFs, whereas the power-meter accuracy and the power-meter resolution were modelled with rectangular (uniform) PDFs. Each PDF is characterised by a location parameter (the best estimate of the quantity) and a scale parameter (its standard uncertainty); $M_{\mathrm{MCS}} = 2 \times 10^5$ samples were then drawn from each parameterised PDF and propagated through the

https://doi.org/10.3390/metrology6030047

model, and the mean and standard deviation of the resulting output distribution were taken as the estimated power and its standard uncertainty, respectively.

The treatment of the mismatch contribution distinguishes the two cases considered in this work and is consistent with the mismatch modelling described by Danaci et al. [22]. In the RCC case, the complex reflection coefficients are available; the mismatch factor is then evaluated from the magnitudes and phases of Γ (each modelled with a Gaussian PDF), so that the resulting mismatch contribution is approximately normal. In the SWR case, only the magnitude of the reflection coefficient is known (derived from the manufacturer's standing-wave ratio); the mismatch factor is bounded by its extreme values and is therefore modelled with a U-shaped (arcsine) PDF [23]. This difference in the mismatch PDF is one of the main reasons for the slightly different uncertainties obtained for the RCC and SWR cases, particularly at higher frequencies, where mismatch effects become more pronounced.

The comparison results and combined uncertainties were used to determine the Comparison Reference Values (x_{CRV}).

The degree of equivalence of each participant and the expanded uncertainty of the degree of equivalence were calculated [16].

The E_n value is stated in ISO/IEC 17043 "Conformity assessment—General requirements for proficiency testing" Standard [24]. The participant results were regarded as satisfactory if $\mid E_n \mid < 1$.

The x_{CRV} was calculated for each measurement point using the weighted mean with normalised weights. The x_{CRV} is given by

$$x_{\mathrm{CRV}} = \frac{\sum_{i=1}^{N} \frac{x_i}{u_{x_i}^2}}{\sum_{i=1}^{N} \frac{1}{u_{x_i}^2}} \tag{1}$$

and the uncertainty of the Comparison Reference Values (x_{CRV}) was calculated as

$$u(x_{\mathrm{CRV}}) = \sqrt{\frac{1}{\sum_{i=1}^{N} \frac{1}{u_{x_i}^2}}} \tag{2}$$

The expanded uncertainty of the Comparison Reference Values (x_{CRV}) was calculated as

$$U(x_{\mathrm{CRV}}) = 2\,u(x_{\mathrm{CRV}}) \tag{3}$$

5. Comparison Results

The x_{CRV} values were calculated for both RCC and SWR cases using GUM and MCS methods at three nominal power levels (−10 dBm, 0 dBm, and 10 dBm). The Comparison Reference Values (CRVs) were determined as weighted means of the participant results, where the weights were derived from the reported uncertainties of each laboratory. The results at 0 dBm, −10 dBm, and 10 dBm are presented in Tables 2, 3, and 4, respectively.

Degrees of equivalence (DoEs) with expanded uncertainties at 0 dBm for the RCC and SWR cases based on the GUM method are presented in Figure 1 and Figure 2, respectively, while the corresponding results based on the MCS method are shown in Figures 3 and 4.

Similarly, the DoEs at −10 dBm for the RCC and SWR cases based on the GUM method are presented in Figure 5 and Figure 6, respectively, while the corresponding results based on the MCS method are shown in Figures 7 and 8.

https://doi.org/10.3390/metrology6030047

Likewise, the DoEs at 10 dBm for the RCC and SWR cases based on the GUM method are presented in Figure 9 and Figure 10, respectively, while the corresponding results based on the MCS method are shown in Figures 11 and 12.

Table 2. x_{CRV} and expanded uncertainties $U(x_{\mathrm{CRV}})$ (k = 2) at 0 dBm.

Freq. (GHz)	GUM-Based				MCS-Based			
	RCC		SWR		RCC		SWR	
	x	U	x	U	x	U	x	U
2	0.041	0.027	0.006	0.034	0.005	0.029	−0.003	0.033
5	0.022	0.032	0.002	0.039	−0.019	0.037	−0.026	0.044
8	0.068	0.032	0.031	0.040	0.035	0.037	0.034	0.043
12	0.027	0.036	0.003	0.046	0.012	0.041	0.017	0.050
15	0.014	0.040	0.010	0.054	0.005	0.048	−0.003	0.060
18	−0.051	0.042	−0.028	0.056	−0.027	0.049	−0.024	0.061

Table 3. x_{CRV} and expanded uncertainties $U(x_{\mathrm{CRV}})$ (k = 2) at −10 dBm.

Freq. (GHz)	GUM-Based				MCS-Based			
	RCC		SWR		RCC		SWR	
	x	U	x	U	x	U	x	U
2	−9.896	0.029	−9.950	0.036	−9.929	0.032	−9.919	0.036
5	−9.917	0.032	−9.939	0.040	−9.949	0.038	−9.941	0.045
8	−9.901	0.033	−9.941	0.043	−9.921	0.039	−9.909	0.044
12	−9.920	0.037	−9.942	0.049	−9.919	0.043	−9.893	0.051
15	−9.949	0.042	−9.958	0.059	−9.942	0.051	−9.928	0.060
18	−9.984	0.043	−9.980	0.060	−9.956	0.050	−9.925	0.062

Table 4. x_{CRV} and expanded uncertainties $U(x_{\mathrm{CRV}})$ (k = 2) at 10 dBm.

Freq. (GHz)	GUM-Based				MCS-Based			
	RCC		SWR		RCC		SWR	
	x	U	x	U	x	U	x	U
2	10.086	0.026	10.051	0.034	10.050	0.029	10.041	0.033
5	10.055	0.031	10.037	0.039	10.014	0.036	10.007	0.041
8	10.101	0.032	10.063	0.041	10.068	0.038	10.066	0.043
12	10.064	0.036	10.036	0.048	10.046	0.042	10.049	0.050
15	10.047	0.041	10.040	0.057	10.035	0.049	10.025	0.060
18	9.979	0.042	10.002	0.059	9.999	0.049	10.002	0.061

The laboratories shown on the x-axis are presented in a randomised order to avoid any implicit ranking or bias in visual interpretation. Each marker represents the DoE of a participating laboratory at a given frequency, while the vertical error bars indicate the associated expanded uncertainty $U(D_i)$. The blue-dotted horizontal line in the Figure 1 to Figure 12 indicates the degrees of equivalence, which is the difference between the result of the participants of the travelling standard, and x_{CRV}. The different marker styles correspond to different frequency points. Measurement results with $E_n \geq 1$ are highlighted with red dotted circles, indicating potential inconsistency with the comparison reference value.

The results showed that most participant measurements were in good agreement with the CRV values across all frequencies and power levels. The majority of participant results satisfied the acceptance criterion $|E_n| < 1$. This indicates a high level of consistency among participating laboratories and confirms the robustness of the measurement methodology.

It should be noted that for one participating laboratory, the uncertainty component associated with measurement non-reproducibility was not fully included in the uncertainty evaluation performed using the AutoRFPower software. As a result, the reported uncertainties at the −10 dBm level were significantly underestimated. For example,

https://doi.org/10.3390/metrology6030047

at 2 GHz and −10 dBm, the expanded uncertainty obtained from the software was approximately four times smaller than the value estimated by the laboratory when including non-reproducibility effects.

A comparison between RCC- and SWR-based evaluations reveals that the use of vector RCC information generally provides slightly improved agreement compared to scalar SWR-based modelling, particularly at higher frequencies where mismatch effects are more pronounced. Similarly, the agreement between GUM and MCS results indicates that the linearisation assumptions of the GUM approach are valid for most cases, while the MCS approach provides additional robustness in scenarios involving non-linear effects.

Some deviations were observed for specific laboratories and frequency points. In particular, significant deviations were identified for one participant, which may be related to instrument zeroing issues or differences in measurement procedures. These deviations are more noticeable at lower power levels and higher frequencies, where measurement sensitivity and mismatch-related effects become more critical.

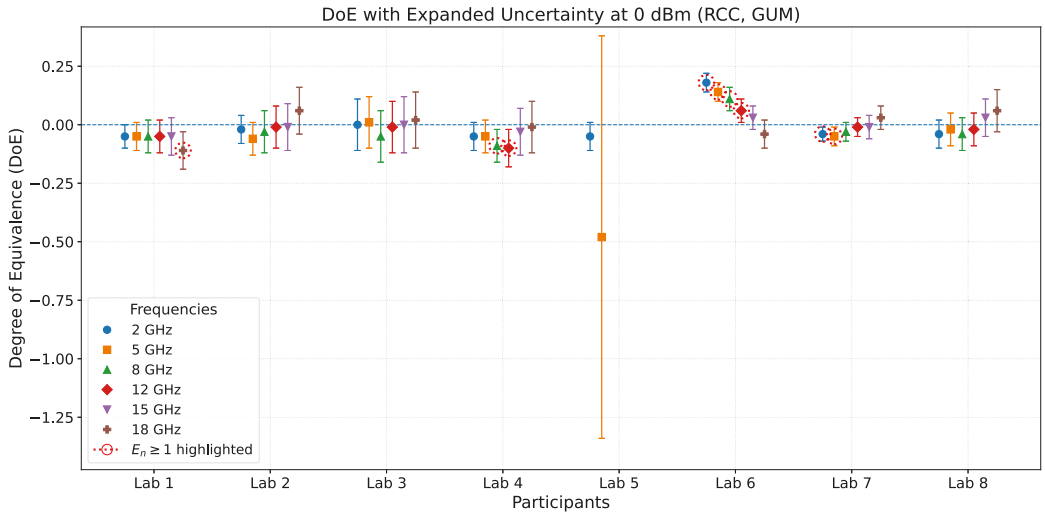


Figure 1. Degrees of equivalence with expanded uncertainties at 0 dBm for the RCC case according to the GUM method. Red dotted circles indicate points with $E_n \geq 1$.

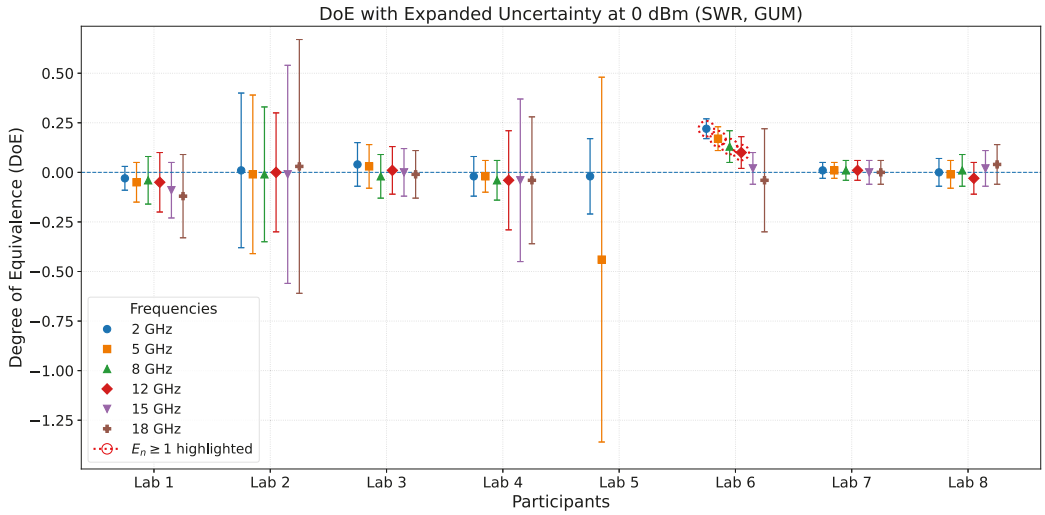


Figure 2. Degrees of equivalence with expanded uncertainties at 0 dBm for the SWR case according to the GUM method. Red dotted circles indicate points with $E_n \geq 1$.

https://doi.org/10.3390/metrology6030047

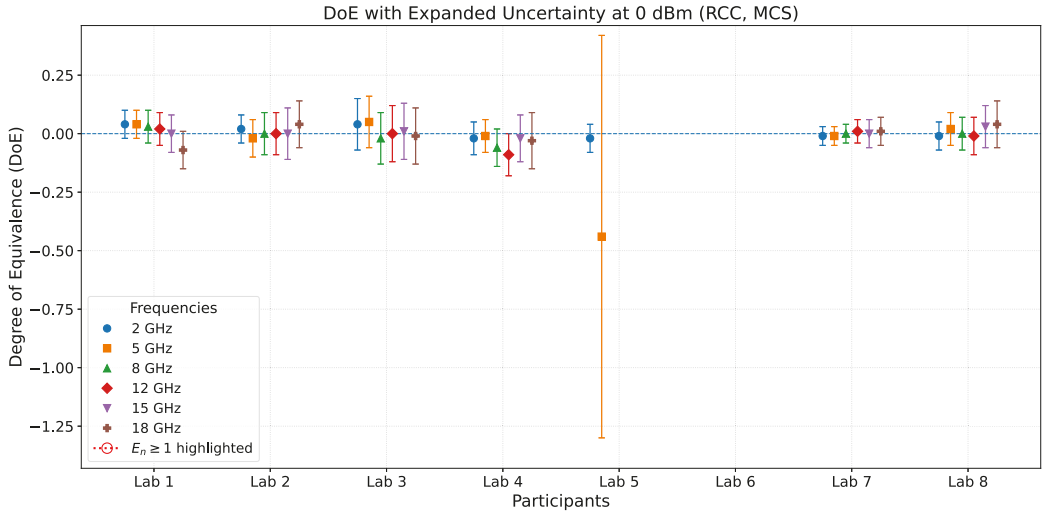


Figure 3. Degrees of equivalence with expanded uncertainties at 0 dBm for the RCC case according to the Monte Carlo simulation (MCS) method. Red dotted circles indicate points with $E_n \geq 1$.

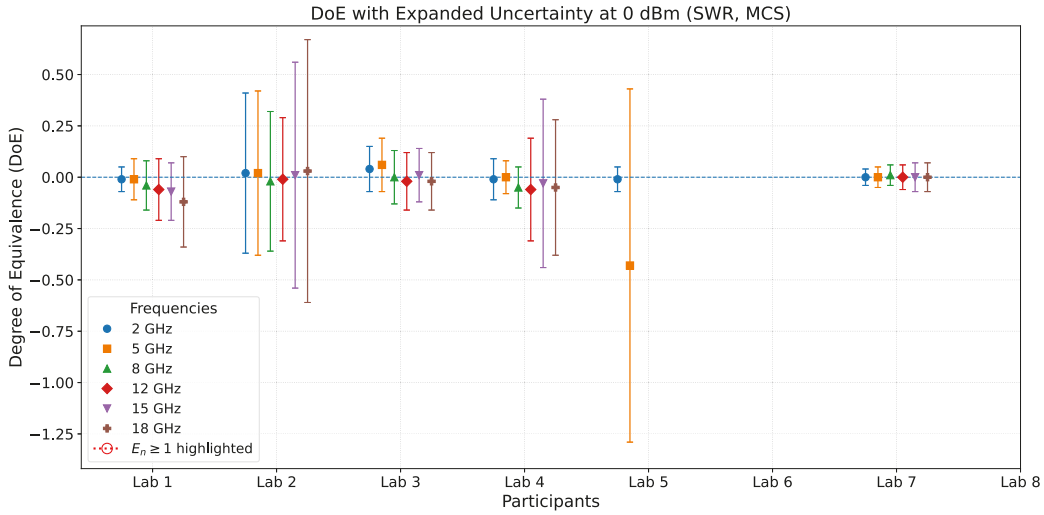


Figure 4. Degrees of equivalence with expanded uncertainties at 0 dBm for the SWR case according to the Monte Carlo simulation (MCS) method. Red dotted circles indicate points with $E_n \geq 1$.

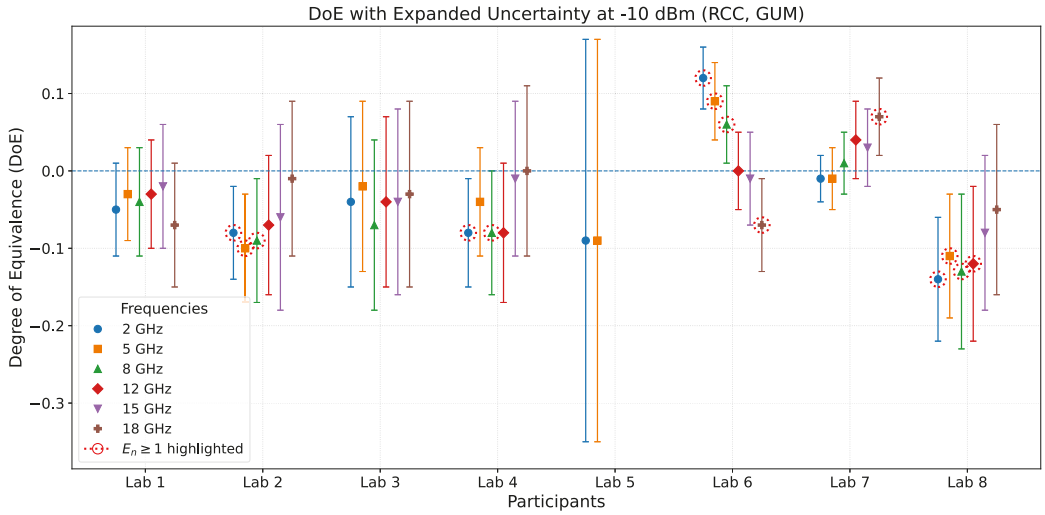


Figure 5. Degrees of equivalence with expanded uncertainties at −10 dBm for the RCC case according to the GUM method. Red dotted circles indicate points with $E_n \geq 1$.

https://doi.org/10.3390/metrology6030047

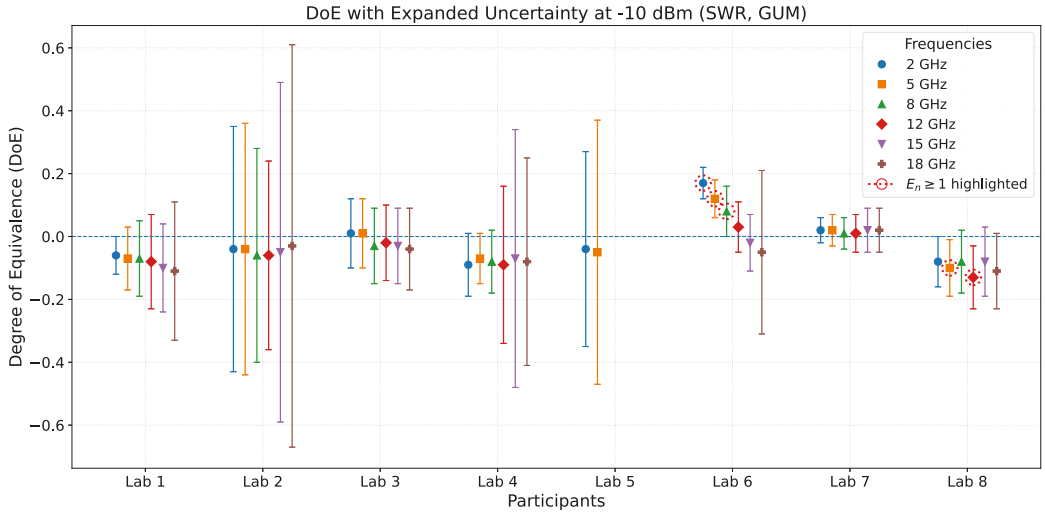


Figure 6. Degrees of equivalence with expanded uncertainties at −10 dBm for the SWR case according to the GUM method. Red dotted circles indicate points with $E_n \geq 1$.

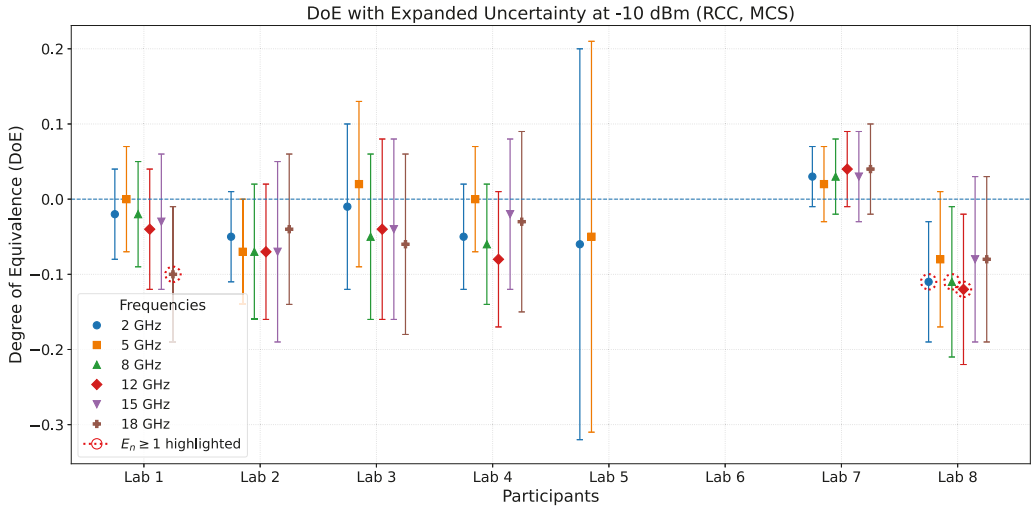


Figure 7. Degrees of equivalence with expanded uncertainties at −10 dBm for the RCC case according to the Monte Carlo simulation (MCS) method. Red dotted circles indicate points with $E_n \geq 1$.

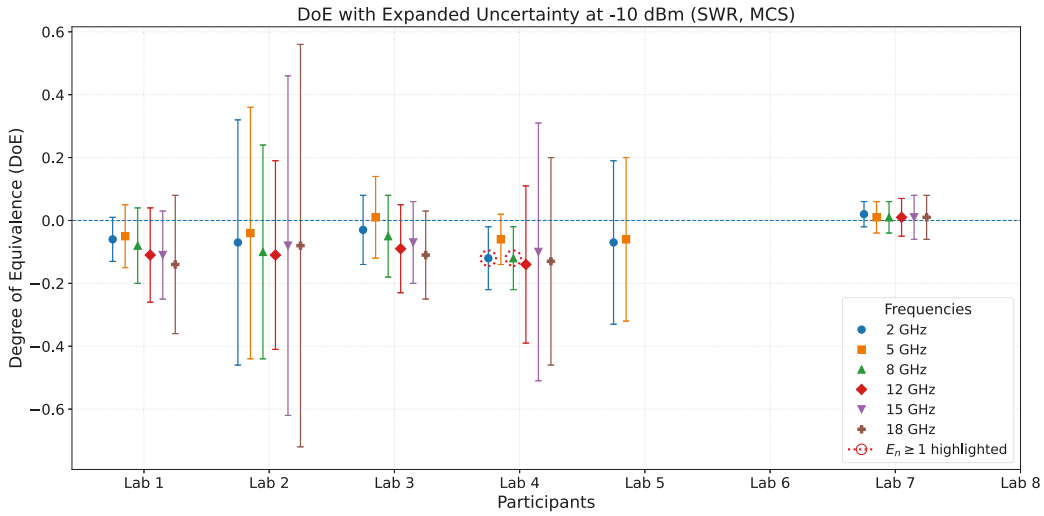


Figure 8. Degrees of equivalence with expanded uncertainties at −10 dBm for the SWR case according to the Monte Carlo simulation (MCS) method. Red dotted circles indicate points with $E_n \geq 1$.

https://doi.org/10.3390/metrology6030047

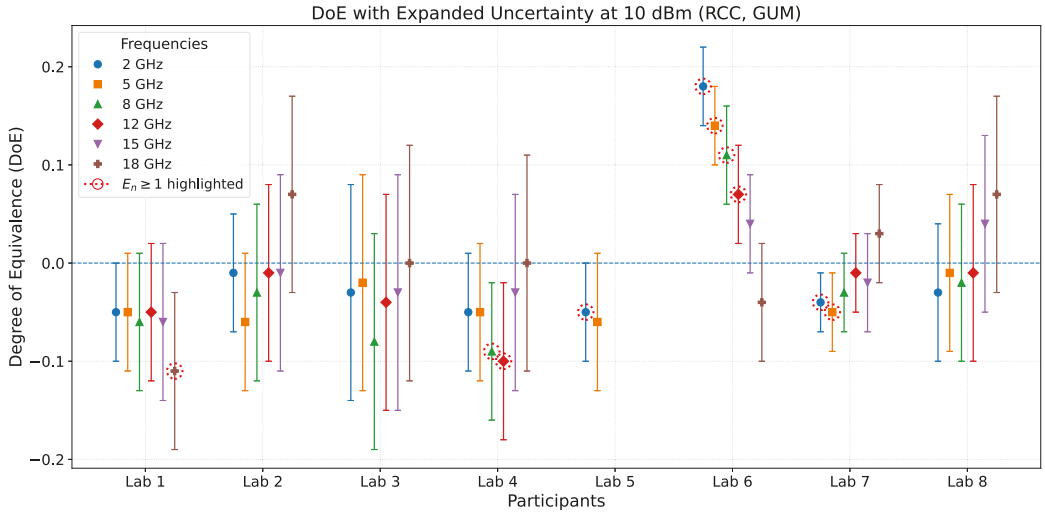


Figure 9. Degrees of equivalence with expanded uncertainties at 10 dBm for the RCC case according to the GUM method. Red dotted circles indicate points with $E_n \geq 1$.

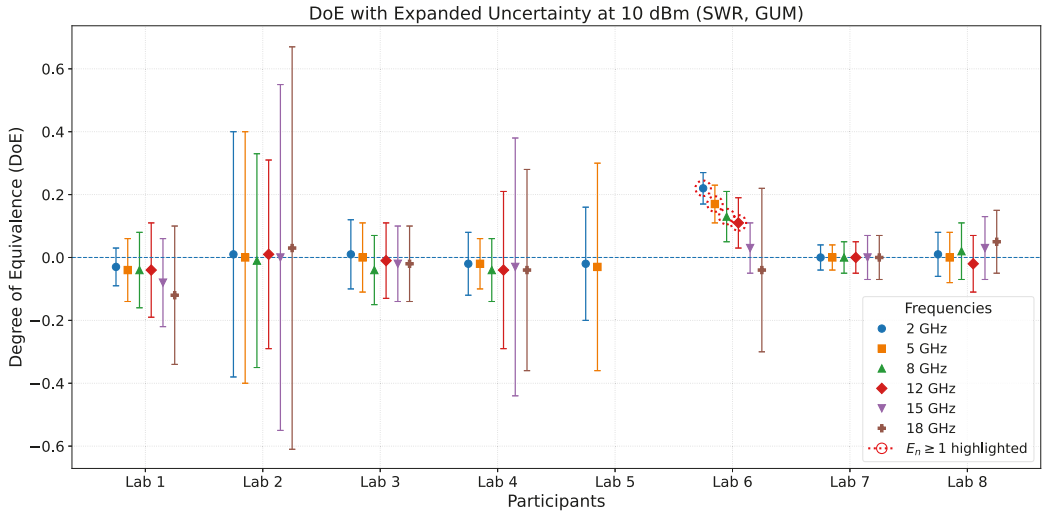


Figure 10. Degrees of equivalence with expanded uncertainties at 10 dBm for the SWR case according to the GUM method. Red dotted circles indicate points with $E_n \geq 1$.

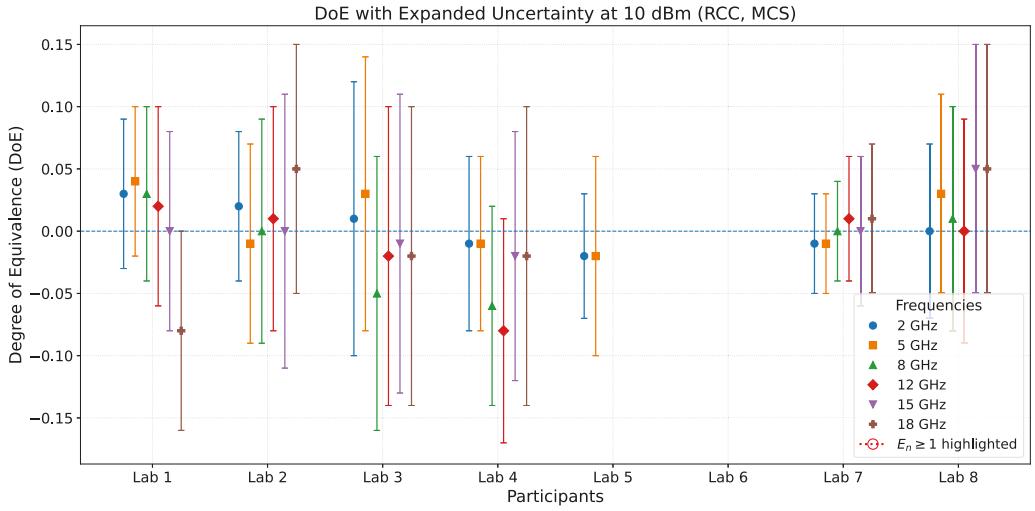


Figure 11. Degrees of equivalence with expanded uncertainties at 10 dBm for the RCC case according to the Monte Carlo simulation (MCS) method. Red dotted circles indicate points with $E_n \geq 1$.

https://doi.org/10.3390/metrology6030047

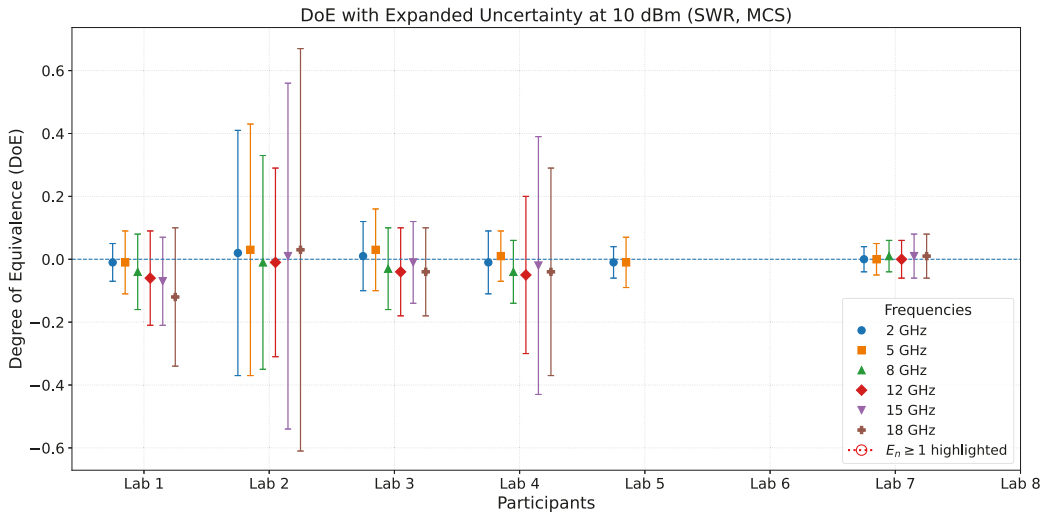


Figure 12. Degrees of equivalence with expanded uncertainties at 10 dBm for the SWR case according to the Monte Carlo simulation (MCS) method. Red dotted circles indicate points with $E_n \geq 1$.

The uncertainty values obtained using GUM and MCS approaches were generally consistent, although slight differences in uncertainty distributions were observed in certain cases.

6. Discussion

The comparison results highlight the influence of reflection coefficient modelling on RF power measurements. Differences between RCC- and SWR-based uncertainty evaluations demonstrate that modelling assumptions can significantly affect comparison outcomes.

The study also shows that the AutoRFPower software can harmonise measurement procedures and uncertainty evaluation across laboratories in conducted interlaboratory comparisons. Thus, the utilisation of such software helps to improve measurement process and uncertainty calculations.

Furthermore, the comparison provides insight into the applicability of automated measurement and uncertainty evaluation tools in RF power metrology. The results indicate that such tools can support reliable interlaboratory comparisons and contribute to the development of consistent RF power measurement methodologies.

The current version of AutoRFPower follows the standard inclusive approach, in which each participant's result also contributes to x_{CRV}. This can introduce a self-correlation bias, since a laboratory's own value pulls the reference value towards itself and may make performance metrics such as E_n appear more favourable. To mitigate this risk, incorporating the "exclusive statistics" proposed by Steele et al. [25], in which each participant is excluded from the reference value used to assess it, represents an important direction for future software refinements aimed at unbiased laboratory evaluations.

7. Conclusions

The comparison was successfully conducted among eight laboratories participating in the EPM project 22RPT04, "RFMicrowave2". The comparison results demonstrate generally good agreement among participants and confirm the feasibility of automated RF power measurement approaches. The high level of agreement observed across different frequencies and power levels confirms the validity of both the measurement methodology and the uncertainty evaluation approaches.

The scope of this project encompassed an interlaboratory comparison of RF power measurements using automatic power measurement software (AutoRFPower), which yielded

https://doi.org/10.3390/metrology6030047

favourable results. This allowed project participants to gain capability for automatic RF power measurement and uncertainty calculation. The study demonstrates that automated measurement workflows can be successfully implemented in RF power metrology without compromising accuracy or reliability.

The findings of this study support the integration of automated measurement and uncertainty evaluation tools into RF metrology practices and provide a basis for future harmonised comparison studies. In addition, the results highlight the importance of using vector-based mismatch modelling (RCC) for improved accuracy in high-frequency measurements.

Based on our findings, we suggest that previously measured vector RCCs of signal generators can be used as a travelling standard for RF power comparisons. This approach offers a practical and scalable alternative for future interlaboratory comparisons, reducing the need for mismatch characterisation.

Future work will focus on extending the automation capabilities demonstrated in this study, in order to design smarter and more adaptive metrology systems. Comprehensive reviews in recent literature have demonstrated that machine learning algorithms can successfully optimise complex measurement procedures and enable robust, data-driven metrology applications [26]. Building upon this, one particularly promising avenue is the integration of artificial intelligence (AI) techniques for the automatic extraction and interpretation of calibration procedures from manufacturers' documentation, thus enabling the generation of harmonised and machine-interpretable calibration workflows and helping less experienced laboratories implement complex measurement procedures in a consistent and traceable manner.

Furthermore, combining automated measurement systems with AI-based decision support mechanisms has the potential to improve uncertainty assessment and method selection processes. By integrating domain knowledge, historical measurement data, and formalised calibration requirements, future systems will be able to help operators choose optimal measurement strategies and identify potential sources of error. These advancements are likely to contribute to ongoing digital transformation efforts in the field of metrology.

Author Contributions: Conceptualisation, A.C., A.K.D., E.D., M.H., J.G., O.S., T.L., S.M., S.P., Ł.U., M.B. and E.Ç.; methodology, A.C., A.K.D., E.D., M.H., J.G., O.S., T.L., S.M., S.P., Ł.U., M.B., E.Ç. and H.O.; software, A.C., M.C.K. and H.O.; validation, A.C., A.K.D. and E.D.; formal analysis, A.K.D., E.D. and J.G.; investigation, A.K.D., E.D., M.H., J.G., O.S., T.L., S.M., S.P., Ł.U., M.B. and E.Ç.; resources, T.L.; data curation, A.K.D.; writing—original draft preparation, A.C. and A.K.D.; writing—review and editing, A.C., A.K.D., M.C.K. and E.D.; visualisation, A.C. and A.K.D.; supervision, H.O., M.H. and E.D.; project administration, E.D. and M.H. All authors have read and agreed to the published version of the manuscript.

Funding: This research was funded by the EPM project titled "RFMicrowave2" with grant number 22RPT04.

Data Availability Statement: No new data were created or analyzed in this study.

Acknowledgments: This study was conducted within the framework of the 22RPT04 RFMicrowave2 project, which has received funding from the European Partnership on Metrology, co-financed by the European Union's Horizon Europe Research and Innovation Programme and by the Participating States.

Conflicts of Interest: Spark Calibration Services and Trescal A/S have no commercial interest in this work. Spark Calibration Services used related software in the article to collect, analyse and interpret datas obtained from the measurements for the purpose of comparison. The software is not

https://doi.org/10.3390/metrology6030047

fully designed by Spark Calibration Services, it is developed by the participating states (Middle East Technical University, TUBITAK UME and Spark Calibration Services) within the 22RPT04 project.

Abbreviations

The following abbreviations are used in this manuscript:

AI	Artificial Intelligence
CIPM	International Committee for Weights and Measures
CMC	Calibration and Measurement Capability
CRV	Comparison Reference Value
DI	Designated Institute
DoE	Degree of Equivalence
EMC	Electromagnetic Compatibility
En	Normalised Error
EPM	European Partnership on Metrology
GUM	Guide to the Expression of Uncertainty in Measurement
IoMT	Internet of Measurement Things
JCGM	Joint Committee for Guides in Metrology
MCS	Monte Carlo Simulation
MRA	Mutual Recognition Arrangement
MW	Microwave
NMI	National Metrology Institute
PDF	Probability Density Function
RCC	Complex Reflection Coefficient
RF	Radio Frequency
SI	International System of Units
SWR	Standing Wave Ratio
UCaaS	Uncertainty Calculation as a Service
VNA	Vector Network Analyser

References

1. Salzenstein, P.; Wu, T.Y.; Pavlyuchenko, E. The Critical Role of International Comparisons in Global Metrology System: An Overview. *Metrology* **2025**, *5*, 74 . [CrossRef]
2. Janik, D.; Inoue, T.; Michaud, A. Final report on CCEM key comparison CCEM. RF-K10. CL (GT-RF/99-2)'Power in 50 Ω coaxial lines, frequency: 50 MHz to 26 GHz'–measurement techniques and results. *Metrologia* **2006**, *43*, 01009.
3. Patel, K.; Negi, P.; Swarup, R.; Kim, J.H.; Kang, J.S.; Chow, M.W.; Tsui, C.; Dressler, E.; Shay, W.T.; Li, H.; et al. Final report on APMP supplementary comparison P1-APMP. EM. RF-S3: APMP comparison of 50 ohm coaxial mismatches. *Metrologia* **2012**, *49*, 01013.
4. Pozar, D.M. *Microwave Engineering*, 4th ed.; John Wiley & Sons, Inc.: Hoboken, NJ, USA, 2012; pp. 26–30.
5. Weidman, M.P. *Direct Comparison Transfer of Microwave Power Sensor Calibrations*; U.S. Government Printing Office: Washington, DC, USA, 1996.
6. Jargon, J.A.; Gu, D.; Long, C.J.; Hagerstrom, A.M.; Stelson, A.C.; Monke, A.F. *Theoretical Basis of the Direct-Comparison System for Power Calibration Including Equivalent Source Mismatch*; Technical Report; National Institute of Standards and Technology (NIST): Gaithersburg, MD, USA, 2019.
7. Jia, J.; Kuang, J.; He, Z.; Fang, J. Design of automated test system based on GPIB. In *Proceedings of the 2009 9th International Conference on Electronic Measurement & Instruments*; IEEE: New York, NY, USA, 2009; pp. 1-943–1-948. [CrossRef]
8. *JCGM 100:2008*; Evaluation of Measurement Data—Guide to the Expression of Uncertainty in Measurement (GUM). Technical Report; Joint Committee for Guides in Metrology (JCGM): Geneva, Switzerland, 2008.
9. *JCGM 101:2008*; Evaluation of Measurement Data—Supplement 1 to the GUM: Propagation of Distributions Using a Monte Carlo Method. Technical Report; Joint Committee for Guides in Metrology (JCGM): Geneva, Switzerland, 2008.
10. RFMicrowave2 Project. Development of RF and Microwave Metrology Capability II. 2026. Available online: https://rfmwii.cmi.gov.cz/index.php (accessed on 11 March 2026).
11. Kaya, M.C.; Saeedi Nikoo, M.; Schwartz, M.L.; Oguztuzun, H. Internet of measurement things architecture: Proof of concept with scope of accreditation. *Sensors* **2020**, *20*, 503. [CrossRef] [PubMed]

https://doi.org/10.3390/metrology6030047

12. Çetinkaya, A.; Doğan, A.K.; Danaci, E.; Oğuztüzün, H. Autorfpower: Automatic rf power measurement software for metrological applications. In *Proceedings of the 2021 2nd International Informatics and Software Engineering Conference (IISEC)*; IEEE: New York, NY, USA, 2021; pp. 1–4.
13. Cetinkaya, A.; Kaya, M.C.; Danaci, E.; Oguztuzun, H. Uncertainty calculation as a service: Integrating cloud-based microservices for enhanced calibration and DCC generation. *Sensors* **2024**, *24*, 5651. [CrossRef] [PubMed]
14. Neyezhmakov, P.; Zub, S.; Pivnenko, S. Preliminary e-infrastructure for digital metrology. *Meas. Sens.* **2022**, *23*, 100398. [CrossRef]
15. Verma, P. Potential role of metrology in digital transformation for quality infrastructure. *MAPAN* **2024**, *39*, 111–118. [CrossRef]
16. Cox, M.G. The evaluation of key comparison data. *Metrologia* **2002**, *39*, 589–595. [CrossRef]
17. Rukhin, A.L.; Sedransk, N. Statistics in metrology: International key comparisons and interlaboratory studies. *J. Data Sci.* **2007**, *5*, 393–412. [CrossRef]
18. Koepke, A.; Lafarge, T.; Possolo, A.; Toman, B. Consensus building for interlaboratory studies, key comparisons, and meta-analysis. *Metrologia* **2017**, *54*, S34–S62. [CrossRef]
19. Cetin, E.; Doğan, A.K.; Cetinkaya, A.; Danaci, E. VNA-Based Vector Reflection Coefficient Measurement Technique for Powered RF Signal Generators. *Sensors* **2026**, *26*, 3590. [CrossRef] [PubMed]
20. Guldbrandsen, T. Uncertainty contributions from mismatch in microwave measurements. *IEE Proc.-Microwaves Antennas Propag.* **2001**, *148*, 393–397. [CrossRef]
21. Kartal Dogan, A.; Berginc, M.; Cetin, E.; Danacı, E.; Grajciar, J.; Lippert, T.; Prendergast, S.; Sibonjic, O. *Comparison on RF Power Measurements Using Automatic Power Measurement Software*; Zenodo: Genève, Switzerland, 2026. [CrossRef]
22. Danacı, E.; Kartal Doğan, A.; Çiçek, E.C.; Çetinkaya, A.; Kaya, M.Ç.; Oğuztüzün, M.S.H.; Tunay, G. Uncertainty Evaluation Using Law of Propagation and Monte Carlo Simulation Methods with the AutoRFPower Measurement Software. *Konya J. Eng. Sci.* **2024**, *12*, 596–607. [CrossRef]
23. Harris, I.; Warner, F. Re-examination of mismatch uncertainty when measuring microwave power and attenuation. In *Proceedings of the IEE Proceedings H (Microwaves, Optics and Antennas)*; IET: Stevenage, UK, 1981; Volume 128, pp. 35–41.
24. *ISO/IEC 17043*; Conformity Assessment—General Requirements for Proficiency Testing. International Organization for Standardization: Geneva, Switzerland, 2023.
25. Steele, A.; Wood, B.; Douglas, R. Exclusive statistics: Simple treatment of the unavoidable correlations from key comparison reference values. *Metrologia* **2001**, *38*, 483–488. [CrossRef]
26. Vallejo, M.; De La Espriella, C.; Gómez-Santamaría, J.; Ramírez-Barrera, A.F.; Delgado-Trejos, E. Soft metrology based on machine learning: A review. *Meas. Sci. Technol.* **2020**, *31*, 032001.

Disclaimer/Publisher's Note: The statements, opinions and data contained in all publications are solely those of the individual author(s) and contributor(s) and not of MDPI and/or the editor(s). MDPI and/or the editor(s) disclaim responsibility for any injury to people or property resulting from any ideas, methods, instructions or products referred to in the content.

https://doi.org/10.3390/metrology6030047

metrology

MDPI

Article

Dual-Mode Standardization of Emerging Material Specifications: Structuring Measurement-Based Information for Market Decision-Making

Akira Ono

National Institute of Advanced Industrial Science and Technology, Tsukuba 305-8560, Japan; onoakira_oozora@yahoo.co.jp

Abstract

Emerging materials often face challenges in market adoption due to limited comparability and reliability of measurement-based material information, despite their potential to drive technological innovation. While standardization is widely recognized as an important mechanism for market diffusion, existing approaches provide limited insight into how material specifications facilitate the comparative evaluation of material characteristics and their use in market decision-making. This study introduces a novel perspective, conceptualizing standardization as an institutional infrastructure designed to coordinate the generation, sharing, and evaluation of measurement-based material information across industries, standards development organizations (SDOs), and markets. Within this framework, the study distinguishes between two complementary types of standards for material specifications. Type A standards enable the structured disclosure of measured characteristic values and associated measurement uncertainties, allowing application-specific evaluation without predefined acceptance criteria. In contrast, Type B standards define predefined characteristic values and compliance criteria, providing a basis for conformity assessment, certification, and quality assurance. These two types may be understood as complementary mechanisms that fulfill different functions of comparability and compliance under varying technological and market conditions in emerging material systems. Consequently, they contribute to both innovation-oriented market evaluation and quality-assured market acceptance.

Keywords: standardization; emerging materials; nanomaterials; innovation; material specifications; comparability; compliance; conformity assessment

1. Introduction

Emerging materials are increasingly developed with the expectation of generating industrial and societal value through market adoption. Despite their unique and enhanced properties, such materials often encounter difficulties in achieving early market entry. One possible reason lies in both technological uncertainty and the limited capacity of existing specification systems to translate material characteristics into decision-relevant information for market use.

This challenge reflects broader issues in how measurement-based information is structured, communicated, and evaluated. Although standardization is acknowledged as a pivotal driver of market diffusion, the current literature offers scarce insight into how specification systems structure information and support decision-making across industries, standards development organizations (SDOs), and markets.

Prevailing perspectives have primarily emphasized compliance and conformity assessment based on predefined criteria, while less attention has been given to the roles of interpretation, comparison, and application-specific evaluation. In this study, comparability refers primarily to the ability to evaluate measurement-based material characteristics across products within common specification frameworks. The terms "Type A" and "Type B" used in this study refer to functional categories of specification standards. To avoid ambiguity with established metrological terminology, it should be clarified that these labels are distinct from the Type A and Type B methods of evaluating measurement uncertainty in the Guide to the Expression of Uncertainty in Measurement (GUM) [1], though both concepts share a fundamental connection to measurement-based data reliability.

The standardization of emerging materials is particularly challenging because it must accommodate heterogeneous characteristics, diverse measurement practices, and evolving application requirements. In contrast to mature material systems—where standardized specifications and conformity assessment schemes are relatively well established—emerging materials are often associated with independently developed product specifications, diverse measurement approaches, and limited comparability across products, which may hinder effective market evaluation.

Existing studies have examined the relationship between standardization and innovation from economic, institutional, and technological perspectives [2–6], while metrological research has focused on measurement validity and applicability [7]. However, relatively limited attention has been paid to how specification systems organize measurement-based information and support market-oriented decision-making processes.

New specification dynamics are clearly observable in the frontlines of nanotechnology standardization. The recent publication of Type A standards—such as ISO/TS 19808:2020 for carbon nanotube suspensions [8], ISO/TS 9651:2025 for graphene-related 2D materials [9], and ISO/TS 21236-2:2021 for clay nanomaterials [10]—demonstrates an increasing industrial reliance on structured data disclosure rather than rigid pass/fail criteria. While these existing deliverables successfully establish a baseline for characterizing emerging materials, the previous literature offers limited general frameworks to translate such measurement-based information into decision-relevant formats for market adoption, underscoring the practical necessity of the proposed dual-mode framework.

In response to this issue, this study proposes a complementary perspective that interprets standardization as an interaction-based infrastructure for organizing and coordinating information across industries, SDOs, and markets. Within this framework, industry generates and discloses specification information, SDOs organize and harmonize it, and markets evaluate its value in relation to specific applications.

Building on this perspective, the study distinguishes between two complementary types of standards for material specifications. Figure 1 illustrates a structural framework in which product specifications in emerging materials are transformed into decision-relevant information through two distinct but complementary pathways.

Type A standards define frameworks for representing characteristic values and associated measurement uncertainties, enabling application-specific evaluation based on disclosed data. Type B standards define predefined characteristic values and compliance criteria, providing a basis for conformity assessment and quality assurance in more mature material markets. Rather than representing sequential stages, these two types may be understood as complementary mechanisms that support different functions of comparability and compliance under varying technological and market conditions. These distinctions are exemplified in nanomaterial standardization practices, including IEC TS 62565-1:2023 [11], other parts of the IEC 62565 series, and ISO nanomaterial standards developed by ISO/TC 229 [12].

https://doi.org/10.3390/metrology6020036

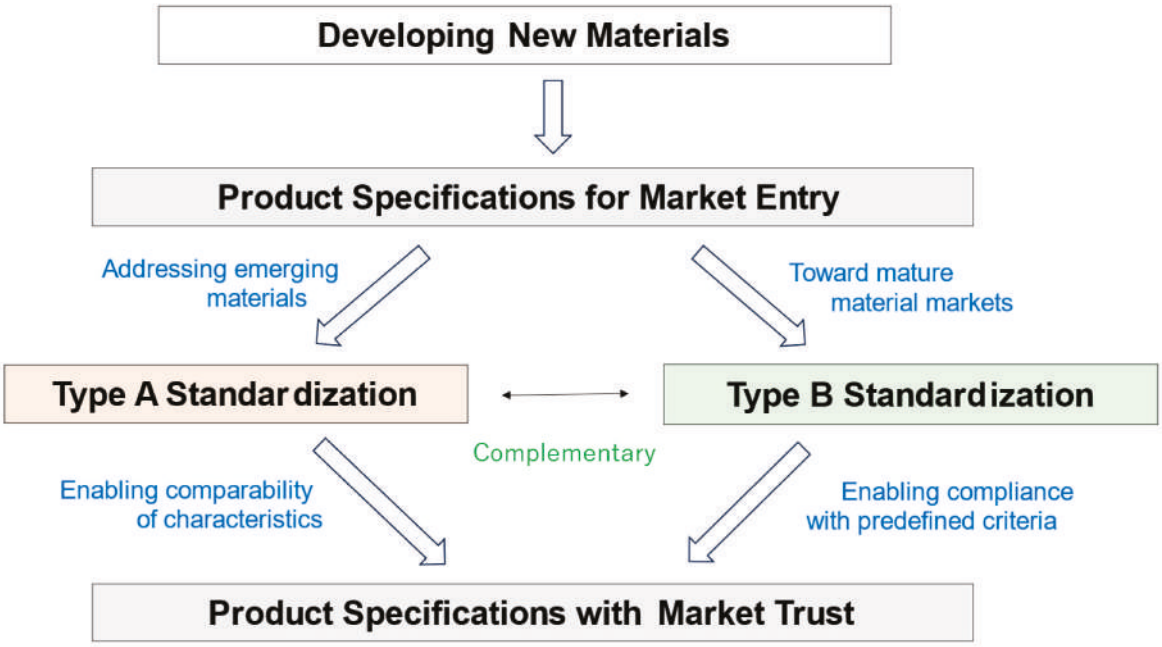


Figure 1. Dual-mode pathways for structuring emerging material specifications.

In addition to serving as a compliance-oriented system, standardization provides a framework for facilitating the comparative evaluation and market utilization of emerging materials. Section 2 examines the structural characteristics of these pathways, Section 3 analyzes their interaction dynamics, and subsequent sections discuss implications for standardization strategies.

2. Structuring of Emerging Material Specification Systems

2.1. Structural Distinction Between Type A and Type B Standards

Figure 2 highlights the structural distinction between Type A and Type B standards in emerging materials. These two complementary pathways exhibit different specification structures and conformity assessment logics. Type A standards enable comparability across diverse characteristics with associated uncertainties through standardized yet adaptable measurement methods. They also support evaluation against manufacturer-declared values within a framework for structured disclosure and interpretation. In contrast, Type B standards support compliance through predefined characteristic values, conformity criteria, and standardized methods.

Type B standards operate under more stabilized conditions. They define predefined characteristic values, adopt standardized measurement methods, and support conformity assessment against established criteria. As a result, Type B standards ensure quality assurance and support certification in mature markets.

Type A and Type B standards thus play complementary roles in the standardization of emerging materials, supporting different modes of decision-making under varying conditions of material and market development.

2.2. Structural Differentiation of Product Specification Systems

Product specification systems in industry may exhibit different structural configurations depending on market and material conditions. Figure 3 illustrates three typical forms of in-market product specification systems.

https://doi.org/10.3390/metrology6020036

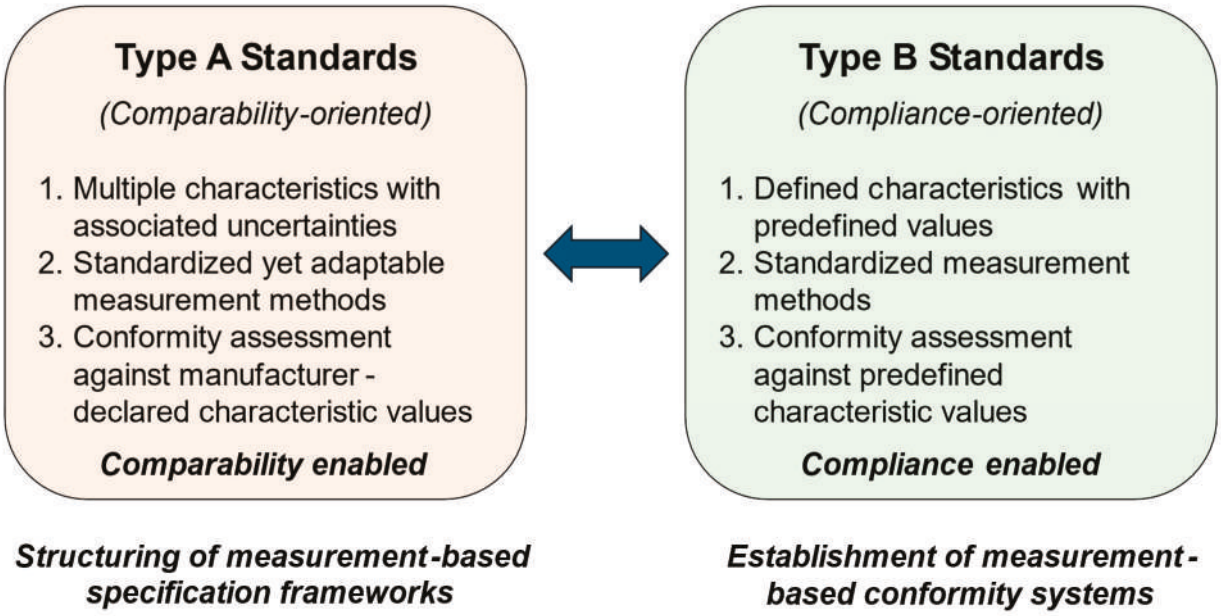


Figure 2. Structural distinction between Type A and Type B standards for emerging materials.

Three Types of In-market Product Specifications

Product specification types	Independent	Type A-aligned	Type B-aligned
	Innovation-oriented	Comparability-oriented	Compliance-oriented
Framework	Diversely structured	Structured for comparative evaluation	Structured for conformity assessment
Characteristics	Limited comparability	Comparable with uncertainty information	Used as acceptance criteria
Measurement Methods	Non-standardized	Standardized yet adaptable	Fully standardized
Conformity assessment	Not yet established	Against manufacturer - declared values	Against predefined acceptance values
Outcome	Diverse innovations with limited comparability	Comparability enabled, preserving innovation	Compliance achieved, quality assured

Figure 3. Structural differentiation of three types of in-market product specifications.

In innovation-oriented domains, product specifications are often independently structured, characterized by diverse characteristics and non-standardized measurement methods. In such contexts, comparability across products remains limited, although this diversity may support a broad range of technological innovations and exploratory product development.

Type A standards provide a framework for structuring comparability across diverse product specifications. Within this configuration, manufacturer-issued specifications become comparable through standardized yet adaptable measurement frameworks while preserving characteristic diversity and ongoing innovation. Such frameworks support market evaluation and early-stage adoption of emerging materials.

https://doi.org/10.3390/metrology6020036

In mature material domains where product characteristics and acceptance criteria are established, Type B standards support conformity assessment against predefined acceptance values. In these contexts, measurement methods are highly standardized, enabling certification, quality assurance, and broad market acceptance. Type B-aligned product specifications refer to manufacturer-issued specifications that demonstrate conformity with predefined acceptance criteria established by Type B standards. When conformity of these product specifications is ascertained by a certification body, certification provides formal assurance of conformity and supports broader market acceptance.

These differentiated specification frameworks suggest that standardization may perform different coordination functions depending on the characteristics of the market and material domain. Type A-aligned systems primarily support comparability across diverse products, whereas Type B-aligned systems support conformity assessment and standardized quality assurance. Rather than representing competing approaches, these frameworks may be understood as complementary forms of specification coordination associated with different industrial and technological contexts.

While Figure 3 illustrates the structural differentiation of product specification systems, the following section focuses on the operational characteristics of Type A- and Type B-aligned systems.

3. Interaction Dynamics in the Standardization of Emerging Material Systems

This section examines how Type A- and Type B-aligned specification systems operate and interact across emerging material markets. The analysis focuses on functional differentiation, institutional arrangements for conformity assessment, and interaction dynamics among markets, industry, and SDOs. It further examines how these relationships evolve across phases of material maturity.

The establishment of standardized material specifications is essential to mitigate information asymmetry and facilitate efficient market transactions. It should be noted, however, that while market decision-making broadly encompasses economic, financial, and political considerations, the functional roles of Type A and Type B standards are strictly focused on supporting technical decisions. These standards serve as a reliable infrastructure specifically for evaluating the technical equivalence, performance, and compatibility of materials.

3.1. Functional Differentiation of Type A- and Type B-Aligned Specifications

As illustrated in Figure 4, Type A- and Type B-aligned systems exhibit different operational characteristics in how measurement-based information is disclosed, interpreted, and utilized for market decision-making and conformity assessment.

Type A-aligned product specifications are characterized by the disclosure of relevant characteristic values together with associated uncertainties, enabling application-specific interpretation and market decision-making. Interlaboratory comparison studies may support the evaluation of measurement uncertainty. This data-centric architecture emphasizes transparent disclosure and user-driven contextual interpretation of measured data rather than predefined acceptance criteria, allowing user industries to determine the suitability of materials according to diverse and evolving requirements.

Within such systems, conformity assessment may be performed relative to manufacturer-declared values using standardized measurement frameworks and procedures. Rather than determining conformity against fixed acceptance thresholds, evaluation is conducted through comparative interpretation of disclosed measurement results under shared measurement conditions. Consequently, Type A-aligned systems enable comparability and adaptive

https://doi.org/10.3390/metrology6020036

decision-making, thereby contributing to market formation in emerging material domains. Furthermore, beyond this enhanced comparability, Type A standards empower users to efficiently screen and select candidate materials by defining a minimum yet essential set of characteristics. In doing so, these standards play a pivotal role in institutionally defining the identity of an emerging material during its early market stages.

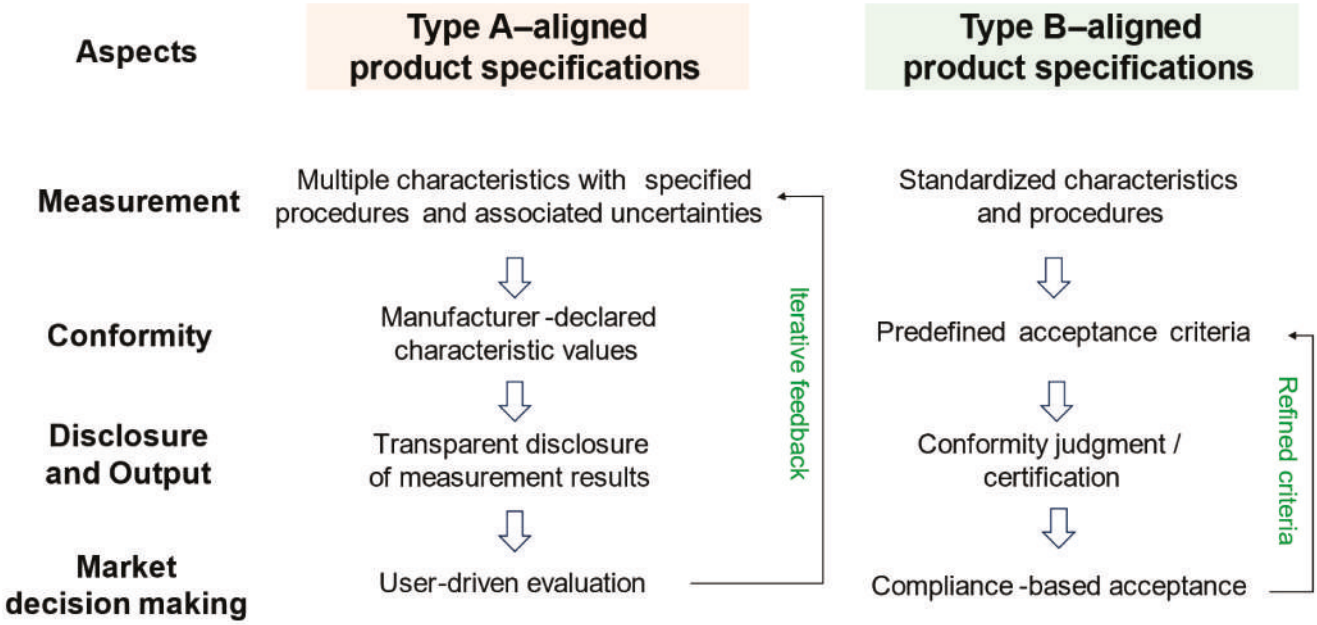


Figure 4. Operational characteristics of Type A- and Type B-aligned specification systems.

In contrast, Type B-aligned systems are structured around predefined characteristic values and acceptance criteria associated with specific applications and performance requirements. Measurement methods and procedures are highly standardized to support reproducible evaluation and conformity assessment against predefined criteria. Under these conditions, certification and quality assurance become increasingly important mechanisms for establishing reliability and market trust.

Compared with Type A-aligned systems, Type B-aligned systems emphasize conformity and consistency rather than contextual interpretation of disclosed measurement results. Such systems support broader industrial harmonization, stable quality assurance, and market acceptance in mature material domains where application requirements and evaluation criteria have become sufficiently stabilized.

These operational differences indicate that Type A- and Type B-aligned systems support distinct but complementary coordination functions. Type A-aligned systems primarily support comparability and adaptive evaluation under conditions of technological and application uncertainty, whereas Type B-aligned systems support conformity assessment and standardized quality assurance under more stabilized market conditions.

3.2. Institutional Architecture of Conformity Assessment and Certification

Conformity assessment in emerging materials is shaped by institutional interactions among market forces, industrial practices, and SDO activities. As illustrated in Figure 5, both Type A and Type B standards are applied to a common institutional process involving testing laboratories and certification bodies. They enable dual pathways to conformity and certification of products: one against manufacturer-declared values and the other against predefined values. This structure extends certification beyond conventional compliance-

https://doi.org/10.3390/metrology6020036

based frameworks, thereby supporting broader market decision-making, including quality evaluation and assurance of emerging materials.

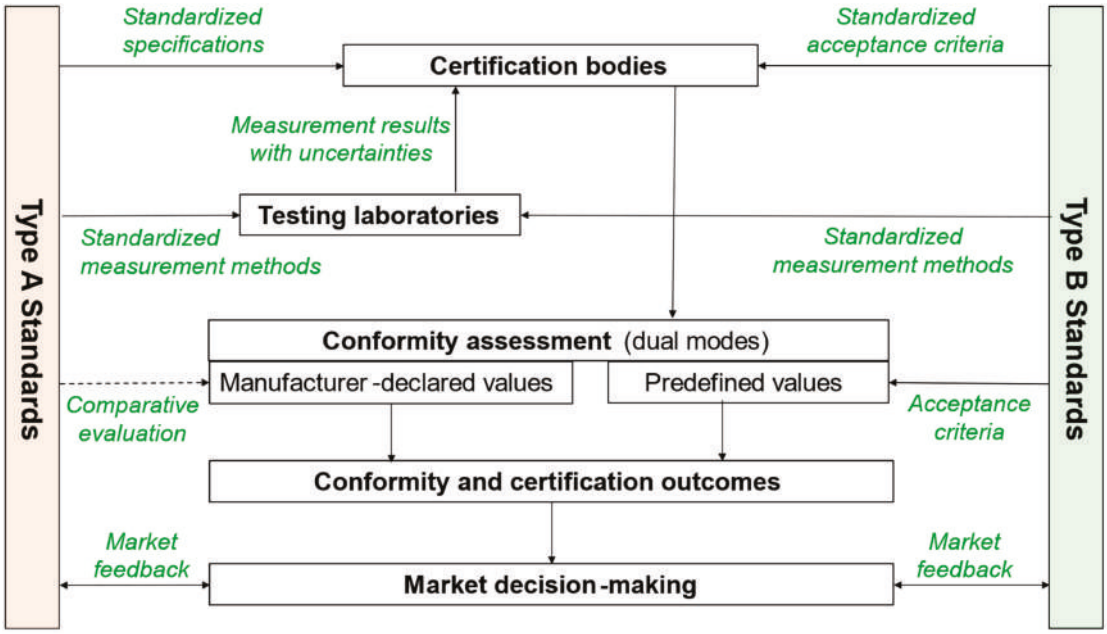


Figure 5. Institutional architecture enabling conformity assessment against manufacturer-declared values and predefined values.

3.3. Interaction Dynamics Among Research Institutions, Industry, SDOs, and Markets

Figure 6 illustrates the interaction dynamics among applied science-oriented research institutions, industry, SDOs and markets. In this study, applied science-oriented research institutions refer to organizations that support the transition of scientific and technological outcomes toward industrial and societal implementation by translating innovations into product specifications through activities such as measurement development, material characterization, specification coordination, and standardization.

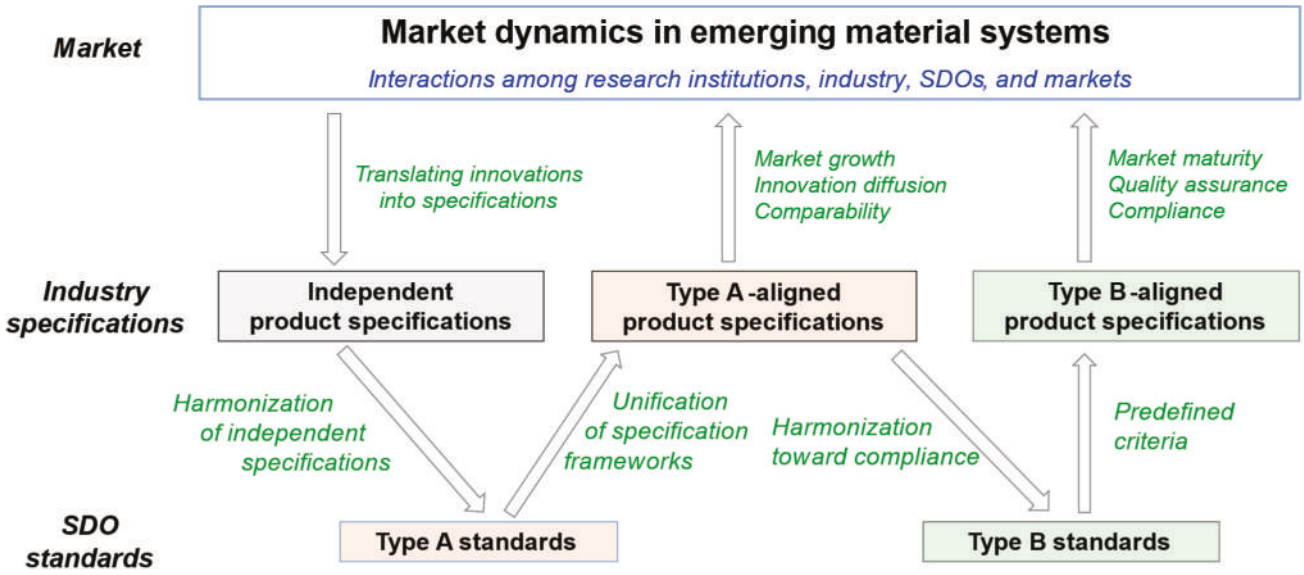


Figure 6. Market dynamics and stakeholder interactions in the standardization of emerging material systems.

https://doi.org/10.3390/metrology6020036

The selection among the three industry product specification forms is not determined solely by material maturity, but also by the strategic discretion of individual manufacturers according to their innovation objectives, technological maturity, target applications, market requirements, and certification needs. While there is an inherent evolutionary time-lag in the development of institutional frameworks—where Type A standards precede Type B standards to establish initial comparability—they fundamentally continue to coexist over the long term during the market utilization phase. In this manner, rather than following a rigid, linear replacement pathway, independent, Type A-aligned, and Type B-aligned product specifications simultaneously coexist across materials and application domains to serve complementary functions.

These processes are closely coupled with market dynamics. In early stages, diverse innovations generate fragmented specifications that reflect technological diversity. Applied science-oriented research institutions may contribute to this process by supporting the development of measurement frameworks, material characterization, harmonization activities, and specification infrastructures that facilitate the translation of emerging technologies into industrial applications.

The introduction of Type A-aligned specifications enables the structuring of specification frameworks and improves the comparability of measurement-based material characteristics without constraining innovation, thereby facilitating industrial adoption and early market growth. As markets expand and demands for reliability increase, further harmonization leads to the emergence and adoption of Type B-aligned specifications, supporting quality assurance, market maturation, and strengthened trust.

These interactions indicate that standardization operates as an adaptive infrastructure in which market dynamics, industrial practices, research institutions, and SDO activities are structurally interdependent. Changes in any one domain may therefore induce adaptive responses and reconfigurations in the others, rather than following a simple linear progression.

To bridge the proposed conceptual framework with the practical operations of standards development organizations (SDOs), the roles of Type A and Type B standards can be explicitly mapped onto existing ISO/IEC deliverables. As illustrated in Figure 6, these standards function to align independent industrial specifications with harmonized frameworks. Consequently, they rely on normative statements realized through Technical Specifications (TSs) for developing technical fields, or International Standards (ISs) for stabilized ones.

For emerging materials, which are often characterized by evolving technologies and markets, it is recommended that a staged evolutionary pathway be prioritized. Under this approach, deliverables are initially published as TSs to capture market feedback and subsequently converted into full ISs. A prominent practical example is found in ISO/TC 229 and IEC/TC 113 (nanotechnologies), where material specification standards are routinely developed first as TSs and later upgraded to ISs as the technology matures.

3.4. Dynamics of Type A and Type B Standards Across Material Maturity Phases

The interactions described in the preceding sections give rise to dynamic relationships among material maturity, market expansion, and standardization. Figure 7 illustrates the distributed contributions of Type A and Type B standards across material maturity phases.

In emerging phases, diverse innovations originating from research and development coexist with limited market adoption. In such contexts, Type A standards play a central role by enabling comparability across products through the comparative evaluation of measurement-based characteristics without constraining technological diversity. In particular, many Type A standards published by ISO/TC 229 require the evaluation and reporting of measurement uncertainty [12], thereby reinforcing the metrological basis for

https://doi.org/10.3390/metrology6020036

the comparative evaluation of material characteristics. Type A standards also provide a basis for conformity assessment against manufacturer-declared values, thereby facilitating market evaluation and the early-stage adoption of emerging materials.

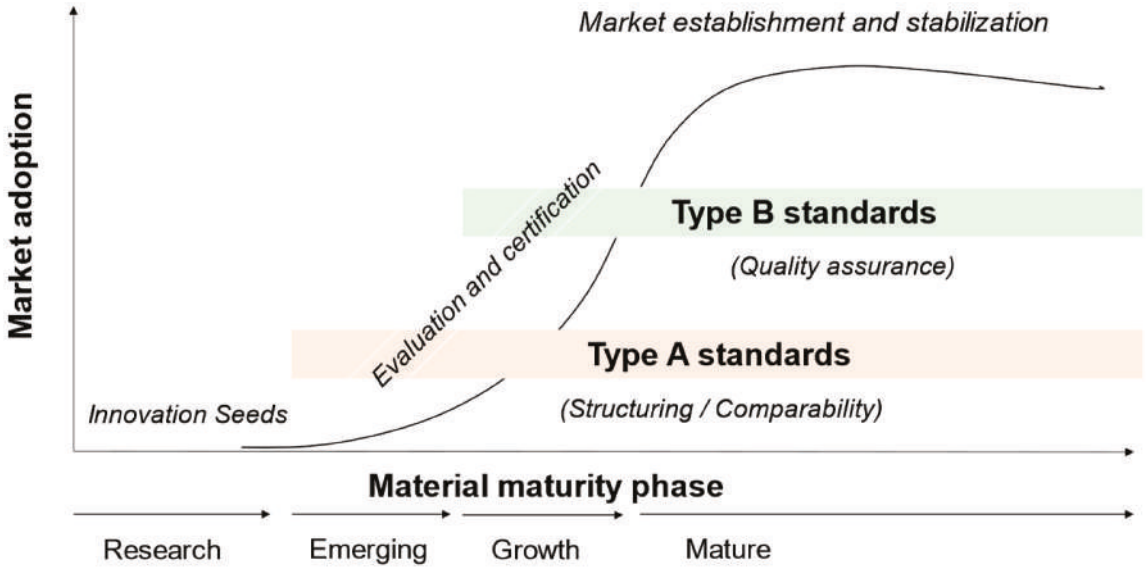


Figure 7. Distributed contributions of Type A and Type B standards across material maturity phases.

As material markets expand, increasing demands for reliability, certification, and standardized quality assurance strengthen the role of Type B standards. These standards provide predefined acceptance values for application-essential characteristics and fully standardized measurement methods that support conformity assessment, certification, and broader market acceptance.

In mature phases, Type B standards contribute significantly to market stabilization by enabling quality assurance, certification, and reliable large-scale commercialization. At the same time, Type A standards continue to enhance comparability and conformity assessment against manufacturer-declared values in response to ongoing technological innovation and evolving market needs. Rather than representing a unidirectional transition, Type A and Type B standards perform complementary functions with the increasing role of Type B standards.

3.5. Standardization Dynamics in Mature Material Systems

This section focuses on standardization dynamics in mature material systems in a stabilized market context.

In this context, these dynamics operate in a configuration where Type B standards dominate the organization of specification and conformity assessment structures across markets, industry, and SDOs. Figure 8 illustrates this configuration. Industry specifications are aligned with Type B standards, enabling consistent conformity assessment and certification against predefined characteristic values. Market maturity is sustained through widespread industrial adoption and established certification systems.

Ongoing improvements in material characteristics are progressively incorporated into product specifications, reflecting application-specific requirements. Notably, Type A-based specification elements are increasingly incorporated into Type B-based systems, supporting ongoing refinement and adaptation without requiring fundamental restructuring.

As a result of this incorporation, and because materials are evaluated in relation to specific applications through standardized measurement procedures, dual modes of conformity assessment are sustained: conformity assessment against characteristic values

https://doi.org/10.3390/metrology6020036

declared by individual companies, and conformity assessment against characteristic values defined by Type B standards.

This stabilized regime demonstrates that standardization in mature material systems combines consolidation and harmonization with sustained dynamics in which stability and flexibility coexist. Type B standards provide a stable foundation for certification and quality assurance, while Type A-based elements sustain adaptability and ongoing innovation.

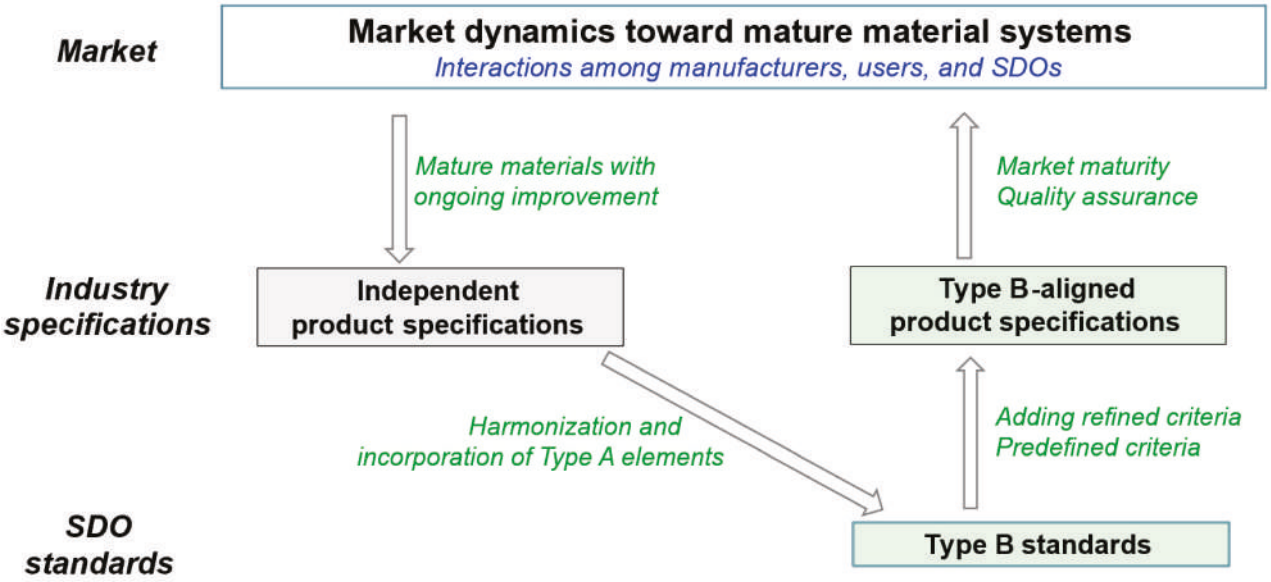


Figure 8. Market dynamics and stakeholder interactions in the standardization toward mature material systems.

4. Integrated Framework for Emerging Material Standardization Systems

This section presents an integrated framework that relates specification architecture and standardization dynamics to provide a conceptual perspective on standardization across phases of material maturity. Rather than describing standardization as a linear progression, the framework explains how different specification systems coexist, interact, and fulfill distinct functions under varying technological and market conditions. From this perspective, standardization may be understood not as a static endpoint, but as an adaptive infrastructure shaped by interactions among technological development, industry practices, and institutional standardization activities.

In emerging material domains, specification activities are often diverse, parallel, and independently developed, reflecting evolving material characteristics, measurement methods, and application requirements. In such contexts, standardization provides organizing principles that improve comparability across diverse specification activities without constraining innovation, as illustrated in Figure 3.

Within this framework, Type A and Type B standards function as complementary but distinct components of an integrated standardization system. Type A standards establish a common structural basis for defining measurement-based characteristics while maintaining flexibility for diverse technological approaches. This contributes to the development of product specifications within a shared framework, translating technological innovation into decision-relevant information, enhancing comparability, and enabling conformity assessment against manufacturer-declared values during early-stage market formation.

In contrast, Type B standards define predefined characteristic values and associated measurement frameworks, providing a shared basis for application-specific performance

https://doi.org/10.3390/metrology6020036

evaluation. This enables conformity assessment against predefined values within a shared reference framework, supporting reliability, quality assurance, certification, and broader market acceptance in more mature material systems.

Across phases of material maturity, the framework illustrates the coexistence of innovation-oriented and quality assurance-oriented standardization. Type A standards sustain comparability and technological differentiation, whereas Type B standards provide acceptance criteria based on standardized methods, thereby enabling conformity assessment and certification. Importantly, this does not represent a unidirectional transition or a final endpoint. Rather, Type B-aligned systems continue to evolve through the ongoing refinement and extension of predefined characteristic values, while increasingly incorporating Type A-based specification elements.

Overall, the proposed framework suggests that standardization may operate as an integrative mechanism linking scientific research, technological development, and market formation. It clarifies how independently developed product specifications, Type A-aligned specifications, and Type B-aligned specifications may be organized as functionally differentiated systems, thereby providing a conceptual basis for understanding standardization as an enabling infrastructure for the market utilization of emerging materials.

5. Discussion

This study proposes an integrated framework for understanding specification standardization in emerging material systems as an adaptive framework linking measurement, conformity assessment, industrial practice, and market formation. Rather than treating standardization as a linear transition from Type A to Type B standards, the framework clarifies how independently developed product specifications, Type A-aligned product specifications, and Type B-aligned product specifications coexist and fulfill distinct but complementary functions under varying technological and market conditions.

5.1. Complementary Roles of Type A and Type B Standards

The findings suggest that Type A and Type B standards should not be understood as sequential stages of a unidirectional progression, but as functionally differentiated mechanisms within specification systems. Type A standards support comparability by structuring characteristic definitions and measurement methods while preserving diversity in manufacturer-declared values. Type B standards provide predefined acceptance criteria that support conformity assessment, certification, and quality assurance.

These functions operate at different but interconnected levels: Type A standards support market evaluation under technological and application uncertainty, whereas Type B standards support conformity assessment and quality assurance under more stabilized market conditions. Their coexistence suggests that standardization can support both innovation and quality assurance.

This perspective broadens conventional compliance-centered interpretations of standardization by positioning comparability as an important and structurally distinct function in emerging material systems.

5.2. Feasibility of Type A-Based Conformity Assessment

The study highlights the potential role of conformity assessment based on Type A standards. Because Type A standards define characteristics and specify standardized measurement methods and procedures, they can provide a basis for conformity assessment based on manufacturer-declared values.

Despite this technical feasibility, Type A-based conformity assessment remains limited in widespread international practice, partly because emerging material markets often lack

https://doi.org/10.3390/metrology6020036

the economic scale and institutional conditions needed for third-party certification [13,14]. In such contexts, manufacturer self-declaration based on Type A standards may provide a practical alternative [15].

Nevertheless, a few industrial initiatives demonstrate the feasibility of Type A-based conformity assessment by third-party certification bodies. An industry-led certification system for fine bubble technologies has been established [16] using ISO-defined measurement methods. Similarly, a certification framework for clay nanomaterials based on ISO Type A standards [10] has been implemented through collaboration among industrial associations, testing laboratories, and certification bodies [17,18]. These cases suggest that conformity assessment may be achievable even without predefined acceptance criteria when supported by appropriate measurement frameworks and institutional arrangements.

From this perspective, standardization in emerging material domains may be understood not as a unidirectional progression toward predefined acceptance criteria, but as a complementary system in which comparability and compliance coexist through different coordination mechanisms.

5.3. Continuing Roles of Type A Functions in Type B Systems

Even in mature material systems dominated by Type B standards, Type A-based comparability functions remain important. Predefined characteristic values and conformity criteria depend on the prior existence of comparable measurement methods and specified characteristics. In this sense, Type B systems do not replace Type A functions but increasingly incorporate them.

This perspective suggests that mature certification systems may accommodate dual modes of conformity assessment: verification against predefined criteria and evaluation against manufacturer-declared values. Standardization may therefore be understood as an integrated system in which comparability and compliance coexist rather than as mutually exclusive approaches.

5.4. Evaluation of Measurement Reliability

To ensure the measurement reliability in the dual-mode standardization framework, establishing a unified guideline for uncertainty evaluation is important. Such a guideline should comprehensively govern both Type A and Type B standards.

The guideline integrates key metrological requirements in an ascending hierarchy of rigor. This includes:

1. Mandatorily reporting and disclosing specific measurement methods and procedures that are used (whether standardized or non-standardized), providing the baseline for uncertainty component analysis;
2. Rigorously evaluating method and procedure validity and cross-laboratory measurement consistency assurance (e.g., through round-robin testing);
3. Systematically analyzing deviations from reference values when using certified reference materials or industrial reference materials to quantify measurement uncertainty, thereby executing traceability path construction.

While fully operationalizing such a comprehensive guideline remains a challenge for future independent research, step-by-step embedding requirements for uncertainty evaluation within Type A standards is crucial as a major contribution to the development of metrology and the field of emerging materials.

5.5. Strategic Implications for Standardization

In applied science-oriented research institutions, accelerating the market deployment of research outcomes has become an increasingly important R&D strategy. Standardization

https://doi.org/10.3390/metrology6020036

is now widely recognized as a key mechanism supporting this transition by enhancing comparability, harmonization, and market confidence. This study provides a conceptual framework for understanding how dual-mode standardization supports the transition from emerging research outcomes to functioning markets through structured material specifications. Such deployment-oriented research has also been discussed in the context of synthetic R&D, which integrates scientific and technological outcomes with stakeholder needs to facilitate societal and industrial implementation [19].

For emerging material systems, excessive reliance on Type B standards in early-stage markets may reduce flexibility for technological differentiation by fixing predefined characteristic values and acceptance criteria before technologies and applications become sufficiently stabilized. In such contexts, Type A standards may provide a practical basis for comparability and early market formation.

For mature material systems, standardization strategies may benefit from perspectives beyond purely compliance-oriented approaches. By recognizing the continuing role of Type A functions, Type B-based systems can support not only certification but also the ongoing refinement of product specifications in response to technological progress and evolving market demands.

Manufacturers of emerging materials may adopt independently developed, Type A-aligned, or Type B-aligned product specifications according to technological maturity, target applications, market conditions, and certification requirements. The effectiveness of standards depends not only on their existence, but also on their strategic selection and industrial implementation. Standardization therefore functions not merely as a prescriptive system, but as an adaptive framework whose value depends on effective industrial adoption.

Overall, standardization in emerging material systems may be understood as an adaptive coordination framework balancing comparability, compliance, and innovation across different phases of technological and market maturity.

6. Conclusions

This study proposes a complementary perspective on standardization in emerging material domains as a framework linking industry, standards development organizations (SDOs), and markets for organizing measurement-based information in market evaluation and decision-making. The analysis suggests that Type A and Type B specifications function as complementary components of standardization. In Type A systems, market acceptance decisions are based on the comparative evaluation of characteristic data relative to manufacturer-declared values, whereas in Type B systems they are based on conformity assessment against predefined criteria.

This perspective broadens prevailing compliance-oriented interpretations of standardization by suggesting that comparability and compliance fulfill distinct but complementary market functions. Excessive reliance on Type B standards in early-stage emerging material markets may reduce flexibility for technological differentiation by fixing predefined acceptance criteria before technologies and applications are sufficiently stabilized. In such contexts, market decisions are often based not only on pass/fail conformity, but also on the ability of stakeholders to compare, interpret, and trust measurement results across suppliers and users.

Type A-based systems may provide important conditions for early-stage market acceptance by establishing comparability through shared measurement frameworks, including standardized data formats, uncertainty evaluation, and transparent representation of measured characteristic values. These structures can facilitate informed decision-making under uncertain conditions while preserving flexibility for technological differentiation and continued innovation.

https://doi.org/10.3390/metrology6020036

Overall, standardization may be understood as an adaptive framework that structures how information is disclosed, interpreted, and validated, enabling the transition from early market entry to sustained market acceptance. This framework may provide a basis for adaptive standardization strategies aligned with different phases of technological and market maturity.

Funding: This research received no external funding.

Data Availability Statement: No new data were created or analyzed in this study. Data sharing does not apply to this article.

Conflicts of Interest: The author declares no conflicts of interest.

Abbreviations

The following abbreviations are used in this paper:

IEC	International Electrotechnical Commission
IS	International Standard
ISO	International Organization for Standardization
SDO	Standards Development Organization
TC	Technical Committee
TS	Technical Specification

References

1. *JCGM 100:2008*; Evaluation of Measurement Data—Guide to the Expression of Uncertainty in Measurement. Joint Committee for Guides in Metrology (JCGM): Sèvres, France, 2008.
2. Farrell, J.; Saloner, G. Standardization, compatibility, and innovation. *Rand J. Econ.* **1985**, *16*, 70–83. [CrossRef]
3. Blind, K. The impact of standardization and standards on innovation. In *Nesta Working Paper*; Nesta: London, UK, 2013.
4. Tassey, G. Innovation in advanced manufacturing systems: The role of standards. In *NIST Economic Analysis Office Working Paper*; National Institute of Standards and Technology: Gaithersburg, MD, USA, 2014.
5. Allen, R.; Sriram, R.D. The role of standards in innovation. *Technol. Forecast. Soc. Change* **2000**, *64*, 171–181. [CrossRef]
6. Blind, K.; Petersen, S.S.; Riillo, C. The impact of standards and regulation on innovation in uncertain markets. *Res. Policy* **2017**, *46*, 249–264. [CrossRef]
7. Ono, A. A metrological approach to developing quality testing standards for emerging advanced materials. *Metrology* **2025**, *5*, 42. [CrossRef]
8. *ISO/TS 19808:2020*; Nanotechnologies—Carbon Nanotube Suspensions—Specification of Characteristics and Measurement Methods. International Organization for Standardization: Geneva, Switzerland, 2020.
9. *ISO/TS 9651:2025*; Nanotechnologies—Classification Framework for Graphene-Related 2D Materials. International Organization for Standardization: Geneva, Switzerland, 2025.
10. *ISO TS 21236-2:2021*; Nanotechnologies—Clay Nanomaterials—Part 2: Specification of Characteristics and Measurements for Clay Nanoplates Used for Gas-Barrier Film Applications. International Organization for Standardization: Geneva, Switzerland, 2021. Available online: https://www.iso.org/standard/73945.html (accessed on 3 May 2026).
11. *IEC TS 62565-1:2023*; Nanomanufacturing—Product Specifications—Part 1: Basic Concepts. International Electrotechnical Commission: Geneva, Switzerland, 2023.
12. International Organization for Standardization. Standards by ISO/TC 229 Nanotechnologies. ISO Catalogue Webpage; International Organization for Standardization: Geneva, Switzerland. Available online: https://www.iso.org/committee/381983/x/catalogue/p/1/u/0/w/0/d/0 (accessed on 3 May 2026).
13. *ISO/IEC 17065:2012*; Conformity Assessment—Requirements for Bodies Certifying Products, Processes and Services. International Organization for Standardization: Geneva, Switzerland, 2012.
14. *ISO/IEC 17067:2013*; Conformity Assessment—Fundamentals of Product Certification and Guidelines for Product Certification Schemes. International Organization for Standardization: Geneva, Switzerland, 2013.
15. *ISO/IEC 17050-1:2004*; Conformity Assessment—Supplier's Declaration of Conformity—Part 1: General Requirements. International Organization for Standardization: Geneva, Switzerland, 2004.

https://doi.org/10.3390/metrology6020036

16. Fine Bubble Industries Association. FBIA Product Certification and Registration System. FBIA Information Webpage; Fine Bubble Industries Association: Tokyo, Japan. Available online: https://fbia.or.jp/en/product-certification-registration/ (accessed on 3 May 2026).
17. Clayteam Association. Material Certification. Clayteam Information Webpage; Clayteam Association: Tokyo, Japan. Available online: https://www.clayteam.jp/product/index.html (accessed on 3 May 2026). (In Japanese)
18. Clayteam Association. Testing Laboratories Designation. Clayteam Information Webpage; Clayteam Association: Tokyo, Japan. Available online: https://clayteam.jp/standardization/index-standard.html (accessed on 3 May 2026). (In Japanese)
19. Ono, A. Advancing Synthetic R&D Through Scenarios: Integrating Science, Technology, and Stakeholder Needs. *Technologies* **2025**, *13*, 432. Available online: https://www.mdpi.com/2227-7080/13/10/432 (accessed on 3 May 2026). [CrossRef]

Disclaimer/Publisher's Note: The statements, opinions and data contained in all publications are solely those of the individual author(s) and contributor(s) and not of MDPI and/or the editor(s). MDPI and/or the editor(s) disclaim responsibility for any injury to people or property resulting from any ideas, methods, instructions or products referred to in the content.

https://doi.org/10.3390/metrology6020036

metrology

MDPI

Communication

High-Frequency Coupled-Resonator CMUT with Stepped Cavity for Enhanced Sensitivity and Bandwidth in Acoustic Emission Detection

Sulaiman Mohaidat [1,*], Mohammad Okour [2], Mutaz Al Fayad [1] and Fadi Alsaleem [1]

[1] Durham School of Architectural Engineering and Construction, College of Engineering, University of Nebraska-Lincoln, Omaha, NE 68182, USA
[2] Mechanical and Materials Engineering Department, College of Engineering, University of Nebraska-Lincoln, Lincoln, NE 68588, USA
* Correspondence: smohaidat2@unl.edu

Abstract

Acoustic emission (AE) monitoring in metal additive manufacturing (AM) requires compact sensors capable of high-frequency operation, broad bandwidth, and high sensitivity. However, increasing structural stiffness to achieve high resonance frequencies typically reduces electromechanical sensitivity. This work presents a finite element study of a coupled-resonator capacitive micromachined ultrasonic transducer (CMUT) designed to address this trade-off. The proposed architecture integrates three mechanically coupled silicon membranes with a stepped capacitive cavity that increases capacitance while preserving structural stiffness, enabling enhanced sensitivity without compromising high-frequency operation. COMSOL Multiphysics simulations were used to evaluate modal characteristics and frequency response under DC pre-stressed conditions. Modal coupling produced closely spaced resonances that broadened the effective bandwidth, while the stepped cavity significantly increased voltage output through improved electromechanical coupling. Compared to a single-resonator flat-cavity design, the coupled stepped-cavity configuration demonstrated nearly a threefold enhancement in output voltage while maintaining operation near 100 kHz. Additionally, adjusting the central resonator length enabled controlled frequency tuning for scalable array implementation. These results establish a proof of concept for a high-frequency, high-sensitivity micro-electro-mechanical systems (MEMS) CMUT architecture suitable for distributed AE monitoring in advanced manufacturing environments.

Keywords: CMUT; coupled-resonators; acoustic emissions; additive manufacturing; sensitivity; bandwidth; COMSOL

1. Introduction

Acoustic emission (AE) is a passive nondestructive testing (NDT) technique that enables real-time monitoring of damage evolution in structures and is increasingly explored for qualification and structural health monitoring of additively manufactured (AM) components [1,2]. AE signals are transient elastic waves produced by the rapid, localized release of strain energy, such as during microcrack initiation, crack growth, delamination, or plastic deformation under external stimuli (e.g., loading, pressure, or temperature) [3,4]. In AM, process-induced defects can degrade mechanical performance and introduce variability that is not reliably captured by visual inspection alone. As a result, AE has been proposed

for in-process defect detection and for linking acoustic signatures to process parameters and resulting mechanical behavior [5].

Although conventional AE systems have demonstrated strong capability in laboratory-scale damage monitoring [6], their performance in complex and dynamic manufacturing environments remains constrained by sensor size and coupling dependence [7]. Beyond deployment constraints, effective AE monitoring in AM requires sensors with sufficient bandwidth, high sensitivity, and adequate spatial density to ensure reliable source localization and defect characterization [8,9].

As AM environments demand higher spatial resolution, broader frequency capture, and improved integration capability, the scalability of traditional AE hardware becomes a limiting factor. Addressing these requirements necessitates sensing platforms that are inherently compact, array-compatible, and fabrication-scalable, characteristics more readily achieved through microfabrication technologies. In this context, micro-electro-mechanical systems (MEMS) transducers offer a fundamentally different implementation paradigm for AE detection. MEMS technologies are widely utilized across various applications, including microswitches [10,11], sensing platforms [12–14], and emerging edge-computing devices [15–17]. Among MEMS-based sensing technologies, several acoustic and ultrasonic implementations have been explored for structural monitoring and high-frequency detection. Piezoelectric micromachined ultrasonic transducers (PMUTs) offer broadband response, low-voltage operation, and CMOS compatibility, enabling compact sensing platforms [18]. MEMS Lamb-wave and bulk acoustic wave sensors have also demonstrated high-frequency guided-wave sensitivity for damage detection in miniaturized formats [19,20]. Furthermore, MEMS microphone technologies provide high sensitivity, wide dynamic range, and scalable array integration adaptable to ultrasonic monitoring applications [21,22]. Collectively, these advances highlight the potential of MEMS acoustic sensing architectures for compact, scalable, and distributed monitoring systems. Among MEMS acoustic technologies, capacitive micromachined ultrasonic transducers (CMUTs) have emerged as particularly compelling candidates for high-frequency sensing applications. Recent work has emphasized the importance of enhancing signal-to-noise ratio (SNR) and sensitivity in such sensors through optimized device design, improved packaging strategies, advanced signal processing techniques, and refined structure–sensor coupling mechanisms [23]. Another work demonstrates the feasibility of using CMUTs for ultrasound-based NDT across various metals and alloys. The results confirm that properly packaged CMUTs provide reliable coupling and broadband performance, supporting their suitability for material inspection and industrial monitoring applications [24]. Additionally, scaling these platforms has enabled 1024-element 2D arrays with custom ASICs and local preamplifiers, overcoming routing bottlenecks, improving sensitivity, and enabling high-resolution 3D beamformed imaging with deep penetration, demonstrating the clinical and industrial viability of highly integrated systems [25].

Prior studies have reported a circular membrane capacitive AE sensor with a sensitivity of -30.8 dB, a signal-to-noise ratio of 35.7 dB, and a minimum detectable signal level of 6.2% at 2.8 MHz [26]. Other work has demonstrated a CMUT linear array achieving transmitting and receiving sensitivity of 146.82 dB and -229.55 dB at 1 MHz [27], highlighting the feasibility of CMUT-based sensing for high-frequency applications. In contrast, the proposed design focuses on enhancing both output voltage and bandwidth through the combined effects of resonator coupling and stepped-cavity geometry. While this study is a proof of concept, the results demonstrate a significant relative improvement (up to ~3$\times$ increase in output voltage) compared to a baseline single-resonator configuration, indicating strong potential for competitive performance once experimentally validated.

https://doi.org/10.3390/metrology6020029

All the modeling was conducted using COMSOL Multiphysics 6.2 commercial finite element software (COMSOL, Inc., Burlington, MA, USA). The modeling also shows the effect of using a stepped-cavity design as opposed to the usual flat-cavity configuration.

2. Materials and Methods

2.1. (A) Basic Design

The design in this work utilizes a rectangular-based membrane as the vibrating element when exposed to sound waves. Design characteristics are based on two elements: resonator coupling and the stepped cavity. The purpose is to test the effect on the output voltage and on the bandwidth of the microphone, as explained in Figure 1.

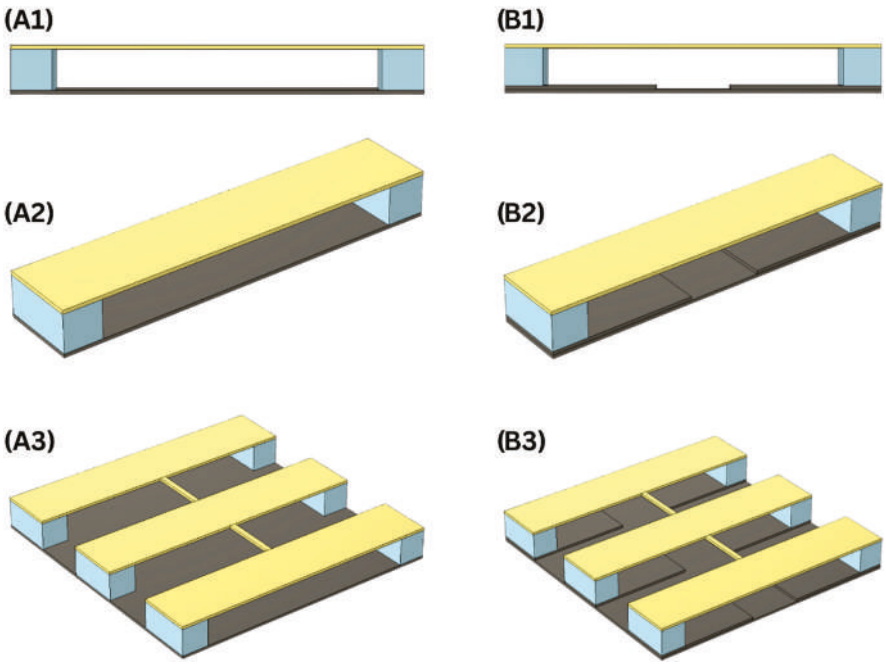


Figure 1. Design elements explored in this work. (**A1**) Flat-cavity CMUT design. (**A2**) 3D representation of a flat-cavity CMUT. (**A3**) 3D representation of a coupled flat-cavity CMUT. (**B1**) Stepped-cavity CMUT design. (**B2**) 3D representation of a stepped-cavity CMUT. (**B3**) 3D representation of a coupled stepped-cavity CMUT.

The goal of the stepped-cavity design is to achieve a larger capacitance since the electrostatic gap is smaller at the edges of the design. The edges of the membrane experience very little displacement, so reducing the thickness of the gap does not restrict the movement of the membrane. Coupling between the resonators not only increases the capacitance of the microphone but also its bandwidth without any large effect on the natural frequency compared to a single resonator.

In this study, the rectangular membrane is made from silicon with a thickness of 0.5 μm. The mechanical properties used for silicon are Young's modulus of 170 Gpa, a density of 2329 kg/m^3, and a Poisson's ratio 0.28. The membrane had a length of 200 μm and a width of 100 μm. These design parameters are chosen as initial values to evaluate the stepped-cavity concept. The reduced gap region is introduced to enhance capacitance, while the larger gap preserves structural stiffness and resonance characteristics. The design will be further optimized based on experimentally validated models in future work.

When fixed at its sides, the resonator has a natural frequency of 100 kHz. The resonator was employed in a three-coupled resonator configuration with a stepped-cavity design, as shown in Figure 2.

https://doi.org/10.3390/metrology6020029

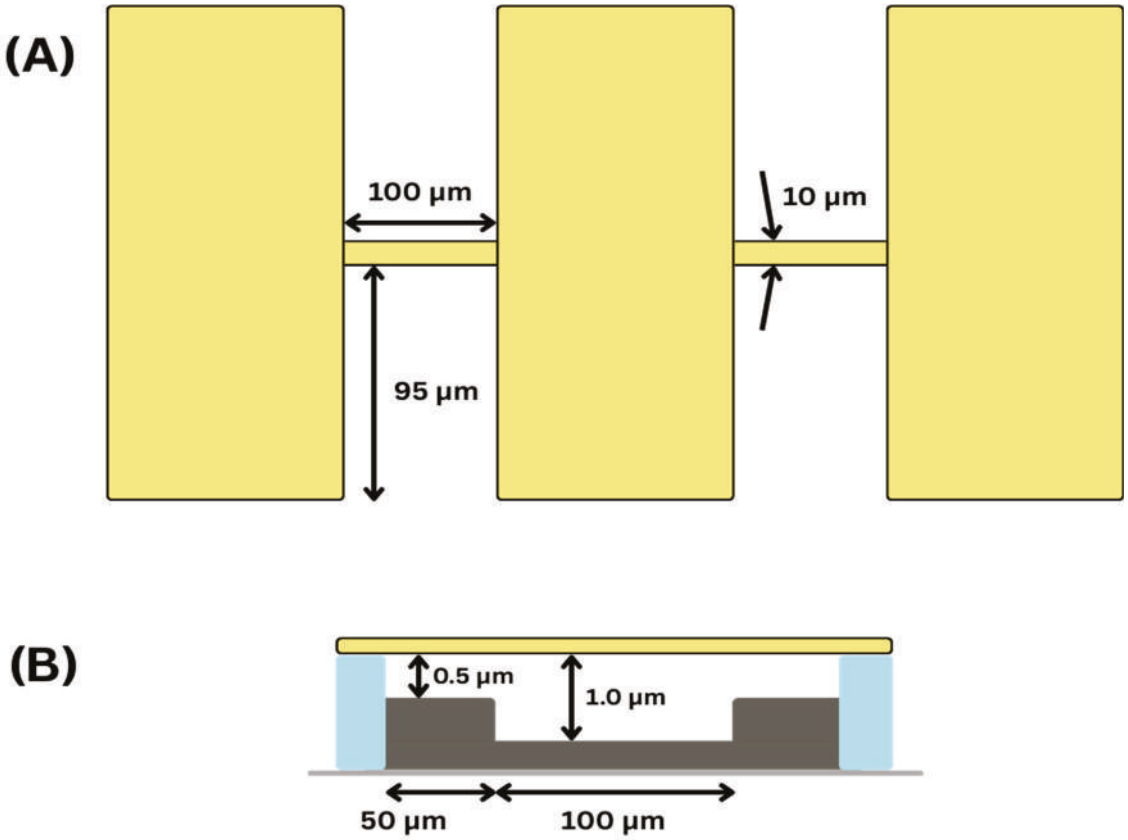


Figure 2. (**A**) Top view of the three-coupled resonator design. (**B**) Side view of the stepped-cavity design for each resonator used in this work.

In order to see the effect of design variations, the effect of the length of the central resonator on the frequency response was also studied. All comparisons in this study were made on the same mesh.

2.2. (B) Modeling Approach: Electromechanical Modeling of the CMUT: Pre-Stressed RC Configuration

COMSOL Multiphysics 6.2 was the main tool in this work. The eigenfrequency study was performed to determine the natural frequency of the microphones and test the performance of each design.

The CMUT will operate as a capacitor within a series RC circuit. The voltage source of the circuit is a DC voltage that charges the capacitor and pre-stresses the membrane. When the sound waves exert pressure on the membrane, an AC voltage is generated across the CMUT (the capacitor) based on the amplitude of the vibrations caused by the sound waves. The sound wave in the simulations has a sound pressure of 0.1 Pa and is modeled as harmonic perturbations. A schematic of the modeling setup is shown in Figure 3.

The value of the voltage of the DC voltage source was chosen as the nearest integer value before the pull-in event. We used the pull-in voltage as the criterion for selecting the pre-stressing voltage, thereby providing a consistent framework for future development of this concept; for the basic design, the DC voltage was 3 V. The resistor value was 1 kΩ. The damping was modeled using an isotropic loss factor of 0.01. The frequency sweep had a 100 Hz resolution. These parameters were selected to provide a consistent comparison framework and to simulate acoustic emission conditions within a reasonable computational cost, while maintaining signal levels comparable to the detection thresholds reported for sensors used in additive manufacturing applications [2].

https://doi.org/10.3390/metrology6020029

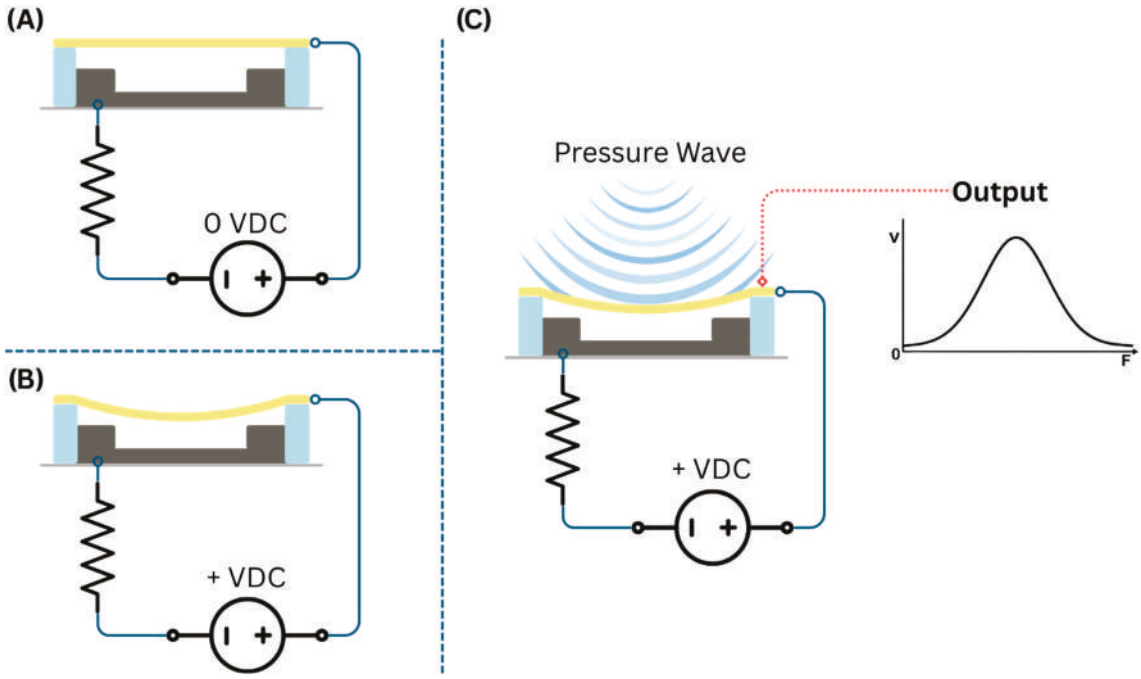


Figure 3. Modeling setup used in COMSOL Multiphysics showing the RC circuit formed using the stepped-cavity CMUT as the capacitor in the circuit. (**A**) RC circuit without voltage application. (**B**) The deflection of the membrane due to DC pre-stressing to charge the CMUT. (**C**) The application of pressure (acoustic) waves on a pre-stressed CMUT and the absolute amplitude of the voltage across it.

COMSOL Multiphysics was also used at this stage by performing a frequency domain perturbation study on electrochemical MEMS problems using the electromechanical forces interface that couples electrostatics and solid mechanics physics. This work was performed on a desktop with an Intel 12900K processor and 32 GB of RAM.

3. Results

3.1. Effect of Resonator Coupling on Natural Frequencies

To investigate the influence of mechanical coupling on the dynamic behavior of the device, the eigenfrequency analysis of the proposed coupled-resonator CMUT was performed. The first three mode shapes are presented in Figure 4. A mesh independence study was conducted using COMSOL automatic mesh settings, and the results are shown in Table 1.

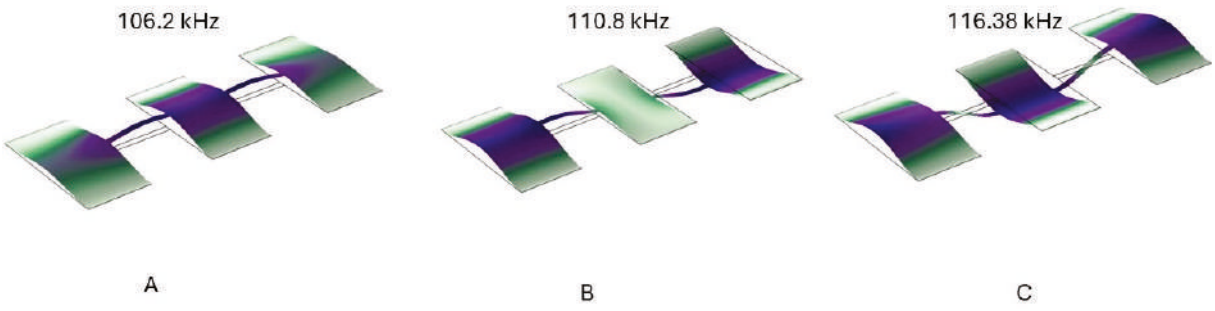


Figure 4. Mode shapes of the proposed coupled CMUT design: (**A**) first mode (106.2 kHz), (**B**) second mode (110.8 kHz), and (**C**) third mode (116.38 kHz).

https://doi.org/10.3390/metrology6020029

Table 1. Mesh independence study for eigenvalue analysis of the coupled CMUT design using COMSOL automatic meshing.

Mesh Size	Type	Count	Natural Frequency (kHz)
Normal	Tetrahedral	7859	116.06
	Triangles	5964	
Fine	Tetrahedral	20,283	106.93
	Triangles	14,518	
Finer	Tetrahedral	115,333	106.2
	Triangles	77,070	
Extra-fine	Tetrahedral	792,380	106.08
	Triangles	522,812	

As shown in Figure 4, the first three resonance frequencies are closely spaced. This modal clustering is a direct consequence of the mechanical coupling between adjacent resonators and is advantageous for bandwidth enhancement. The proximity of these modes enables a broadened effective frequency response, thereby improving the operational bandwidth of the microphone.

3.2. Comparison of CMUT Resonator Configurations

Figure 5 presents the normalized frequency response of four CMUT configurations: single-resonator and coupled-resonator designs, each implemented with flat and stepped cavities. For consistency, the flat-cavity thickness was fixed at 1.0 μm. The comparison highlights the influence of resonator coupling and cavity geometry on the voltage response near resonance.

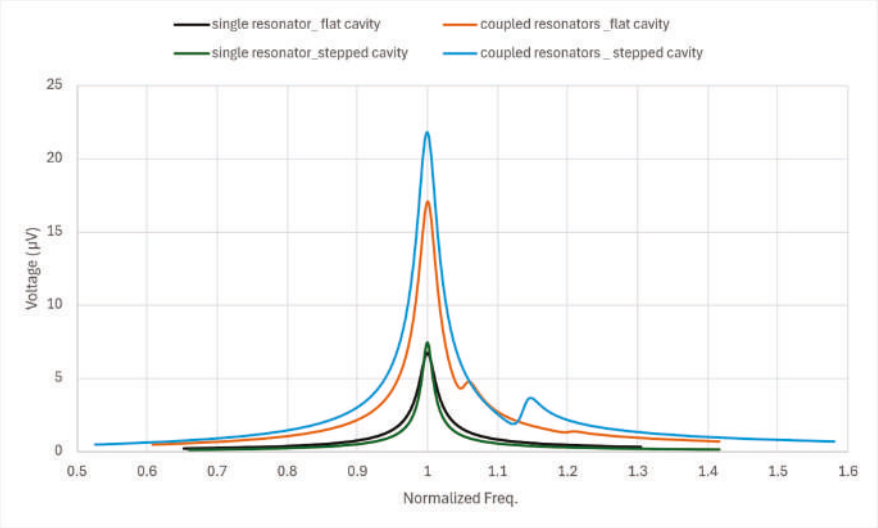


Figure 5. Normalized frequency response comparison of four CMUT configurations: single-resonator and coupled-resonator designs with flat and stepped cavities.

Figure 5 quantitatively demonstrates the performance enhancement achieved through resonator coupling and stepped-cavity implementation. The single-resonator flat-cavity configuration exhibits a peak voltage of approximately 6.75 μV at resonance. Introducing a stepped cavity slightly improves the response, yielding a comparable peak of about 7 μV.

In contrast, the coupled-resonator flat-cavity design shows a substantial increase in peak magnitude to approximately 16.5 μV, representing more than a twofold improvement

https://doi.org/10.3390/metrology6020029

compared to the single-resonator case. The highest performance is achieved with the coupled stepped-cavity configuration, which reaches a peak voltage of approximately 21.5 μV, corresponding to nearly a threefold enhancement over the baseline single-resonator flat-cavity design.

Additionally, the coupled configurations exhibit a wider effective response region around the normalized resonance frequency due to modal interaction, contributing to bandwidth expansion. These results confirm that resonator coupling significantly enhances sensitivity, while the stepped-cavity geometry provides further amplification. The combination of both design strategies yields a synergistic improvement in both voltage output and operational bandwidth, making it the most advantageous configuration among the four investigated cases.

3.3. Finer Mesh Comparison Between Single and Coupled Resonators

To verify the numerical stability and accuracy of the simulations, the frequency response analysis was repeated in COMSOL using an automatically generated finer mesh for both the single- and coupled-resonator designs with stepped-cavity configurations. The normalized frequency results are presented in Figure 6.

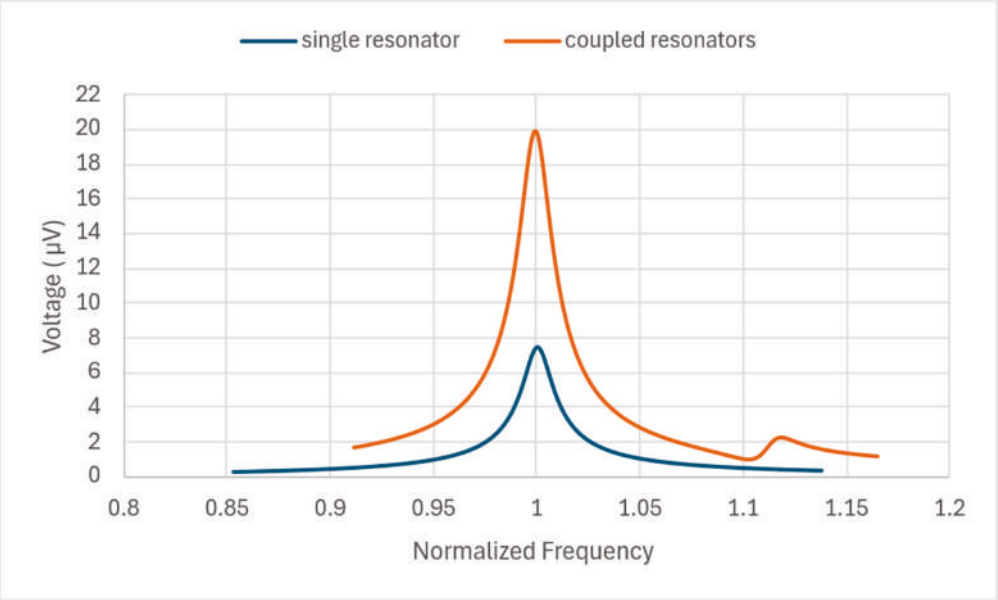


Figure 6. Normalized frequency response obtained using a finer mesh for stepped-cavity single and coupled CMUT resonators.

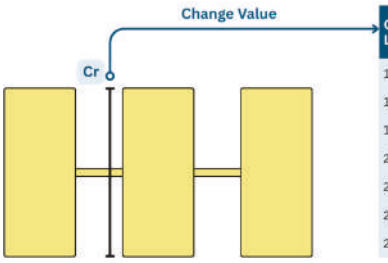
As shown in Figure 6, the overall trend remains consistent with the results presented in Figure 5. The coupled-resonator configuration continues to exhibit a significantly higher peak voltage compared to the single-resonator design. With the finer mesh, the peak voltage of the coupled resonator is approximately 20 μV, compared to about 21.5 μV obtained with the standard mesh. This minor variation is attributed to the improved spatial resolution of the structural and electrostatic fields.

Importantly, the relative enhancement between single and coupled resonators remains unchanged, confirming that the observed performance improvement is not a mesh-dependent artifact. The preservation of both the resonance frequency location and the amplitude enhancement trend demonstrates that the results are mesh-convergent and numerically reliable.

https://doi.org/10.3390/metrology6020029

3.4. Effect of the Dimensions of the Central Resonator

The effect of varying the length of the central resonator on the modal frequencies of the coupled CMUT MEMS microphone is illustrated in Figure 7. As the central resonator length increases from 170 μm to 230 μm, a significant shift in the modal frequencies is observed, particularly in the first and third modes.



Central resonator Length (μm)	Frequency (kHz)		
	1st mode	2nd mode	3rd mode
170	111.39	111.43	146.78
180	110.99	111.22	134.19
190	109.86	111.02	123.34
200	106.2	110.79	116.38
210	99.194	110.54	114.04
220	91.72	110.24	113.31
230	84.817	109.88	112.98

Figure 7. Effect of central resonator length (170–230 μm) on the first three modal frequencies of the stepped-cavity coupled CMUT MEMS microphone. The first and third modes exhibit a strong inverse relationship with resonator length, while the second mode remains nearly constant, indicating different modal sensitivities to structural scaling.

To further illustrate the dynamic behavior, the frequency responses (using a finer mesh for improved accuracy) of the 190 μm, 200 μm, and 210 μm designs are presented in Figure 8. The resonance peaks clearly shift toward lower frequencies as the central resonator length increases. The 190 μm design exhibits a dominant peak near ~102.5 kHz, while the 200 μm and 210 μm designs shift toward ~98.5 kHz and ~89 kHz, respectively. Additionally, changes in peak amplitude and bandwidth can be observed, reflecting variations in modal coupling and effective stiffness. These results confirm that the central resonator length provides an effective tuning parameter for controlling the primary resonance frequency without significantly disturbing the second mode, enabling flexible frequency tailoring of the stepped-cavity coupled CMUT microphone.

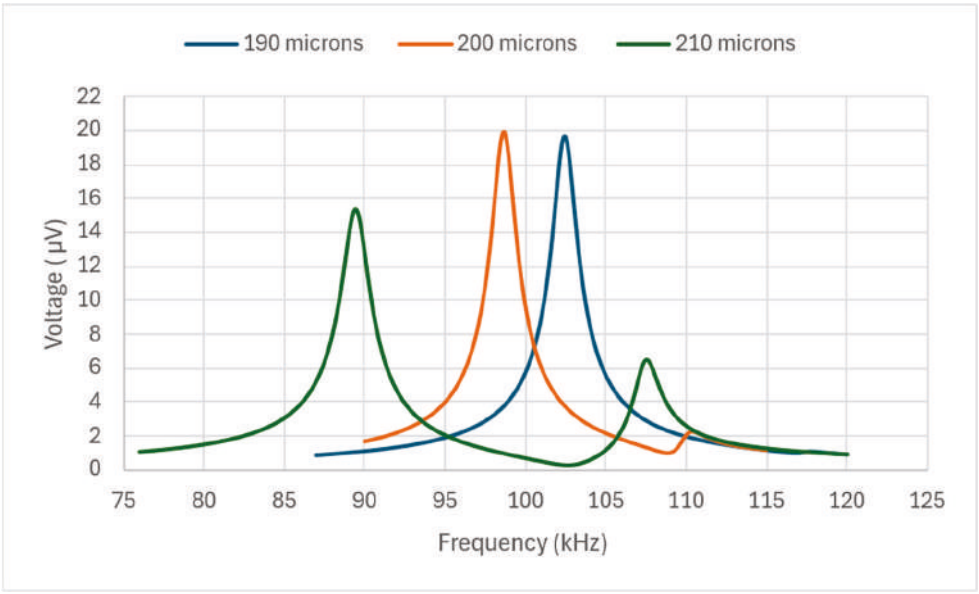


Figure 8. Frequency responses of the stepped-cavity coupled CMUT MEMS microphone for central resonator lengths of 190 μm, 200 μm, and 210 μm (finer mesh simulation). Increasing the central resonator length shifts the dominant resonance peak toward lower frequencies, demonstrating effective mechanical tuning of the device.

https://doi.org/10.3390/metrology6020029

4. Discussion

The performance enhancement observed in this work stems from the combined effects of resonator coupling and stepped-cavity geometry. While both design modifications increase capacitance, they influence device behavior through different physical mechanisms.

The stepped cavity improves electromechanical sensitivity by reducing the electrostatic gap at the membrane edges, where displacement is minimal. This increases capacitance without significantly altering structural stiffness, leading to higher output voltage while preserving resonance characteristics. In contrast, mechanical coupling primarily affects the dynamic response. The interaction between adjacent resonators produces closely spaced modes, resulting in a broader effective bandwidth and higher voltage response due to increased vibrating area and modal interaction.

Adjusting the length of the central resonator provides an effective tuning mechanism. Increasing its length lowers the primary resonance frequency while minimally affecting the intermediate mode, indicating that different modes are governed by different stiffness and coupling contributions. The emergence of secondary peaks in longer configurations suggests the possibility of multi-band operation, which could be advantageous for broadband AE detection.

Once this design is fabricated and the model is experimentally validated, several parameters will be evaluated, including SNR, residual stresses, crosstalk, and uncertainty quantification, as these cannot be fully captured within the current simulation framework. Additionally, fabrication tolerances, thermal effects, and noise sources are expected to influence device performance and will be systematically investigated in future experimental studies.

Overall, the coupled stepped-cavity architecture offers a practical strategy to simultaneously enhance sensitivity and bandwidth while maintaining geometric scalability. These characteristics make the proposed design particularly suitable for compact and distributed AE monitoring systems in AM environments.

5. Conclusions

This work presented a finite element study that is focused on developing a coupled-resonator CMUT that can have enhanced performance in terms of output voltage and frequency bandwidth while remaining within the same desired frequencies.

This work provides proof of concept for a MEMS microphone that can be used for the detection of AE for applications in areas such as in situ diagnosis of metal AM and structural health monitoring.

Future work includes the fabrication and testing of MEMS microphones based on this design methodology, developing experimentally verified models that can be used to further design exploration and optimization.

Author Contributions: Conceptualization, S.M. and F.A.; methodology, S.M. and F.A.; software, S.M.; validation, S.M.; formal analysis, S.M. and F.A.; investigation, S.M. and F.A.; resources, S.M. and M.O.; data curation, S.M.; writing-original draft preparation, S.M., M.O., M.A.F. and F.A.; writing-review and editing, S.M., M.O. and F.A.; visualization, M.A.F.; supervision, F.A.; project administration, F.A.; funding acquisition, F.A. All authors have read and agreed to the published version of the manuscript.

Funding: This work was funded by the United States Department of Energy, grant # DE-SC0025550.

Data Availability Statement: The original contributions presented in this study are included in the article.

Conflicts of Interest: The authors declare no conflict of interest.

https://doi.org/10.3390/metrology6020029

References

1. Strantza, M.; Van Hemelrijck, D.; Guillaume, P.; Aggelis, D.G. Acoustic emission monitoring of crack propagation in additively manufactured and conventional titanium components. *Mech. Res. Commun.* **2017**, *84*, 8–13. [CrossRef]
2. Prem, P.R.; Sanker, A.P.; Sebastian, S.; Kaliyavaradhan, S.K. A review on application of acoustic emission testing during additive manufacturing. *J. Nondestruct. Eval.* **2023**, *42*, 96. [CrossRef]
3. Vidya Sagar, R.; Basu, D.J. Damage assessment of reinforced concrete structures under elevated-amplitude cyclic loading using sentry values based on acoustic emission testing. *Nondestruct. Test. Eval.* **2023**, *38*, 612–630. [CrossRef]
4. Kannivel, S.; Vellayaraj, A.; Kolimi, I.; Thomas, J. Effect of thickness on indentation response and tensile loading behaviour of glass/epoxy laminates under acoustic emission monitoring. *Nondestruct. Test. Eval.* **2021**, *36*, 158–175. [CrossRef]
5. Wu, H.; Yu, Z.; Wang, Y. A new approach for online monitoring of additive manufacturing based on acoustic emission. In *International Manufacturing Science and Engineering Conference*; American Society of Mechanical Engineers: New York, NY, USA, 2016; Volume 49910, p. V003T08A013.
6. Shi, Z.; Li, J.; Ranjith, P.G.; Lin, H.; Liu, T.; Li, K.; Han, D. Laboratory study on acoustic emission signals and damage mechanism of rock with thermal storage potential under fatigue loading. *J. Energy Storage* **2024**, *103*, 114414. [CrossRef]
7. Grosse, C.; Linzer, L. Signal-Based AE Analysis. In *Acoustic Emission Testing*; Grosse, C., Ohtsu, M., Eds.; Springer: Berlin/Heidelberg, Germany, 2008. [CrossRef]
8. Huang, S.F.; Li, M.M.; Xu, D.Y.; Zhou, M.J.; Xie, S.H.; Cheng, X. Investigation on a kind of embedded ae sensor for concrete health monitoring. *Res. Nondestruct. Eval.* **2013**, *24*, 202–210. [CrossRef]
9. Hassan, F.; Mahmood, A.K.B.; Yahya, N.; Saboor, A.; Abbas, M.Z.; Khan, Z.; Rimsan, M. State-of-the-art review on the acoustic emission source localization techniques. *IEEE Access* **2021**, *9*, 101246–101266. [CrossRef]
10. Cao, T.; Hu, T.; Zhao, Y. Research status and development trend of MEMS switches: A review. *Micromachines* **2020**, *11*, 694. [CrossRef]
11. Lucyszyn, S.; Pranonsatit, S.; Choi, J.Y.; Moseley, R.W.; Yeatman, E.M.; Holmes, A.S. Novel rf mems switches. In *2007 Asia-Pacific Microwave Conference*; IEEE: Piscataway, NJ, USA, 2007; pp. 1–4.
12. Mohaidat, S.; Okour, M.; Alsaleem, F. A sensing material-free and simple readout MEMS sensor for detecting helium. *J. Micromech. Microeng.* **2025**, *35*, 025013. [CrossRef]
13. Mohaidat, S.; Nikfarjam, H.; Okour, M.; Megdadi, M.; Al Fayad, M.; Pourkamali, S.; Alsaleem, F. A large-stroke thermomechanical MEMS actuator with lever amplification for helium detection. *Sens. Actuators A Phys.* **2025**, *395*, 117091. [CrossRef]
14. Bogue, R. MEMS sensors: Past, present and future. *Sens. Rev.* **2007**, *27*, 7–13. [CrossRef]
15. Okour, M.; Nikfarjam, H.; Al Fayad, M.; Tafti, F.F.; Takallou, M.A.; Pipinos, I.I.; Pourkamali, S.; Myers, S.; Alsaleem, F. A MEMS network operating as a reservoir computer to classify peripheral artery disease signal from a healthy signal. *Sens. Actuators A Phys.* **2025**, *385*, 116318. [CrossRef]
16. Nikfarjam, H.; Megdadi, M.; Okour, M.; Pourkamali, S.; Alsaleem, F. Energy efficient integrated MEMS neural network for simultaneous sensing and computing. *Commun. Eng.* **2023**, *2*, 19. [CrossRef]
17. Phillips, E. Structural Health Monitoring: The Use of Acoustic Emission to Optimize the FDM Additive Manufacturing Process. Master's Thesis, Prairie View A&M University, Prairie View, TX, USA, 2023.
18. Muralt, P. Recent progress in materials issues for piezoelectric MEMS. *J. Am. Ceram. Soc.* **2008**, *91*, 1385–1396. [CrossRef]
19. Giurgiutiu, V. *Structural Health Monitoring with Piezoelectric Wafer Active Sensors*; Academic Press: Cambridge, MA, USA, 2014.
20. Wang, L.; Wang, C.; Wang, Y.; Quan, A.; Keshavarz, M.; Madeira, B.P.; Zhang, H.; Wang, C.; Kraft, M. A review on coupled bulk acoustic wave MEMS resonators. *Sensors* **2022**, *22*, 3857. [CrossRef] [PubMed]
21. Wang, Q.; Zhang, Y.; Cheng, S.; Wang, X.; Wu, S.; Liu, X. MEMS acoustic sensors: Charting the path from research to real-world applications. *Micromachines* **2024**, *16*, 43. [CrossRef]
22. Zhu, J.; Liu, X.; Shi, Q.; He, T.; Sun, Z.; Guo, X.; Liu, W.; Sulaiman, O.B.; Dong, B.; Lee, C. Development trends and perspectives of future sensors and MEMS/NEMS. *Micromachines* **2019**, *11*, 7. [CrossRef]
23. Boubenia, R.; Le Moal, P.; Bourbon, G.; Ramasso, E.; Joseph, E. CMUT-based sensor for acoustic emission application: Experimental and theoretical contributions to sensitivity optimization. *Sensors* **2021**, *21*, 2042. [CrossRef] [PubMed]
24. Selvam, K.; Saeidi, N.; Schwarzmann, Y.; Wiemer, M.; Kuhn, H. Investigation of Capacitive Micromachined Ultrasound Transducer for NDT and material inspection in metals and alloys. In *2025 IEEE International Instrumentation and Measurement Technology Conference (I2MTC)*; IEEE: Piscataway, NJ, USA, 2025; pp. 1–5.
25. Wodnicki, R.; Foiret, J.; Liu, B.; Lu, N.; Sun, X.; Zhang, J.; Kang, H.; Fu, L.; Notard, C.; Legros, M.; et al. Handheld Large 2D Array with Azimuthal Planewave and Row-Multiplexed Elevation Beamforming Enabled by local ASIC Electronics. *IEEE Trans. Ultrason. Ferroelectr. Freq. Control* **2025**, *72*, 962–978. [CrossRef]

https://doi.org/10.3390/metrology6020029

26. Zhang, S.; Wang, A.; Cui, S.; Wang, Z.; Pan, S.; Wang, R.; Zhang, W.; Yilmaz, M. Design and Acoustic Performance Study of Capacitive Acoustic Emission Sensors Based on MEMS Technology. *IEEE Sens. J.* **2025**, *25*, 29422–29436. [CrossRef]
27. He, C.; Luo, M.; Chai, H.; Wang, H.; Zhang, G.; Wang, R.; Cui, J.; Yang, Y.; Zhang, W.; Jia, L. Design and Evaluation of a Capacitive Micromachined Ultrasonic Transducer (CMUT) Linear Array System for Thickness Measurement of Marine Structures Under Varying Environmental Conditions. *Micromachines* **2025**, *16*, 898. [CrossRef] [PubMed]

Disclaimer/Publisher's Note: The statements, opinions and data contained in all publications are solely those of the individual author(s) and contributor(s) and not of MDPI and/or the editor(s). MDPI and/or the editor(s) disclaim responsibility for any injury to people or property resulting from any ideas, methods, instructions or products referred to in the content.

https://doi.org/10.3390/metrology6020029

metrology

MDPI

Article

A Cost-Effective Cylindrical Capacitive Sensor for Liquid Dielectric Characterization from 1 to 30 MHz

Thet Pai Oo [1], Thipamas Phakaew [2], Muhammad Uzair [1], Prayoot Akkaraekthalin [3], Wutthinan Jeamsaksiri [4] and Suramate Chalermwisutkul [1,*]

[1] The Sirindhorn International Thai-German Graduate School of Engineering, King Mongkut's University of Technology North Bangkok, Bangkok 10800, Thailand; thetpai.oo@email.kmutnb.ac.th (T.P.O.); muhammad.uzair@email.kmutnb.ac.th (M.U.)
[2] Department of Electrical Engineering, Faculty of Engineering, Chiang Mai University, 239 Huay Kaew Road, Muang District, Chiang Mai 50200, Thailand; thipamas.p@cmu.ac.th
[3] Faculty of Engineering, King Mongkut's University of Technology North Bangkok, Bangkok 10800, Thailand; prayoot.a@eng.kmutnb.ac.th
[4] Thai Microelectronics Center, National Electronics and Computer Technology Center, Chachoengsao 24000, Thailand; wutthinan.jeamsaksiri@nectec.or.th
* Correspondence: suramate.c@tggs.kmutnb.ac.th

Abstract

A cost-effective and practical method for characterizing the dielectric properties of liquids at 1 MHz is presented in this article. A cylindrical parallel-plate capacitive sensor was developed, in which the circular end plates function as electrodes and the sidewall is formed by a thin polyvinyl chloride ring cut from a standard water pipe to enclose the liquid sample. Dielectric constant values of air, distilled water, ethanol, and methanol were determined through analytical calculations, electromagnetic simulations, and experimental measurements at 1 megahertz. Consistent results were obtained across all methods, and the extracted values were found to agree well with theoretical values, yielding extraction errors of 0.06% for methanol and 1.85% for ethanol with respect to theoretical values from the literature. A calibration technique was applied in which air and water were used as reference materials with known dielectric constants, effectively mitigating uncertainties associated with sensor geometry, spacer material, and fringing fields. Through this work, a practical and effective technique for dielectric characterization at low frequency has been demonstrated, with core validation of four reference materials (air, deionized water, ethanol, and methanol) at 1 MHz and an additional application example in which cow's milk is characterized over 10–30 MHz. The 10–30 MHz measurement demonstrates the applicability of the proposed method in the low megahertz region, while the primary validation is conducted at 1 MHz. The technique is applicable to a wide range of applications in materials science, chemical, and biomedical engineering.

Keywords: capacitance measurement; parallel-plate capacitor; dielectric constant; calibration

1. Introduction

Permittivity measurements are essential for characterizing dielectric properties of materials, with important applications in material science, food science, chemistry, biology, and biomedical engineering [1–5]. This material parameter quantifies a material's ability to store electrical energy within an electric field. By measuring relative permittivity—also referred to as dielectric constant—over a wide frequency range, dielectric spectroscopy has

been effectively applied in the food industry for quality control processes [6,7]. A comprehensive review of dielectric measurement techniques across different frequency ranges, including low-frequency methods, broadband spectroscopy, and high-frequency imaging, is presented in [8]. The frequency range of interest varies depending on the specific application and the physical phenomena used to characterize the material under test (MUT).

Although sensors operating in the optical frequency range, such as near-infrared spectroscopy, offer high sensitivity, their limited penetration depth makes them unsuitable for characterizing bulky MUTs [9,10]. To characterize MUTs based on the presence of polar or non-polar molecules, the relevant phenomenon is dipolar or orientational polarization dominating in the microwave frequency range. Various measurement techniques have been reported in the literature to capture this effect. For example, ref. [11] proposed a resonance-based method that detects material property changes by observing shifts in the sensor's resonant frequency, offering high sensitivity. However, this approach relies on a single frequency point. For applications requiring permittivity characterization over a broad radio and microwave frequency range, the techniques are typically based on coaxial waveguides or transmission line-based test cells [12–14]. Another type of broadband dielectric spectroscopy sensor uses the free-space technique, where antennas transmit and receive RF or microwave signals through the MUT. However, this method is prone to external noise, making it challenging to maintain accuracy due to environmental influences [15].

For composite materials and biomedical samples, sensing is typically performed at lower megahertz frequencies. The dominant physical phenomenon in this frequency range is interfacial polarization, which occurs when charges accumulate at the interfaces between different materials or phases within a composite. This effect diminishes as the frequency exceeds its natural resonance. Blande et al. [16] presented a low-frequency capacitive sensor designed to detect the void fraction of dielectric fluids in industrial applications. The study compares three electrode configurations: rod, concave, and parallel plate—and demonstrates that the parallel plate design, combined with a guard electrode and a high-dielectric-constant insulating material, provides the highest sensitivity. The authors attribute this to the uniform electric-field distribution and enhanced capacitance response enabled by the chosen materials and geometry.

Despite its simplicity, commercial capacitive sensing systems are often expensive, making them less accessible for small research labs and universities. In addition, a major challenge lies in the accuracy of the measurement, which is affected by fringing electric fields at the edges of the sensing electrodes. In commercial parallel-plate capacitance test fixtures, the fringing effect is typically compensated by using a guard electrode. This additional electrode is integrated coplanar to the sensing electrode and maintained at the same potential. By doing so, the guard electrode eliminates electric-field coupling at the edges, effectively preventing fringing fields from contributing to the measurement results [16–18]. The electric field between the driving electrode and the low-potential electrode remains straight and uniform near the electrode edges due to the presence of a guard electrode. While this is an effective way to eliminate fringing effects from the measured capacitance, the inclusion of a guard electrode increases system complexity. Specifically, the guard electrode must be held at the same potential as the sensing electrode, requiring additional circuitry such as a high-input-impedance voltage follower to prevent current draw. Furthermore, a specially designed fixture incorporating the guard electrode is needed. Due to these requirements, implementing this accuracy-enhancement technique entirely from scratch poses significant challenges in an educational or small laboratory setting.

In another study, Piuzzi et al. [19] designed and experimentally characterized a parallel-plate admittance cell, introducing a method to mitigate fringing-field effects using a correction factor derived from electromagnetic simulations of the sensor configuration. Their

https://doi.org/10.3390/metrology6020023

admittance cell is compatible with standard LCR meters, including two-terminal devices, and does not require a guard electrode. However, constructing the admittance cell requires precision machining of its components, making it too complex for in-house development or educational purposes. Another limitation is that the correction factor used to mitigate fringing effects must be derived from electromagnetic simulations. This means that any change in geometry or material of the admittance cell requires a new round of simulations to determine an appropriate correction factor. Moreover, limited access to commercial electromagnetic simulation software can present a practical challenge for small laboratories seeking to adopt this approach.

This paper presents a novel and low-frequency dielectric measurement approach using a low-cost cylindrical capacitive sensor (CCS). The study focuses on four non-ionic substances—air, deionized water (DI water), ethanol, and methanol—demonstrating the effectiveness of capacitance-based measurements for determining their dielectric constant at 1 MHz. Air and water, with well-known dielectric constants, are used as calibration standards to eliminate the effects of fabrication tolerance, parasitic capacitance, and fringing fields at the electrodes' edges. The proposed CCS is easy to fabricate in-house using readily available materials like a PVC spacer, cut from a standard water pipe, and circular copper plates cut from a copper sheet. This low-cost construction requires no precision machining, and exact cell dimensions are not critical, as calibration compensates for fabrication tolerances. Capacitance is measured using an LCR meter, and the dielectric constant of the MUT is extracted from the measured values. The proposed design, combined with this straightforward calibration method, enables the creation of an effective low-frequency capacitive sensor for liquids at minimal cost. Furthermore, the calibration approach allows flexibility in MUT volume, as reliable permittivity extraction is independent of the test cell's physical size and dielectric properties of the spacer. In this work, the CCS is validated at 1 MHz using four reference materials (air, deionized water, ethanol, and methanol), representing the lower megahertz region of interest. In addition, a frequency-swept measurement from 10 to 30 MHz is presented for cow's milk to demonstrate the applicability of the sensor concept beyond 1 MHz.

2. Materials and Methods

2.1. Theoretical Background

By assuming a homogeneous electric field between the electrodes, the capacitance C_{pc} of a parallel-plate capacitor can be expressed as follows:

$$C_{pc} = \frac{\varepsilon_r \cdot \varepsilon_0 \cdot A}{d} \tag{1}$$

where ε_0 is the permittivity of free space, a physical constant with an approximate value of 8.854×10^{-12} F/m; ε_r is the dielectric constant of the material filling the gap between the two electrodes of the parallel-plate capacitor; d is the spacing between the electrodes; and A is the area of each electrode plate. In the ideal case, the dielectric constant specific to the type and composition of the MUT can easily be extracted.

In practical measurements, the total measured capacitance consists of three components: the capacitance contributed by the MUT sandwiched between the electrodes, the fringing-field capacitance at the electrode edges, and the parasitic capacitance from connecting wires and other elements of the admittance cell. The measured capacitance can be expressed as follows:

$$C_{meas} = C_{MUT} + C_{fr} + C_p \tag{2}$$

where C_{meas} is the total capacitance measured by the instrument, C_{MUT} is the contribution from the MUT, C_{fr} is the fringing-field capacitance, and C_p is the parasitic capacitance of the

https://doi.org/10.3390/metrology6020023

admittance originating from peripheral structures like connecting wires that connect the electrodes of the capacitor to the measurement equipment. Figure 1 shows an illustration of a typical parallel-plate capacitor configuration with all capacitive components from Equation (2). Blue electric field lines in the figure depict the homogeneous electric field between the electrode plates. The green lines represent the fringing electric fields at the edge of the electrodes. Finally, the red lines illustrate the electric field lines of parasitic capacitance originating from the connecting wires of both electrode plates. For the extraction of MUT's dielectric constant, it is important to extract C_{MUT} from the measured value. The procedure for this extraction is described in Section 3.2.

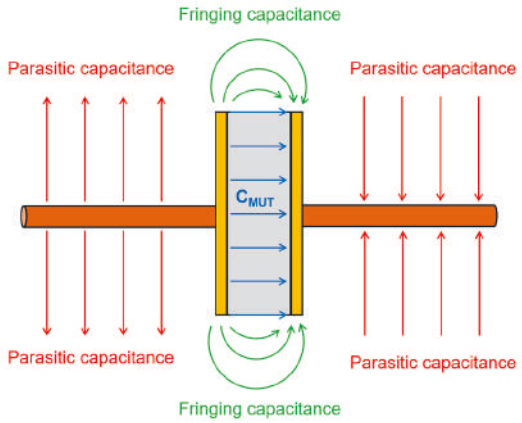


Figure 1. Components of the measured capacitance, including contributions from the MUT, fringing fields, and parasitic capacitance from the connecting wires. Arrows indicate the instantaneous electric field direction, and colors represent the different capacitive contributions.

2.2. Sensor Structure and Fabrication

Our proposed test cell is a cylindrical-shaped parallel-plate capacitive sensor designed for dielectric liquid characterization. It comprises two circular electrodes made from 0.1 mm-thick copper sheets, positioned parallel to each other and separated by a cylindrical spacer constructed from a PVC hollow section cut from a commercially available water pipe, effectively defining the active sensing area and maintaining a fixed distance between the electrodes. The PVC spacer has an inner diameter of 20.2 mm, an outer diameter of 26 mm, and a height of 3.22 mm. This PVC section also serves as the side wall of the cylindrical container for the MUT with a sample volume of approximately 1.03 mL. The height of the spacer corresponds to the electrode separation distance, denoted as d, as found in Equation (1). Circular geometry is chosen for a more uniform electric field distribution between the plates and to reduce edge effects, which can introduce inaccuracy in the capacitance measurement. The proposed CCS is employed in both electromagnetic field simulations using ANSYS Q3D Extractor 2025 R2 (Ansys Inc., Canonsburg, PA, USA) and experimental measurements using an Agilent 4285A LCR meter (Agilent Technologies, Penang, Malaysia). An illustration of the CCS with all geometrical dimensions is shown in Figure 2, and the fabricated sensor is presented in Figure 3a,b. The copper electrodes were aligned coaxially on either side of the PVC spacer and bonded using a thin adhesive layer to ensure mechanical stability, maintain a uniform electrode separation, and prevent liquid leakage during measurements. The adhesive was applied only at the electrode periphery to minimize any influence on the effective sensing region.

The CCS incorporates a 1 mm inlet and a vent, implemented as small through-holes drilled in the PVC spacer, to ensure bubble-free filling of the sensing region with the MUT. The liquid is introduced using a needle and a syringe, while the vent enables trapped air to escape during injection. This design enhances accuracy and repeatability, as air bubbles disturb the electric field distribution and cause unstable measurements.

https://doi.org/10.3390/metrology6020023

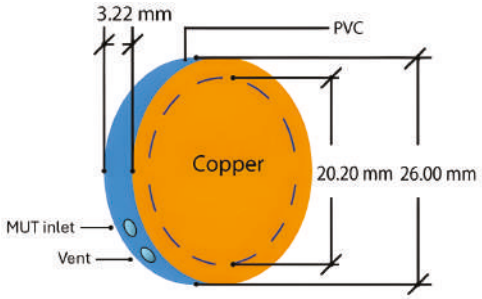
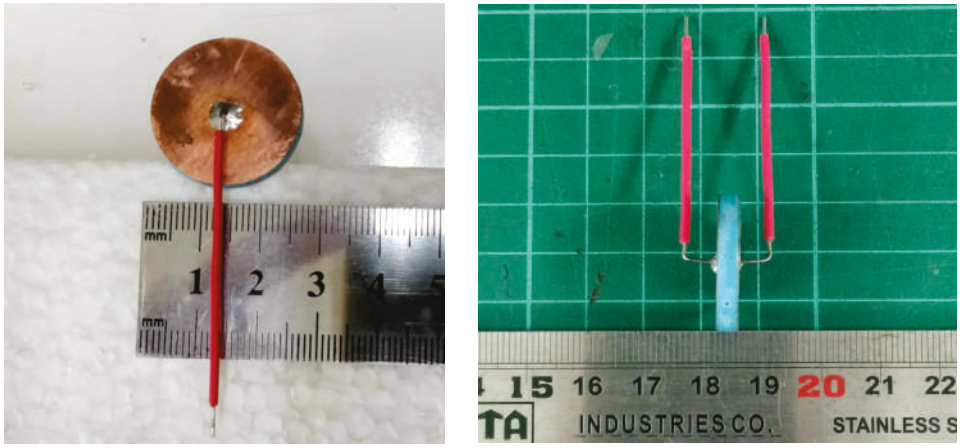


Figure 2. Geometry and dimensions of the proposed cylindrical capacitive sensor (drawing not to scale). The dashed line denotes the inner radius of the PVC spacer.



(**a**) (**b**)

Figure 3. (**a**) Photograph of the fabricated cylindrical capacitive sensor (CCS) with connecting wires soldered to the circular electrodes. (**b**) Side view of the CCS sensor arrangement showing the sensor body and the two connecting wires.

The materials under test were air, DI water, ethanol, and methanol. DI water used for the experiments was laboratory-grade DI water (Puricare, Samut Prakan, Thailand), specified to be clear and colorless with pH 5.5–7.0 at 25 °C with a low electrical conductivity in the order of a few µS/cm, according to the manufacturer. Ethanol used in the experiments was high-purity analytical-grade reagent (assay $\geq$ 99.9% by gas chromatography, water content $\leq$ 0.2% by coulometry). Methanol (CH_3OH, $\geq$99.8% purity, analytical grade) was likewise used as received without further processing.

2.3. Mathematical Modeling

In Section 2.1, the general operating principle of a parallel-plate capacitive sensor was introduced, where the measured capacitance arises from the dielectric material placed between two electrodes and additional contributions from fringing electric fields and measurement-related parasitics. Building on this foundation, the mathematical model is now extended to reflect the specific geometry and materials of the proposed sensor described in Section 2.2.

Due to the PVC sidewall from Figure 2, the measured capacitance value consists of multiple capacitive components. Accordingly, the measured capacitance can be expressed as follows:

$$C_{meas} \approx C_{MUT} + C_{fr} + C_p + C_{PVC} \tag{3}$$

where C_{MUT} represents the capacitance contribution from the liquid-filled region, C_{PVC} accounts for the contribution of the PVC sidewall, C_{fr} represents the fringing-field capacitance due to finite electrode dimensions, and C_p includes parasitic capacitances associated

https://doi.org/10.3390/metrology6020023

with connecting wires, connectors, leads, and the test fixture. In the experimental setup, C_{fr} was minimized by applying OPEN and SHORT compensation at the ends of the two-wire connections of the CCS using the LCR meter. This procedure effectively shifts the reference plane of the measurement to the electrode terminals of the sensor. Consequently, the parasitic contribution is assumed to be negligible in the analytical formulation, and the sensor capacitance can be approximated as follows:

$$C_{meas} \approx C_{MUT} + C_{fr} + C_{PVC} \tag{4}$$

2.3.1. Capacitance Contribution of the MUT

Since the circular electrodes fully cover the outer diameter of the PVC spacer, the effective sensing region can be approximated as a liquid-filled core bounded by the inner diameter of the PVC spacer. Under this assumption, the capacitance contribution of the MUT is therefore modeled using the parallel plate approximation as follows:

$$C_{MUT} \approx \varepsilon_{r,MUT}\varepsilon_0 \frac{A_{MUT}}{d} \tag{5}$$

where

$\varepsilon_{r,MUT}$ is the dielectric constant of the MUT;
d is the height of the PVC spacer; and
A_{MUT} is the base area of the MUT cylinder with

$$A_{MUT} = \pi\left(\frac{D_{in}}{2}\right)^2 \tag{6}$$

where D_{in} is the inner diameter of the PVC spacer.

2.3.2. Capacitance Contribution of the PVC Spacer

In addition to the liquid-filled core region, the annular region between the inner and outer diameters of the spacer is occupied by rigid PVC and lies within the electric field established between the electrodes. Because the electrodes extend to the outer diameter of the PVC spacer, this annular region contributes an additional capacitance that can be approximated as follows:

$$C_{PVC} = \varepsilon_{r,PVC}\varepsilon_0 \frac{A_{ann}}{d} \tag{7}$$

where

$\varepsilon_{r,\,PVC}$ is the dielectric constant of rigid PVC;
d is the height of the PVC spacer; and
A_{ann} is the area of the annular region with

$$A_{ann} = \pi\left[\left(\frac{D_{out}}{2}\right)^2 - \left(\frac{D_{in}}{2}\right)^2\right] \tag{8}$$

with D_{out} and D_{in} as the outer and inner diameters of the PVC spacer.

2.3.3. Treatment of Fringing Capacitance

Due to the finite dimensions of the circular electrodes, fringing electric fields are inevitably present at the electrode edges and extend partially into the surrounding air. The resulting fringing capacitance, denoted as C_{fr}, depends on the detailed three-dimensional field distribution and MUT's property. Thus, C_{fr} cannot be expressed in a closed analytical form for the present geometry. Instead, it is assessed indirectly through comparison between analytical predictions, numerical simulations, and experimental measurements, which will be discussed in detail in Section 3.

https://doi.org/10.3390/metrology6020023

2.3.4. Final Analytical Expression

Based on the above considerations, the total capacitance for the proposed CCS configuration is modeled as follows:

$$C_{CCS} = \varepsilon_{r,MUT}\varepsilon_0 \frac{A_{MUT}}{d} + \varepsilon_{r,PVC}\varepsilon_0 \frac{A_{ann}}{d} + C_{fr} \quad (9)$$

This analytical formulation provides a physically intuitive description of the sensor behavior and serves as a baseline for comparison with numerical simulations and experimental measurements presented in the subsequent sections.

2.4. Numerical Modeling and Simulation

Numerical simulations were performed using ANSYS Q3D Extractor, which employs three-dimensional quasi-static electromagnetic field solvers for the extraction of resistance, inductance, capacitance, and conductance matrices. This approach is well-suited to electrically small, low- to mid-frequency interconnect and capacitive structures, where wave propagation effects can be neglected.

The three-dimensional geometry of the capacitive sensor was modeled according to the dimensions described in Section 2.2. The circular copper electrodes and the PVC spacer were explicitly included in the model, as shown in Figure 4. To emulate an unbounded environment, the sensor was enclosed within a surrounding air region whose outer boundary was placed at least five times the spacer outer diameter away from the structure so that the electric field decayed to negligible levels before reaching the computational boundary.

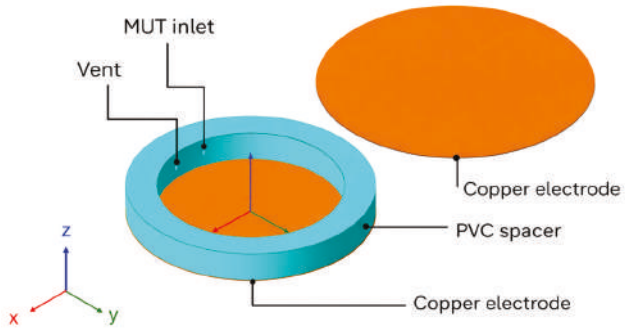


Figure 4. Three-dimensional geometrical model of the proposed CCS used in numerical simulations, showing the circular copper electrodes and the PVC spacer with the MUT inlet and the vent.

A floating reference at infinity was applied during matrix reduction to avoid artificial grounding effects and to retain only the coupling between conductors. Under this condition, the terminal capacitance between the two electrodes was extracted from the reduced capacitance matrix and interpreted as the two-terminal capacitance corresponding to the LCR meter measurement. This procedure ensures direct comparability between numerical simulation, analytical modeling, and experimental measurements.

The electrodes were modeled as perfect electric conductors. The surrounding region was defined as air with a dielectric constant of $\varepsilon_r = 1$. The PVC spacer was assigned a dielectric constant of $\varepsilon_{r,PVC} = 3.2$ [20–24], consistent with reported values at low frequencies near our operating frequency of 1 MHz. The MUTs in this study were air, DI water, ethanol, and methanol. In numerical simulations, DI water was modeled with a dielectric constant of $\varepsilon_{r,\text{water}} = 80.1$ [25,26] at the temperature of 20 °C. Ethanol and methanol were modeled using dielectric constant values of $\varepsilon_{r,\text{ethanol}} = 24.3$ [27–30], and $\varepsilon_{r,\text{methanol}} = 33.1$ [31,32] at 20 °C, respectively.

Capacitance extraction was performed at a single frequency point of 1 MHz in both simulations and experimental measurements. The default adaptive meshing strategy in

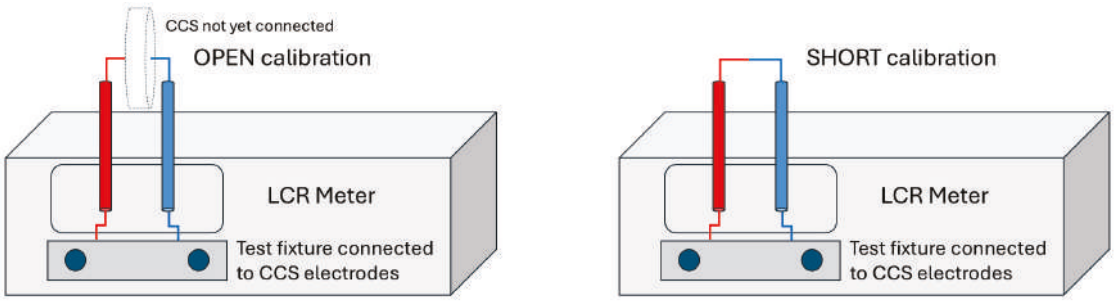
https://doi.org/10.3390/metrology6020023

ANSYS Q3D was employed, with the solver iterating until the relative change in extracted terminal capacitance between subsequent passes was below 1%, thereby ensuring convergence of the solution. The converged terminal capacitance values obtained at 1 MHz were then used for subsequent comparison with analytical predictions and experimental results.

2.5. Measurement Procedure

Capacitance measurements were performed using the LCR meter configured in a two-terminal measurement arrangement. The instrument was operated in the parallel capacitance mode, which is appropriate for low-loss capacitive structures at the selected operating frequency. The liquid measurements at 1 MHz were conducted at 20 ± 1 °C, which was verified using a glass thermometer immediately before loading each liquid sample into the CCS. This temperature condition is consistent with the value used in the numerical simulations.

Prior to measurement, OPEN and SHORT compensation were performed using the same two-wire connection as for the CCS. During OPEN calibration, the measurement leads were left unterminated to account for stray capacitances, whereas SHORT calibration was carried out with the terminals shorted to compensate for residual series impedance of the leads and connections, as shown in Figure 5. This procedure effectively removes lead- and fixture-related parasitic effects and shifts the electrical reference plane to the sensor electrodes, ensuring that the measured capacitance corresponds primarily to the CCS. OPEN and SHORT compensation was performed on the connecting wires prior to soldering them to the CCS electrodes. For the OPEN calibration, the free ends of the wires were left unterminated, while for the SHORT calibration, the same wire ends were directly shorted using a small socket. After completing both calibration steps, the wires were soldered once to the CCS electrodes and were not subsequently desoldered or re-soldered. This procedure minimizes the risk of contact degradation and avoids additional parasitic effects associated with repeated soldering.



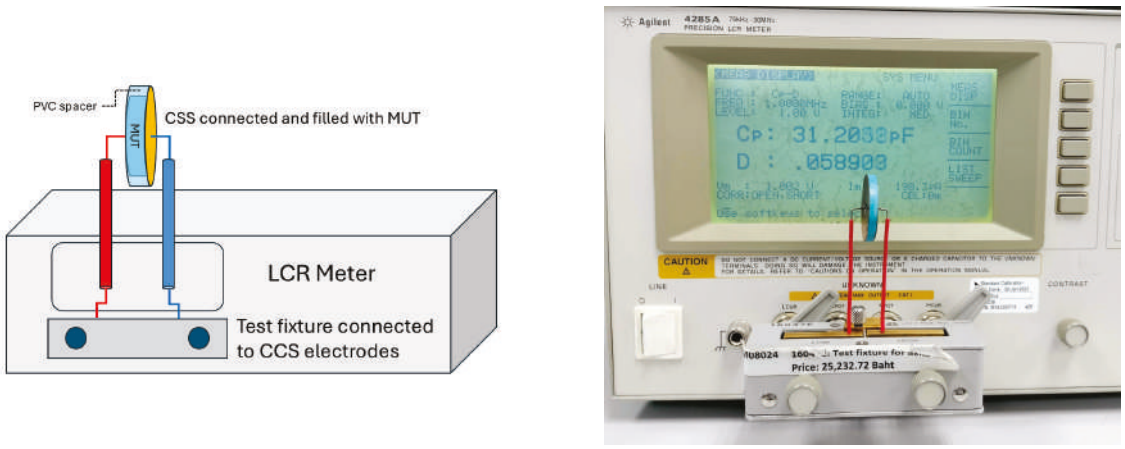
(**a**) (**b**)

Figure 5. (**a**) OPEN and (**b**) SHORT calibration configuration of the LCR meter using a two-wire connection, with the measurement leads disconnected from the CCS. The connecting wires are colored red and blue to represent different electrical potentials.

After OPEN and SHORT compensation, the CCS was filled with MUT, and capacitance readings were recorded once the displayed value stabilized, as shown in Figure 6. Separate measurements were carried out for air, DI water, ethanol, and methanol under identical measurement conditions, and the stabilized capacitance values obtained from the LCR meter were used for subsequent comparison with analytical predictions and numerical simulation results. To evaluate repeatability of the measurement setup, five consecutive measurements were performed for each base material (air, DI water, ethanol, and methanol) at 1 MHz. Parallel capacitance C_p and dissipation factor D were recorded using the LCR meter operated in C_p–D mode. OPEN–SHORT compensation was applied at the end of the

https://doi.org/10.3390/metrology6020023

two-wire connection prior to all measurements, thereby shifting the reference plane to the CCS electrodes.



(**a**) (**b**)

Figure 6. Illustration (**a**) and photograph (**b**) of the experimental capacitance measurement setup for MUT characterization. The sensor was filled with MUT and connected to the LCR meter for the determination of the capacitance value.

3. Results and Discussion

This section presents and discusses the analytical, numerical, and experimental results obtained using the proposed CCS. First, analytically calculated capacitance values derived from (9), neglecting fringing capacitance, are presented to establish a theoretical baseline. Next, simulation results obtained using ANSYS Q3D Extractor are reported and compared with the measurements. Finally, the dielectric constants of the MUT extracted using the analytical and calibration-based methods are compared.

3.1. Capacitance Comparison

Capacitance values from simulation, calculation, and measurement are summarized in Table 1. The calculations were performed using known geometrical parameters of the CCS and literature-reported dielectric constants of the MUTs. Fringing electric field effects and higher-order parasitic contributions were not explicitly included in the analytical model. Therefore, the calculated capacitance represents an idealized approximation of the CCS response.

For all MUTs, the simulated results show small deviations from the measurements. These discrepancies are attributed to fringing fields, fabrication tolerances (e.g., spacer thickness and electrode alignment), and residual parasitic effects in the experimental setup that are not fully captured in the simulation model. The calculated values are consistently lower than both simulation and measurement results because the analytical model neglects fringing fields. Overall, the close agreement among calculated, simulated, and measured capacitance values across MUTs with markedly different dielectric constants demonstrates the robustness and reliability of the proposed CCS.

Table 1. Capacitance values of the CCS loaded with different MUTs.

MUT	Simulated (pF)	Calculated (pF)	Measured (pF)
Air	2.91	2.73	2.75
DI water	72.56	72.39	72.82
Ethanol	23.76	23.25	23.78
Methanol	31.43	31.03	31.21

https://doi.org/10.3390/metrology6020023

Table 2 summarizes the means and standard deviations of C_p and the dissipation factor D extracted from five repeated measurements. The relatively small standard deviations for C_p and D confirm repeatability of the measurement and support the applicability of the model used in the subsequent relative permittivity extraction.

Table 2. Statistical summary of five repeated measurements at 1 MHz. including mean ± sample standard deviation using the LCR meter operated in C_p–D mode after OPEN–SHORT compensation.

MUT	C_p (pF), Mean ± SD	D (Mean ± SD)
Air	2.75251 ± 0.00032	0.012602 ± 0.000053
DI water	72.81522 ± 0.00819	0.1230144 ± 0.000143
Ethanol	23.77860 ± 0.00700	0.087424 ± 0.000439
Methanol	31.21012 ± 0.00190	0.0600022 ± 0.0000145

From the experimentally measured capacitance values, the dielectric constant of the MUT can be extracted either through analytical calculation or via a calibration-based approach. In the latter, the capacitance of the CCS is measured when loaded with two reference MUTs with known dielectric constants. A detailed comparison of the dielectric constants obtained from these methods is presented in the following section.

3.2. Dielectric Constant Extraction

To extract the dielectric constant of the MUT from the measured capacitance, two different extraction approaches are employed in this study. The first approach is based on a conventional analytical formulation derived from the sensor geometry, while the second approach utilizes an air–water two-point calibration method to account for geometry-dependent offsets and fringing field effects. Both methods are described below.

3.2.1. Extraction Method Using Known CCS Geometries

In the conventional analytical approach, the dielectric constant of the MUT is extracted directly from the measured capacitance of the CCS using a geometry-based formulation. After OPEN and SHORT compensation of the measurement leads, the measured capacitance C_{meas} is assumed to represent the intrinsic capacitance of the sensor structure, where the fringing capacitance in Equation (9) is simply neglected. The total measured capacitance is modeled as the superposition of the capacitance contributions associated with the PVC spacer and the MUT, and can be expressed as follows:

$$C_{meas} = \varepsilon_{r,MUT}\varepsilon_0\frac{A_{MUT}}{d} + \varepsilon_{r,PVC}\varepsilon_0\frac{A_{ann}}{d} \tag{10}$$

Rearranging the above expression, the dielectric constant of the MUT can be extracted with:

$$\varepsilon_{r,MUT} = \frac{d\left(C_{meas} - \varepsilon_{r,PVC}\varepsilon_0\frac{A_{ann}}{d}\right)}{\varepsilon_0 A_{MUT}} \tag{11}$$

In this formulation, the dielectric properties and geometry of the PVC spacer are treated as known parameters. Fringing field effects and residual geometry-dependent parasitic contributions are not explicitly modeled and are therefore implicitly absorbed into the effective capacitance term. Consequently, the accuracy of this method depends on the assumed PVC dielectric properties and the validity of the simplified field distribution.

3.2.2. Extraction Method Using Air–DI Water Calibration

To overcome the accuracy limitations of the analytical method described in Section 3.2.1, a calibration-based extraction approach is proposed. This method employs

https://doi.org/10.3390/metrology6020023

air and DI water as reference materials with well-established dielectric constants, thereby eliminating the need for explicit knowledge of the dielectric constant of the spacer material (PVC in this work). In addition, fabrication tolerances in the CCS geometry do not influence the extracted dielectric constant of the MUT. Although fringing fields are still present, their influence on the extracted permittivity is reduced because the higher dielectric constant of the PVC spacer confines a larger portion of the electric field within the spacer rather than the surrounding air.

For simplification, the measured capacitance of the CCS from Equation (10) can be expressed as follows:

$$C_{meas} = \varepsilon_{r,MUT} k + C_0 \tag{12}$$

where k is an effective geometry-dependent proportionality constant, and C_0 is a constant offset term accounting for fixed capacitance contributions, including the PVC spacer capacitance, fringing electric fields, and residual geometry-dependent parasitic effects. Both k and C_0 are treated as effective calibration parameters. This equation assumes a linear relationship between the measured capacitance and the real part of permittivity. This approximation is only valid when the sensor operates in the quasi-static regime, where its physical dimensions are much smaller than the wavelength, and the electric field distribution does not change significantly with different MUTs. Under this condition, the total capacitance can be expressed as the sum of a constant parasitic contribution and a term proportional to the permittivity of the MUT. Moreover, the electrode spacing should be small compared to the lateral dimensions of the electrodes, such that fringing field effects remain similar for different MUTs and can be effectively treated as a constant offset. Consequently, geometry-dependent factors, including spacer material properties and electrode configuration, are implicitly accounted for through calibration rather than requiring explicit modeling. It should be noted, however, that this assumption holds only when variations in spacer permittivity and electrode geometry do not significantly perturb the field distribution. In practice, the use of smooth electrode geometries (e.g., circular plates) and operation over a limited frequency range helps to minimize such effects and preserve the validity of the linear approximation.

To determine these parameters, two reference measurements are performed using air and DI water under identical measurement conditions. Substituting the known dielectric constant of air ($\varepsilon_{\text{air}} = 1$) into the above expression yields:

$$C_{air} = k + C_0 \tag{13}$$

while for DI water with dielectric constant $\varepsilon_{\text{water}}$, the measured capacitance is given by:

$$C_{water} = \varepsilon_{r,water}\, k + C_0 \tag{14}$$

By subtracting the air reference Equation (13) from the water reference Equation (14), the constant offset term C_0 is explicitly eliminated, as is common to both measurements. These yields:

$$C_{water} - C_{air} = (\varepsilon_{r,water} - 1)k \tag{15}$$

from which the effective proportionality constant k can be determined implicitly. Consequently, the capacitance C_0 can be derived from Equation (13). Substituting k and C_0 back into the generalized capacitance expression from (12) leads to a formulation for extracting the dielectric constant of an arbitrary MUT with:

$$\varepsilon_{r,MUT} = 1 + \frac{C_{meas} - C_{air}}{C_{water} - C_{air}} (\varepsilon_{r,water} - 1) \tag{16}$$

https://doi.org/10.3390/metrology6020023

Through this air–DI water calibration, the dominant geometry- and spacer-dependent contributions to the measured capacitance are absorbed into the model parameters k and C_0. As long as the conditions for the assumption of a linear relationship from Equation (12) are fulfilled, the extraction of $\varepsilon_{r,\mathrm{MUT}}$ becomes largely insensitive to the exact value of the spacer permittivity and to moderate fabrication tolerances in electrode dimensions. The performance of this proposed method is evaluated and compared with the conventional analytical approach in the next section.

3.3. Dielectric Constant Extraction from CCS Measurement Results

To evaluate the accuracy of the dielectric constant extraction, the values obtained using the conventional analytical method described in Section 3.2.1 and the proposed air–water calibration method (Section 3.2.2) were compared with literature-reported values at comparable frequency and temperature. The comparison, together with the corresponding percentage errors, is summarized in Table 3. The relative permittivity of water $\varepsilon_{r,\mathrm{water}} = 80.1$ used in the simulations corresponds to 20 °C, which matches the experimental temperature of the liquid measurements and thus minimizes temperature-induced discrepancies in Table 3. For ethanol and methanol, the remaining deviations from literature values may partly arise from residual water content and trace impurities present in the commercial solvents, despite their high nominal purities ($\geq$99.9% and $\geq$99.8%, respectively). The dielectric constants of the MUTs were first extracted using the conventional geometry-based analytical method from Equation (11). In this approach, the measured capacitance is decomposed into contributions from the MUT and the PVC spacer, assuming an ideal CCS configuration and dimensions. The accuracy of this method relies on the known sensor geometry as mentioned in Section 2.2, low fabrication tolerance, and PVC's dielectric constant close to 3.2 as reported in the literature. Using the experimentally measured capacitance values at 1 MHz, the dielectric constants extracted using the conventional analytical method are 1.02 for air, 80.577 for DI water, 24.90 for ethanol, and 33.34 for methanol. These values are in close agreement with commonly reported reference data, indicating that the analytical model provides a reasonable first-order estimate of the dielectric properties of the MUTs.

Table 3. Comparison of extracted dielectric constants with reference values from the literature and error analysis.

MUT	$\varepsilon_{r,MUT}$ from Literature	$\varepsilon_{r,MUT}$ Extracted Using Equation (11)	Error (%) Extracted Using Equation (11)	$\varepsilon_{r,MUT}$ Extracted Using Equation (16)	Error (%) Extracted Using Equation (16)
Air	1	1.02	2	N/A	N/A
DI water	80.1	80.58	0.6	N/A	N/A
Ethanol	24.3	24.9	2.47	24.75	1.85
Methanol	33.1	33.34	0.73	33.12	0.06

The dielectric constants of the MUTs were then extracted using the proposed air–DI water calibration method from Equation (16). Capacitance values of the CCS loaded with air and DI water from Table 1 are used to extract the dielectric constant from the measured capacitance value of the CCS loaded with an unknown MUT. The extracted dielectric constant of MUT obtained from this method is 24.75 for ethanol and 33.12 for methanol. These values exhibit close agreement with literature-reported data. Since air and DI water served as calibration references, extracted dielectric constants are identical to the theoretical values reported in the literature, so that errors compared to theoretical values are not applicable (N/A) in Table 3.

https://doi.org/10.3390/metrology6020023

Compared with the conventional analytical method, the proposed air–DI water calibration approach demonstrates improved accuracy by reducing sensitivity to uncertainties in spacer material properties, fabrication tolerances, and idealized field assumptions. For ethanol, the extraction error in dielectric constant is 2.47% using the conventional method with known CCS geometric and material parameters. This error decreases to 1.85% with the proposed air–DI water calibration method. For methanol, the error is reduced from 0.73% to 0.06%.

This improvement arises since the calibration procedure removes the explicit dependence on the PVC dielectric constant and detailed sensor geometry. By referencing the measurements to air and DI water, fabrication tolerance, spacer material uncertainty, and fringing field effects are inherently compensated. Consequently, the sensor does not require highly precise fabrication or exact prior knowledge of the spacer dielectric constant. In practice, the spacer can be fabricated from a range of dielectric materials without precise permittivity characterization. Also, moderate geometric variations do not significantly degrade the extraction accuracy. This enhances the robustness and practical applicability of the proposed method for the characterization of the MUT.

Although the numerical errors obtained with the conventional analytical method and the proposed air–DI water calibration method are of comparable magnitude for the well-controlled CCS prototype investigated in Table 3, the two approaches differ in their robustness with respect to practical implementation. The analytical method relies explicitly on accurate knowledge of the sensor geometry and spacer permittivity, as well as on simplified assumptions regarding the field distribution; therefore, its accuracy can degrade when fabrication tolerances, unknown spacer materials, or modified electrode geometries are introduced. In contrast, the calibration-based extraction absorbs residual parasitic effects as well as geometry- and spacer-dependent variations into the effective parameters k and C_0, and thus does not require precise prior characterization of the spacer or exact cell dimensions. Moreover, the proposed calibration approach is inherently scalable and adaptable: it can be directly applied when the CCS is resized or when the spacer material is changed, without the need to re-measure physical dimensions or reformulate the analytical model. A simple recalibration step is sufficient to maintain accuracy. As a result, the method is particularly suitable for low-cost, in-house fabricated sensors or applications involving design variations, where it preserves accuracy despite fabrication uncertainties and configuration changes.

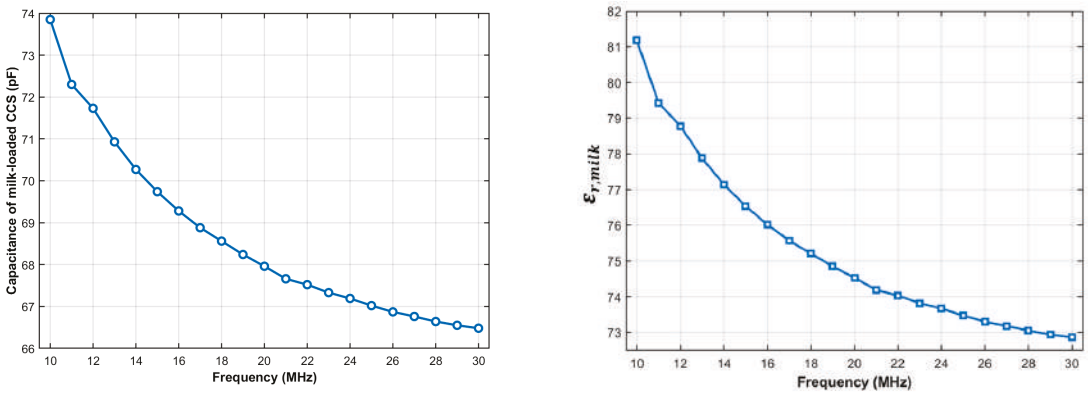
3.4. Application Example: Frequency-Dependent Characterization of Cow's Milk

To further validate the proposed sensor and extraction method using a realistic biological sample, additional measurements were conducted on a commercial ultra-high temperature (UHT) cow's milk product (Thai–Denmark, plain 100% cow's milk, Saraburi, Thailand). The sensor was operated at a controlled temperature of 25 °C, and all calibration procedures were performed at the same temperature to ensure fair comparison with literature data. This condition is consistent with Zhu et al. and Liu et al., who characterized raw cow's milk over 10–4500 MHz at approximately 22–25 °C [33–35]. The UHT milk sample in this experiment is produced from 100% fresh cow's milk and has typical whole-milk macronutrient levels, with fat, protein, and lactose contents in the same order of magnitude as standard whole cow's milk reported in dairy composition references [36].

To calibrate the CCS at the working temperature of 25 °C, the capacitance values of CCS filled with air and DI water were first measured using the LCR meter. At least five consecutive readings were taken without disturbing the setup, showing an insignificant difference in the measured values. The results were averaged and used as the representative value for calibration. The DI water measurements yielded an extracted dielectric

https://doi.org/10.3390/metrology6020023

constant of 78.3 at 25 °C. This result is in good agreement with reported values of 78.3–78.4 at this temperature [25,37]. Because the dielectric constant of water decreases with temperature (for example, from about 80.1 at 20 °C to about 78.3 at 25 °C), performing the DI water calibration at 25 °C is essential to avoid inaccuracy when extracting the dielectric constant of the milk at the same temperature. The same protocol with at least five repeated measurements per condition was then applied to measure the UHT milk sample at each frequency point between 10 and 30 MHz. The average capacitance value was used to extract the dielectric constant as described in Section 3.2.2. Figure 7a,b plots the measured CCS capacitance and the extracted dielectric constant of the UHT milk sample at 25 °C in a frequency range from 10 to 30 MHz.



(**a**) (**b**)

Figure 7. Measured capacitance of the proposed CCS filled with UHT milk sample (circles denote measurement points connected by straight-line segments to show the trend) (**a**), and extracted dielectric constant of UHT whole cow's milk at 25 °C (squares denote extracted data points connected by straight-line segments to show the trend) (**b**), as a function of frequency from 10 to 30 MHz.

The monotonic decrease in dielectric constant with increasing frequency follows the expected dielectric relaxation behavior of milk as a multiphase polydisperse system composed of liquid fat globules emulsified in a water-based solution containing dissolved lactose, minerals, and suspended proteins. At low radio frequencies, several polarization mechanisms contribute to the dielectric constant, including dipolar rotation of water molecules, migration and accumulation of mobile ions, and interfacial polarization at boundaries between fat globules, casein micelles, and the aqueous phase. As frequency increases to tens of MHz, the interfacial polarization mechanism can no longer fully follow the rapidly oscillating electric field within each cycle, so its contribution to stored electric energy diminishes and the dielectric constant decreases with frequency. Similar decreasing trends of the dielectric constant with frequency have been reported for raw milk, soy milk, and other high moisture foods, confirming that the measured $\varepsilon_{r,milk}$ curve in Figure 8 is consistent with established dielectric relaxation behavior in aqueous, multi-phase food systems [38,39].

The observed dispersion can be interpreted in terms of Maxwell–Wagner–Sillars (MWS) interfacial polarization in heterogeneous dielectrics. In such systems, contrasts in permittivity and conductivity between dispersed and continuous phases lead to charge accumulation at internal interfaces and to a characteristic low-frequency dielectric dispersion, as rigorously analyzed for composite materials by Samet et al. and for heterogeneous polymers and emulsions by Samet et al. [40] and Qian et al. [41]. Hanai's classical emulsion theory further shows that interfacial polarization is a key contributor to the dielectric spectra of concentrated emulsions, providing a widely used framework for interpreting frequency-dependent permittivity in oil-in-water systems [42]. Within this perspective,

https://doi.org/10.3390/metrology6020023

cow's milk can be viewed as a multiphase emulsion in which fat globules and protein aggregates are dispersed in an aqueous electrolyte phase, and the decrease of $\varepsilon_{r,milk}$ between 10 and 30 MHz is consistent with the high-frequency tail of a Maxwell–Wagner–Sillars interfacial relaxation process.

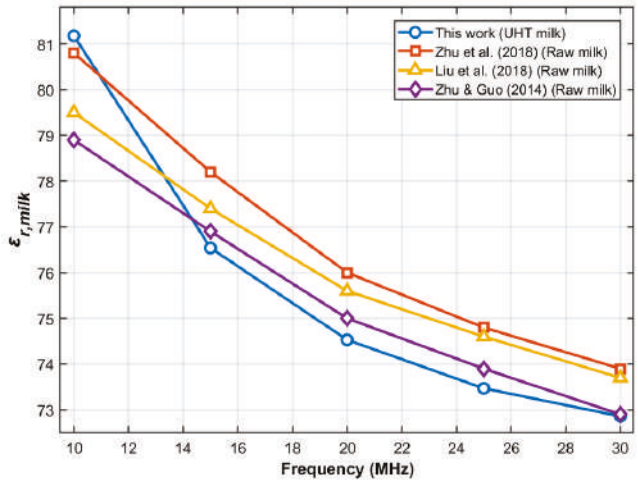


Figure 8. Comparison of the extracted dielectric constant of UHT cow's milk (this work) and raw cow's milk reported in the literature at approximately 25 °C over the frequency range 10–30 MHz. Literature values were digitized from figures in the publications [33–35].

To validate the extracted dielectric constant of the UHT milk sample over the frequency range from 10 to 30 MHz, the measured values are compared with literature data reported at 25 °C within a comparable frequency range [33–35]. For consistency, dielectric constant data were exclusively chosen from the unmodified baseline raw cow's milk curves presented in those studies. Only measurements corresponding to 25 °C were considered to ensure thermal comparability with the present work. Data obtained under altered salt, fat, or lactose concentrations, skimmed conditions, or different temperatures were intentionally excluded. The comparison is presented in Figure 8. All datasets exhibit monotonic dielectric dispersion, with the UHT milk sample showing slightly lower permittivity at higher frequencies. This discrepancy is reasonably attributed to the use of commercially UHT-processed milk in the present study, whereas the referenced works investigated raw milk. Additional variation may arise from differences in fat, protein, lactose, and mineral composition among sample sources, as well as differences in measurement fixture geometry and calibration methodology.

Although the milk samples are not identical, their compositions are sufficiently similar to yield consistent dielectric behavior. All datasets show the characteristic decrease in dielectric constant with increasing frequency. This trend is consistent with the relaxation of Maxwell–Wagner interfacial polarization in milk as a heterogeneous oil-in-water emulsion. The comparison, therefore, provides a strong trend-based validation under closely matched conditions rather than an exact numerical replication.

Table 4 summarizes the performance of the proposed CCS compared with representative low- and high-frequency techniques reported in the literature for pure DI water, methanol, ethanol, and other liquids. Our results are comparable to or better than many reported low-frequency and microwave techniques. While cavity and resonator-based methods can reach sub-percent errors under carefully controlled conditions, they generally require complex calibration procedures and high-frequency measurement equipment. In contrast, the proposed air–water calibrated capacitive approach offers competitive accuracy with a simple cylindrical parallel plate geometry, low cost, low frequency instrumentation, and reduced sensitivity to spacer permittivity, fringing fields, and geometric tolerances.

https://doi.org/10.3390/metrology6020023

Table 4. Comparison of dielectric permittivity measurement accuracy with the representative literature (pure liquids).

Work	Method and Frequency	MUT	Reference for Comparison	Reported Error/Uncertainty (%)
This work (conventional extraction)	Low-frequency capacitive sensor, 1 MHz	Air, DI water, ethanol, methanol	Literature values	Air: 2%, DI: 0.6%, Ethanol: 2.47%, Methanol: 0.73%
This work (Air–DI water calibration)	Low-frequency capacitive sensor, 1 MHz	Air, DI, dl, UHT milk	Literature values	Ethanol: 1.85% Methanol: 0.06%,
[19]	Parallel-plate admittance cell, 100 kHz–1 MHz	Water, ethanol, methanol (plus 3 other liquids)	NPL MAT-23 reference liquids	Expanded relative uncertainty $\leq$ 1.5% for all reference liquids.
[31]	RC low-pass method, 60 Hz	Water, ethanol, methanol	Kirkwood model	Maximum absolute deviation < 0.12%; repeatability scatter < 0.05%
[32]	RC low-pass method, 60 Hz	Water–ethanol, water–methanol	Correlation model	Average absolute deviation $\approx$ 1% over most compositions
[43]	CPW-based impedance sensor, simulation, up to 20 GHz	Ethanol, methanol, NaCl solutions	Value used in simulation/ Literature data	<0.1% (5% NaCl) to ~1.7% (Ethanol) at 10 GHz/Up to 10% at 5 GHz vs. literature data
[44]	Multi-element CSRR, $\approx$2.9 GHz	Water, ethanol–water solutions	Literature data	Minimum of 0.2% (50% ethanol) and maximum of 1.3% (water)
[45]	SIW filter-based sensor, $\approx$5 GHz	Ethanol–water mixtures (includes pure ethanol and DI water)	Mixing-model reference	Minimum of 0.93% (0.6 volume fraction) and maximum of 6.8% (0.1 volume fraction)

4. Conclusions

In this study, a cylindrical parallel-plate capacitive sensor was designed, fabricated, and experimentally validated for the characterization of liquid materials in a lower megahertz frequency range. The sensor employs circular copper electrodes separated by a PVC spacer, providing a compact and repeatable capacitive test cell suitable for low-frequency small-volume liquid characterization. Analytical calculations, numerical simulations using ANSYS Q3D Extractor, and experimental measurements performed at 1 MHz were carried out to comprehensively evaluate the sensor performance. A close agreement was observed among analytically calculated, numerically simulated, and experimentally measured capacitance values for air, DI water, ethanol, and methanol, confirming the robustness and reliability of the proposed CCS design.

Two extraction methods for the extraction of the liquid sample's dielectric constant from measured capacitance values were investigated. The conventional geometry-based analytical method provided reasonable first-order estimates of the dielectric constants; however, its accuracy depends on precise knowledge of the PVC spacer permittivity and idealized field assumptions. To address these limitations, an air–DI water calibration-based extraction method was proposed. By measuring the capacitance of air and DI water-loaded CCS as reference materials with known dielectric properties, this method effectively eliminated geometry-dependent offsets, spacer material uncertainty, and fringing field contributions. The proposed calibration-based method demonstrated improved accuracy and reduced sensitivity to experimental and modeling uncertainties, yielding extracted dielectric constants for ethanol and methanol that closely matched literature-reported values. These results highlight the practical advantage of the proposed approach for dielectric sensing applications where exact material properties and geometrical parameters of the CCS are not required. Future work will focus on extending the proposed sensing and calibration framework to a broader range of liquids and frequencies, as well as exploring sensor

https://doi.org/10.3390/metrology6020023

miniaturization and integration with microfluidic platforms for real-time characterization of biomedical and agricultural samples.

Author Contributions: Conceptualization, T.P.O., W.J. and S.C.; Data curation, T.P.O. and S.C.; Formal analysis, T.P.O., T.P. and S.C.; Visualization, T.P.O. and S.C.; Funding acquisition, S.C.; W.J. and P.A.; Investigation, T.P.O., T.P. and S.C.; Methodology, T.P.O., M.U., W.J. and S.C.; Software, T.P.O. and T.P.; Supervision, S.C., W.J. and P.A.; Validation, T.P.O., T.P. and S.C.; Writing—original draft, T.P.O., T.P. and S.C.; Writing—review and editing, T.P.O., T.P. and S.C.; All authors have read and agreed to the published version of the manuscript.

Funding: This research was funded by the National Science, Research, and Innovation (NSRF) and King Mongkut's University of Technology North Bangkok under grant no. KMUTNB-FF-69-A-01, King Mongkut's University of Technology North Bangkok (KMUTNB), and the National Science and Technology Development Agency (NSTDA) under grant no. B.003/2564.

Institutional Review Board Statement: Not applicable.

Informed Consent Statement: Not applicable.

Data Availability Statement: The data presented in this study are available on request from the corresponding author.

Acknowledgments: The High Frequency Systems Laboratory, King Mongkut's University of Technology North Bangkok gratefully acknowledges CADFEM Thailand, an Ansys Elite Channel Partner, for providing the Ansys (Version 2024 R2) license used in this study.

Conflicts of Interest: The authors declare no conflicts of interest.

References

1. Bao, X.; Ocket, I.; Crupi, G.; Schreurs, D.; Bao, J.; Kil, D.; Puers, B.; Nauwelaers, B. A planar one-port microwave microfluidic sensor for microliter liquids characterization. *IEEE J. Electromagn. RF Microw. Med. Biol.* **2018**, *2*, 10–17. [CrossRef]
2. Grenier, K.; Dubuc, D.; Poleni, P.-E.; Kumemura, M.; Toshiyoshi, H.; Fujii, T.; Fujita, H. Integrated broadband microwave and microfluidic sensor dedicated to bioengineering. *IEEE Trans. Microw. Theory Tech.* **2009**, *57*, 3246–3253. [CrossRef]
3. Abdelnour, A.; Rennane, A.; Kaddour, D.; Tedjini, S. Non-destructive dielectric characterization method for food products. In Proceedings of the 2017 IEEE MTT-S International Microwave Symposium (IMS), Honolulu, HI, USA, 4–9 June 2017; pp. 2022–2024.
4. Komarov, V.; Wang, S.; Tang, J. Permittivity and measurements. In *Encyclopedia of RF and Microwave Engineering*; Chang, K., Ed.; Wiley: Hoboken, NJ, USA, 2005; pp. 3693–3711.
5. Gabriel, C.; Gabriel, S.; Corthout, Y.E. The dielectric properties of biological tissues: I. Literature survey. *Phys. Med. Biol.* **1996**, *41*, 2231–2249. [CrossRef] [PubMed]
6. Tieri, A.; Pisa, S.; Piuzzi, E.; Frezza, F.; Cavagnaro, M. Wideband measurement of dielectric properties of wheat flour. *IEEE Trans. Instrum. Meas.* **2023**, *72*, 6000509. [CrossRef]
7. Piccinno, F.; Naccarata, F.; Colella, R.; Chietera, F.P.; Catarinucci, L.; Marrocco, G. Exploiting self-tunable RFID chips for wireless sensing of permittivity to enable passive low-cost food-quality monitoring systems. In Proceedings of the 2023 IEEE 13th International Conference on RFID Technology and Applications (RFID-TA), Aveiro, Portugal, 4–6 September 2023; pp. 45–48. [CrossRef]
8. Kaatze, U. Measuring the dielectric properties of materials. Ninety-year development from low-frequency techniques to broadband spectroscopy and high-frequency imaging. *Meas. Sci. Technol.* **2013**, *24*, 012005. [CrossRef]
9. Leblon, B.; Adedipe, O.; Hans, G.; Haddadi, A.; Tsuchikawa, S.; Burger, J.; Stirling, R.; Pirouz, Z.; Groves, K.; Nader, J.; et al. A review of near-infrared spectroscopy for monitoring moisture content and density of solid wood. *For. Chron.* **2013**, *89*, 595–606. [CrossRef]
10. Barreira, E.; Almeida, R.M.S.F.; Delgado, J.M.P.Q. Infrared thermography for assessing moisture-related phenomena in building components. *Constr. Build. Mater.* **2016**, *110*, 251–269. [CrossRef]
11. Chuma, E.L.; Iano, Y.; Fontgalland, G.; Bravo Roger, L.L. Microwave sensor for liquid dielectric characterization based on metamaterial complementary split ring resonator. *IEEE Sens. J.* **2018**, *18*, 9978–9983. [CrossRef]

https://doi.org/10.3390/metrology6020023

12. Kalisiak, M.; Wiatr, W. Broadband permittivity measurement of liquids in a semi-open coaxial test cell with meniscus-effect removal. In Proceedings of the 2018 22nd International Microwave and Radar Conference (MIKON), Poznan, Poland, 14–17 May 2018; pp. 546–549. [CrossRef]
13. Sorocki, J.; Piekarz, I. Broadband dielectric spectroscopy of liquids using two-wire sensor towards their content analysis. In Proceedings of the 2023 IEEE MTT-S International Microwave Biomedical Conference (IMBioC), Leuven, Belgium, 18–20 September 2023; pp. 139–141. [CrossRef]
14. Chedurupalli, S.; Vishwam, T.; James, R.K.C. Complex permittivity measurement of liquids using half mode corrugated substrate integrated waveguide structure. In Proceedings of the 2022 98th ARFTG Microwave Measurement Conference (ARFTG), Las Vegas, NV, USA, 19–24 June 2022; pp. 1–4. [CrossRef]
15. Ghiri, R.E.; Saghati, A.P.; Kaya, E.; Entesari, K. A miniaturized contactless UWB microwave system for time-domain dielectric spectroscopy. *IEEE Trans. Microw. Theory Tech.* **2017**, *65*, 5334–5344. [CrossRef]
16. Blande, V.S.; de Araujo, R.A.; Azevedo, W.L.M.; Filho, J.P.; Callegari, R.H.M. Optimizing capacitive sensor designs for precise void fraction measurement in industrial applications. In Proceedings of the 2024 IEEE URUCON, Montevideo, Uruguay, 18–20 November 2024; pp. 1–5. [CrossRef]
17. Halalay, I.C. Versatile cell for complex permittivity measurements on liquids. *Rev. Sci. Instrum.* **1999**, *70*, 3432–3434.
18. Goad, D.G.W.; Wintle, H.J. Capacitance corrections for guard gaps. *Meas. Sci. Technol.* **1990**, *1*, 965. [CrossRef]
19. Piuzzi, E.; Chicarella, S.; Cataldo, A.; De Benedetto, E.; Cannazza, G. Design, realization, and experimental characterization of an admittance cell for low-frequency dielectric permittivity measurements on liquids. *IEEE Trans. Instrum. Meas.* **2016**, *65*, 104–111. [CrossRef]
20. Vijayakumar, V.; Nam, S.Y. Dielectric properties of polyvinylchloride (PVC) composites and nanocomposites. In *Poly(Vinyl Chloride) Based Composites and Nanocomposites*; Akhina, H., Sabu, T., Eds.; Springer: Cham, Switzerland, 2024. [CrossRef]
21. Sugumaran, C.P. Diagnosis on mechanical and electrical properties of cable insulation PVC with nanofiller. In Proceedings of the 2013 IEEE 1st International Conference on Condition Assessment Techniques in Electrical Systems (CATCON), Kolkata, India, 6–8 December 2013; pp. 223–226. [CrossRef]
22. Ahmad, Z. Polymer dielectric materials. In *Dielectric Material*; Silaghi, M.A., Ed.; InTech: Rijeka, Croatia, 2012. [CrossRef]
23. Cardarelli, F. *Materials Handbook*; Springer International Publishing: Cham, Switzerland, 2018; ISBN 978-3-319-38923-3.
24. Khan, S.M.; Gull, N.; Khan, R.U.; Butt, M.T.Z. Polyvinylchloride (PVC): Structure and properties relationship. In *Polyvinylchloride-Based Blends*; Misra, V.P., Darie-Nita, R., Eds.; Springer: Cham, Switzerland, 2022; pp. 19–47. [CrossRef]
25. Malmberg, C.G.; Maryott, A.A. Dielectric constant of water from 0° to 100° C. *J. Res. Natl. Bur. Stand.* **1956**, *56*, 1–8. [CrossRef]
26. Gregory, A.P.; Clarke, R.N. Traceable measurements of the static permittivity of dielectric reference liquids over the temperature range 5–50 °C. *Meas. Sci. Technol.* **2005**, *16*, 1506–1516. [CrossRef]
27. Khalid, N.; Zainuddin, M.F.; Abbas, Z.; Mohamed, T.N.; Sabli, N. Determination of ethanol concentration of ethanol/water mixture solutions with open-ended coaxial method. In Proceedings of the 2016 International Conference on Advances in Electrical, Electronic and Systems Engineering (ICAEES), Putrajaya, Malaysia, 14–16 November 2016; pp. 652–656. [CrossRef]
28. Barthel, J.; Bachhuber, K.; Buchner, R.; Gill, J.; Kleebauer, M. Dielectric spectra of some common solvents in the microwave region. Dipolar aprotic solvents and amides. *Chem. Phys. Lett.* **1990**, *167*, 62–66. [CrossRef]
29. Kindt, J.T.; Schmuttenmaer, C.A. Far-infrared dielectric properties of polar liquids probed by femtosecond terahertz pulse spectroscopy. *J. Phys. Chem.* **1996**, *100*, 10373–10379. [CrossRef]
30. Saiz, L.; Guàrdia, E.; Padró, J.-À. Dielectric properties of liquid ethanol: A computer simulation study. *J. Chem. Phys.* **2000**, *113*, 2814–2822. [CrossRef]
31. Mohsen-Nia, M.; Amiri, H.; Jazi, B. Dielectric constants of water, methanol, ethanol, butanol, and acetone: Measurement and computational study. *J. Solut. Chem.* **2010**, *39*, 701–708. [CrossRef]
32. Mohsen-Nia, M.; Amiri, H. Measurement and modelling of static dielectric constants of aqueous solutions of methanol, ethanol and acetic acid at T = 293.15 K and 91.3 kPa. *J. Chem. Thermodyn.* **2013**, *57*, 67–70. [CrossRef]
33. Zhu, X.; Liu, Q.; Guo, W. Dielectric properties of raw milk as influenced by frequency, salts, and salt contents. *J. Food Process Eng.* **2018**, *41*, e12885. [CrossRef]
34. Liu, Q.; Guo, W.; Zhu, X. Effect of lactose content on dielectric properties of whole milk and skim milk. *Int. J. Food Sci. Technol.* **2018**, *53*, 2037–2047. [CrossRef]
35. Zhu, X.; Guo, W. Determination of the fat content in cow's milk based on dielectric properties. *Int. J. Food Prop.* **2014**, *17*, 1379–1392.
36. Pereira, P.C. Milk Nutritional Composition and Its Role in Human Health. *Nutrition* **2014**, *30*, 619–627. [CrossRef] [PubMed]
37. Fernandez, D.P.; Goodwin, A.R.H.; Lemmon, E.W.; Levelt Sengers, J.M.H.; Williams, R.C. A formulation for the static permittivity of water and steam at temperatures from 238 K to 873 K at pressures up to 1200 MPa. *J. Phys. Chem. Ref. Data* **1997**, *26*, 1125–1166. [CrossRef]

https://doi.org/10.3390/metrology6020023

38. Sosa-Morales, M.E.; Valerio-Junco, L.; López-Malo, A.; García, H.S. Dielectric properties of foods: Reported data in the 21st century and their potential applications. *LWT-Food Sci. Technol.* **2010**, *43*, 1169–1179. [CrossRef]
39. Nelson, S.O. Dielectric properties of agricultural products and some applications. *Res. Agric. Eng.* **2010**, *56*, 104–112. [CrossRef]
40. Samet, M.; Kallel, A.; Serghei, A. Maxwell–Wagner–Sillars interfacial polarization in dielectric spectra of composite materials: Scaling laws and applications. *J. Compos. Mater.* **2022**, *56*, 3197–3217. [CrossRef]
41. Qian, J.; Yan, S.; Li, Z.; Yu, L.; Wang, X.; Zhang, Z.; Sun, J.; Han, X. Modification of the Maxwell–Wagner heterogeneous dielectric model for heterogeneous polymers and emulsions. *Polymers* **2022**, *14*, 2743. [CrossRef]
42. Hanai, T. Theory of dielectric dispersion due to the interfacial polarization and its application to emulsions. *Kolloid Z.* **1960**, *171*, 23–31. [CrossRef]
43. Savić, A.; Stepputtis, A.; Jacob, A.F. Impedance sensor for fluid permittivity measurements up to 20 GHz with single-liquid calibration. In Proceedings of the 48th European Microwave Conference (EuMC 2018), Madrid, Spain, 23–27 September 2018; pp. 227–230. [CrossRef]
44. Wang, C.; Liu, X.; Huang, Z.; Yu, S.; Yang, X.; Shang, X. A sensor for characterization of liquid materials with high permittivity and high dielectric loss. *Sensors* **2022**, *22*, 1764. [CrossRef]
45. Yasin, A.; Gogosh, N.; Sohail, S.I.; Abbas, S.M.; Shafique, M.F.; Mahmoud, A. Relative permittivity measurement of microliter volume liquid samples through microwave filters. *Sensors* **2023**, *23*, 2884. [CrossRef]

Disclaimer/Publisher's Note: The statements, opinions and data contained in all publications are solely those of the individual author(s) and contributor(s) and not of MDPI and/or the editor(s). MDPI and/or the editor(s) disclaim responsibility for any injury to people or property resulting from any ideas, methods, instructions or products referred to in the content.

https://doi.org/10.3390/metrology6020023

metrology

MDPI

Article

Interlaboratory Comparison of SI-Traceable Flow Metering Calibration Facilities with Gaseous Carbon Dioxide

Ara Abdulrahman [1,*], Gabriele Chinello [2], Revata Seneviratne [2], Kurt Rasmussen [3], Dennis van Putten [4] and Pier Giorgio Spazzini [5]

[1] VSL B.V. National Metrology Institute, 2629JA Delft, The Netherlands
[2] TÜV SÜD National Engineering Laboratory, East Kilbride G75 0AF, UK; gabriele.chinello@tuvsud.com (G.C.); revata.seneviratne@tuvsud.com (R.S.)
[3] FORCE Technology, 2605 Brøndby, Denmark; ktr@forcetechnology.com
[4] DNV Netherlands B.V., 9747AA Groningen, The Netherlands; dennis.vanputten@dnv.com
[5] Istituto Nazionale di Ricerca Metrologica (INRIM), 10135 Torino, Italy; p.spazzini@inrim.it
* Correspondence: aabdulrahman@vsl.nl

Abstract

Carbon capture, utilization, and storage (CCUS) plays an important role in meeting the European Union's target to reduce greenhouse gas emissions by 55% by 2030 and become carbon neutral by 2050. Accurate flow metering is required throughout the carbon capture and storage (CCS) chain to meet fiscal and regulatory requirements. To establish accurate CO_2 flow metering, flow meters must be calibrated with traceability to international standards of measurement at relevant flow conditions. To ensure confidence, reliability, and comparability of calibration results, calibration facilities perform interlaboratory comparisons. However, there is currently a lack of CO_2 gas flow meter calibration facilities. The flow metering calibration facilities of VSL, NEL, INRIM, DNV, and FORCE participated in an interlaboratory comparison with CO_2 up to 400 m^3/h and 31 bar(a) to compare the calibration results with several flow metering principles. At the intermediate-scale facilities of NEL, VSL, and INRIM, the difference in results between the VSL and INRIM facilities were within the facilities' CMC values, while NEL's facility showed a significant difference primarily due to vibrational relaxational effects of CO_2 with small critical flow Venturi nozzles. At the large-scale facilities of NEL, DNV, and FORCE, 91% of the test points passed the equivalency criteria in the range of 20 m^3/h to 400 m^3/h with a Coriolis meter, confirming traceability for carbon dioxide across the facilities. Overall, the interlaboratory comparison has made it possible for the CCUS industry to calibrate gaseous CO_2 flow meters with traceability to international standards.

Keywords: carbon dioxide (CO_2) flow measurement; Interlaboratory comparison; flow meter calibration; carbon capture, utilization, and storage (CCUS); SI-traceable metrology standards; CO_2 flow meter calibration facility; decarbonisation

1. Introduction

Europe must make reductions in CO_2 emissions in order to meet stringent reduction targets related to global warming. The European Union set a target to reduce greenhouse gas emissions by 55% by 2030 and become carbon neutral by 2050 [1]. To support meeting these ambitious targets the Green Deal was introduced which specifically states that "priority areas include clean hydrogen, fuel cells and other alternative fuels, energy storage, and carbon capture, storage and utilization."

Carbon capture, utilization, and storage (CCUS) can be used to remove the CO_2 produced by industrial processes to be re-used or stored either underground or locked in an alternative material. It is versatile, in the sense that the CO_2 removal step can complement any process (e.g., production of power, fuels, chemicals and heating). In order to facilitate efficient and safe operation of CCUS technologies across Europe and to support the CCUS industry, accurate flow measurement of carbon dioxide transferred across the CCUS chain is required for operational, fiscal and regulatory purposes [2–5]. For example, the accuracy requirement for the European Union's Emission Trading System (EU ETS) can be as low as 2.5% on the emitted mass of CO_2 [2,5,6], where it is estimated that flow measurement accuracy needs to be 1.5% or better in order to meet the 2.5% requirement after accounting for the uncertainties in the measurement of composition, temperature and pressure, and equations of state (EoS) [3].

To ensure accurate flow measurement across the CCUS chain, flow meter calibration facilities that are traceable to international standards (SI-traceable facilities) are required. These facilities are preferably ISO 17025 [7] certified and can calibrate flow meters with CO_2 to create similar flow conditions as experienced by the meters in the field [3,8]. There is currently a lack of flow meter calibration facilities that can calibrate flow meters in the relevant range of flow conditions in the CCUS chain [3].

Interlaboratory comparisons are used to gain confidence in the calibration of the flow meters, establish effectiveness in measurements and comparability of measurements, demonstrate validity of calibration results, and enable SI-traceable calibrations [7,9]. While there are many flow meter calibration facilities that can calibrate flow meters with CO_2, there is no assurance with regard to SI traceability and, to the authors' best knowledge, interlaboratory comparisons with CO_2 have not been performed.

An interlaboratory comparison was conducted between several laboratories in the intermediate and large scale with gaseous CO_2, as part of the "Metrology Support for Carbon Capture Utilisation and Storage" (21GRD06 MetCCUS) project. In the intermediate scale, the comparison was performed up to 30 m^3/h at atmospheric pressure between VSL, NEL and INRIM with a rotary meter and a Coriolis meter. In the large scale, the comparison was performed up to 400 m^3/h and 31 bar(a) between NEL, FORCE and DNV with a Coriolis and a turbine meter.

This paper includes a description of the facilities participating in the comparison, the methodology of assessing equivalence between the laboratories, results and discussions, conclusion, and recommendations for future work.

2. Facilities Descriptions

2.1. Intermediate Scale

2.1.1. VSL Mercury-Seal Piston Prover

The VSL mercury-seal piston prover is a primary flow measurement standard for calibration of flow meters and other mercury piston provers. The system consists of four mass flow controllers (MFCs) and four mercury ring tubes, also called measuring tubes. The system uses one mercury ring tube at a time, which is chosen based on the flow rate at which the device or meter under test (MuT) is calibrated. The mercury ring tubes serve as reference devices for calibrations. The system is ISO 17025 accredited and has a range of 0.0001 m^3/h to 3.5 m^3/h at ambient conditions, with a calibration and measurement capability (CMC) of 0.2–0.4% (k = 2). The system can calibrate volume and flow rate measuring instruments.

A simplified process flow diagram and photo of the mercury-seal piston prover system are shown in Figures 1 and 2 below.

https://doi.org/10.3390/metrology6020022

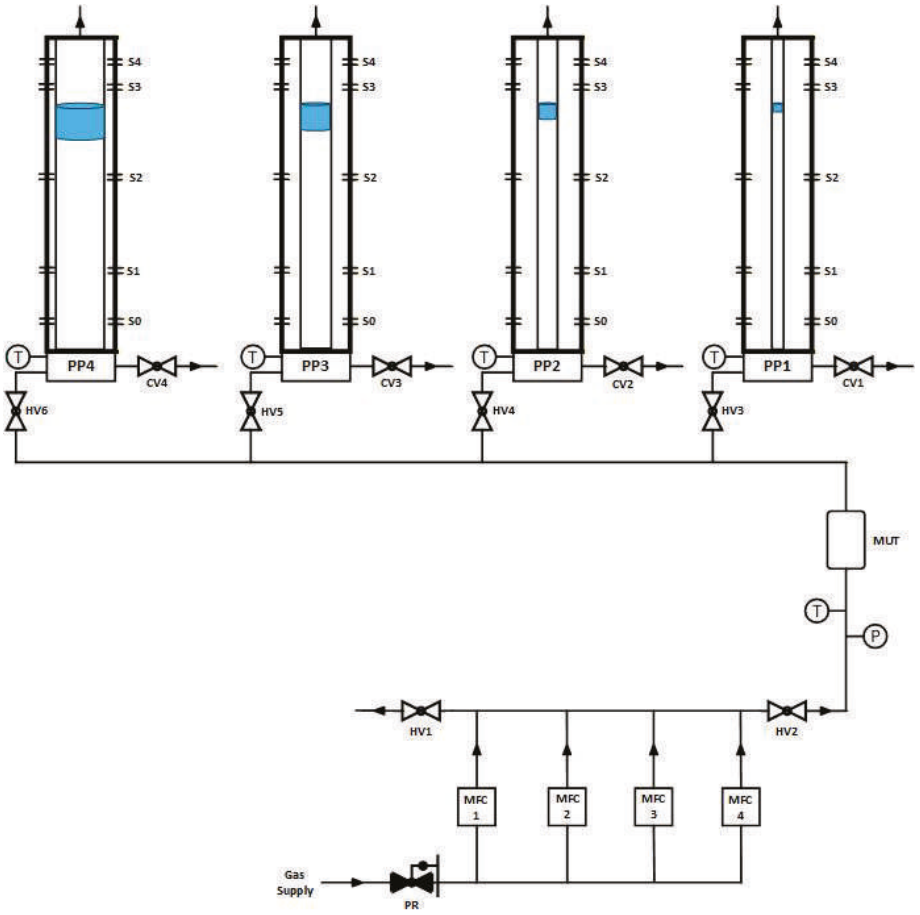


Figure 1. VSL's mercury-seal piston prover facility. For the tests in this comparison, the meter was placed in the MUT (meter under test) position. T represents a temperature sensor. P represents a pressure sensor. PR represents a pressure reducer. PP represents a piston prover. MFC represents a mass flow controller. HV represents a hand valve, and CV represents an automatic control valve. S0–S4 represent the infrared sensors. The arrows represent the flow direction.

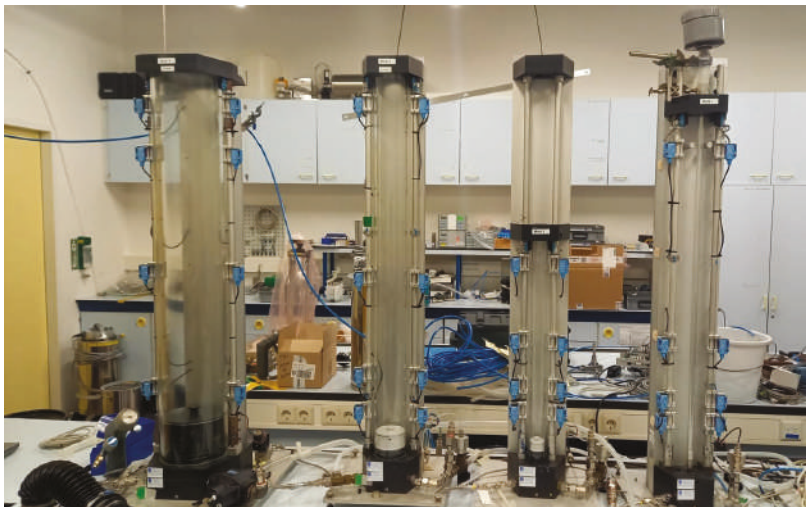


Figure 2. A photo of the mercury-seal piston provers at VSL.

The MFCs are used to generate a constant flow rate and consist of a control valve and a thermal mass flow meter. To maintain a constant inlet pressure, a pressure regulator is installed just before the inlet of the MFCs. This allows the MFCs to maintain the desired flow rate more consistently.

https://doi.org/10.3390/metrology6020022

A mercury ring tube consists of a precision glass tube containing a piston with a mercury-seal. By using mercury, the piston can move through the glass tube virtually friction-free, while the mercury ensures a gas-tight seal.

Infrared and laser sensors are located at various heights on guides placed parallel to the tube. These sensors emit an electrical pulse at time t_i when the piston interrupts the light beam. The size of a single volume therefore depends on the difference in height between two sensors and the diameter of the tube between the two sensors.

The length between the two sensors and the diameter of the tube between the two sensors are calibrated with direct traceability to the "meter", ensuring SI-traceability. The system also includes calibrated timers that are directly traceable to the "second". Since the calibration of the internal volume is independent of the gas, the provers can provide SI-traceable calibrations with any gas.

The MFCs generate a flow rate, which is directed to the flow meter under test and then a mercury ring tube via the valves. To initiate a flow measurement, a valve behind the tube is closed, causing the piston to move. When the piston passes the first sensor (s0), a time measurement is initiated. When the piston passes the next sensor, the time between s0 and this sensor is stored. A temperature measurement recording is also initiated while passing s0, which stops once the stop sensor is reached. Using the measured time and the known volume, the flow rate can now be determined.

2.1.2. NEL High-Pressure Low-Flow Facility

The NEL high-pressure low-flow facility, illustrated in Figures 3 and 4, is built around a DN25 nominal bore line, with gas supplied via an off take from the NEL high-pressure gas flow facility's 60 bar(g) gas supply line. The inlet pressure to the meter under test (MUT) is regulated using a pressure regulator. A plate heat exchanger installed between the pressure regulator and MUT compensates for temperature changes due to the pressure changes through the regulator and also enables testing at different gas temperatures from 0 °C to 40 °C. Gas flow rates are controlled using a needle valve installed downstream of the MUT. The reference flow rate is determined using a range of critical flow Venturi nozzles (CFVN) installed further downstream and the outlet piping from the CFVN is open to the atmosphere. All static pressure, differential pressure, and temperature measurements are taken with traceable calibrated instrumentation. Gas properties are calculated using REFPROP from NIST [10].

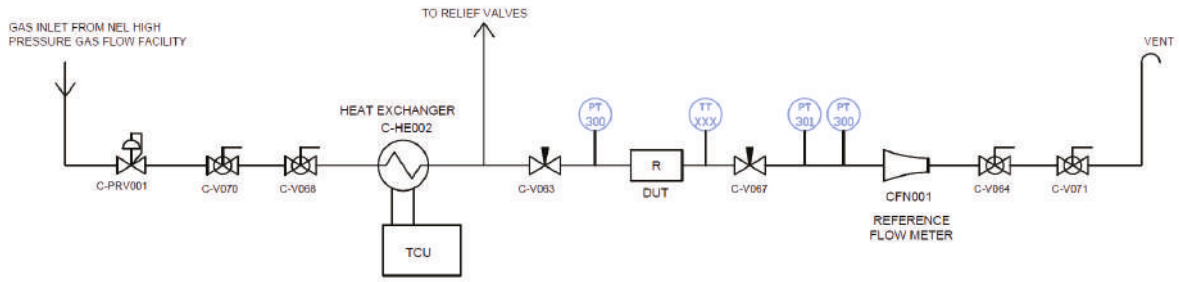


Figure 3. Schematic of the NEL high-pressure low-flow facility. PT is pressure transmitter. TT is temperature transmitter. C-V is the control valve. DUT is device under test. C-PR is pressure regulator. The arrows represent the flow direction.

https://doi.org/10.3390/metrology6020022



Figure 4. A photo of the NEL high-pressure low-flow facility.

When the facility operates with nitrogen gas at 40 bar(g) and 20 °C, it has the capability to calibrate flow meters at gas flow rates from 0.2 kg/min (0.259 m^3/h) to 4 kg/min (5.18 m^3/h) with expanded uncertainty of the reference flow measurement of 0.3% (k = 2). The recent upgrade to this facility includes the capability to test with carbon dioxide gas.

2.1.3. INRIM Piston Prover

For the intermediate-scale comparison INRIM used its large piston prover (MeGAS) for the high flow rates and its bell prover (BellGAS) for the low flow rates.

The MeGas test rig is a single-stroke, plunger-type piston prover. The device is a 6 m high structure (see Figure 5) that has a platform at the top where a finely controlled brushless motor drives, through a gearbox, the female ball-screw of a lead screw connected with the piston. This apparatus causes the vertical movement of the piston and the emission of pulses from a rotating encoder fitted on the female screw. The piston is constituted by a 1000 mm nominal diameter, 1630 mm long and 14 mm thick carbon steel cylinder fitted to a large bottom flange. The leak-proof gasket at the top of the chamber is a Teflon-coated, 1000 mm diameter O-ring compressed to the necessary and adjustable extent by an upper flange.

The internal diameter of the measurement chamber is 1095 mm; in the clearance between its walls and the piston, 10 platinum resistance temperatures (PRTs) are installed at different heights and positions in order to measure the average gas temperature and to detect possible non uniformities. The chamber rests on the 1950 mm diameter base of the prover. A bended pipe is connected to a 100 mm bore at the center of the base which conveys the gas displaced by the piston towards the test line. A group of automatically operated valves (a safety valve, one for admission of atmospheric air and one for gas delivery to the test line) are installed at the facility exit.

The MeGAS itself is calibrated through the dimensional calibration of the piston, making the standard directly traceable to the "metre". The claimed expanded uncertainty of the facility MeGAS is 0.1% (k = 2). More detail on the calibration of the MeGAS can be found in the paper by Piccato et al. [11].

The BellGAS facility is a standard bell prover, with an internal volume of about 150 L. the original facility was improved by modifying the position reading through addition of a high resolution encoder, allowing a reading of the movement with a resolution of about 0.5 mL/pulse, and a special movable compensation weight, which allows to maintain the stability of the pressure within the bell to +/−2 Pa throughout the bell run. The flow capacity of the device ranges between approximately 0.03 m^3/h and 7.2 m^3/h, and the

https://doi.org/10.3390/metrology6020022

claimed expanded uncertainty of the BellGAS facility is 0.12% (k = 2). The internal volume of the BellGAS bell prover is calibrated using the volume displacement method against a calibrated scale. Therefore the standard is traceable to the kilogram.

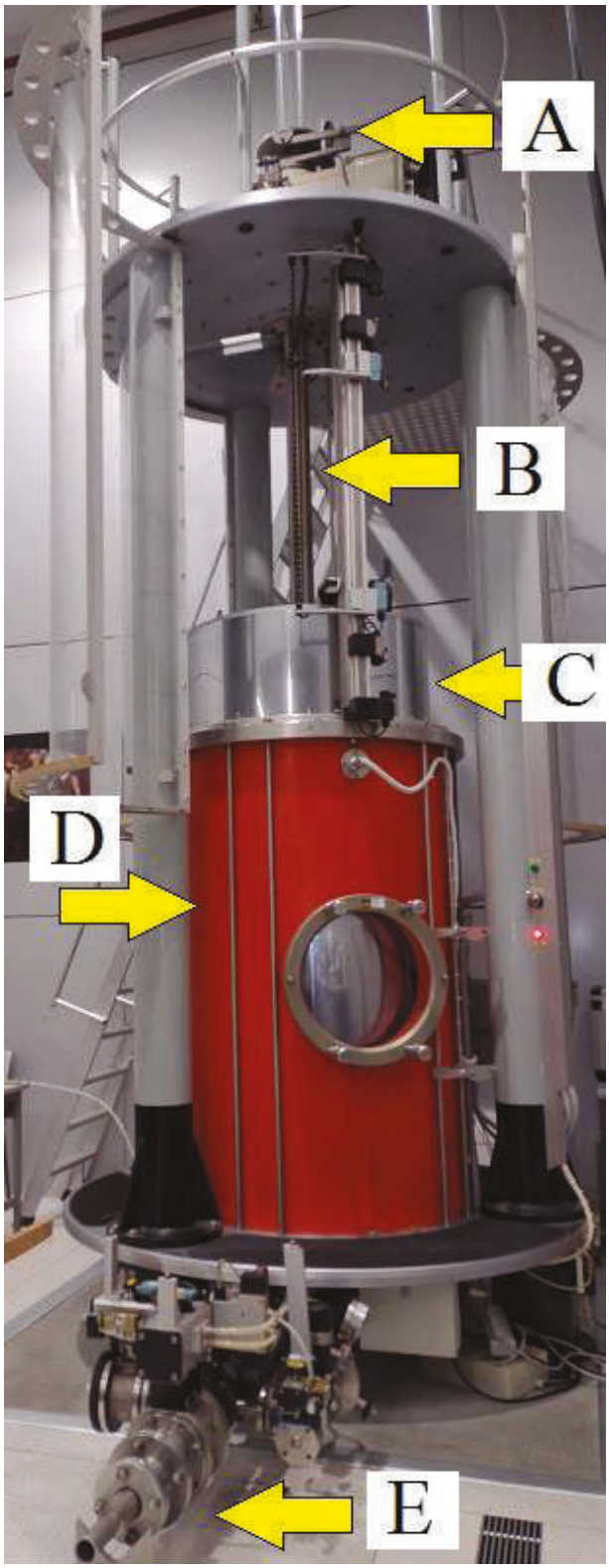


Figure 5. MeGas facility, A: MeGas encoder and piston control, B: screw, C: piston, D: measurement chamber, E: facility outlet.

https://doi.org/10.3390/metrology6020022

2.2. Large Scale

2.2.1. NEL High-Pressure Gas Flow Facility

The NEL large-scale gas flow facility is based around a DN150 nominal bore flow loop as illustrated in Figures 6 and 7. The gas used for testing is nitrogen or carbon dioxide. Mixtures of carbon dioxide and inert gases (i.e., N_2, Ar, He) can also be tested. The gas properties are calculated from using REFPROP from NIST [10].

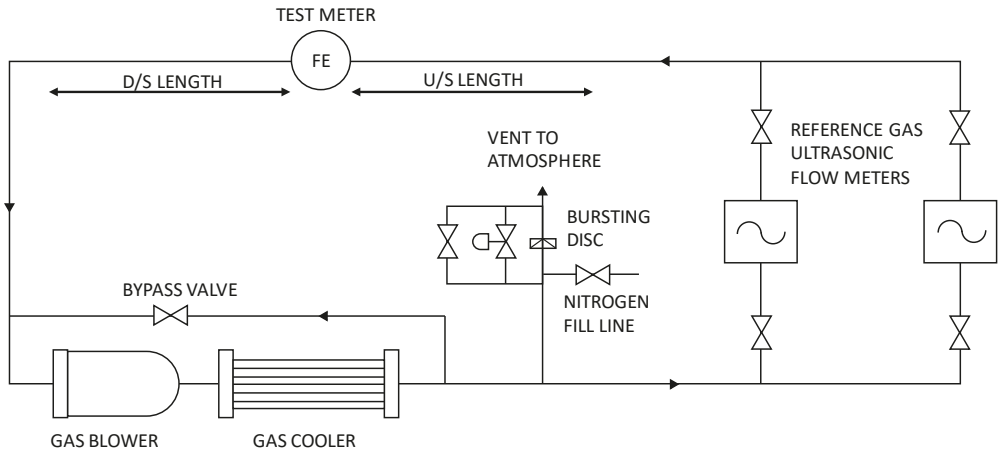


Figure 6. Schematic of the NEL high-pressure gas flow facility. U/S means upstream. D/S means downstream. The arrows represent the flow directions.



Figure 7. A photo of the NEL high-pressure flow facility.

The facility operates at a nominal temperature of 20 °C, over a nominal pressure range of 10 bar(g) to 63 bar(g) for nitrogen (which corresponds to a gas density range of approximately 13 kg/m^3 to 74 kg/m^3) and 20 bar(g) to 40 bar(g) for carbon dioxide (which corresponds to a gas density range of approximately 43 kg/m^3 to 101 kg/m^3).

The gas is driven around the flow loop by a 200 kW fully encapsulated gas blower and the flow rate is controlled by varying the speed of the blower. The maximum achievable gas volumetric flow rate is dependent upon the size and type of reference/test flow meter installed. The facility is ISO 17025 accredited (UKAS) for a flow range of 20 m^3/h to 1600 m^3/h, and can reach up to 2100 m^3/h.

The reference master meter used for the tests described in this report is a DN200 FLOWSIC600-XT ultrasonic gas meter (serial number 22101021 and calibrated K factor 7992 pulse/m^3 for nitrogen, and 7962 pulse/m^3 for carbon dioxide).

https://doi.org/10.3390/metrology6020022

The ultrasonic meter K factor was obtained against a 6-inch turbine meter from PTB [12], and it is checked for drift at regular intervals against an in-house 8-inch orifice package. All static pressure, differential pressure, and temperature measurements are taken using SI-traceable calibrated instrumentation.

In this interlaboratory comparison, the NEL gas flow facility was operated in 'recirculation' mode with the transfer package compared against the reference master meter system. For this mode, the overall uncertainty in the volumetric quantity of gas passed through the meter under test (MUT), is 0.35% (k = 2).

2.2.2. FORCE Piston Prover

The primary standard at FORCE Technology's gas flow test facility is a piston prover system. It is based on a closed-loop, bidirectional configuration, consisting of two parallel cylinders with a bore diameter of 0.6 m. Each piston is hydraulically driven, and its position is monitored by a linear transducer to ensure precise control of the flow. Four directional control valves maintain a consistent flow path during both forward and reverse operation.

The facility supports calibration of flowmeters with nominal pipe sizes ranging from 2 inches to 6 inches. It operates at a nominal temperature of 20 °C and can handle pressures from 1 bar(a) to 66 bar(a). The test gases include natural gas, CO_2, nitrogen, and air. The system accommodates flow rates from 2 m^3/h to 400 m^3/h, with differential pressures up to 500 mbar.

The piston prover serves as a primary standard with metrological traceability to the meter, based on dimensional measurements of the piston and its displacement. All measurements of static pressure, differential pressure, and temperature are performed using traceable calibrated instrumentation, and the gas property calculations were performed using the REFPROP database developed by NIST [10].

2.2.3. DNV Flow Facility

The All Gas Flow Loop Groningen (AGFLG) test facility at DNV is a closed loop system based on DNV's existing multiphase test facility, extended with a dedicated gas reference system [13]. The facility can handle 25 bar differential pressure, which makes it suitable for testing several meters in series and uses critical flow Venturi nozzles (CFVN) as reference meters. The operational range of the facility is summarized in Table 1.

Table 1. Specifications of the All Gas Flow Loop Groningen (AGFLG) test facility at DNV.

Test Fluids:	Nitrogen, hydrogen (up to 30% in natural gas, and 100% in future), methane, carbon dioxide
Flow Range:	16 am^3/h to 1000 am^3/h
Test Sections:	2-inch to 8-inch
Operating Pressure:	5 bar(g) to 33 bar(g)
Test section differential pressure:	25 bar
Temperature Range:	−45 °C to 35 °C
Reference meters:	Sonic nozzles, turbine meters, Coriolis meters
Claimed reference uncertainty:	0.12% to 0.15% (k = 2)

The AGFLG reference system consists of a sonic nozzle skid (containing CFVNs) in series with 4-inch and 6-inch dual lines containing a turbine and Coriolis reference meter, as outlined in Figure 8. A 4-inch turbine meter (FMG MT400, 40 m^3/h to 400 m^3/h) and a 2-inch Coriolis meter (Emerson Micromotion CMF200) are installed in the 4-inch line,

https://doi.org/10.3390/metrology6020022

while a 6-inch turbine meter (FMG MT1000, 100 m^3/h to 1000 m^3/h) and an 3-inch Coriolis meter (Emerson Micromotion CMF300) are installed in the 6-inch line.

Each reference meter has its own traceability chain [14]. The CFVNs are traceable via dimensional measurements (throat diameter and curvature) [15,16] and air calibration tests at Physikalisch-Technische Bundesanstalt (PTB) [14], the German national metrology institute. The Coriolis meters were calibrated at the manufacturer's ISO 17025 accredited calibration facility with water (Emerson's test facility in Ede, NL) to achieve its traceability. The turbine gas meters are traceable via DNV and FORCE, the Danish Designated Institute for flow measurement. The corrections of the turbine meters are determined according to the PTB turbine meter model [17,18] and the Coriolis meters are corrected for pressure and compressibility effects [19–21]. The reference system is installed downstream of the test section as shown in Figures 8 and 9 below.

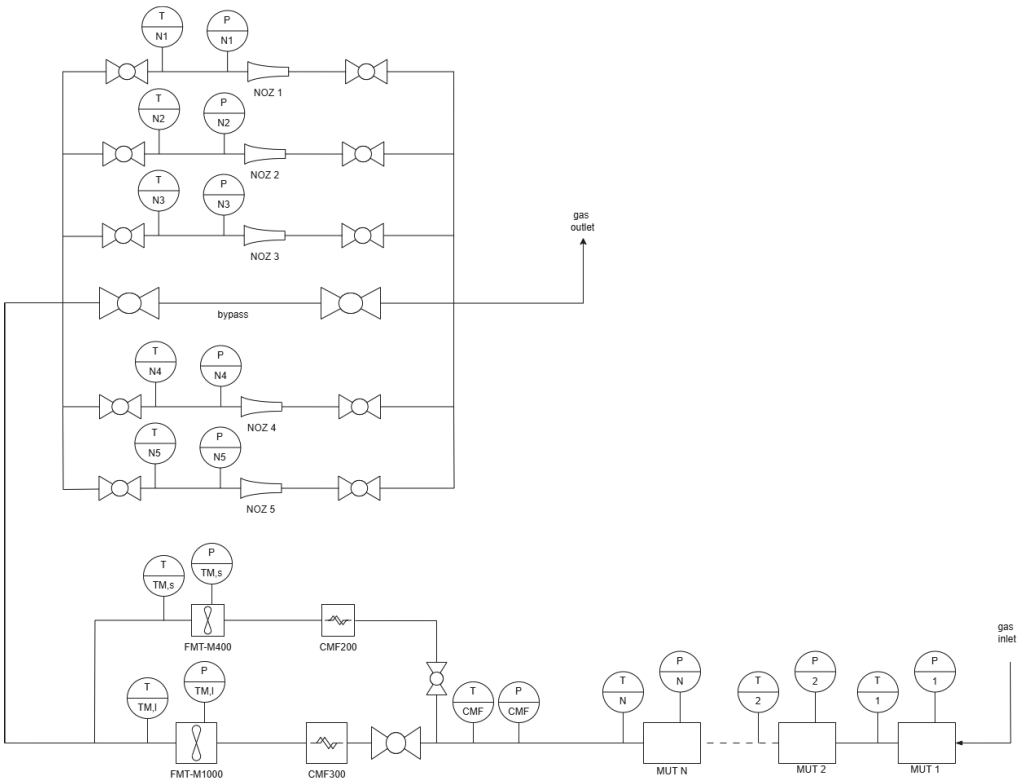


Figure 8. Schematic of the reference section of the All Gas Flow Loop Groningen (AGFLG) test facility at DNV. From the right, the gas flows first through the meter under test (MUT), then through the reference Coriolis meters, reference turbine meters, and the reference critical flow Venturi nozzles. T represents temperature sensors. P represents pressure sensors. NOZ represents sonic nozzles. The dashed lines represents a series of MUT devices that can be installed in series. CMF200 and CMF300 are reference Coriolis meters. FMT-M400 and FMT-M1000 are reference turbine meters.

The metrological evaluation and facility uncertainty estimation was performed independently by PTB, and detailed information is provided in the report by Van der Grinten et al. [14]. The facility uncertainty is estimated to be between 0.12% and 0.15% (k = 2) for the range of gases tested in [14] and is expected to be applicable/transferable to CO_2 as well. Compared to reference [14], an additional ultrasonic flow meter is installed to verify the composition measurement by means of the speed of sound comparison.

https://doi.org/10.3390/metrology6020022

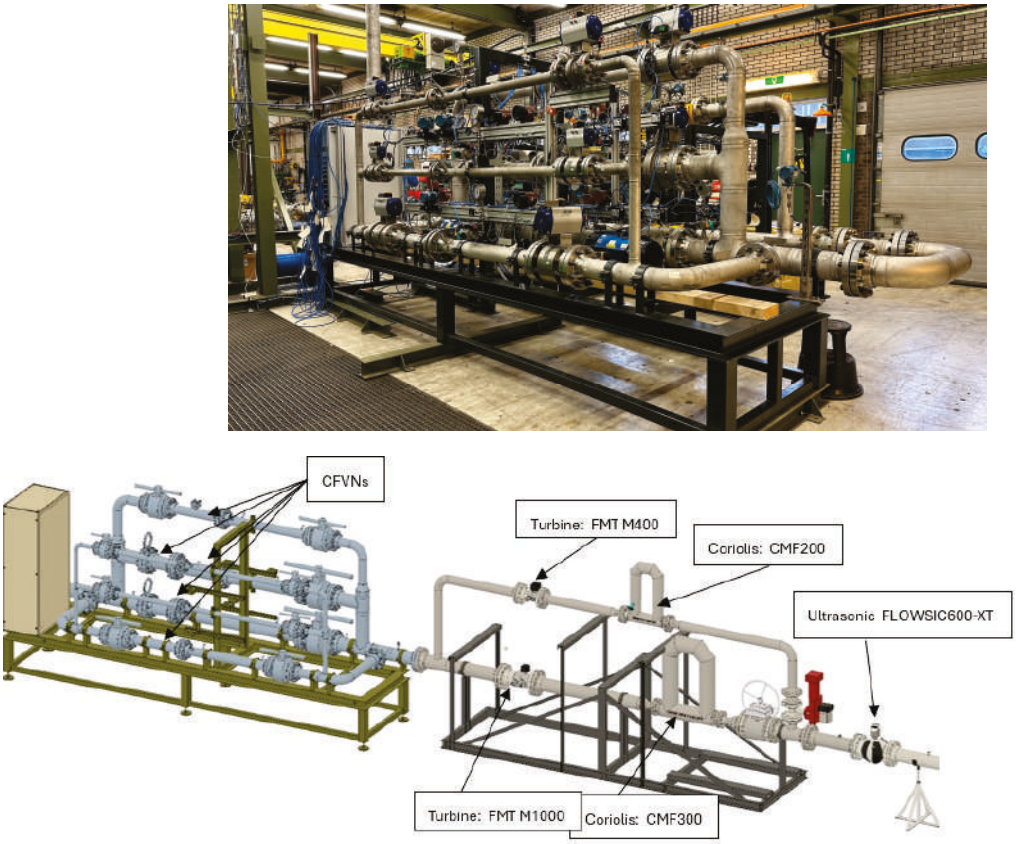


Figure 9. Photo of the CFVN section of gas flow reference system of the All Gas Flow Loop Groningen (AGFLG) test facility at DNV (top). Bottom figure indicates the different measurement principles with flow from right to left.

3. Methodology

Each flow measurement facility conducted the calibrations and processed the recorded data in accordance with their respective internal procedures. The comparison calculations were based on standardized methods as found in [22–25]. The comparison of the facilities was undertaken at each flow condition by using the mean value of the flow measurement from the three repeats. Expanded uncertainty of the mean value for each test point, U_r was determined using the expression in Equation (1).

$$U_r = \frac{t^* \sigma}{\sqrt{n}} \tag{1}$$

where

t^* is Students t value at 95% confidence, σ is the sample standard deviation of the results, and n is the number of repeats (i.e., 3).

In the case of these interlaboratory comparison calibrations, the degrees of freedom for each test point, $v = n - 1 = 2$.

Hence, for a t-distribution with 2 degrees of freedom at 95% confidence, t (4.95%); $t^* = 4.303$.

Equation (1) then becomes:

$$U_r = \frac{4.303\ \sigma}{\sqrt{3}} \tag{2}$$

https://doi.org/10.3390/metrology6020022

The overall expanded uncertainty for each test facility, U_i is calculated by combining the reference lab expanded uncertainty, U_{lab} quoted by the test facility and the repeatability uncertainty of the mean, U_r [25], as follows:

$$U_i = \sqrt{{U_{lab}}^2 + {U_r}^2} \tag{3}$$

Calibration and measurement capability (CMC) values for each facility were used as the reference uncertainty, U_{lab}. Tables 2 and 3 below summarize the CMC values applied in this inter-comparison, which vary depending on the test conditions. It is worth noting that Equation (3) is rearranged from the equation included in the "WGFF Guideline for CMC Uncertainty and Calibration Report Uncertainty" [24] as follows:

$$U_i = \quad 2 \quad \sqrt{\left(\frac{U_{lab}}{2}\right)^2 + \left(\frac{t_{95}}{2}\,\frac{\sigma}{\sqrt{n}}\right)^2} = \sqrt{{U_{lab}}^2 + \left(t_{95}\,\frac{\sigma}{\sqrt{n}}\right)^2} = \sqrt{{U_{lab}}^2 + {U_r}^2} \tag{4}$$

Table 2. Calibration and measurement capabilities (CMC) of each intermediate-scale facility.

Transfer Meter	Calibration and Measurement Capability (%) (k = 2)		
	NEL	**VSL**	**INRIM**
PGM meter (volume flow)	0.39	0.2	0.1

Table 3. Calibration and measurement capabilities (CMC) for each large-scale facility.

Transfer Meter	Calibration and Measurement Capability (%) (k = 2)		
	NEL	**DNV**	**FORCE**
Coriolis meter (mass flow)	0.35	0.22 to 0.29	0.27
Turbine meter (volumetric flow)	0.35	0.22 to 0.27	0.15

The normalized error, E_n between each laboratory's results and the comparison reference value, CRV were calculated following the procedure outlined by Cox [23] and is summarized as follows.

The CRV and its associated uncertainty are determined using the weighted mean formula, as expressed in Equations (5) and (6), respectively.

$$CRV = \frac{\sum_{i=0}^{n} \frac{e_i}{U_i^2}}{\sum_{i=0}^{n} \frac{1}{U_i^2}} \tag{5}$$

$$U^2(CRV) = \frac{1}{\sum\limits_{i=0}^{n} \frac{1}{U_i^2}} \tag{6}$$

where e_i is the mean relative error of the transfer meter for each test facility and U_i is the overall uncertainty of the test facility as defined by Equation (3).

The difference between mean relative error for each test facility, d_i and the CRV was calculated by using Equation (7).

$$d_i = e_i - CRV \tag{7}$$

And the expanded uncertainty $U(d_i)$ was calculated using Equation (8).

$$U^2(d_i) = U_i^2 - U^2(CRV) \tag{8}$$

https://doi.org/10.3390/metrology6020022

Since the facilities operated independently and contributed to the CRV, the normalized error, E_n was calculated for each test facility according to Equation (9).

$$E_n = \frac{d_i}{U(d_i)} \tag{9}$$

E_n provides a measure of the equivalence of each of the facilities' results relative to the CRV. The interpretation of the absolute value of E_n is as follows:

- $|E_n| < 1$: the result of the laboratory is consistent with the CRV (passed).
- $1 < |E_n| < 1.2$: the result of the laboratory might indicate a possible warning in the measurement process. For this particular situation the particular facility is recommended to check the procedures and methodology.
- $|E_n| > 1.2$: the result of the laboratory is not consistent with CRV (failed).

3.1. Intermediate-Scale Comparison

3.1.1. Intermediate-Scale Test Conditions

The intermediate-scale comparison was performed between VSL, NEL and INRIM with carbon dioxide and nitrogen. The calibrations with nitrogen gas establishes a baseline for the laboratories and comparison because the laboratories readily calibrate meters with nitrogen. The test conditions are reported in Table 4. It should be noted that test pressure at NEL was higher than at VSL and INRIM because the NEL facility uses sonic nozzles as reference meters which require sufficient upstream pressure to ensure sonic velocity at the nozzle throat.

Table 4. The test conditions of the intermediate-scale comparison.

Calibration Fluid	Pressure (bar.a)	Temperature (°C)	Density (kg/m^3)	Flow Rate Range (m^3/h)	VSL	INRIM	NEL
N_2	Atmospheric (6 to 11 at NEL)	20	1.13 to 1.20 (7 to 13 at NEL)	0.1 to 30	0.1 to 3 m^3/h	Yes	Yes
CO_2	Atmospheric (3 to 7 at NEL)	20	1.16 to 1.8 (6 to 12 at NEL)	0.1 to 30	0.1 to 2.2 m^3/h	Yes	0.6 to 15 m^3/h

3.1.2. Intermediate-Scale Test Meter and Sequence of Testing

The test meter for this comparison was a DN50 PGM rotary gas meter provided by NEL (PGM triple master meter G16 serial number 100218/2023) with a flow range of 0.25 m^3/h to 30 m^3/h. See Figure 10 below. The PGM flow meter was calibrated with upstream and downstream 2-inch flanges spools as shown in Figure 11. The DN50 rotary meter was initially calibrated at VSL in July 2024. The meter was subsequently calibrated by NEL in March 2025, followed by the final set of calibrations conducted by INRIM in June 2025. Figures 11 and 12 show the meter installed in the VSL and NEL facilities, respectively. It should be noted that a Coriolis meter was also calibrated at the three facilities. However, the results of the comparison with the Coriolis meter are not presented here because the results were inconclusive.

To calibrate the meter, its pulse output was used to calculate the volume and volume flow rate. Each facility used its own pressure and temperature measurement devices. The pressure was measured at the pressure port located at the rotary meter body. VSL and INRIM measured the temperature at temperature port located at the rotary meter body. NEL measured the temperature in the downstream rotary meter spool.

https://doi.org/10.3390/metrology6020022

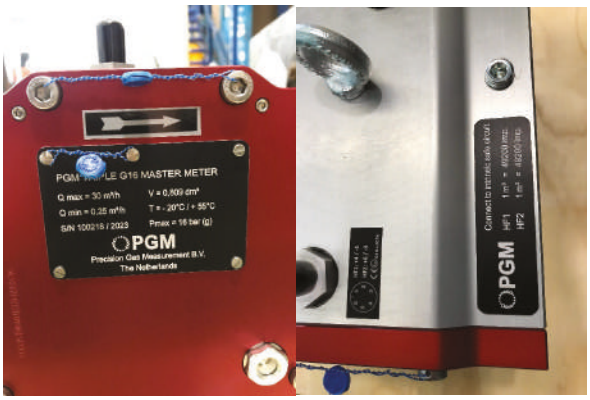


Figure 10. Photo of the PGM triple G16 test meter. The arrow on the meter represents the flow direction such that the meter is installed properly.

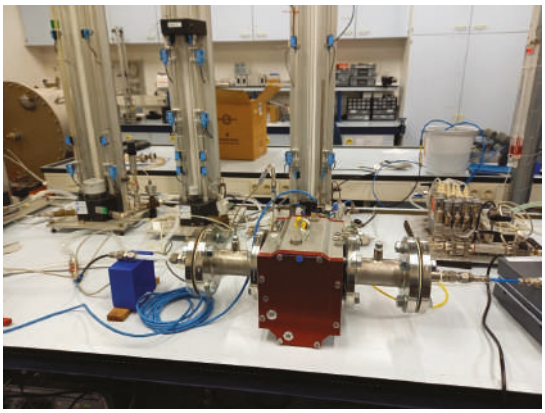


Figure 11. A photo of the PGM G16 DN50 rotary meter installed at VSL. The meter is installed in series with and upstream of the VSL mercury piston prover. The flow is from right to left.

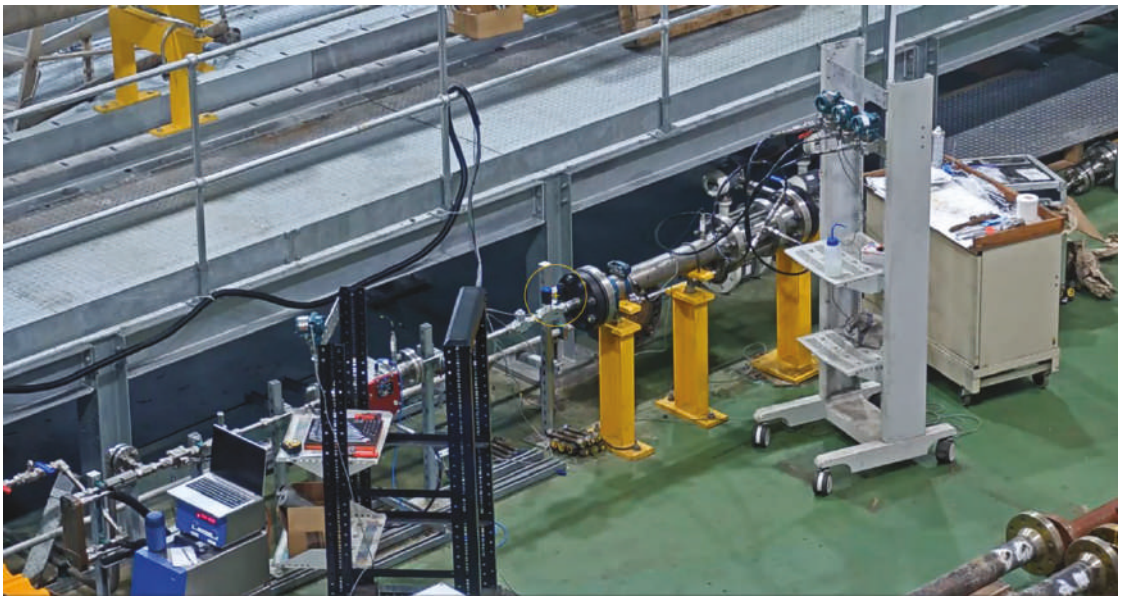


Figure 12. Pictures of the DN50 rotary meter installed at NEL. The meter is installed upstream of the reference sonic nozzle holder. The flow is from left to right.

https://doi.org/10.3390/metrology6020022

3.2. Large-Scale Comparison

3.2.1. Large-Scale Test Conditions

The large-scale comparison was performed between NEL, DNV and FORCE for carbon dioxide. The test conditions are reported in Table 5.

Table 5. Large-scale facilities comparison test conditions.

Test Fluid	Pressure (bar.a)	Temperature (°C)	Density (kg/m^3)	Flow Rate Range (kg/s)	Flow Rate Range (m^3/h)	NEL	DNV	FORCE Coriolis	FORCE Turbine
CO_2	31	20	69	0.4 to 7.8	20 to 400	Yes	Yes	Only 80, 160 and 280 m^3/h	From 40 m^3/h
CO_2	21	20	44	0.25 to 4.9	20 to 400	Yes	Yes	Up to 280 m^3/h	Yes

3.2.2. Large-Scale Test Meter and Sequence of Testing

Two meters were selected as the transfer package for the interlaboratory comparison. The first is an Emerson 3-inch Coriolis meter (CMF300M serial number 21046486) provided by NEL. The second flow meter is a DN100 Honeywell turbine gas meter provided by FORCE (SM-RI-X G250 serial number 10533326). Employing two different types of transfer standards allows evaluation of whether the comparison results vary using different meter types.

The 3-inch Coriolis meters was previously calibrated at NEL in the Elevated Pressure and Temperature (EPAT) oil facility up to 90 bar(g). The EPAT facility has an uncertainty in mass of ±0.08% at 95% confidence level. This calibration provided a reference baseline of the meter's response and allowed the derivation of an experimental pressure correction factor. The resulting oil flow error was within ±0.05% after pressure correction was applied.

The 3-inch Coriolis meter was initially calibrated at NEL in November 2023 as part of a separate previous project [12]. Upon receiving the turbine meter from the manufacturer, FORCE conducted preliminary calibrations using air and natural gas.

The first calibration of the turbine and Coriolis meters took place at NEL in July 2024. The package was subsequently tested by DNV in January 2025, followed by the final set of comparison calibrations conducted by FORCE between March and May 2025. To assess for any potential drift, the Coriolis meter was returned to NEL and re-calibrated in July 2025.

Figures 13–15 show the meters installed at the NEL, DNV and FORCE facilities, respectively.

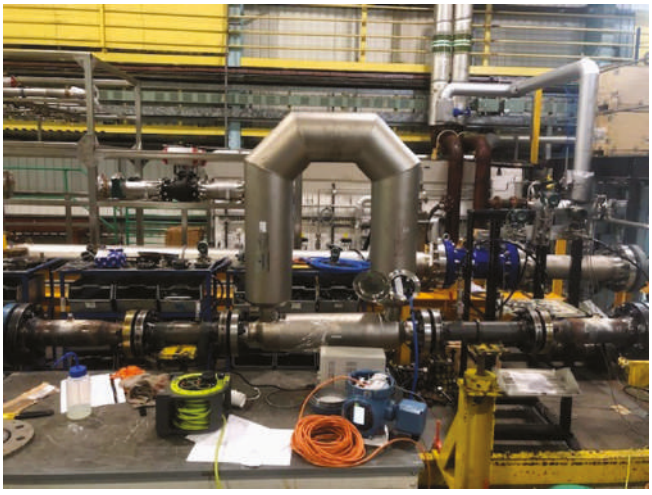




Figure 13. *Cont.*

https://doi.org/10.3390/metrology6020022



Figure 13. Photos of the 4-inch turbine and Coriolis meter installed at NEL. The meters are installed in series with the turbine upstream of the Coriolis meter. The flow is from right to left.

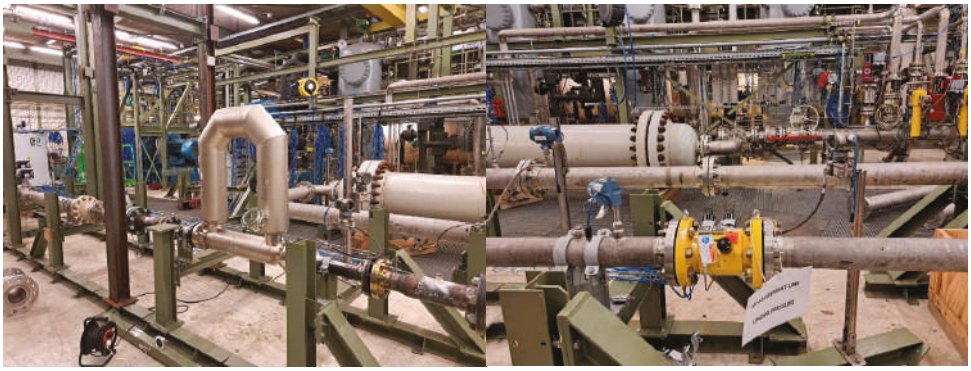


Figure 14. Photos of the 4-inch turbine and Coriolis meter installed at DNV. The meters are installed in series with the turbine upstream of the Coriolis meter. The flow is from right to left.



Figure 15. *Cont*.

https://doi.org/10.3390/metrology6020022

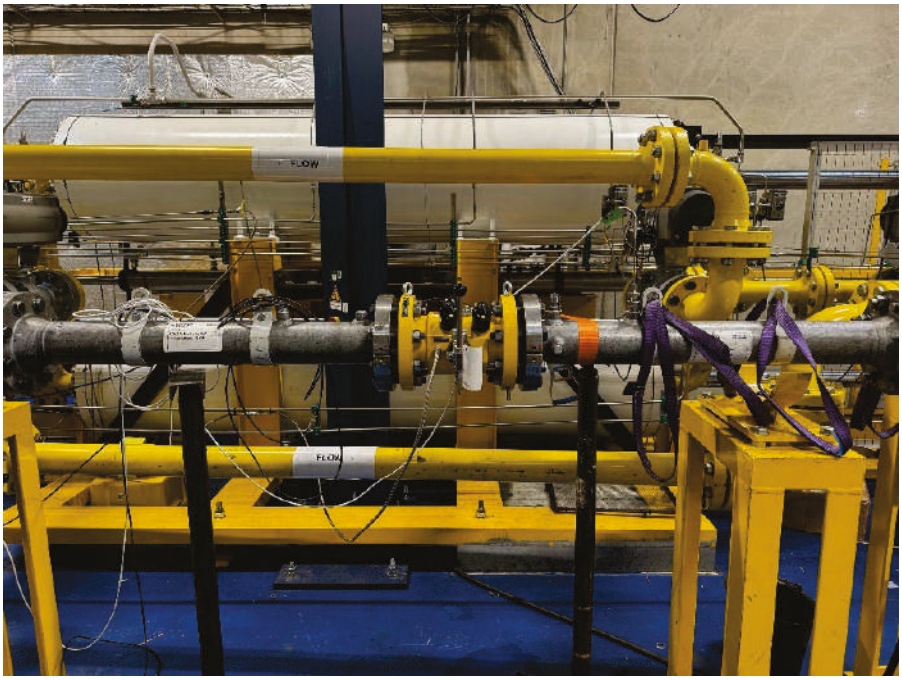


Figure 15. Photos of the 4-inch turbine (bottom) and Coriolis meter (top) installed at FORCE. The meters are calibrated separately due to length constraints.

4. Results and Discussion

4.1. Intermediate-Scale Comparison Results

The comparison results for the rotary meter along with the average uncertainties associated with each facility are presented in Figures 16 and 17 for nitrogen, and Figures 18 and 19 for carbon dioxide. Each plotted test result is the averaged value of three consecutive repeats. It should be noted that the average uncertainties plotted in the figures also include the repeatability associated with the three repeats.

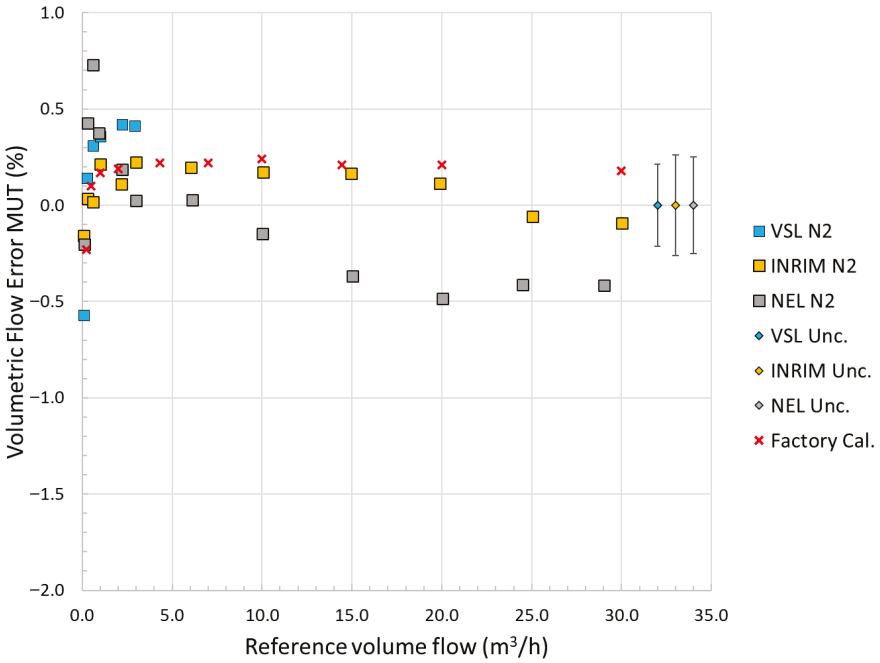


Figure 16. Rotary meter relative error in gas volumetric flow rate at each facility as a function of the reference volumetric flow rate; the results are for nitrogen. Factory calibration with air is also shown. The uncertainties are the facilities' CMCs. The uncertainties may be higher at lower flow rates.

https://doi.org/10.3390/metrology6020022

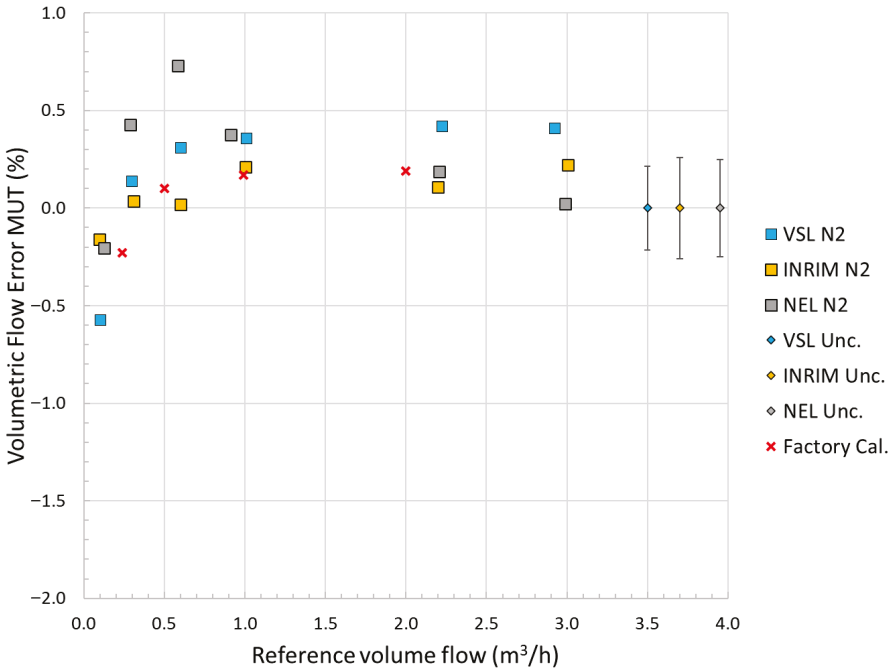


Figure 17. Rotary meter relative error in gas volumetric flow rate at each facility as a function of the reference volumetric flow rate; results are for nitrogen. The graph is zoomed in to better visualize the test results below 4 m^3/h. Factory calibration with air is also shown. The uncertainties are the facilities' CMCs. The uncertainties may be higher at lower flow rates. It can be noted that the results from the three laboratories agree with each other within the laboratories' CMCs.

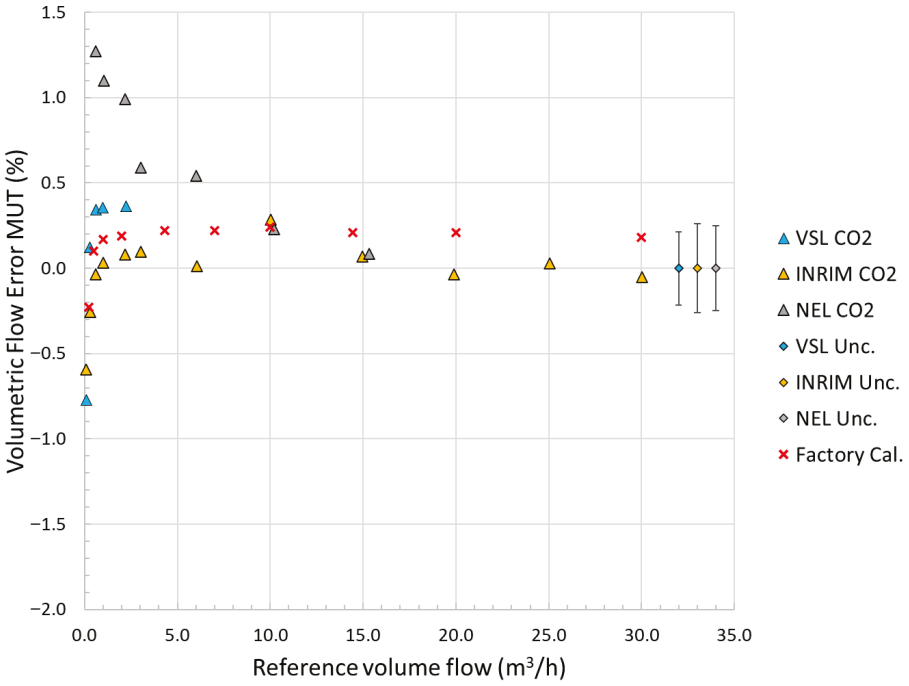


Figure 18. Rotary meter relative error in gas volumetric flow rate at each facility as a function of the reference volumetric flow rate; results are for carbon dioxide. Factory calibration with air is also shown. The uncertainties are the facilities' CMCs. The uncertainties may be higher at lower flow rates. It can be noted that the results from the three laboratories agree with each other within the laboratories' CMCs, except the meter errors from NEL diverge below 5 m^3/h (as explained in Section 4.1 above).

https://doi.org/10.3390/metrology6020022

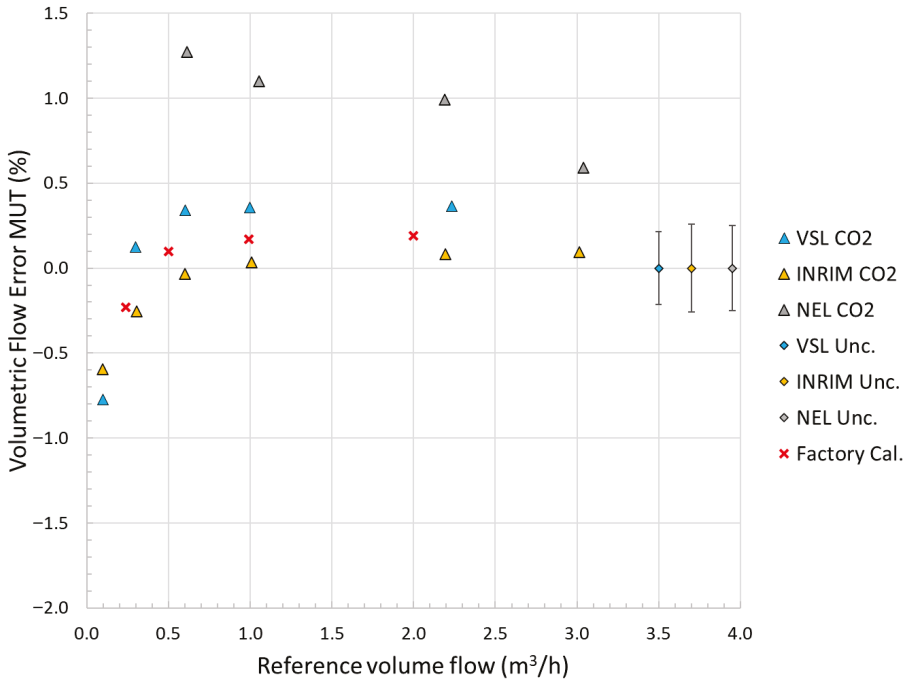


Figure 19. Rotary meter relative error in gas volumetric flow rate at each facility as a function of the reference volumetric flow rate; the results are for carbon dioxide. The graph is zoomed in to better visualize the test results below 4 m^3/h. Factory calibration with air is also shown. The uncertainties are the facilities' CMCs. The uncertainties may be higher at lower flow rates. It can be noted that the results from VSL and INRIM agree with each other within the laboratories' CMCs, while the meter errors from NEL diverge below 5 m^3/h (as explained in Section 4.1 above).

The results indicate that the facilities show better agreement when using nitrogen than with carbon dioxide. The most notable deviation is observed in the NEL test results with carbon dioxide. This discrepancy is attributed to the performance of NEL's reference sonic nozzles, which previous studies suggested may be affected when operated with CO_2 [26–36]. The CFVNs used for NEL's CO_2 tests had throat diameters ranging from 1.9 mm to 8.0 mm, while the throat Reynolds number was between 0.9×10^5 and 4.1×10^5. Earlier studies have shown that CFVNs with similar small throat diameters, when calibrated with air, exhibit vibrational relaxation effects when operated with carbon dioxide, leading to higher experimentally determined discharge coefficients at Reynolds numbers comparable to those used in the NEL CO_2 tests. However, there is currently no standardized method available to correct for this effect. Hence further research is required to enable appropriate corrections when CFVNs are operated with CO_2.

Normalized Error $|E_n|$ Intermediate Scale

Figures 20 and 21 present the normalized error, $|E_n|$ values for each test facility based on the PGM meter measurements with carbon dioxide. It can be seen that the normalized errors fall mostly above the critical level, deeming the comparison inconclusive. The normalized error at the higher flow rates between NEL and INRIM standards are well below the warning level, showing good consistency between the two facilities at the higher flow rates. As per Section 4.1 above, NEL's small size sonic nozzles introduce significant errors when calibrated with air and used with CO_2 and their performance and a correction model with CO_2 must be further investigated in the future. Figure 22 then presents the normalized error, $|E_n|$ values between only VSL and INRIM's facilities up to 4 m^3/h with CO_2. It can be noted that the normalized error is at or below the warning level at four out

https://doi.org/10.3390/metrology6020022

of the five test points, with only one test point falling above the critical level, suggesting that the facilities are consistent with each other.

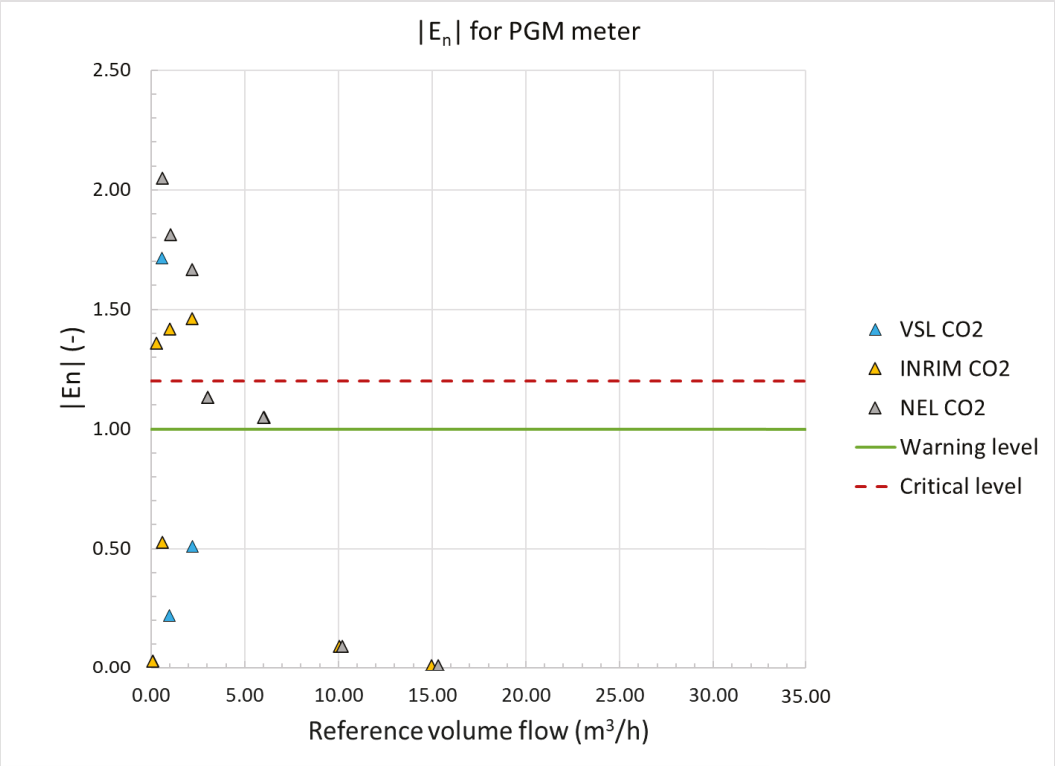


Figure 20. $|E_n|$ for each facility's calibrations with the rotary gas meter for CO_2. Most test points below 5 m^3/h fall outside of the critical level as outlined in Section 4.1.

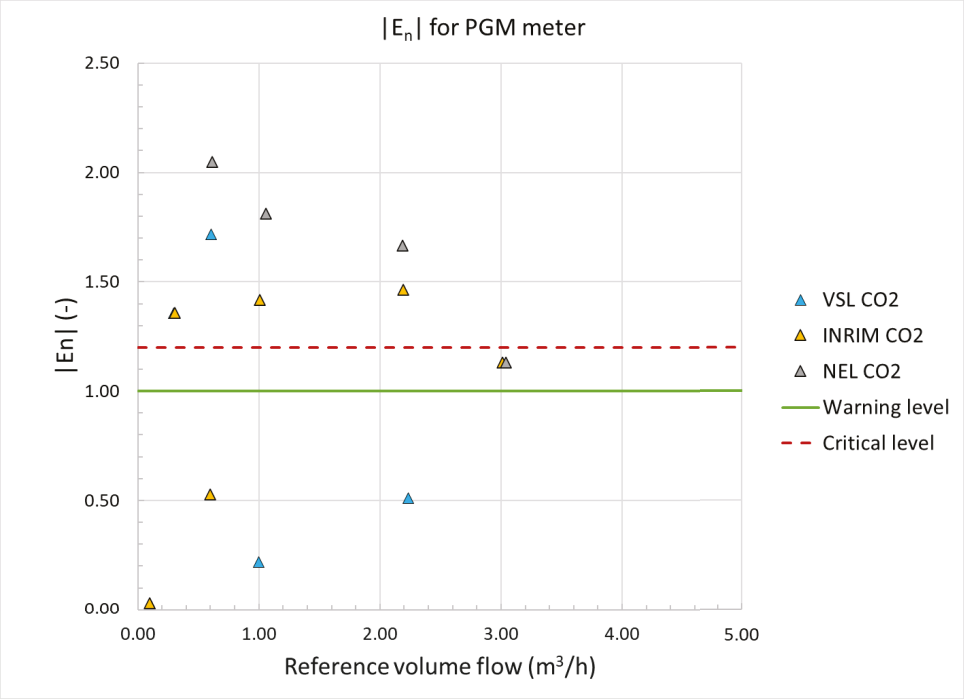


Figure 21. $|E_n|$ for each facility's calibrations with the rotary gas meter for CO_2. The graph is zoomed in to better visualize the test results below 4 m^3/h. Most test points fall outside of the critical level as outlined in Section 4.1.

https://doi.org/10.3390/metrology6020022

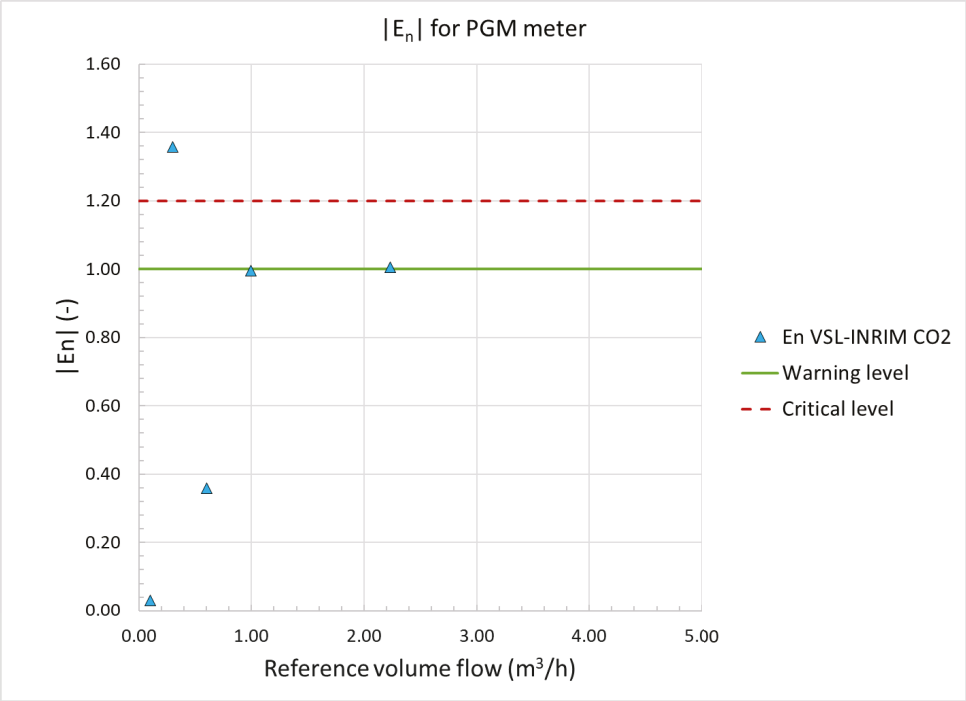


Figure 22. $|E_n|$ between VSL and INRIM's facilities calibrations with the rotary gas meter for CO_2. When considering only the results between VSL and INRIM, most test points fall within the warning level.

Figure 23 presents the normalized error, $|E_n|$ values for each test facility based on the PGM meter measurements with nitrogen. Approximately 80% of the test points shown in this graph have $|E_n| < 1$, demonstrating that the three test facilities—NEL, VSL and INRIM—are consistent with the CRV with nitrogen gas.

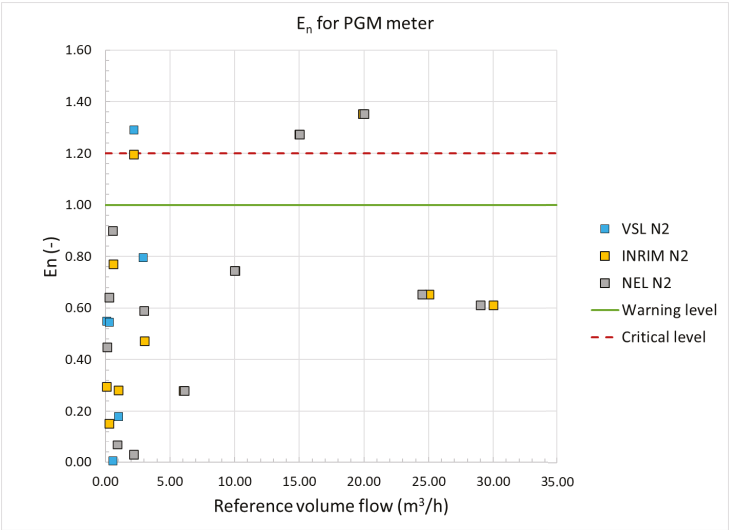


Figure 23. $|E_n|$ for each facility's calibrations with the rotary gas meter for nitrogen. At flow rates between 5 m^3/h and 20 m^3/h, only one data point appears because the test flow rates were virtually identical and the $|E_n|$ was calculated between two laboratories; hence, both have the same $|E_n|$ values, resulting in identical coordinates on the plot. It can be noted that most test points fall within the warning level.

Figure 23 also highlights six test points where $|E_n|$ exceeded 1, which are listed below. One of these points had $|E_n|$ value between 1 and 1.2, suggesting a potential warning

https://doi.org/10.3390/metrology6020022

regarding the measurement processes at these facilities under the respective test conditions. Five results had $|E_n| > 1.2$, indicating that the test facility failed the equivalency test under these specific flow conditions.

4.2. Large-Scale Comparison Results

The comparison results for the Coriolis meter and turbine gas meter at each facility along with the average uncertainties (as indication) associated with each facility are presented in Figures 24 and 25, respectively. Figure 26 presents the calibration results of the turbine meter as a function of Reynolds number. Each plotted calibration result is the averaged value of three consecutive repeats. It should be noted that the average uncertainties plotted in the figures also include the repeatability associated with the three repeats.

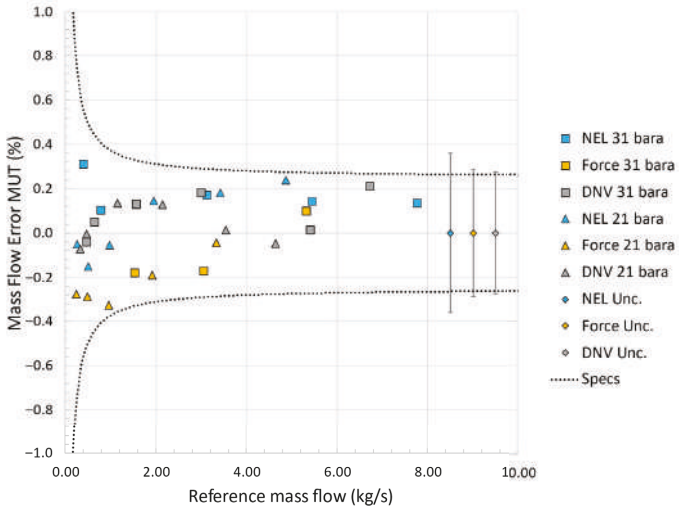


Figure 24. Coriolis meter relative error in gas mass flow rate at each facility as a function of the reference mass flow rate. The accuracy specification of the flow meter is also shown in dotted lines. It can be noted all the test points fall within the specifications of the flow meter.

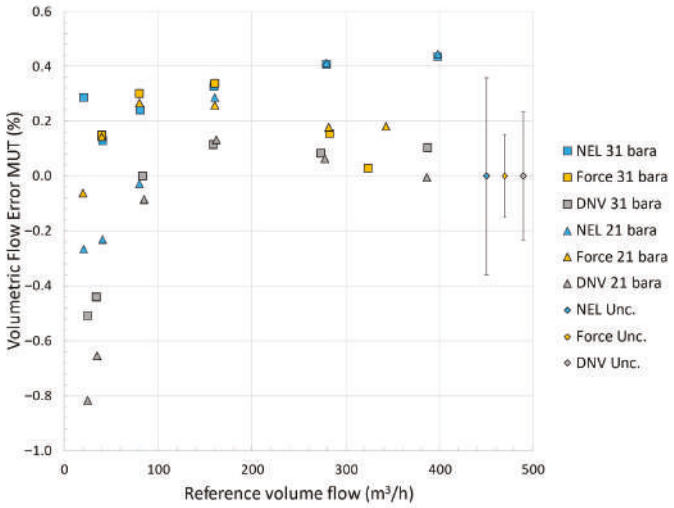


Figure 25. Turbine meter relative error in gas volumetric flow rate at each facility as a function of the reference volumetric flow rate. It can be noted that the flow rates above 80 m^3/h agree within the laboratories' CMCs. While NEL results appear higher at higher flow rates, the claimed uncertainty is also higher. At flow rates below 80 m^3/h there are large discrepancies due to lower measurement accuracy of turbine meters at low flow rates, as explained below.

https://doi.org/10.3390/metrology6020022

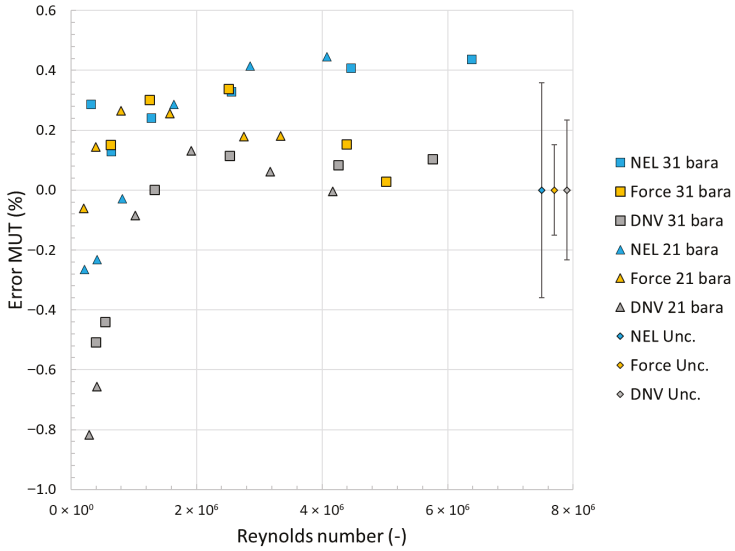


Figure 26. Turbine meter relative error in gas volumetric flow rate at each facility as a function of the Reynolds number. It can be noted that at Reynold numbers above 2×10^6 the test points agree within the laboratories' CMCs. While NEL results appear higher at higher flow rates, the claimed uncertainty is also higher. At Reynold numbers below 2×10^6 there are large discrepancies due to lower measurement accuracy of turbine meters at low flow rates, as explained below.

The results indicate that the difference in meter error in the flow measurements with both meters between the three test facilities generally fall within the uncertainty range of these test facilities, except at the bottom of the flow range.

Normalized Error $|E_n|$ Large Scale

Figure 27 presents the $|E_n|$ values for each test facility based on the Coriolis meter measurements. Approximately 91% of the test points shown in this graph have $|E_n| < 1$, demonstrating that the three test facilities—NEL, DNV and FORCE—are consistent with the CRV, and therefore have successfully passed the equivalency test for the specific flow conditions maintained during these test runs.

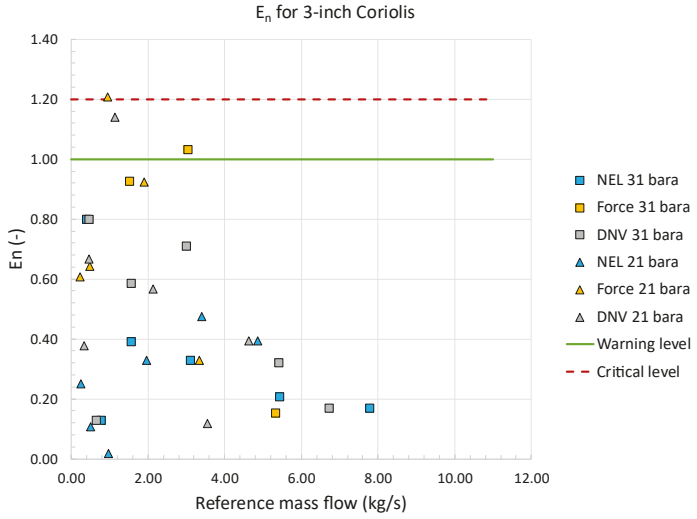


Figure 27. The $|E_n|$ of the large-scale comparison for each facility at the various test conditions with the Coriolis meter. It can be noted that most test points fall within the warning level, with three test points falling between the warning and critical level.

https://doi.org/10.3390/metrology6020022

Figure 27 also highlights three test points where $|E_n|$ exceeded 1. These points had $|E_n|$ values between 1 and 1.2, suggesting a potential warning regarding the measurement processes at these facilities under the respective test conditions.

Figure 28 presents the normalized error ($|E_n|$) values for each test facility based on the turbine gas meter measurements. Over 68% of the test points shown in this graph have $|E_n| < 1$. The figure also highlights eleven test points where $|E_n|$ exceeded 1. Two of these points had $|E_n|$ values between 1 and 1.2, suggesting a potential warning regarding the measurement processes at these facilities under the respective test conditions. However, nine results had $|E_n| > 1.2$, indicating that the test facility failed the equivalency test under these specific low-flow conditions. It should be noted that the reported uncertainties do not include the effect of long-term stability of the meters, increasing the normalized errors. See more in the recommendations section.

The failed test points all occurred at flow rates below 85 m^3/h—a range where turbine meter performance typically deteriorates due to increased bearing friction. Additionally, measurement reliability tends to decrease in this region due to limitations of the test facility itself. Furthermore, for a given nominal test flow rate, the actual flow rates achieved at each facility can differ significantly. This discrepancy can have a considerable impact in low-flow regions, where the turbine meter's response is highly sensitive to small changes in flow rate.

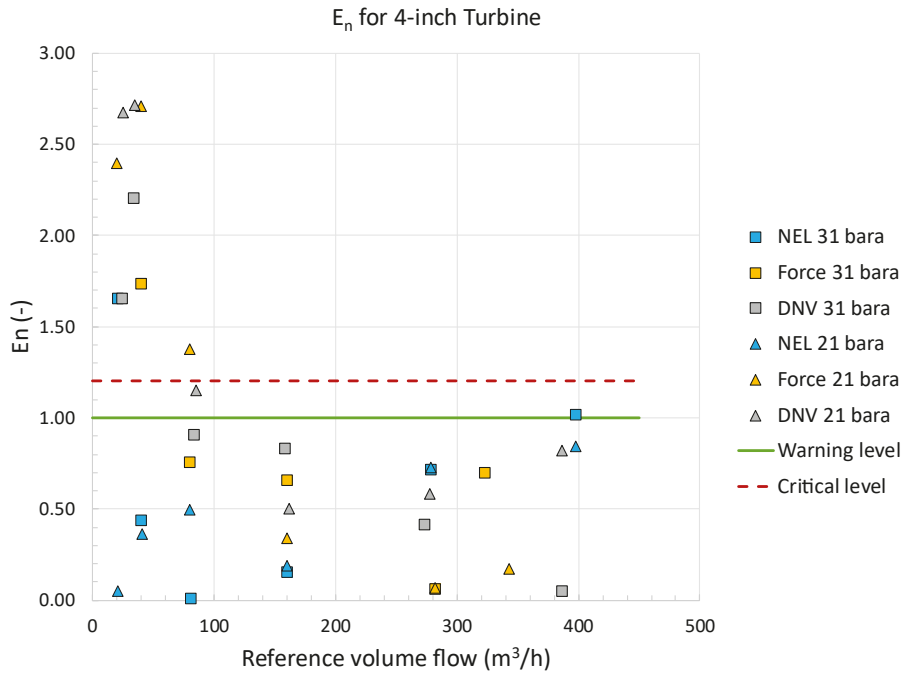


Figure 28. The $|E_n|$ of the large-scale comparison for each facility at the various test conditions with the turbine gas meter. It can be noted that the $|E_n|$ values at flow rates above 80 m^3/h are below the warning level. At flow rates below 80 m^3/h the $|E_n|$ values are outside the critical limits due to lower measurement accuracy of turbine meters.

Nevertheless, the discrepancies are believed to be primarily attributable to the turbine meter's performance at low flow rates, as supported by the fact that the facilities showed better agreement at low flow rates when using the Coriolis flow meter (Figures 24 and 27). It should be noted that the turbine meter was also tested at atmospheric pressure at FORCE in the beginning of the comparison and when the meter was returned to FORCE at the end of the comparison, and at flow rates below 80 m^3/h, a meter shift in the range of 0.2–0.8% was detected in the positive direction, suggesting a drift in the meter itself in the lower end of the flow rate range that contributes to the discrepancies between the laboratories.

https://doi.org/10.3390/metrology6020022

Additionally, the turbine meter was a new meter and since new turbine meters typically need sufficient initial volume throughput to achieve long-term stability (also known as "run-in" time), the meter likely drifted during the duration of the comparison.

5. Conclusions

This paper presented the results of interlaboratory comparisons for the calibration of flow meters at intermediate and large-scale facilities with carbon dioxide to establish traceability of CO_2 flow meter calibrations and support accurate flow metering across the carbon capture and storage (CCS) chain.

In the large-scale comparison between FORCE, DNV, and NEL the facilities passed the equivalency criteria in 91% of the test points in the flow range of 20 m^3/h to 400 m^3/h with the Coriolis meter, demonstrating traceability for carbon dioxide across facilities. Results with the turbine meter below 85 m^3/h were less satisfactory, primarily due to known limitations in turbine meter performance at low flow rates.

Intermediate-scale comparisons between INRIM, VSL, and NEL confirmed traceability for nitrogen across all facilities. Agreement was also observed between VSL and INRIM for carbon dioxide. However, NEL's results for carbon dioxide differed significantly, which was traced to the use of small-diameter sonic nozzles calibrated in air, known to produce errors when used with carbon dioxide primarily due to vibrational relaxation effects, particularly at low Reynolds numbers. These findings are also consistent with existing literature.

Having performed the interlaboratory comparison between the NEL, DNV, and FORCE in the large-scale range and VSL and INRIM in the intermediate-scale range, the facilities have established traceable calibration capabilities of CO_2 flow meters, which enables accurate CO_2 flow metering and accounting to help the CCUS industry meet the operational, fiscal and regulatory requirements, and help Europe meet its CO_2 emissions reduction target.

6. Recommendations

In the large-scale facilities at NEL, DNV, and FORCE, it is recommended to conduct additional comparisons at flow rates above 400 m^3/h to extend the validated range and better serve the CCUS industry. When using the turbine meter, the tests could be done after the meter has had the necessary "run-in" volume through it so that it is more stable over time. The meter could also be tested at 21 bar(a) and 31 bar(a) with CO_2 when it is returned to the pilot laboratory to determine the meter drift, such that the uncertainty due to the drift can be calculated and included in the determination of the normalized error. As such, the measurement uncertainty U_i in (4 can be updated as follows (Equation (10)):

$$U_i = \sqrt{{U_{lab}}^2 + {U_r}^2 + U_{LTS}} \tag{10}$$

where U_{LTS} is the uncertainty due to the long-term stability of the meter (drift) and is calculated as follows:

$$U_{LTS}(k=1) = \frac{Meter\ error\ at\ start\ of\ comparison - Meter\ error\ at\ end\ of\ comparison}{\sqrt{3}} \tag{11}$$

where the meter errors at start and end of the comparison are determined at the pilot laboratory. In Equation (11) above, the error is divided by square root of three to convert the absolute error to standard uncertainty contribution assuming a rectangular distribution.

In the intermediate-scale comparison between NEL, VSL, and INRIM, it is recommended to conduct a comparison with an additional meter of a different technology that is

https://doi.org/10.3390/metrology6020022

compatible with all the facilities to gain more confidence in the traceability of the facilities with carbon dioxide.

At NEL's intermediate-scale facility, further experimental and theoretical investigations into the performance of critical flow Venturi nozzles with CO_2 are recommended, with the aim of developing suitable correction methods to mitigate vibrational relaxation effects.

Author Contributions: Conceptualization, A.A., G.C., K.R., D.v.P. and P.G.S.; methodology, G.C., A.A., P.G.S., K.R. and D.v.P.; validation, G.C., R.S., D.v.P., P.G.S., A.A. and K.R.; formal analysis, G.C., R.S., D.v.P., P.G.S., A.A. and K.R.; investigation, G.C., R.S., D.v.P., P.G.S., A.A. and K.R.; resources, G.C., D.v.P., P.G.S., A.A. and K.R.; data curation, G.C., D.v.P., P.G.S., A.A. and K.R.; writing—original draft preparation, A.A., G.C., R.S., D.v.P., P.G.S. and K.R.; writing—review and editing, A.A., G.C., R.S., D.v.P., P.G.S. and K.R.; visualization, A.A., G.C. and R.S.; supervision, A.A., G.C., R.S., D.v.P., P.G.S. and K.R.; project administration, A.A., G.C., D.v.P., P.G.S. and K.R.; funding acquisition, G.C., D.v.P., P.G.S. and K.R. All authors have read and agreed to the published version of the manuscript.

Funding: This research was funded by the European Metrology Programme for Innovation and Research (EMPIR), co-financed by the participating States and from the European Union's Horizon 2020 research and innovation program, with grant number 21GRD06.

Data Availability Statement: The original data presented in the study are openly available in Zenodo at https://doi.org/10.5281/zenodo.17734594.

Acknowledgments: This work was carried out as part of the project "Metrology Support for Carbon Capture Utilisation and Storage" 21GRD06 MetCCUS, www.metccus.eu. The "Metrology Support for Carbon Capture Utilisation and Storage" 21GRD06 project has received funding from the European Metrology Programme for Innovation and Research (EMPIR), co-financed by the participating States and from the European Union's Horizon 2020 research and innovation program. The authors would like to thank the teams at TÜV SÜD National Engineering Laboratory, VSL, DNV, FORCE and INRIM for their contributions towards the realization of this work.

Conflicts of Interest: The authors declare that they have no known competing financial interests or personal relationships that could have appeared to influence the work reported in this paper.

References

1. European Commission. The European Green Deal-European Commission. Available online: https://commission.europa.eu/strategy-and-policy/priorities-2019-2024/european-green-deal_en (accessed on 8 September 2025).
2. European Union. *Commission Implementation Regulation 2018/2066, On the Monitoring and Reporting of Greenhouse Gas Emissions Pursuant to Directive 2003/87/EC of the European Parliament and of the Council and of the Council and Amending Commission Regulation (EU) No 601/20*; European Union: Brussels, Belgium, 2025.
3. Mills, C.; Chinello, G.; Henry, M. Flow measurement challenges for carbon capture, utilisation and storage. *Flow Meas. Instrum.* **2022**, *88*, 102261. [CrossRef]
4. Arellano, Y. An overview of the measurement landscape needs for CCS. In Proceedings of the 12th Trondheim Conference on Carbon Capture, Transport and Storage, Trondheim, Norway, 19–21 June 2023.
5. van Putten, D.; ten Cate, R.; Al Saleem, M. Considerations for CO_2 metering and allocation systems. In Proceedings of the Global Flow Measurement Workshop, Tønsberg, Norway, 24–27 October 2023.
6. EU Commission. *Implementation Regulation 2018/2067, On the Verification of Data and on the Accreditation of Verifiers Pursuant to Directive 2003/87/EC of the European Parliament and of the Council*; European Union: Brussels, Belgium, 2025.
7. *ISO/IEC 17025*; General Requirements for the Competence of Testing and Calibration Laboratories. ISO: Geneva, Switzerland, 2017.
8. Porthos CO_2 Transport and Storage C.V., "Standard CO_2 Transport and Storage Conditions," 2023. Available online: https://www.porthosco2.nl/wp-content/uploads/2022/03/Porthos-standard-CO2-Transport-and-Storage-Conditions.pdf (accessed on 18 February 2026).
9. ISO/IEC. *Conformity Assessment-General Requirements for the Competence of Proficiency Testing Providers*; ISO: Geneva, Switzerland; IEC: Geneva, Switzerland, 2023.
10. Lemmon, E.W.; Bell, I.H.; Huber, M.L.; McLinden, M.O. *NIST Standard Reference Database 23: Reference Fluid Thermodynamic and Transport Properties-REFPROP; Version 10.0*; National Institute of Standards and Technology: Gaithersburg, MD, USA, 2018.

https://doi.org/10.3390/metrology6020022

11. Piccato, A.; Bisi, M.; Spazzini, P.G.; Bertiglia, F.; La Piana, G.; Audrita, E.; Santiano, M.; Bellotti, R.; Francese, C. Metrological features of the large piston prover at INRIM. *Measurement* **2022**, *192*, 110841. [CrossRef]
12. Brown, R.; Chinello, G.; Workamp, M.; Mickan, B. Experimental evaluation of various flow meters using gaseous CO_2. *Flow Meas. Instrum.* **2024**, *99*, 102672. [CrossRef]
13. Chinello, G.; de kater, A.; Sadri, M.; Modrego, J.; van Putten, D.; Stiphout, W.; Workamp, M.; Anderson, D. Calibration facilities and test results for gas network hydrogen and hydrogen enriched natural gas flow meters. *Int. J. Hydrogen Energy* **2025**, *160*, 150431. [CrossRef]
14. van der Grinten, J.; Mickan, B.; Riezebos, H.; van Putten, D. Gas flow traceability for non-conventional and renewable gases. In Proceedings of the 39th International North Sea Flow Measurement Workshop, Tønsberg, Norway, 26–29 October 2021.
15. Mickan, B.; Kramer, R.; Dopheide, D. Determination of discharge coefficient of critical nozzles based on their geometry and the theory of laminar and turbulent boundary layer. In Proceedings of the 6th International Symposium on Fluid Flow Measurement, Querétaro, Mexico, 14–19 May 2006.
16. Mickan, B.; van der Grinten, J.; Kappes, T. Primary and secondary flow standards for a wide variety of gas compositions-a solid base for reliable traceability facing the energy transition. In Proceedings of the 38th International North Sea Flow Measurement Workshop, Virtual Event, 27–29 October 2020.
17. Böckler, H.B. *Messrichtigkeit von Mechanischen Gasmessgeräten bei Verwendung von Unterschiedlichen Gasbeschaffenheiten*; Universität Duisburg-Essen: Essen, Germany, 2019.
18. van der Grinten, J.G.; Gunnarsson, A.; van der Beek, M.; Mickan, B. An intercomparison between primary high-pressure gas flow standards with sub-permille uncertainties. In Proceedings of the 37th Internationsl North Sea Flow Measurement Workshop, Tønsberg, Norway, 22–25 October 2019.
19. Mills, C. Calibrating and operating Coriolis flow meters with respect to process effects. *Flow Meas. Instrum.* **2020**, *71*, 101649. [CrossRef]
20. Hemp, J.; Kutin, J. Theory of errors in Coriolis flowmeter readings due to compressibility of the fluid being metered. *Flow Meas. Instrum.* **2006**, *17*, 359–369. [CrossRef]
21. Costa, F.; Mills, C.; Garcia, D.; Gomez, J.; Pereira, L.O. Optimizing Coriolis Flowmeter Performance for the Brazilian O&G Industry: Influence Factors and Calibration Strategies. In Proceedings of the Global Flow Measurement Workshop, Tønsberg, Norway, 24–26 October 2023.
22. *JCGM 200:2008*; International Vocabulary of Metrology—Basic and General Concepts and Associated Terms (VIM) Vocabulaire International de Métrologie—Concepts Fondamentaux et Généraux et Termes Associés (VIM). BIPM: Sèvres, France, 2008.
23. Cox, M.G. The evaluation of key comparison data. *Metrologia* **2002**, *39*, 589. [CrossRef]
24. Working Group For Fluid Flow. WGFF Guidelines for CMC Uncertainty and Calibration Report Uncertainty. 21 October 2013. Available online: https://www.bipm.org/documents/20126/44756349/ccm-wgff-guidelines.pdf/eda74c50-1192-a20e-fc16-a3760e11329e (accessed on 4 September 2025).
25. Wright, J.; Toman, B.; Mickan, B.; Wubbeler, G.; Bodnar, O. Pass/Fail/Inconclusive Criteria for Inter-Laboratory Comparisons. In Proceedings of the 9th International Symposium on Fluid Flow Measurement, Arlington, VA, USA, 14–17 April 2015.
26. Johnson, A.N.; Espina, P.I.; Wright, J.D.; Mattingly, J.D.; Merkle, C.L. Numerical Characterization Of The Discharge Coefficient In Critical Nozzles. In Proceedings of the 1998 National Conference of Standards Laboratories Workshop & Symposium, Albuquerque, NM, USA, 19–23 July 1998.
27. Ishibashi, M.; Takamoto, M. Very Accurate Analytical Calculation of the Discharge Coefficients of Critical Venturi Nozzles with Laminar Boundary Layer. In Proceedings of the FLUCOME, Hayama, Japan, 1–4 September 1997.
28. Nakao, S.; Hirayama, T.; Takamoto, M. Effects of Thermalphysical Properties of Gases on the Discharge Coefficients of the Sonic Venturi Nozzle. In Proceedings of the ASME FLuids Engineering Division Summer Meeting, Vancouver, BC, Canada, 22–26 June 1997.
29. Nakao, S.-I.; Takamoto, M. Discharge Coefficients of Critical Venturi Nozzles for CO_2 and SF6. *J. Fluids Eng.* **2000**, *122*, 730–734. [CrossRef]
30. Johnson, A.N.; Wright, J.D.; Nakao, S.; Merkle, C.L.; Meldover, M.R. The effect of vibrational relaxation on the discharge coefficient of critical flow venturis. *Flow Meas. Instrum.* **2000**, *11*, 315–327. [CrossRef]
31. Wright, J.D. What Is the "Best" Transfer Standard for Gas Flow? In Proceedings of the 11th Conference on Flow Measurement, Groningen, The Netherlands, 12–14 May 2003.
32. Johnson, A.N.; Merkle, C.L.; Moldover, M.R.; Wright, J.D. Relaxation Effects in Small Critical Nozzles. *J. Fluids Eng.* **2006**, *128*, 170–176. [CrossRef]
33. *ISO 9300:2022*; Measurement of Gas Flow by Means of Critical flow Nozzles. ISO: Geneva, Switzerland, 2022.
34. Bobovnik, G.; Sambol, P.; Kutin, J. *Characterisation of the Discharge Coefficient of CFVNs for Different Gases*; EURAMET: Braunschweig, Germany, 2022.

https://doi.org/10.3390/metrology6020022

35. Bobovnik, G.; Mickan, B.; Sambol, P.; Maury, R.; Kutin, J. Investigation of the discharge coefficient in the laminar boundary layer regime of critical flow Venturi nozzles calibrated with different gases including hydrogen. *Measurement* **2023**, *217*, 113134. [CrossRef]
36. Nagao, J.; Matsuo, S.; Mohammad, M.; Setoguchi, T. Numerical Study on Characteristics of Real Gas Flow Through a Critical Nozzle. *Int. J. Turbo Jet Engines* **2012**, *29*, 21–27. [CrossRef]

Disclaimer/Publisher's Note: The statements, opinions and data contained in all publications are solely those of the individual author(s) and contributor(s) and not of MDPI and/or the editor(s). MDPI and/or the editor(s) disclaim responsibility for any injury to people or property resulting from any ideas, methods, instructions or products referred to in the content.

https://doi.org/10.3390/metrology6020022

metrology

MDPI

Article

Geometrical Prediction of Copper-Coated Solid-Wire Deposition by Wire-Arc Additive Manufacturing Based on Artificial Neural Networks and Support Vector Machines

Miroslav Petrov [1,*], Grazia Lo Sciuto [1,2,*], Evgeni Tongov [1], Yavor Sofronov [1], Georgi Todorov [1], Todor Todorov [1], Valentin Mishev [1], Antonio Nikolov [1] and Krum Petrov [1]

[1] Department of Production Technology and Systems, Faculty of Industrial Technology, Technical University of Sofia, 1000 Sofia, Bulgaria; e_tongov@tu-sofia.bg (E.T.); ysofronov@tu-sofia.bg (Y.S.); todorttodorov@tu-sofia.bg (T.T.); v-mishev@tu-sofia.bg (V.M.); kpetrov@tu-sofia.bg (K.P.)

[2] Department of Electrical, Electronics and Informatics Engineering, University of Catania, Viale Andrea Doria 6, 95125 Catania, Italy

* Correspondence: miropetrov@tu-sofia.bg (M.P.); grazia.losciuto@unict.it or grazia.losciuto@tu-sofia.bg (G.L.S.)

Abstract

Wire and arc additive manufacturing is a promising technology for fabricating large and complex metallic components. Wire arc methods, like MIG and MAG, use an electric arc to melt and deposit metal wire layer-by-layer. The improvement of the surface depends on the multi-bead overlapping model. However, the high quality of multi-layer deposits is reduced by structural irregularities, such as geometric defects, poor fusion, and reduced mechanical properties of the weld bead. The analysis of a single weld bead that solidifies on a base material can be carried out to improve the geometry of the microstructure, to improve the mechanical properties, and to understand the relationship between welding parameters and the bead dimensions. In the present study, current metal welding technologies and strategies in wire-arc additive manufacturing were discussed, and different weld bead geometries using BÖHLER SG2 solid wire were realized, varying the robot's trajectory length and welding speed. The computational models are proposed to create a dependence between the controllable welding input parameters and resulting geometrical weld bead outputs (width, height, length, and radius) for prediction and optimization. These models, using techniques such as support vector machines and artificial neural networks, can be a good tool for controlling quality by understanding these input–output relationships. However, the SVM has revealed a superior performance based on metrics for the nonlinear and intricate relationships between the geometrical weld beads and welding parameters.

Keywords: additive manufacturing; metal active gas; neural network; support vector machine

1. Introduction

In engineering and manufacturing technologies, welding-based industrial coatings for small or micro-scale parts are formulated to protect surfaces from corrosive chemicals, abrasive wear under harsh conditions, and high or cryogenic temperatures, which can lead to degradation mechanisms such as oxidation, sulfidation, thermal fatigue, abrasion, sliding, and erosion in the materials [1,2]. Metal structures are realized using modern welding techniques, such as metal inert gas (MIG), tungsten inert gas (TIG), stick, and flux-cored welding [3]. Welding is a manufacturing process that is useful for the construction industry, especially in fabrication and construction processes in which two parts are joined

by means of filler material, and, thanks to the fusion process, a weld pool is obtained, which, when cooled, will transform into a fixed joint [4]. Industrial robots have degrees of freedom (number of axes), speed of action, weight to be supported, workspace, and level of programming [5]. The robotic wire-arc additive manufacturing (WAAM) is a 3D printing method that uses a robotic arm with a welding torch to melt a wire and deposit it layer by layer to create large, complex metal parts [6]. It's a type of directed energy deposition (DED) process that offers high deposition rates, making it suitable for industrial-scale applications in aerospace, naval, and other manufacturing sectors to produce components like wings or engine parts [7,8]. Wire-arc additive manufacturing (WAAM) utilizes an electric arc as a heat source to melt the wire and create a 3D structure via layer-by-layer material deposition [9–11]. The quality of the surface and the complexity of the component can be a disadvantage, especially when high accuracy is required [12]. In the WAAM process, the main critical parameters include the welding source, intensity, welding speed, arc voltage and amperage, arc length correction, and dynamic correction [13]. The interaction between parameters of the kinematic system, such as welding speed and welding source, affects the molten pool dynamics, influencing the mechanical properties and surface of the final product by controlling heat input. The welding source is defined by its energy intensity (i.e., arc) and power parameters (current, voltage, and speed)—it is the primary driver of molten pool behavior, directly influencing its geometry, stability, fluid dynamics, and microstructure. A higher-intensity source, such as a laser or hybrid (laser-arc) system, creates a deeper, narrower, and more turbulent pool, whereas lower-intensity arc welding creates a more stable, smaller pool. In contrast, conventional arc welding tends to create shallower, wider, and more rounded pools [14]. Increasing the welding current in arc processes increases the volume of the molten pool and reduces the ratio of depth to width, leading to wider, flatter beads [15]. High-power sources create a larger temperature difference, which influences the final weld shape. The welding source dictates the heat input, which directly controls the volume (size), depth (penetration), velocity (flow), and solidification speed (microstructure) of the molten pool. Heat input is linearly correlated with the characteristic weld bead geometry, including the weld bead height, width, penetration, penetration area, and reinforcement area [16–18]. Generally, multiple fusion and solidification thermal cycles produce irregular heat propagation in the microstructure and shape of the bead. The amount of liquefied material increases as heat input increases, increasing the possibility of cracking and internal defect formation, phase transformation, residual stresses, and distortion [19,20]. The effect of torch travel speed and other parameters on microstructure and bead geometry is studied by applying statistical tools to determine the effect of process parameters (wire feed, travel speed, current, and argon flow rate) on the bead's microstructure and geometry [21–23]. In [24,25], travel speed and current significantly affect the weld bead's microstructure and geometry. Thus, the pre-heat of the substrate leads to smoother material deposition, improving the surface deformation of the deposited metal [6]. Many studies report the effect of WAAM processes on the deformation of microstructure components and the mechanical properties of the deposited layers, influenced by the pool morphology and solidification behavior [26–29]. These factors are inevitably involved in the optimization of the additive manufacturing process. Numerical computational methods, including artificial neural networks (ANNs) and finite element (FE) simulation, are used for the prediction of bead geometry [30]. An autoregressive model (ARX) estimates outputs based on a sequence of previous inputs and output responses, and has been used to simulate input–output data with noise or the thermal response of a bridge. It has also been used to enhance the geometrical precision of the modified metal inert gas (MIG) welding process based on the short-circuiting (dip) transfer process by associating a nonlinear ARX model with

https://doi.org/10.3390/metrology6010018

wavelet networks [31,32]. The manufactured additives are produced using cold spray additive manufacturing, suitable for coatings that adopt a supersonic gas jet to accelerate powder particles to 500 to 1000 m/s and enable solid-state deposition onto a substrate through the kinetic energy of the particles without melting, resulting in a mean absolute error of 8.3% [33,34]. An alternative artificial neural network (ANN) model using the backpropagation algorithm was proposed to predict the cross-sectional geometry of a single symmetric track profile in the pulsed-laser powder deposition process, which is highly nonlinear [35]. The performance of the developed models in bead height and width predictions was compared to the track profile using the Gaussian model [36,37]. Other investigations have provided numerical simulations within the WAAM process; however, these are limited by complex models described by physical processes and by the ideal cuboid geometry used in most FE simulations to represent sedimentary layers [38–40]. Therefore, the influence of process parameters on the dimensions and microstructure of manufactured parts to achieve optimization should be studied with an efficient, intelligent, and less complex method.

In this study, the prediction of the geometrical dimensions of a deposited layer microstructure fabricated via the WAAM process with copper-coated solid wire BÖHLER SG 2 was achieved using ANN (artificial neural networks) and SVM (support vector machines) under different welding and geometrical parameters. These computational models have established a mathematical relationship between input and output data. The welding parameters, namely welding speed and the robot's trajectory length, are the input data, and the output data are the geometrical parameters, such as the total continuous length of the weld, weld toe and root radius, the widths of a deposited weld bead at different positions along its length measured using a microscope with high accuracy, and the height of the weld metal measured in the middle of the bead using a caliper. The input data, namely the welding speed, were set in the moderate-high speed range to achieve narrower and shallower weld beads with faster cooling rates, and the trajectory length was considered an independent variable defined as the spatial path programmed for the robot's end-effector, but it does not directly affect the physics of the melt pool. However, the model analysis can be a useful tool to vary a few parameters, as in this case, welding speed and trajectory length, to accurately predict the complex system geometry with a small number of key parameter combinations. The machine learning models are compared and used for the complex dataset in the analysis of the morphology (weld height, weld width, etc.) of the single deposited layer under different welding speeds and path trajectories. The prediction result of the SVM model is superior to that of the ANN model, and the mean error of the SVM is much lower than that of the ANN. Although the ANN model fits the training data very well, it has poor test performance. The main contributions of this work include the following:

- A comprehensive overview of fundamental process characteristics of significant additive manufacturing techniques for fabricating large and complex metallic components, including binder jetting, powder bed fusion, sheet lamination, and wire arc directed energy deposition, is investigated. The main parameters of various additive manufacturing technologies are explored, including layer thickness, deposition speed, and temperature, which are crucial for mechanical properties and print quality. In particular, the key parameters for additive manufacturing, such as travel speed, deposition strategy, path planning, current, voltage, and wire feed speed, determine the desired geometry and significantly influence the characteristics of multi-layer structures in terms of bead geometry.
- The geometry inspection of high-quality weld beads of copper-coated solid wire BÖHLER SG 2 was performed using a microscope and a caliper, offering high levels

https://doi.org/10.3390/metrology6010018

of accuracy for post-process treatment. The welding procedure was performed using a wire feeding system to melt the metal wire, controlled by the robotic arm controller. In the experiment, the weld bead samples with different trajectory path lengths and welding speeds were realized.

- A comparison of ANN and SVM for geometry prediction of weld beads (i.e., width, height, radius, and length) from welding parameters, such as welding speed and the robot's trajectory length.

In Section 2, current metal welding technologies, including material jetting, directed energy deposition (DED), powder bed fusion (PBF), and binder jetting within additive manufacturing (AM) processes, with particular attention to various process variables, challenges, and strategies in wire-arc additive manufacturing, are presented. In Section 3, the welding process conducted using the welding robotic arm and control system, the measurement and testing procedures for quality control of the weld bead, and a brief discussion of the computational models are presented. The results of the ANN and SVM computational models are presented in Section 4. Thus, in Section 5, the conclusion is given.

2. Literature Overview: Metal Additive Manufacturing Methods

Additive manufacturing (AM) is a 3D printing technology used in various industries for the design process involving adding material layer by layer to create objects from 3D model data achieved by utilizing computer-aided design (CAD) software tools [41–43]. The additive manufacturing methods can be classified by the American Society for Testing and Materials (ASTM) into VAT photopolymerization, powder bed fusion, binder jetting, material jetting, sheet lamination, material extrusion, and directed energy deposition. One common type of 3D printing technology is material extrusion (ME), also known as fused deposition modeling (FDM), which involves the creation of parts by extruding thermoplastics layer by layer using polylactic acid (PLA), deposited to create each object at a temperature between 190 and 230 degrees Celsius [44]. Metals like super-alloys are processed using fusion-based additive manufacturing (AM) techniques like powder bed fusion (PBF) and directed energy deposition (DED), which melt material layer-by-layer [45]. Wire-arc additive manufacturing (WAAM) and thermal-based methods like high-velocity oxygen fuel (HVOF) are also used. PBF uses a laser or electron beam to fuse powders, DED adds material to a substrate with an energy source, while WAAM uses an arc to melt wire, and HVOF uses a jet of gas to heat and propel molten powder [46]. Using AM with welding methods can be classified as welding-based additive manufacturing (WAM) processes, like wire-arc additive manufacturing (WAAM), laser additive manufacturing (LAM), and electron beam additive manufacturing (EBAM). Previous studies have examined the impact of prominent process variables on mild steel, such as welding speed, welding current, welding voltage, wire feed rate, and gas flow rate, and the quality of the weld based on two key process responses, namely joint penetration and percentage defect, determined by the response surface methodology (RSM) using a central composite design (CCD) method in order to establish the best parameter settings [47]. In the regression analysis, the current and the wire feed rate are the key factors that have a substantial impact on joint penetration, whereas the percentage of defects is heavily dependent on the voltage and the feed rate [48]. Therefore, the ambient environmental conditions can affect the thermal cycle of the weld (heating and cooling rates) and the characteristics of the welded joint, affecting microstructure, hardness, grain morphology, and bead geometry [49]. The desired welding quality can be achieved with high melting power and high welding speed [7]. The essential features and methods of additive manufacturing techniques, such as ultra-torque friction

https://doi.org/10.3390/metrology6010018

stir deposition, metal binder jetting, sheet lamination, powder bed fusion, and directed energy deposition, based on scientific knowledge, are presented.

2.1. Ultra-Torque Friction Stir Deposition

Ultra-torque friction stir deposition can create components and microstructures with simpler or less complicated geometry, with the capacity to fuse a wide range of multiple materials [50]. In the solid-state technique, the material is not melted, minimizing defects like porosity, and it uses a rotating tool to heat and plastically deform feedstock material and to process structural metals and alloys [51]. The tool moves along a predetermined path, resulting in heat generation by friction and severe plastic deformation and leading to metallurgical bonding between the layers of the sheets. The important process parameters are the rotational speed and tool traverse rate, which influence frictional heat generation (i.e., higher rotational speeds increase frictional heat generation in deposition stages), material feed rate, and the axial force that generates friction between the tool–work material interfaces, which can plasticize the material in the welding zone [52]. The size of the tool and feedstock set limits on the size of features and overall geometric forms. The maximum feed rate is constrained by the axial force limit of the machine, as a higher feed rate causes a higher axial force due to the increased rate of material buildup behind the tool [53]. Cooling and heating conditions also influence the resulting mechanical properties during the build process. The achieved in-plane resolution is very low compared to other AM processes, limited to approximately 10 mm or higher, depending on the tool and feedstock geometry [54]. The poor surface quality on the side walls is primarily caused by flash as a result of excess material forced beyond the deposition tool, causing weak bonds between layers at the edges of the deposited track, where the flash is not mixed with the underlying substrate or previously deposited layers [55,56]. Poor quality on the surface is due to the concentric ring pattern known as onion skin [57]. The layer height is set to a value between 1 and 2 mm; however, higher layer thicknesses (2 and 3 mm) affect the tensile properties of the deposited material in the build direction. Layers of 1 mm present considerably lower fracture strains and ultimate tensile strength [58]. Thinner layers effectively have more layer interfaces in the build direction, but also have an increased number of interface defects than thicker layers.

2.2. Metal Binder Jetting Additive Manufacturing

Metal binder jetting (MBJ) or material jetting is an additive manufacturing technique that builds metal parts layer by layer using a liquid-based binding agent to join the material in a powder bed. The powder parameters and properties, such as particle porosity, impurity levels, and powder flow behavior, substantially influence the process stability and robustness [59]. Tap density plays an important role in the powder bed characteristics, and finer powders, which are more active in sintering, increase the interparticle friction, promoting particle bridging and agglomeration [60]. The powder, or skeletal, density, usually measured with an inert gas pycnometer, is used to analyze particle inner porosity, possible cracks, satellites, and also the phase composition of the material or alloy content, as density depends on possible alloying elements of the metallic material [61]. Particle morphology influences the powder packability and flowability. The metal binder jetting process can build walls with widths from approx. 1.5 mm to more than 80 mm without defects; however, the maximum wall height is limited to eight times the wall width [62].

2.3. Sheet Lamination

Sheet lamination is an additive manufacturing method used to create 3D parts or very large prototypes using sheets of fused metals. The sheet lamination process can be classified into laminated object manufacturing (LOM) and ultrasonic consolidation [63]. The objects

https://doi.org/10.3390/metrology6010018

are made by a machine that deposits the material sheets or composite prefabricated layers at 0° and 90° and then heats, compresses them from a continuous roll, and cuts the layers to form a single part. The desired geometry is created by bonding these layers using a heat-activated resin [64]. The sheets are first welded together in layers using ultrasonic welding or friction stir welding, and then the desired 2D cross-section is cut from the stacked layers with a laser or a blade. The excess material is removed, leaving a finished part, although some techniques, like ultrasonic additive manufacturing (UAM), integrate CNC machining to build the final shape [65]. However, the traditional LOM method is not able to work on multi-material structures.

2.4. Powder Bed Fusion Additive Manufacturing for Metals

Powder bed fusion (PBF) can produce 3D objects with complex geometries and high accuracy using a heat source, like a laser or electron beam, to melt and fuse layers of metal powder; however, it has a high operational cost and uses toxic metal powder [66,67]. The process involves metal and ceramic powders with grain shape (spherical, irregular, granulated), grain size, and composition that play a crucial role in powder selection for the product [68]. The control and selection of irregular powder grains' shape and size distribution can increase the density of the powder deposited in a layer before sintering or melting [69]. In powder bed fusion, layers of powder are repeatedly fused; in fact, the platform lowers by one layer's thickness, and a recoater (or roller) spreads a new layer of powder over the previous one. A heat source, like a laser or electron beam, then fuses the new layer, overlapping with the previous one to ensure strong bonding [70]. This layer-by-layer overlap builds a 3D object from the bottom up. Lack of fusion porosity can affect the mechanical behavior of layers containing defects, irregularly shaped pores, and unmelted powder particles attributed to incorrectly selected processing parameters, such as laser beam fluctuations, surface gas flow, and raw material characteristics [71].

2.5. Direct Energy Deposition

Directed energy deposition (DED) is a process with high deposition rates that utilizes an electric arc or laser to melt metals and alloys in the form of wires or powders employed for producing 3D structures of metallic materials, including the formation of gradient structures [72,73]. DED utilizes wire or powder, employing a robotic arm, and can be classified into wire and arc additive manufacturing (WAAM), wire and laser additive manufacturing (WLAM), and wire and electron beam additive manufacturing (WEAM) processes [74]. The types of DED processes may use a laser as a thermal energy source; wire-fed DED uses an electric arc, a plasma arc, a laser, and an electron beam as a thermal energy source.

2.6. Wire-Arc Additive Manufacturing and Gas Metal Arc Welding

The additive manufacturing technology that uses MIG (metal inert gas) and MAG (metal active gas) deposition is wire-arc additive manufacturing (WAAM), which is a form of directed energy deposition [73,75]. WAAM utilizes a combination of an electric arc as a heat source and a filler wire operated typically as an anode to form a liquid metal pool, thus depositing material layer by layer and creating objects, including large-sized parts. The tip of the wire, as well as the workpiece (cathode), melts under the impact of arc attachment. Gas metal arc welding (GMAW) has revealed many advantages, such as providing shaped parts with high precision dimensional tolerances with a higher deposition rate (15–130 gr/min) compared to AM processes at a lower cost of raw material [76]. The metal inert gas (MIG) welding is the process that is used to melt and join metals by establishing an arc between a continuously fed filler wire and the base metal. The arc and molten weld pool are usually shielded by inert gases (Ar and He), important for weld

https://doi.org/10.3390/metrology6010018

metal toughness and for preventing oxygen and water vapor from reacting at the point of merger [77]. However, the MIG arc is unstable in pure argon because of instabilities in the cathode spots on the base metal surface, creating weld defects and irregularity of the weld bead, so metal active gas (MAG) welding uses some active gas, like O_2, H_2, or CO_2 mixed with inert shielding gas, improving the arc stability and welding execution [78]. Tungsten inert gas (TIG) has fewer spatters and better weld bead surfaces than welding using MIG with pure Ar, although its process has a slow speed and a small amount of deposited metal [72]. In WAAM, the final product can be optimized by controlling and managing the process parameters like current, voltage, welding speed, welding rate, welding angle, polarity, preheat temperature, shielding gas, gas flow rate, and deposition strategies that also affect the texture, size, shape, and penetration of the joints, along with overall quality, costs, and productivity [79]. Bead roughness decreases with the increasing current and process parameters, including bead thickness, wetting angle, and melt-through depth, which escalates with an increase in arc current [80]. Arc length is controlled by voltage, while wire feed depends on bead height and amperage. The increase of wire feed rates or amperage reduces the wetting angle [81]. Travel speed affects joint quality; in fact, with increasing travel speed, the wetting angle, melt-through depth, and bead width decrease, while bead roughness increases slightly [82]. Conversely, a slower travel speed leads to excessive buildup. By progressively increasing travel speed with each layer, the heat input is reduced by 5–20% between adjacent layers. In wire-arc additive manufacturing, the weld source can move freely around the workspace, processing layer by layer. The large thermal gradient caused by the weld source can lead to condensation on the workpiece and electrode, stress, and cracks inside the workpiece, resulting in lower product quality [83]. The rapid cooling rates and thermal gradients lead to the presence of residual stresses, thus part deformation, layer delamination, reduced geometric tolerance, and compromised mechanical properties, including fracture resistance and fatigue performance [84]. The residual stresses can be described using destructive methods, such as a combination of the ring-core method and hole-drilling, and, in general, by semi-destructive methods. The porosity due to the presence of gas trapped in the material negatively affects its mechanical characteristics, including fatigue resistance, anisotropy, oxidation, and corrosion resistance [85]. Irregularly shaped pores can reduce the strength and structural integrity of the material, leading to substantial dislocation accumulation and stress concentration. The porosity and density can be measured using gas psychrometry, hard X-rays at synchrotron facilities, X-ray micro computed tomography (μ-CT), image analysis of metallographic cross-sections, ultrasonic pulse-echo velocity measurements, and the Archimedes technique [86]. The porosity can be minimized below 0.035% using the techniques of pulsed GMAW or cold metal transfer with monitored short-circuiting (CMT-PADV) [87]. Cracking and delamination are defects that can compromise the coating's performance and mechanical properties and lead to grain boundary cracks [88]. Process monitoring and real-time vision process control, integrated with additive manufacturing to enhance part quality, can improve the accuracy of the geometries of multi-layer, multi-bead components where the layers are overlapped [89]. A layer-overlapping (LOS) process is achieved when the new layer is deposited over the previous one to build up the part, despite limitations such as a non-uniform surface profile or height. This process is analyzed through mathematical models, taking into account the position and deposition amount of the layer. The temperature distribution and number of layers determine the quality of deposition after each layer and the profile quality [90]. The trajectory-planning strategy that affects the deposition quality and temperature distribution, causing warping, stress, and defects, includes raster, contour, and zig-zag strategies for the creation of geometrical complexities and the calculation of process parameters incorporated in the weld robot [91].

https://doi.org/10.3390/metrology6010018

Therefore, the grain size and morphology are influenced by the temperature gradient. They affect the mechanical properties and anisotropy of metals; for example, finer grain sizes improve the metal's mechanical properties [92]. In metal manufacturing, metal active gas welding is considered efficient and versatile in automation processes [41–43].

3. Materials and Methods

3.1. Experimental Set-Up Description

In this study, the single-layer samples of the weld bead were realized using the arc wire welding process with the aim of optimizing the weld bead geometry and process parameters. The welding workstation integrates a welding robotic arm, welding power supply, human–machine interface, and robotic arm control system for the metal-melting process in order to deposit metal wire in layers. The experiments were carried out using a robot-based WAAM system implemented at the laboratory of the Department of Production Technology and Systems, Faculty of Industrial Technology, Technical University—Sofia. The functional architecture of the system is shown in Figure 1.

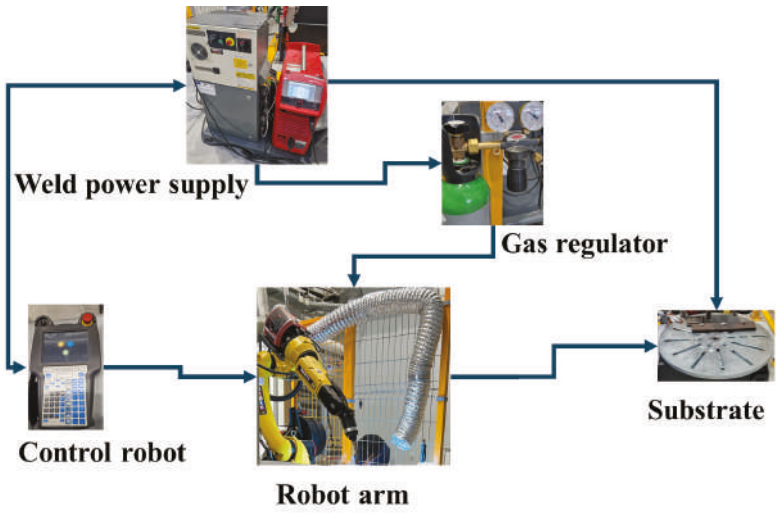


Figure 1. Schematic diagram of the robotic melting wire.

It includes a FANUC Arc Welding Robot ARC Mate 100iD industrial robot with a R30iB Plus controller from FANUC America Corporation, integrated into a welding application using the Roboguide software (FANUC ROBOGUIDE V10), a welding source provided by the Inverter MIG/MAG wire feeder Fronius TPS 320i, and a manufacturing platform made of a structural steel base plate. The compact design of the Inverter MIG/MAG wire feeder Fronius TPS 320i C/4R/FSC Standard/320 A/ manufactured by FRONIUS INTERNATIONAL GMBH, Froniusstraße 1, A-4643 Pettenbach, Austria, integrates a pipe feeder and a multifunctional, pulsed power source designed for MIG-MAG welding. The built-in wire feeder is designed for spools up to 300 mm. The flexible manufacturing structure uses the ARC Mate 100iD robot, an articulated-arm robot integrated into the arc welding application, using the Roboguide software and the R30iB Plus controller. The welding equipment is based on a TPS/i welding system with a power capacity of up to 600 A and a working voltage of 16.8 V. R-R30iB Plus A-Cabinet is a FANUC standard cabinet with dimensions of 600 × 500 × 470 mm, including the R30i controller, which is designed for very high performance in terms of cycle time, speed, accuracy, and safety, and complete connectivity via an Ethernet network. The iPendant Touch is a control device with an intuitive iHMI interface.

https://doi.org/10.3390/metrology6010018

The simple strip geometry samples were printed using wire-arc additive manufacturing. The electrode copper-coated solid wire BÖHLER SG 2, Voestalpine BÖHLER Welding Germany GmbH, with a diameter of 0.8 mm, was used for welding deposition, suitable for many carbon steel welding applications, with the typical mechanical properties (as welded) shown in Table 1.

Table 1. Mechanical properties of BÖHLER SG 2.

Typical Mechanical Properties (as Welded)	
Shielding Gas	75% Ar/25% CO_2
Tensile Strength	580 MPa
Yield Strength	480 MPa
Elongation	30% (minimum $\geq$ 20% or $\geq$ 22%) ($L_0 = 5d_0$)

SG2 contains moderate amounts of manganese and silicon to provide sufficient deoxidation over light mill scale. The nominal chemical composition of the studied BÖHLER SG 2 is: C 0.07%, Si 0.85%, and Mn 1.5%, as provided by the manufacturer [93]. The BÖHLER SG2 strip samples were manufactured by the robot ARC Mate 100iD onto a solid steel support structure. In total, 16 samples were printed on the solid structure build plate at the same time. All samples were oriented in the same direction and located in four columns side by side, with five or three samples per row, as shown in Figure 2.

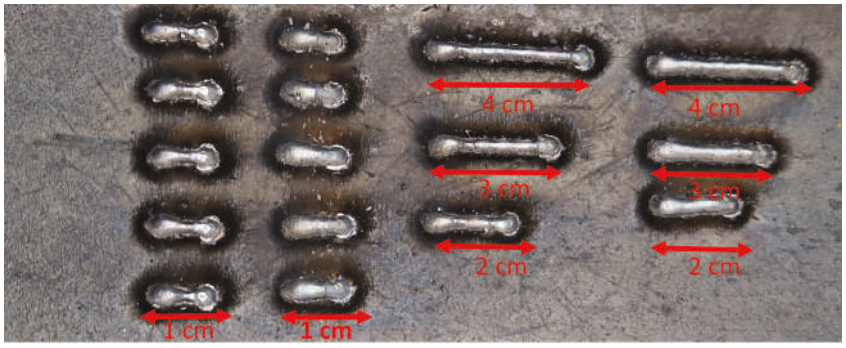


Figure 2. Bead samples realized with different sizes and different welding speeds.

In the melting process, an inert and non-toxic gas mixture of (Ar = 82%) and (CO_2 = 18%), stored in a pressurized gas cylinder, is used to produce a smooth, quiet, and stable arc. The pressure of the gas cylinder was 20 MPa (200 bar) at the T = +15 °C. In the procedure, the gas purge is 0.35 s, with gas pre-flow and post-flow of 0.20 s. The arc start (and end) pre-time is 100 msec. The welding parameters controlled to produce acceptable welds include arc current, arc voltage, wire feed speed, electrode travel speed, current density, and preheat temperature. The welding voltage is 16.8 V. The experiments were conducted on a mild steel substrate (S235J2) with dimensions of 26 × 10 × 6 cm, which was cleaned before carrying out the depositions. In the experiment, deposition samples of different sizes were realized using gas metal arc additive manufacturing. The motion termination type, which determines how the robot moves between points, and the taught points determine the "length" of a trajectory path in FANUC robotics. In particular, the weld bead samples with trajectory path lengths of 10 mm, 20 mm, 30 mm, and 40 mm for speeds of 8 mm/s and 5 mm/s were realized. In Fronius TPS1 Inside Enet, the welding conditions are set by the controller, which communicates with the Fronius power source to control welding parameters like current, voltage, and process selection. In this case, the wire-feed speed is set to 5.2 m/min, the welding voltage is 16.8 V, and the current

https://doi.org/10.3390/metrology6010018

is 80 A. The welding process was performed in 15 minutes to obtain the final welded structures. The welding arc temperature exceeds 1400 °C to melt both the BÖHLER SG 2 wire and the base metal, as reported by [93]. The welding voltage is set to 16.8 V, and the welding speed was varied and set to 5 mm/s and 8 mm/s. The deposited beads with varying welding speeds of 8 mm/s and 5 mm/s demonstrate significant differences in bead geometry, heat input, and solidification in welding processes. Generally, a higher speed (8 mm/s) results in a smaller, narrower, and shallower bead, while a lower speed (5 mm/s) produces a wider, deeper, and more heavily built-up bead due to increased heat input per unit length [94]. The entire procedure of material deposition lasted 2 min for one weld bead. For all tests, a single directional deposition strategy was used for each sample. The contact tip-to-work distance was fixed at 15 mm to maintain stable metal transfer, preventing excessive burn-back or stubbing, and optimizing melting and deposition to achieve a consistent deposition rate and a stable weld bead [95,96]. After the melting process, the next step involved 15 min of cooling at room temperature for the weld beads, and external measurements of dimensions were conducted using a Vernier caliper with high accuracy and under a microscope.

3.2. Measurement Method in Wire-Arc Additive Manufacturing

Measurement and testing procedures utilizing a post-process inspection microscope and a caliper are used for quality control of weld size and geometry. However, before the microscope measurements, the strips were treated using the post-process treatment introduced in the process diagram in Figure 3.

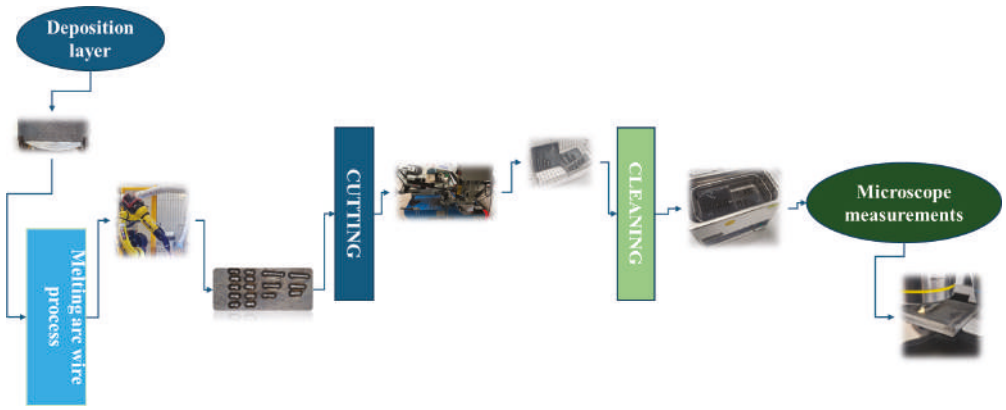


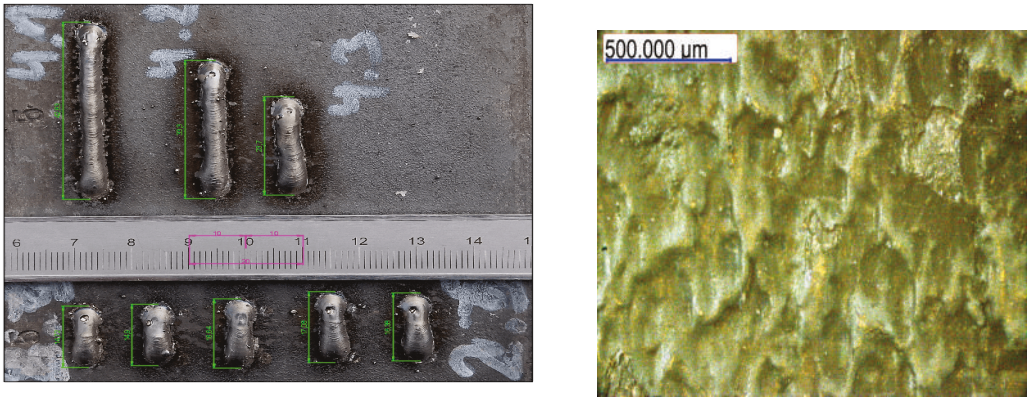
Figure 3. Diagram of the process chart of samples.

After the printing, as-built samples located on a steel plate were cut using the Harris BS260G horizontal bandsaw machine, which has specifications including a blade size of 2455 × 27 × 0.9 mm, a motor power of 1.1 kW (1.5 HP), and a blade speed of 36/72 m/min. Its cutting capacity includes a maximum round capacity of 230 mm at 90° and a rectangular capacity of 260 × 150 mm. After that, the samples were cleaned and fully immersed in distilled water for 20 min using a BANDELIN SONOREX SUPER RK ultrasonic bath with internal dimensions of 240 × 140 × 100 mm to remove impurities and prevent any interference with subsequent testing. Distilled water was used because it is free from minerals and other contaminants present in tap water. Then, they were air-dried in the same conditions as the treatment to remove all water. The width and height of the deposited beads are considered critical parameters that significantly influence the accuracy and quality of the final product. In fact, the relevant measurements have demonstrated that the dimensions for each sample change after the deposition, as shown in Figure 2.

In this case, the deposited beads exhibiting different sizes as shown in Table 2 were realized with a welding speed of 8 mm/s and 5 mm/s and an initial trajectory path

https://doi.org/10.3390/metrology6010018

defined by the FANUC robot set to 10, 20, 30, and 40 mm. The inconsistent lengths in single-pass weld specimens can be attributed to several factors. For example, welding can introduce localized heat, causing expansion, followed by cooling-induced contraction, which can result in different final lengths. Small variations in the initial length of base metal plates, or inaccuracies in trimming/cutting after welding, can lead to uneven specimen lengths. The measurement tests were initially conducted using a caliper to get a rough estimation of the sample size, as standard practice. After that, the strip dimensions were compared to the morphology measurements conducted using the metallurgical microscope for material analysis, BestScope model BS: BS-6022TRF, with a magnification range of 100×–1000×. Initially, to make accurate measurements, it was required to calibrate the microscope images. The scale calibration process maps a known number of pixels to a known real-world distance (e.g., millimeters or micrometers), also using the stick meter placed within the image frame for measuring the dimensions of different welds obtained in AM (Figure 4a). Therefore, the morphology of the surface metal strip (number 2.2) obtained by additive manufacturing was analyzed under a microscope to identify the weld's quality, geometric features, and potential defects. The digital image of the metal strip surface shown in Figure 4a was captured with the microscope objective L PLAN 5x 0.12″, ×100 magnification and a resolution of 5472 × 3648 pixels using the Capture 2.1 software. The microstructure image of the weld metal illustrates the formation of distinct grain zones due to varying heat input, with an average grain size of approximately 100 μm, as shown in Figure 4b.



(**a**) (**b**)

Figure 4. (**a**) Measurement size of some weld beads under a microscope; (**b**) surface of the metal strip under the BestScope model BS:BS-6022TR microscope without active cooling.

As shown in Figure 4b, a direct correlation between welding parameters, welding geometric parameters (such as weld height and width), and the weld microstructure (grain size and phase composition) is exhibited [97]. Variations in parameters like welding current, voltage, and travel speed can change the heat input and cooling rate, which in turn dictate the weld pool size, grain refinement or coarsening, and phase transformations. Lower welding speeds result in higher heat input, leading to lower cooling rates, which produce coarser grains and wider, less-desirable columnar zones. Conversely, higher welding speeds or lower heat input result in narrower welds with finer grain structures. Increasing the welding heat input, which is reflected in wider and higher weld beads, produces a more pronounced mixed grain zone, coarser grain sizes, and different phase compositions compared to lower, more controlled heat inputs [98]. Higher current or lower speed produces wider or higher beads with coarser microstructures, while lower current or higher speed produces narrower or shallower beads with refined microstructures.

https://doi.org/10.3390/metrology6010018

Table 2. Relevant measurement results for weld beads deposited in one layer, performed using a caliper and a microscope for welding speeds of 5 mm/s and 8 mm/s.

Deposition of One Layer	Sample	1.1	1.2	1.3	1.4	1.5	2.1	2.2	2.3	2.4	2.5	3.1	3.2	3.3	4.1	4.2	4.3
Input welding Robot	Welding Speed [mm/s]	8	8	8	8	8	5	5	5	5	5	8	8	8	5	5	5
	Trajectory path (Length) [mm]	10	10	10	10	10	10	10	10	10	10	40	30	20	40	30	20
Measurements after the deposition	Middle Height [mm]	2	2	2	2	2.1	2.5	2.5	2.2	2.3	2.5	2	2	1.9	2.1	2.1	2.2
	Length [mm]	16.53	16.38	15.42	16.65	15.31	14.72	14.9	16.64	17.08	16.38	41.64	32.41	23.18	42.63	33.3	23.7
	Width 1 [mm]	5.47	5.1	5.97	5.18	5.5	4.58	5.37	5.29	5.41	5.59	4.43	4.69	4.32	5.16	4.75	4.98
	Width 2 [mm]	3.15	3.73	3.84	3.84	4.16	4.4	4.5	4.85	4.17	4.63	3.57	4.12	3.54	4.04	4.17	4.6
	Width 3 [mm]	3.08	3.15	3.22	3.04	3	4.17	4.77	4.26	4.19	4.5	2.93	3.27	2.94	4.04	4.18	3.92
	Width 4 [mm]	3.69	3.76	3.58	3.26	3.4	4.16	5.02	4.58	4.44	4.63	3.28	3.09	3.35	4.24	3.98	4.26
	Width 5 [mm]	4.05	4.31	4.38	3.55	4.71	4.83	5.31	4.94	4.93	4.81	3.28	2.98	3.07	3.89	3.92	4.93
	Width 6 [mm]	4.52	4.38	4.63	5.25	4.78	4.97	4.29	4.15	5.36	5.59	3.22	3.16	4.83	4.79	5.08	5.19
	Weld toe radius [mm]	2.58	2.57	2.87	2.55	2.61	2.25	2.43	2.61	2.53	2.65	2.11	2.23	2.09	2.49	2.29	2.45
	Root radius [mm]	2.31	2.18	2.26	2.44	2.42	2.53	2.57	2.69	2.54	2.47	2.81	2.47	2.7	2.53	2.7	2.63

https://doi.org/10.3390/metrology6010018

3.3. Computational Method: Neural Networks and Support Vector Machine

This study focuses on the prediction of weld geometric parameters for copper-coated solid wires in the WAAM process. ANN and support vector machine models are employed to establish correlations between welding speed, trajectory length, and weld geometric parameters (e.g., width, height, radius). In particular, the welding speeds were set from 5 mm/s to 8 mm/s, which represents a moderate-to-high speed range often used in precision applications, and the trajectory length was chosen within the range from 10 mm to 40 mm [99]. A narrower and shallower weld bead and faster cooling rates result from the decrease in heat input per unit length caused by an increase in welding speed from 5 mm/s to 8 mm/s. A speed of 5 mm/s is typically considered a good compromise between productivity and sufficient heat input for appropriate penetration. Faster speeds (about 8 mm/s) usually result in grain refinement and higher hardness in the weld seam, whereas slower speeds (about 5 mm/s) may create a coarser microstructure due to increased heat input. While the trajectory length is considered an independent variable defined as the spatial distance or path programmed for the robot's end-effector (e.g., path length in mm), it does not directly affect the physics of the melt pool. A change in trajectory path—such as at sharp corners—can force the FANUC robot to decelerate, which indirectly increases local heat accumulation, affecting the melt pool size. The other parameters, like current, heat input, interpass temperature, and arc mode, are not considered in the computational models, although a significant risk can be introduced to the accuracy of the final product and its structural integrity due to non-homogeneous and defective parts. However, the model analysis can be a useful tool to vary a few parameters, as in this case, welding speed and trajectory length, to accurately predict the complex system geometry with a small number of key parameter combinations. The computational method, the neural network (or artificial neural network, ANN) that consists of interconnected nodes and neurons in layers to process complex data for mapping inputs to outputs, and the support vector machine (SVM), are compared and proposed to produce high-quality and repeatable weld beads. The precise control of the welding process using a specialized FANUC robot can be combined with the predictive mathematical model to define the geometry of weld beads based on welding parameters such as the FANUC robot's trajectory length and welding speed. The welding parameters, such as the FANUC robot's trajectory length and welding speed, can be used to forecast the geometrical size parameters of the weld bead, such as width, height, and radius, in order to ensure the quality of the deposited weld bead. In particular, welding speed can lead to narrower or wider welds with less or higher penetration, while the robot trajectory length refers to the distance traveled by the robot from its starting point to its destination. Therefore, the relationships between the welding and geometrical parameters can be described and modeled using an artificial neural network, and the performance can be enhanced with an SVM.

The FANUC robot's trajectory length and the welding speed are provided as inputs to the ANN computational model. In particular, based on the proposed melting procedure, the welding speed and trajectory length vary in the range from 5 mm/s to 8 mm/s and from 10 mm to 40 mm, respectively. The geometrical parameters, such as the height of a weld bead measured using a caliper, as well as the different widths, lengths, and weld toe and root radii of the weld bead measured using a microscope, are considered as output data of the ANN computational model. Some relevant measurement data are reported in Table 2. The developed architecture of the neural network method is shown in Figure 5.

https://doi.org/10.3390/metrology6010018

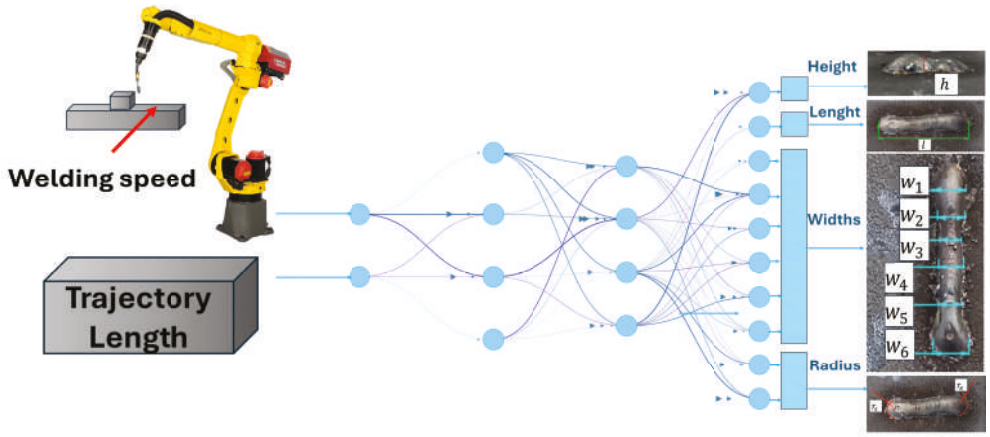


Figure 5. Developed architecture of ANN with inputs and outputs.

The support vector machine (SVM) was adopted due to its nonlinear data regression capability, using the same parameters as those used in the ANN.

The choice between ANN and SVM for data fitting has involved the balance of performance metrics against dataset size, computational resources, and data dimensionality. The SVM is preferred for small to medium datasets with high dimensionality, as it is more robust to noise and less prone to overfitting. However, ANN is suitable for mapping complex datasets with nonlinear relationships and high-dimensional functions, but it requires regularization to manage overfitting. It is often trained via backpropagation, which can lead to local minima, although it often achieves lower error on extremely complex, large-scale data.

4. Results and Discussion

4.1. Artificial Neural Network

In the first scenario, the feedforward neural network approach was used for multi-target training for all weld metal geometries as output data, and referred to welding speed and weld length parameters as input data. The feedforward neural network model is applied to formulate the mathematical relationships between the input values of the processing parameters, such as weld length and welding speed, and the output geometrical values due to intrinsic nonlinear characteristics. Furthermore, the input parameters, such as welding speed, can influence the final products, determining different geometrical shapes. A feedforward neural network equation defines a function:

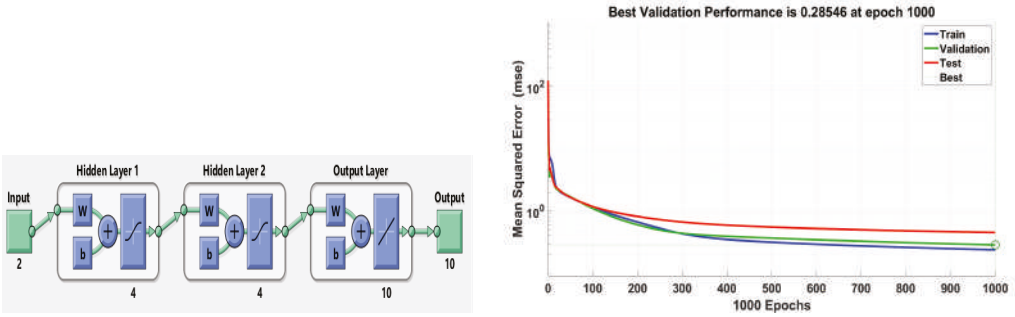
$$y = f(x;\theta) = \sigma^{(L)}(W^{(L)}\sigma^{(L-1)}(\ldots\sigma^{(1)}(W^{(1)}x + b^{(1)})\ldots) + b^{(L)}) \quad (1)$$

This function maps inputs (x) to outputs (y) through layers, with each layer performing a weighted sum of the previous layer's output, with W representing the matrix of the weights plus a bias (b), followed by an activation function (σ) to approximate complex functions.

4.2. Feedforward Neural Network Results

In this work, the feedforward neural network contains three layers: the input layer has three neurons, the only hidden layer has three neurons, and the output layer has ten neurons, as shown in Figure 6a.

https://doi.org/10.3390/metrology6010018



(**a**) (**b**)

Figure 6. (**a**) Design view of the neural network structure; (**b**) training performance of the neural network.

The number of neurons in the input layer and output layer is determined by the problem itself. However, the number of neurons in the hidden layers has been selected rigorously due to underfitting and overfitting problems. The activation function is the nonlinear transformation of the input signal. The hyperbolic tangent (tanh) function is used in the first and second layers of this network as a nonlinear activation function. It maps inputs to an output range of −1 to +1. It is expressed by a mathematical formula:

$$tanh(x) = \frac{e^x - e^{-x}}{e^x + e^{-x}} \tag{2}$$

where x is the neuron's input. Therefore, the sigmoid activation function is used to take the x_1, the neuron's input weighted sum of the previous layer's outputs, and to squash it for binary classification. The sigmoid activation function is used using the following formula:

$$\sigma(x_1) = \frac{1}{1 + e^{-x_1}} \tag{3}$$

The number of neurons in the hidden layer was iteratively determined to train the network and identify the optimum number of neurons in the hidden layer. To minimize the differences between the target (experimental weld metal geometrical parameters) and the output (the response of the ANN generated by a weight-adjusting process), the gradient descent algorithm (traingd) was used. The network training function traingd sets the network properties, with the role of minimizing the squared error and updating the weight and bias values according to gradient descent. The mean square error (MSE), which measures the distance between the vector of predictions and the vector of target values, has given the best validation performance of 0.28546 at epoch 1000, as shown in Figure 6b. The selection of epochs, namely the number of complete passes through the training dataset, is a critical hyperparameter optimization process. The role is to find the balance between underfitting (too few epochs) and overfitting (too many epochs), ensuring the model generalizes well to unseen data. The optimal number of epochs is the point where training and validation curves are both low and close together, just before the gap between them widens (a sign of overfitting). As seen in Figure 6b, the green line (validation curve), the train curve, and the red line (test best curve) are low and close together, which signifies that the model is learning effectively and generalizing well to unseen data, without overfitting. After the training, learning, and validation process, the weight parameters associated with hidden layer 1 and input 1 are shown in Table 3, the weight parameters associated with hidden layer 2 and hidden layer 1 are shown in Table 4, and the weights associated with hidden layer 3 (or the output layer) and hidden layer 2 are shown in Table 5. The bias parameters associated with the layers are shown in Tables 6 and 7.

https://doi.org/10.3390/metrology6010018

Table 3. Weight to hidden layer 1 from input 1.

i/j	1	2
1	1.9276	1.9729
2	−1.8407	1.5628
...	...	...
4	−2.1323	−2.0933

Table 4. Weight to hidden layer 2 from hidden layer 1.

i/j	1	2	3	4
1	−0.17577	1.3751	−1.4229	−0.24299
2	1.1146	0.58799	−1.3797	−0.44353;
...	...	...	...	...
4	0.0049168	−0.76937	0.26311	−1.0153

Table 5. Weight to hidden layer 3 (or output layer) from hidden layer 2.

i/j	1	2	3	4
1	−0.69624	0.69233	−0.45496	−0.27289
2	−0.011152	0.87821	−0.55114	0.080929
3	−0.11743	−0.011739	0.2064	0.87849
4	...	...	...	...
...	...	...	...	...
10	0.73341	0.14311	−0.089988	−0.03193

Table 6. Bias to layer 1 and bias to layer 2.

i/j	1	2	3	4
b(1)	−2.5965	−0.018938	−0.75416	−2.596
b(2)	1.857	−0.036711	0.018685	−2.3999

Table 7. Bias to layer 3.

i/j	1	2	3	4	10
b(3)	−0.11821	0.087478	0.7627	...	0.20099

All response plots used to evaluate how well a model's predictions align with real-world target data are shown in Figure 7. In particular, the comparisons between the predictions and the actual data achieved by ANN are reported in Figure 7 for height, length, weld toe radius (r_s), and root radius (r_e), and in Figure 8 for $w_1, \ldots, w_6$.

For measuring data forecasting, the metrics involved are mean absolute percentage error (MAPE), which is calculated as the average absolute percentage difference between predicted and actual data, and mean absolute error (MAE), calculated as the average absolute difference between actual and predicted values. Lower MAPE/MAE means higher forecasting accuracy, often suggesting low deviations. Generally, an MAPE under 10% is considered excellent. For robust forecasting, it is common to report both metrics along with others to fully understand model performance. The results of the predicted

https://doi.org/10.3390/metrology6010018

model for weld bead heights as a function of the sample number are reported in Figure 7a with an MAPE of 12.51% and an MAE of 0.26 mm. The results of the predicted model for weld bead lengths as a function of the sample number are reported in Figure 7b, with an MAPE of 4.24% and an MAE of 0.95 mm, showing a more accurate prediction than height, although with a low level of accuracy. In Figure 7d, the MAPE and MAE between predicted and actual values for weld toe radius (r_s) are 11.0514% and 0.2669 mm, and for root radius (r_e) are 6.1668% and 0.1516 mm, respectively. Definitely, the weld bead length is identified as the most accurate prediction due to its low MAPE, even though its absolute error is higher than that of other parameters. The predicted model for the root radius is notably more accurate than the model for the weld toe radius.

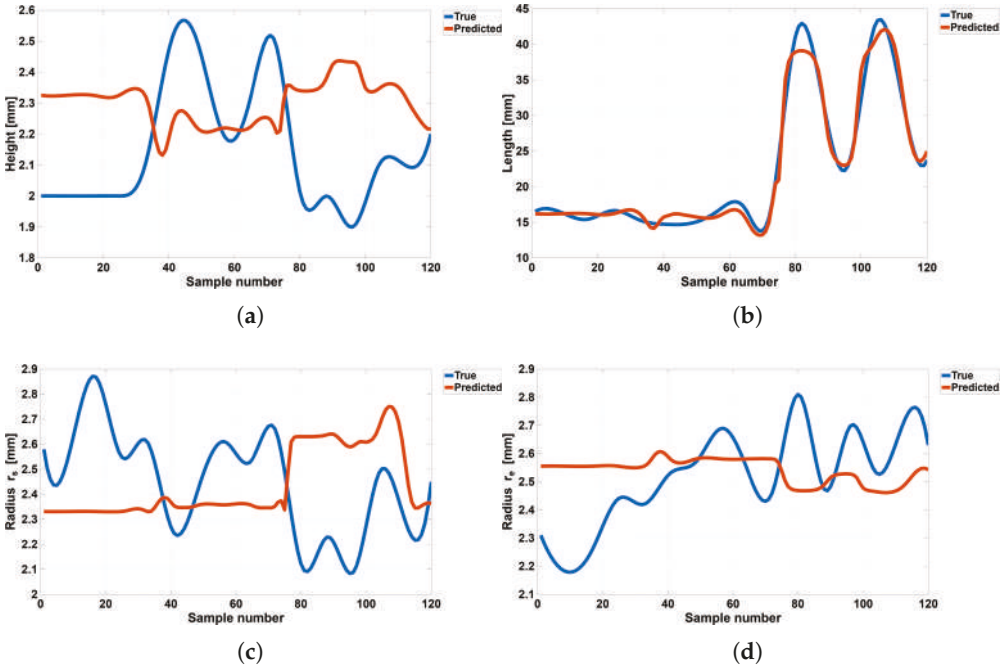


Figure 7. The response plots for the ANN prediction model show the predicted and observed weld bead geometrical values as a function of the sample number for (**a**) weld bead heights, (**b**) weld bead lengths, (**c**) weld toe radius, and (**d**) weld bead root radius.

In Figure 8, the response plots of the ANN prediction model for weld bead widths as a function of the sample number are shown. In Figure 8a, the response plot for the ANN prediction model for width w_1 is reported with an MAPE of 6.13% and an MAE of 0.31 mm; in Figure 8b, for width w_2 with an MAPE of 8.01% and an MAE of 0.324 mm; in Figure 8c, for width w_3 with an MAPE of 17.12% and an MAE of 0.628 mm; in Figure 8d, for width w_4 with an MAPE of 13.34% and an MAE of 0.5104 mm; in Figure 8e, for width w_5 with an MAPE of 10.59% and an MAE of 0.4167 mm; in Figure 8f, for width w_6 with an MAPE of 11.79% and an MAE of 0.5190 mm. The ANN model has demonstrated an average MAPE of ∼11% and an MAE of ∼7.33 mm for the prediction of weld bead width, indicating a low level of precision.

Finally, the weld bead width prediction has provided high MAPE and MAE values, showing the low forecasting accuracy of the ANN model.

For this reason, various machine learning model types (tree, efficient linear least squares, SVM, etc.) have been analyzed and compared for predicting the geometrical properties of the weld bead in order to select the suitable algorithm for the specific dataset.

The comparison aims to maximize the predictive accuracy using relevant metrics (e.g., root mean square error (RMSE), mean squared error (MSE), mean absolute error (MAE), . . .), and computational efficiency based on training time, processing speed, and

https://doi.org/10.3390/metrology6010018

memory usage (model size). Thus, mean squared error (MSE) is the average of the squared differences between predicted and actual values, root mean squared error (RMSE) is the square root of the MSE, and mean absolute error (MAE) is the average of the absolute differences between predicted and actual values. In this case, the good trade-off between predictive performance and computational efficiency is the cubic support vector machine (SVM), as shown in Table 8. The cubic SVM has revealed a superior performance based on metrics (i.e., MSE $\sim$ 0.0002 mm) for the non-linear and intricate relationships in the weld bead datasets, but at the disadvantage of prediction speed and training time.

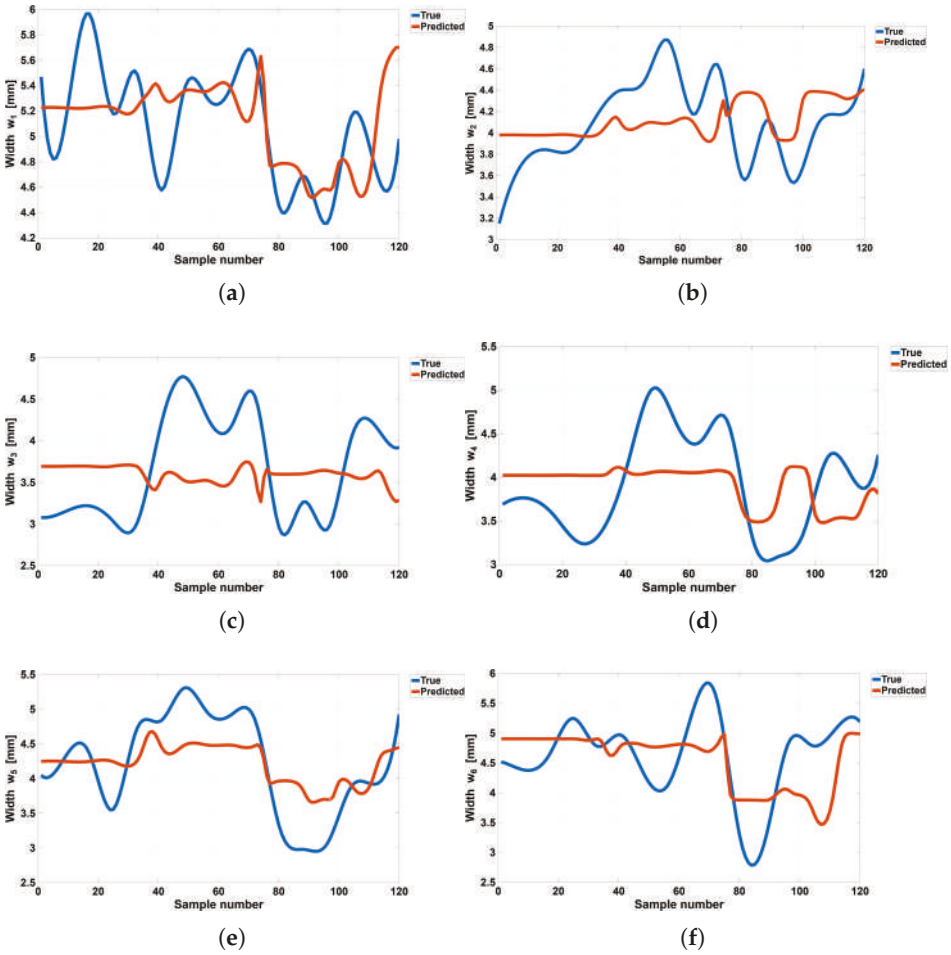


Figure 8. The response plots for the ANN prediction model show the predicted and observed geometrical values of weld bead widths as a function of the sample number for (**a**) width w_1, (**b**) width w_2, (**c**) width w_3, (**d**) width w_4, (**e**) width w_5 and (**f**) width w_6.

Table 8. Comparison of some machine learning model types.

Training Results	Model SVM	Model Tree	Model Efficient Linear Least Squares
RMSE [mm]	0.0131	0.0816	0.137
MSE [mm]	0.0001715	0.067	0.019
MAE [mm]	0.0118	0.064	0.0134
MAPE [%]	0.5	2.6	4.6
Prediction speed [obs/s]	4300	10,000	24,000
Training Time [s]	2.9744	4.8897	2.894
Model size (Compact) [kB]	8	5	11

https://doi.org/10.3390/metrology6010018

4.3. Support Vector Machine

The support vector machine (SVM) is considered a mathematical extension of the neural network for the best performance. It is considered a powerful supervised machine learning algorithm used for classification and regression, finding the optimal hyperplane in multidimensional space to separate classes in the best possible way by maximizing the distance between them. Given the training dataset:

$$D = \{(\mathbf{x}_1, y_1), \ldots, (\mathbf{x}_k, y_k), \ldots, (\mathbf{x}_N, y_N)\},\ \mathbf{x}_k \in R^n, y_k \in R \tag{4}$$

The general equation used by a trained nonlinear SVM to predict the class of a new data point ($\mathbf{x}$) is a linear combination of the kernel function applied to the support vectors:

$$f(x) = \sum_{i=1}^{N} \alpha_i y_i \kappa(x_i, x) + b \tag{5}$$

where N is the number of support vectors (data points closest to the decision boundary).α_i denotes the Lagrange multipliers, which are non-zero only for the support vectors. y_i denotes the labels of the support vectors (either +1 or −1).

$K(\mathbf{x}_i, \mathbf{x})$ is the kernel function that calculates the similarity between a support vector ($\mathbf{x}_i$) and the new data point ($\mathbf{x}$). b is the bias or intercept term. The nonlinear mapping function maps the input space to a so-called high-dimensional feature space where linear regression is performed. The optimization problem of the SVM method solves the objective function as follows:

$$\min_{w,\xi,b} \left\{ \frac{1}{2}\|w\|^2 + C \sum_{i=1}^{n} \xi_i \right\} \tag{6}$$

where w represents the model weights and b defines a linear classifier, since ξ is in R^n. The first term aims to minimize the norm of the model weights ($\mathbf{w}$). Minimizing $\|\mathbf{w}\|$ is equivalent to maximizing the geometric margin between the decision boundary and the nearest data points (support vectors). The second term aims to minimize the committed errors, specifically the total magnitude of the slack variables (ξ_i). The constant C determines the trade-off between minimizing this training error and maximizing the margin.

4.4. Cubic Support Vector Machine Results

The cubic support vector machine (SVM) is a type of non-linear SVM that uses a cubic polynomial kernel function to compute the relationships between the observations in a higher-dimensional space. The polynomial kernel function has the following equation:

$$\kappa(x_i, x_J) = \left(x_i^T x_J\right)^3$$

where $\mathbf{x}_i \cdot \mathbf{x}$ is the dot product (inner product) of the two vectors in the original feature space, with an exponent coefficient equal to 3, which is the degree of the polynomial. The cubic SVM is used for classification, specific complex tasks, and non-linear decision boundaries, generally providing high accuracy on complex and non-linearly separable data. The cubic SVM approximation model was useful for performing nonlinear regression with many observations and for predicting the data. The same training dataset used for ANN investigation has been considered in the cubic SVM method. The geometrical properties measured using the caliper and the microscope, and the welding parameters, such as the welding speed and the FANUC robot's trajectory length, are defined as the input and output data, respectively, with a total of 120 data points. The dataset involved in this model has a number of observations with a sample size (120 observations) relative to the number of predictors (8) and response classes (11), considered a minimum threshold to

https://doi.org/10.3390/metrology6010018

avoid extreme overfitting in linear or simple non-linear models. From this perspective, the 8 predictors are reasonably supported by the total sample size. The technique used for cross-validation is k-fold cross-validation to prevent overfitting and guarantee the generalization of the model. The data are partitioned into five folds. The accuracy of the prediction model based on cubic SVM is evaluated based on the following statistical error tests, namely, mean absolute error (MAE) of 0.0118 mm and root mean squared error (RMSE) of 0.0131 mm, as shown in Table 8, allowing us to consider the best model to correctly predict all geometrical dimensions in the weld bead. Therefore, the SVM model for the weld bead geometrical prediction requires kernel parameters to avoid overfitting and maintain high accuracy. The kernel function was chosen as a polynomial with order 3 and a scale of 0.8922. The high computational complexity of SVMs presents significant challenges for real-time applications, making them slower than ANNs. SVMs can be sensitive to noise in experimental data, which can negatively affect the precision of bead width and height predictions. However, from the sensitivity analysis with a low sensitivity index of ∼0.0167, the SVM model remains robust in practical applications, indicating stability in input parameter influence; in contrast, ANNs display much higher sensitivity, ∼0.99, which may reflect lower stability [100]. All calculations were carried out using MATLAB mathematical software (version R2025a) with the linear regression app. All geometrical prediction results for weld beads are reported in response plots in Figures 9 and 10. The response plots in Figures 9 and 10 display the predicted responses of weld bead height, length, widths, and radii versus all recorded sample numbers, demonstrating a high level of accuracy and low error. For robust model training, the dataset for the predictive model, constituted by 120 observations, did not present critical issues that could increase the risk of overfitting. Figure 9a shows the response plot for the cubic SVM prediction model for the height of a weld bead with an MAPE of 0.821% and an MAE of 0.018 mm, and Figure 9b shows the response plot for the cubic SVM prediction model for the length of a weld bead with an MAE of 0.74 mm, MSE of 0.86 mm, and MAPE of 3.81%. Figure 9c shows the response plot for the cubic SVM prediction model for weld toe radius (r_s) with an MAPE of 0.82% and an MAE of 0.020 mm, and Figure 9d shows the response plot for the cubic SVM prediction model for root radius (r_e) with an MAPE of 0.47% and an MAE of 0.012 mm. The calculation of the average MAPE (0.65%) and MAE (0.016 mm) for both radii r_s and r_e represents the accuracy and precision of a measurement or prediction model for the radius of a weld bead, indicating that, on average, the predicted radius deviates from the actual value by only micrometers. A MAPE of 0.65% confirms that this error is extremely small relative to the total size of the bead, signifying a highly reliable model.

In Figure 10a, the response plot for the cubic SVM model prediction for width w_1 is reported with an MAPE of 0.77% and an MAE of 0.039 mm; in Figure 10b, the response plot is reported for width w_2 with an MAPE of 0.86% and an MAE of 0.034 mm; in Figure 10c, the response plot is reported for width w_3 with an MAPE of 1.74% and an MAE of 0.062 mm; in Figure 10d, the response plot is reported for width w_4 with an MAPE of 1.33% and an MAE of 0.050 mm; in Figure 10e, the response plot is reported for width w_5 with an MAPE of 1.94% and an MAE of 0.079 mm; in Figure 10f, the response plot is reported for width w_6 with an MAPE of 1.10% and an MAE of 0.048 mm. The calculated average values of MAPE (1.29%) and MAE (0.052 mm) for all widths $w_1 \ldots w_6$ have confirmed the better model performance and greater predictive accuracy, signifying that the average physical deviation is negligible (only 52 μm), likely falling within standard manufacturing tolerances.

https://doi.org/10.3390/metrology6010018

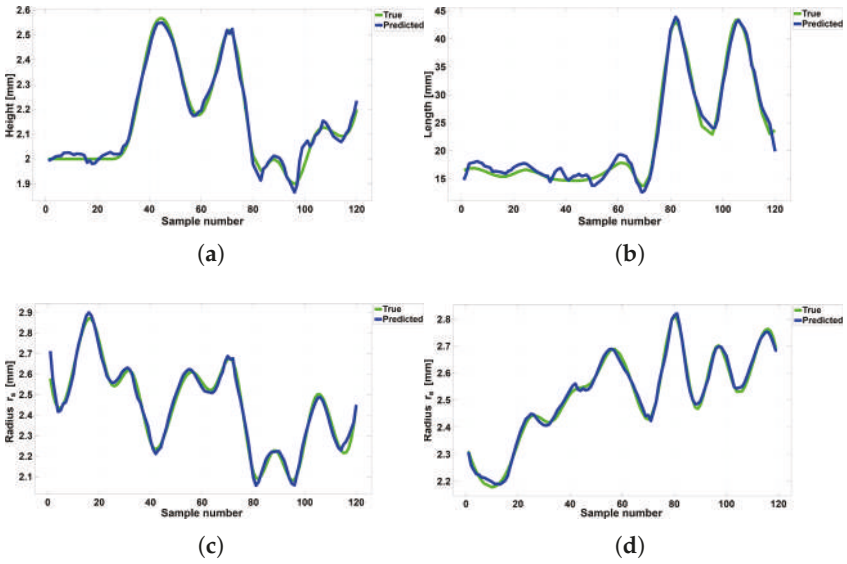


Figure 9. Response plot for cubic SVM prediction models: (**a**) the predicted and observed geometrical values of height as a function of the sample number, (**b**) the predicted and observed geometrical values of length as a function of the sample number, (**c**) the predicted and observed geometrical values of weld toe radius (r_s) as a function of the sample number, and (**d**) the predicted and observed geometrical values of weld root radius (r_e) as a function of the sample number.

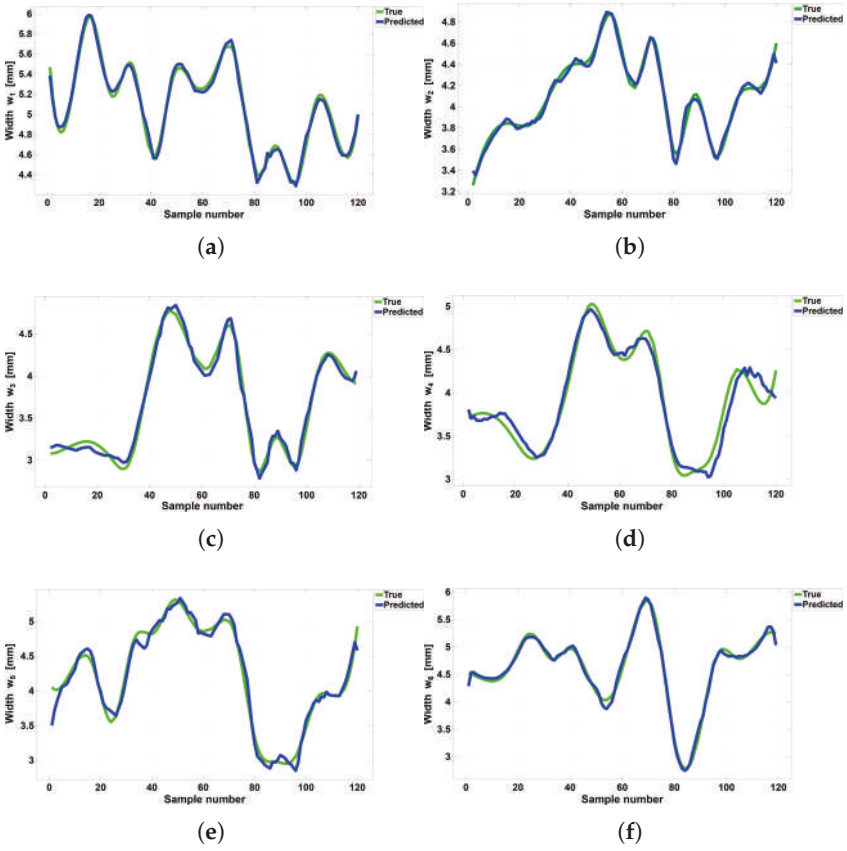


Figure 10. Response plot for cubic SVM prediction models: the predicted and observed geometrical values of all weld bead widths (**a**) width w_1, (**b**) width w_2, (**c**) width w_3, (**d**) width w_4, (**e**) width w_5 and (**f**) width w_6 as a function of the sample number.

The SVM approach can be considered a good approach to model the dependence of the weld bead geometry on the welding speed and trajectory length. In fact, the SVM

https://doi.org/10.3390/metrology6010018

model gives better results for all geometrical parameters, and the dependence between the input parameters (welding speed and trajectory length) and the geometrical parameters is calculated. The predicted responses of the geometrical output parameters are plotted against the actual welding speed and trajectory length, and the true responses are reported in Figure 11.

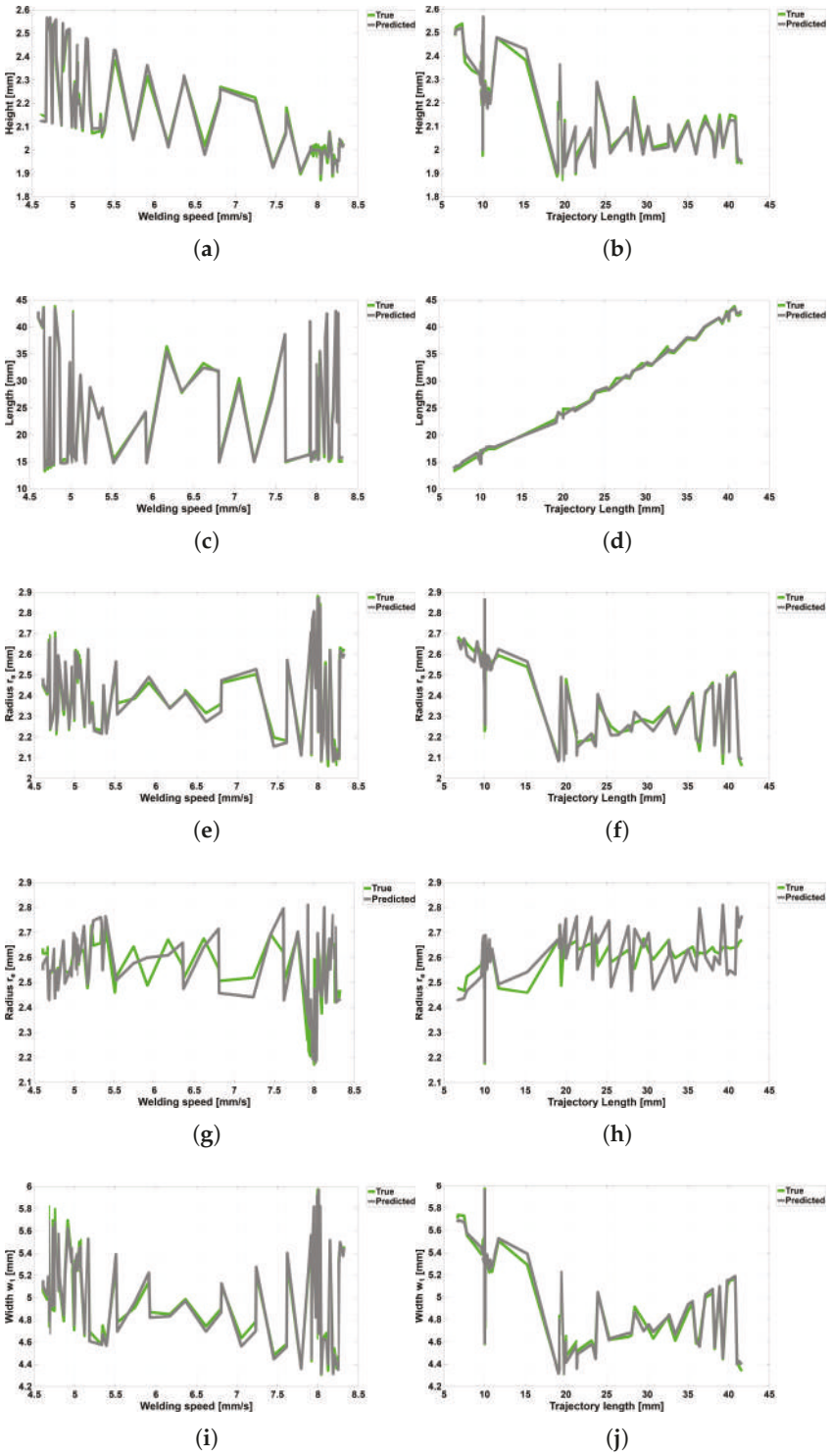


Figure 11. Response plot for cubic SVM prediction models: the predicted and observed geometrical values of weld bead heights as a function of (**a**) welding speed and (**b**) trajectory length, weld bead length as a function of (**c**) welding speed and (**d**) trajectory length, weld toe radius (r_s) as a function of (**e**) welding speed and (**f**) trajectory length, weld root radius (r_e) as a function of (**g**) welding speed and (**h**) trajectory length, weld bead width w_1 as a function of welding speed (**i**) and trajectory length (**j**).

https://doi.org/10.3390/metrology6010018

The response plot of the relationship between welding speed and weld bead height (predicted and actual values) is shown in Figure 11a, and the relationship between trajectory length and weld bead height is shown in Figure 11b, with error metrics of MAE of 0.0164 mm, MSE of 0.0004 mm, and MAPE of 0.7651%, indicating low errors for both plots. The decreasing trend of predicted and actual values is exhibited for both plots. The response plot of the relationship between welding speed and weld bead length (predicted and actual values) is shown in Figure 11c, and the relationship between trajectory length and weld bead length is shown in Figure 11d, with error metrics of MAE of 0.0017 mm, MSE of 0.27 mm, and MAPE of 2.29%, indicating low errors for both plots, especially for weld length as a function of trajectory length, which shows a linear dependence. The response plot of the relationship between welding speed and the weld toe radius r_s is shown in Figure 11e and the relationship between trajectory length and the weld toe radius r_s is shown in Figure 11f, with error metrics of MAE of 0.018 mm, MSE of 0.0005 mm, and MAPE of 0.77%. The response plot of the relationship between welding speed and the weld bead root radius r_e is shown in Figure 11e, and the relationship between trajectory length and the weld bead root radius r_e is shown in Figure 11f, with the following error metrics: an MAE of 0.2396 mm, an MSE of 0.0052 mm, and an MAPE of 2.34%, which are higher than those for the other geometrical parameters, but still acceptable. The response plot of the relationship between welding speed and weld bead width w_1 is shown in Figure 11i, and the relationship between trajectory length and weld bead width w_1 is shown in Figure 11j. For simplicity, the dependence of weld bead width on trajectory length and welding speed is shown only for width w_1, with low error metrics of MAE of 0.04 mm, MSE of 0.002 mm, and MAPE of 0.80%. The predictive model for weld width is highly accurate.

5. Conclusions

This study presents a brief overview of the AM process and describes a metal welding process with the experimental setup and equipment for the realization of weld beads using BÖHLER SG2 solid wire. During the welding process, the key welding parameters controlled and monitored by a FANUC robot, such as the robot's trajectory length and welding speed, were varied to ensure consistent and high-quality welds. However, the designs of the visible weld bead lines deposited during the welding process exhibit an irregular weld bead profile that impacts the mechanical properties and structural integrity of a weld, increasing the likelihood of cracking and premature failure under stress and cyclic loading. The shape and size of a weld bead are obviously determined by several factors, including the welding process and specific operational parameters. So, it is important to analyze and improve the weld bead geometry to minimize defects that could lead to premature failure. In fact, the geometrical properties of a weld bead were measured using both a caliper and a microscope for detailed measurements and morphology analysis. Subsequently, mathematical models (like neural networks and SVM) are proposed to create a dependence between the controllable welding input parameters and resulting geometrical weld bead outputs (width, height, length, and radius) for prediction and optimization. These models, using techniques such as support vector machines (SVMs) and artificial neural networks (ANNs), can be a good tool for controlling quality by understanding these input–output relationships. The neural network model is capable of estimating the geometrical properties of the weld bead based on measurements from the caliper and microscope as a faster and general model with the best validation performance, MSE of 0.28546 mm, and highly non-linear relationships. However, the cubic SVM has revealed better performance for geometrical prediction of weld beads with an MSE of 0.000175 mm and efficiency for non-linear dataset mapping, with complex input-to-output relationships in the weld bead application. The SVM model has given better results than the neural

https://doi.org/10.3390/metrology6010018

network for the prediction of all geometrical parameters and dependence on welding speed and trajectory length. In fact, the accuracy of the SVM model is very high, as shown by the difference between predicted and actual values of geometric weld bead characteristics, using the metric error MAE. For example, MAE is ∼0.017 mm for height, ∼0.0017 mm for length, ∼0.04 mm for width, and ∼0.01 mm for radius; these values are extremely small relative to the total size of the bead, signifying a highly reliable model. For future research, the models can be used to predict the geometry and characteristics of multiple layers in a multi-pass weld for an automated and intelligent welding system in WAAM, and can be implemented in welding machines to allow real-time monitoring of the process for the optimization of process parameters in industrial applications. Therefore, other machine learning models can be proposed to identify defects on the weld bead surface.

Author Contributions: Conceptualization, G.L.S., M.P., E.T. and G.T.; methodology, G.L.S., M.P., E.T., T.T.; software, G.L.S.; validation, G.L.S., M.P., E.T., T.T. and Y.S.; formal analysis, G.L.S., M.P., E.T., G.T. and T.T.; investigation, T.T. and G.L.S.; resources, G.T. and T.T.; data curation, E.T., M.P., V.M. and G.L.S.; writing—original draft preparation, G.L.S., E.T. and M.P.; writing—review and editing, G.L.S.; visualization, G.L.S.; supervision, G.T. and Y.S.; project administration, G.T., A.N. and K.P.; funding acquisition, G.T. All authors have read and agreed to the published version of the manuscript.

Funding: This work has been realized with financial support from the European Regional Development Fund within the Operational Programme "Bulgarian national recovery and resilience plan", the procedure for direct provision of grants "Establishing of a network of research higher education institutions in Bulgaria", under the Project BG-RRP-2.004-0005 "Improving the research capacity and quality to achieve international recognition and resilience of TU-Sofia".

Informed Consent Statement: This article does not contain any studies with human participants or animals performed by any of the authors.

Data Availability Statement: The data presented in this study are available upon request from the corresponding authors. The data are not publicly available due to public funding requirements.

Conflicts of Interest: The authors declare no conflicts of interest.

References

1. Sellés Cantó, M.Á.; Sánchez-Caballero, S. *Book of Abstracts from the 10th International Conference on Tribology in Manufacturing Processes and Advanced Surface Engineering*; Trans Tech Publications: Baech, Switzerland, 2024.
2. Rashid, A.B.; Haque, M.; Islam, S.M.; Uddin Labib, K.R.; Chowdhury, P. Breaking boundaries with ceramic matrix composites: A comprehensive overview of materials, manufacturing techniques, transformative applications, recent advancements, and future prospects. *Adv. Mater. Sci. Eng.* **2024**, *2024*, 2112358. [CrossRef]
3. Chakravarthy, P.; Agilan, M.; Neethu, N. *Flux Bounded Tungsten Inert Gas Welding Process: An Introduction*; CRC Press: Boca Raton, FL, USA, 2019.
4. Rahadian, N. Advancements in Welding Technology: A Comprehensive Review of Techniques, Materials, and Applications. *J. PEP Bdg.* **2025**, *2*, 62–110.
5. Singh, S.R.; Khanna, P. Wire arc additive manufacturing (WAAM): A new process to shape engineering materials. *Mater. Today Proc.* **2021**, *44*, 118–128. [CrossRef]
6. Patel, A.; Patel, V.; Bansal, P.; Bhuva, B. Optimization and Performance Analysis of Submerged Arc Welding: Influence of Bead Geometry, Process Parameters, and Heat-Affected Zone-A review. *Int. Res. J. Eng. Technol.* **2025**, *12*, 1012–1015.
7. BİLİR, G.; ŞİMŞİR, M. Investigation of T-Joint Butt Welding of Plain Carbon Steels With Metal Active Gas Welding in Pb Position. *MAS J. Appl. Sci.* **2025**, *10*, 249–258.
8. Mallikarjuna, B.; Reutzel, E.W. Reclamation of intermetallic titanium aluminide aero-engine components using directed energy deposition technology. *Manuf. Rev.* **2022**, *9*, 27. [CrossRef]
9. Iqbal, H. Wire-Arc Additive Manufacturing (WAAM): Investigation of Process Dynamics, Material Insights, and Application Prospects. Ph.D. Thesis, Università di Bologna, Bologna, Italy, 2025.
10. Jadhav, S.; Kusekar, S.; Belure, A.; Digole, S.; Mali, A.; Cheepu, M.; Mugale, M.; Alkunte, S.; Kim, D. Recent Progress and Scientific Challenges in Wire-Arc Additive Manufacturing of Metallic Multi-Material Structures. *J. Manuf. Mater. Process.* **2025**, *9*, 284. [CrossRef]

11. Kerber, E.; Knitt, H.; Fahrendholz-Heiermann, J.L.; Ergin, E.; Brell-Cokcan, S.; Dewald, P.; Sharma, R.; Reisgen, U. Variable layer heights in wire arc additive manufacturing and WAAM information models. *Machines* **2024**, *12*, 432. [CrossRef]
12. Lambiase, F.; Yanala, P.B.; Pace, F.; Andreucci, E.; Paoletti, A. A state of the art review of wire arc additive manufacturing (WAAM)—Part 1: Process fundamentals, parameters and materials. *Int. J. Adv. Manuf. Technol.* **2025**, *138*, 4965–4993. [CrossRef]
13. Ozaner, O.C.; Talemi, R.; Tjahjowidodo, T.; Sharma, A. The influence of the wire and arc additive manufacturing parameters on the surface irregularities. *J. Micromanuf.* **2025**, *8*, 22–31. [CrossRef]
14. Fan, H.; Zhou, P.; Li, J.; Huang, J.; Ni, Y.; Hui, Y. Microstructure and mechanical properties of arc zone and laser zone of TC4 titanium alloy laser–TIG hybrid welded joint. *Metals* **2022**, *12*, 1854. [CrossRef]
15. Ehlen, G.; Ludwig, A.; Sahm, P.R. Simulation of time-dependent pool shape during laser spot welding: Transient effects. *Metall. Mater. Trans. A* **2003**, *34*, 2947–2961. [CrossRef]
16. Ai, Y.; Liu, X.; Huang, Y.; Yu, L. Numerical analysis of the influence of molten pool instability on the weld formation during the high speed fiber laser welding. *Int. J. Heat Mass Transf.* **2020**, *160*, 120103. [CrossRef]
17. Wang, J.; Li, J.; Liu, Z.; Liu, X.; Li, Z.; Zhan, X. Experimental and numerical analysis of molten pool dynamics in adjustable ring-mode laser welding of TC4 titanium alloys. *Int. J. Therm. Sci.* **2026**, *222*, 110548. [CrossRef]
18. Guo, K.; Tang, F.; Jia, H.; Zhao, W.; Wei, Y. Study on the influence of ring power ratio on heat flow behavior and solidification characteristics of the molten pool during ring-mode laser welding of aluminum alloy. *Int. J. Therm. Sci.* **2026**, *222*, 110584. [CrossRef]
19. Kumar, B.; Bag, S. Phase transformation effect in distortion and residual stress of thin-sheet laser welded Ti-alloy. *Opt. Lasers Eng.* **2019**, *122*, 209–224. [CrossRef]
20. Meena, P.; Anant, R. Residual stress formation and distortion in austenitic AISI304 steel pipe weldment with consideration of latent heat using novel prescribed weld temperature. *J. Mater. Eng. Perform.* **2025**, *34*, 5933–5949. [CrossRef]
21. Gupta, D.K.; Mulik, R.S. Selection of Process Parameters and its Effect on Bead Geometry, Mechanical Properties, and Microstructure of Inconel 825 Fabricated Using Wire Arc Additive Manufacturing. *Met. Mater. Int.* **2025**, *31*, 3744–3760. [CrossRef]
22. Yildirim, M.S.; Ayhan, E.; Aydin, K.; Durgutlu, A. The effect of welding parameters on weld bead geometry in gas tungsten arc welding applications by response surface methodology model. *Proc. Inst. Mech. Eng. Part E J. Process Mech. Eng.* **2025**, 09544089251364992. [CrossRef]
23. Cho, Y.H.; Shehryar Khan, M.; Goodwin, F.E.; Zhou, Y.N. Effect of torch angle and position on bead geometry and joint strength during arc brazing of thin-gauge dual-phase steel. *Int. J. Adv. Manuf. Technol.* **2022**, *121*, 543–557. [CrossRef]
24. Khrais, S.; Al Hmoud, H.; Abdel Al, A.; Darabseh, T. Impact of gas metal arc welding parameters on bead geometry and material distortion of AISI 316L. *J. Manuf. Mater. Process.* **2023**, *7*, 123. [CrossRef]
25. Roshan, R.; Kumar Naik, A.; Kumar Saxena, K.; Arora, K.S.; Shajan, N.; Msomi, V.; Mehdi, H. Effect of welding speed and wire feed rate on arc characteristics, weld bead and microstructure in standard and pulsed gas metal arc welding. *J. Adhes. Sci. Technol.* **2023**, *37*, 3297–3314. [CrossRef]
26. Li, X.; Chen, J.; Wang, Y.; Shi, L.; Wu, D.; Wu, C. Grain morphology characteristics and formation mechanism of wire-arc additive manufactured 316L stainless steel. *Int. J. Therm. Sci.* **2026**, *221*, 110445. [CrossRef]
27. Arana, M.; Ukar, E.; Rodriguez, I.; Aguilar, D.; Alvarez, P. Influence of deposition strategy and heat treatment on mechanical properties and microstructure of 2319 aluminium WAAM components. *Mater. Des.* **2022**, *221*, 110974. [CrossRef]
28. Ty, A.; Balcaen, Y.; Mokhtari, M.; Alexis, J. Influence of deposit and process parameters on microstructure and mechanical properties of Ti6Al4V obtained by DED-W (PAW). *J. Mater. Res. Technol.* **2022**, *18*, 2853–2869. [CrossRef]
29. Wang, J.; Lin, X.; Li, J.; Hu, Y.; Zhou, Y.; Wang, C.; Li, Q.; Huang, W. Effects of deposition strategies on macro/microstructure and mechanical properties of wire and arc additive manufactured Ti6Al4V. *Mater. Sci. Eng. A* **2019**, *754*, 735–749. [CrossRef]
30. So, M.S.; Mahdi, M.M.; Kim, D.B.; Shin, J.H. Prediction of Metal Additively Manufactured Bead Geometry Using Deep Neural Network. *Sensors* **2024**, *24*, 6250. [CrossRef]
31. Singh, V.P.; Kuriachen, B.; Mahesh, V.; Harursampath, D. Tungsten and Metal Inert Gas Welding: Automation in Welding. In *Advanced Welding Techniques*; CRC Press: Boca Raton, FL, USA, 2024; pp. 136–152.
32. Mu, H.; Polden, J.; Li, Y.; He, F.; Xia, C.; Pan, Z. Layer-by-layer model-based adaptive control for wire arc additive manufacturing of thin-wall structures. *J. Intell. Manuf.* **2022**, *33*, 1165–1180. [CrossRef]
33. Prasad, C.D.; Tiwari, A.; Suryawanshi, S.R.; Dileep, B.; Gowda, A.C.; Masum, H.; Dutt, K.M.; Sunil Prashanth Kumar, S.; Bavan, S. Overview of thermal spray coating on additive manufacturing. *Prog. Addit. Manuf.* **2025**, *10*, 4327–4347. [CrossRef]
34. Ashokkumar, M.; Thirumalaikumarasamy, D.; Sonar, T.; Deepak, S.; Vignesh, P.; Anbarasu, M. An overview of cold spray coating in additive manufacturing, component repairing and other engineering applications. *J. Mech. Behav. Mater.* **2022**, *31*, 514–534. [CrossRef]
35. Dananjaya, V.; Marimuthu, S.; Yang, R.; Grace, A.N.; Abeykoon, C. Synthesis, properties, applications, 3D printing and machine learning of graphene quantum dots in polymer nanocomposites. *Prog. Mater. Sci.* **2024**, *144*, 101282. [CrossRef]

36. Xiong, J.; Zhang, G.; Gao, H.; Wu, L. Modeling of bead section profile and overlapping beads with experimental validation for robotic GMAW-based rapid manufacturing. *Robot. Comput.-Integr. Manuf.* **2013**, *29*, 417–423. [CrossRef]
37. Le-Hong, T.; Lin, P.C.; Chen, J.Z.; Pham, T.D.Q.; Van Tran, X. Data-driven models for predictions of geometric characteristics of bead fabricated by selective laser melting. *J. Intell. Manuf.* **2023**, *34*, 1241–1257. [CrossRef]
38. Chen, Z.; Yuan, L.; Pan, Z.; Zhu, H.; Ma, N.; Ding, D.; Li, H. A comprehensive review and future perspectives of simulation approaches in wire arc additive manufacturing (WAAM). *Int. J. Extrem. Manuf.* **2025**, *7*, 022016. [CrossRef]
39. Feng, G.; Wang, H.; Wang, Y.; Deng, D.; Zhang, J. Numerical simulation of residual stress and deformation in wire arc additive manufacturing. *Crystals* **2022**, *12*, 803. [CrossRef]
40. Gupta, D.K.; Mulik, R.S. Numerical simulation and experimental investigation of temperature distribution during the wire arc additive manufacturing (WAAM) process. *Prog. Addit. Manuf.* **2025**, *10*, 631–645. [CrossRef]
41. Yao, G.R.; Chang, C.; Cox, S.C.; Zhang, X.F.; Yang, C.; Li, X.Q.; Liu, M.; Song, B.; Cui, Z.Q.; Yin, S.; et al. Establishing the intrinsic connection between microstructure, 3D defects, and the corrosion behavior of selective laser melted WE43 alloys: G.-R. Yao et al. *Rare Met.* **2025**, *44*, 9217–9234. [CrossRef]
42. Karouanas, I.; Foteinopoulos, P.; Bikas, H.; Stavropoulos, P. A practical simulation approach for the support of wire arc DED additive manufacturing systems design. *Procedia Comput. Sci.* **2024**, *232*, 3161–3172. [CrossRef]
43. Sitharaj, A.; Balasubramanian, A.; Sivanraju, R. Artificial Intelligence in Wire Arc Additive Manufacturing: A Systematic Review and Patent Landscape Analysis. *Eng. Rep.* **2025**, *7*, e70518. [CrossRef]
44. Bănică, C.F.; Sover, A.; Anghel, D.C. Printing the future layer by layer: A comprehensive exploration of additive manufacturing in the era of industry 4.0. *Appl. Sci.* **2024**, *14*, 9919. [CrossRef]
45. Lehmann, T.; Rose, D.; Ranjbar, E.; Ghasri-Khouzani, M.; Tavakoli, M.; Henein, H.; Wolfe, T.; Jawad Qureshi, A. Large-scale metal additive manufacturing: A holistic review of the state of the art and challenges. *Int. Mater. Rev.* **2022**, *67*, 410–459. [CrossRef]
46. Zhang, W.; Xu, C.; Li, C.; Wu, S. Advances in ultrasonic-assisted directed energy deposition (DED) for metal additive manufacturing. *Crystals* **2024**, *14*, 114. [CrossRef]
47. Pramanik, D.; Roy, N.; Das, R.K.; Das, S.; Das, S. Optimisation of Metal Active Gas Welding on Mild Steel Using Response Surface Methodology. *Int. J. Eng. Inf. Manag.* **2025**, *1*, 55–66. [CrossRef]
48. Casalino, G.; Karamimoghadam, M.; Contuzzi, N. Metal wire additive manufacturing: A comparison between arc laser and laser/arc heat sources. *Inventions* **2023**, *8*, 52. [CrossRef]
49. Das, D.; Mitra, J.; Khan, S.; Roy, B.S. A comparative experimental study on metal active gas welding process at low temperature and room temperature. *Proc. Inst. Mech. Eng. Part E J. Process Mech. Eng.* **2025**, 09544089251364577. [CrossRef]
50. Lin, T.C. *Experimental Study on Laser Additive Manufacturing of Metal Matrix Nanocomposite*; University of California: Los Angeles, CA, USA, 2018.
51. Atwater, M.A.; Guevara, L.N.; Darling, K.A.; Tschopp, M.A. Solid state porous metal production: A review of the capabilities, characteristics, and challenges. *Adv. Eng. Mater.* **2018**, *20*, 1700766. [CrossRef]
52. Prabhakar, D.; Shettigar, A.K.; Herbert, M.A.; GC, M.P.; Pimenov, D.Y.; Giasin, K.; Prakash, C. A comprehensive review of friction stir techniques in structural materials and alloys: Challenges and trends. *J. Mater. Res. Technol.* **2022**, *20*, 3025–3060. [CrossRef]
53. Qiao, Q.; Tam, C.W.; Guo, D.; Qian, H.; Lin, Y.; Li, Z.; Tam, L.M. In situ monitoring of temperature, force and torque in additive friction stir deposition of AA6061: Effect of rotational driving mode. *Mater. Charact.* **2025**, *227*, 115326. [CrossRef]
54. Su, H.; Wu, C.S.; Pittner, A.; Rethmeier, M. Simultaneous measurement of tool torque, traverse force and axial force in friction stir welding. *J. Manuf. Process.* **2013**, *15*, 495–500. [CrossRef]
55. Ahmed, M.M.; El-Sayed Seleman, M.M.; Elfishawy, E.; Alzahrani, B.; Touileb, K.; Habba, M.I. The effect of temper condition and feeding speed on the additive manufacturing of AA2011 parts using friction stir deposition. *Materials* **2021**, *14*, 6396. [CrossRef] [PubMed]
56. Mugada, K.K.; Adepu, K. Material flow and mechanical properties of friction stir welded Al-Mg-Si alloy: Role of concentric circles shoulder with non-circular pins. *Proc. Inst. Mech. Eng. Part C J. Mech. Eng. Sci.* **2021**, *235*, 5487–5499. [CrossRef]
57. Yasa, E.; Poyraz, O.; Molyneux, A.; Sharman, A.; Bilgin, G.M.; Hughes, J. Systematic review on additive friction stir deposition: materials, processes, monitoring and modelling. *Inventions* **2024**, *9*, 116. [CrossRef]
58. Li, X.; Li, X.; Hu, S.; Liu, Y.; Ma, D. Additive friction stir deposition: A review on processes, parameters, characteristics, and applications. *Int. J. Adv. Manuf. Technol.* **2024**, *133*, 1111–1128. [CrossRef]
59. Oladunni, O.J.; Lee, C.K.; Ibrahim, I.D.; Olanrewaju, O.A. Advances in sustainable additive manufacturing: A systematic review for construction industry to mitigate greenhouse gas emissions. *Front. Built Environ.* **2025**, *11*, 1535626. [CrossRef]
60. Li, M.; Du, W.; Elwany, A.; Pei, Z.; Ma, C. Metal binder jetting additive manufacturing: A literature review. *J. Manuf. Sci. Eng.* **2020**, *142*, 090801. [CrossRef]
61. Meenashisundaram, G.; Kumar, Z.; Xu, M.; Nai, S.; Lu, J.; Sheuan Ten, J. Binder jetting additive manufacturing of high porosity 316L stainless steel metal foams. *Materials* **2020**, *13*, 3744. [CrossRef]

62. Brika, S.E.; Letenneur, M.; Dion, C.A.; Brailovski, V. Influence of particle morphology and size distribution on the powder flowability and laser powder bed fusion manufacturability of Ti-6Al-4V alloy. *Addit. Manuf.* **2020**, *31*, 100929. [CrossRef]
63. Gibson, I.; Rosen, D.W.; Stucker, B. Sheet lamination processes. In *Additive Manufacturing Technologies: Rapid Prototyping to Direct Digital Manufacturing*; Springer: Boston, MA, USA, 2010; pp. 223–252.
64. Pilipović, A. Sheet lamination. In *Polymers for 3D Printing*; William Andrew Publishing: Norwich, NY, USA, 2022; pp. 127–136.
65. Haddad, M.; Nixon, K.B.; Wolff, S. Sheet Lamination. In *Springer Handbook of Additive Manufacturing*; Springer International Publishing: Cham, Switzerland, 2023; pp. 407–423.
66. Ladani, L.; Sadeghilaridjani, M. Review of powder bed fusion additive manufacturing for metals. *Metals* **2021**, *11*, 1391. [CrossRef]
67. King, W.E.; Anderson, A.T.; Ferencz, R.M.; Hodge, N.E.; Kamath, C.; Khairallah, S.A.; Rubenchik, A.M. Laser powder bed fusion additive manufacturing of metals; physics, computational, and materials challenges. *Appl. Phys. Rev.* **2015**, *2*, 041304. [CrossRef]
68. Bhavar, V.; Kattire, P.; Patil, V.; Khot, S.; Gujar, K.; Singh, R. A review on powder bed fusion technology of metal additive manufacturing. In *Additive Manufacturing Handbook*; CRC Press: Boca Raton, FL, USA, 2017; pp. 251–253.
69. Trapp, J.; Rubenchik, A.M.; Guss, G.; Matthews, M.J. In situ absorptivity measurements of metallic powders during laser powder-bed fusion additive manufacturing. *Appl. Mater. Today* **2017**, *9*, 341–349. [CrossRef]
70. Dejene, N.D.; Lemu, H.G. Current status and challenges of powder bed fusion-based metal additive manufacturing: Literature review. *Metals* **2023**, *13*, 424. [CrossRef]
71. Bidulsky, R.; Gobber, F.S.; Bidulska, J.; Ceroni, M.; Kvackaj, T.; Grande, M.A. Coated metal powders for laser powder bed fusion (L-PBF) processing: A review. *Metals* **2021**, *11*, 1831. [CrossRef]
72. Nagalingam, A.P.; Shamir, M.; Tureyen, E.B.; Sharman, A.R.C.; Poyraz, O.; Yasa, E.; Hughes, J. Recent progress in wire-arc and wire-laser directed energy deposition (DED) of titanium and aluminium alloys. *Int. J. Adv. Manuf. Technol.* **2025**, *136*, 2035–2073. [CrossRef]
73. Costello, S.C.; Cunningham, C.R.; Xu, F.; Shokrani, A.; Dhokia, V.; Newman, S.T. The state-of-the-art of wire arc directed energy deposition (WA-DED) as an additive manufacturing process for large metallic component manufacture. *Int. J. Comput. Integr. Manuf.* **2023**, *36*, 469–510. [CrossRef]
74. Ahn, D.G. Directed energy deposition (DED) process: State of the art. *Int. J. Precis. Eng. Manuf.-Green Technol.* **2021**, *8*, 703–742. [CrossRef]
75. Ugla, A.; Khaudair, H.J.; Almusawi, A.R. Metal inert gas welding-based-shaped metal deposition in additive layered manufacturing: A review. *Int. J. Mech. Mater. Eng.* **2019**, *13*, 3.
76. Nabi, S.; Rathee, S.; Wani, M.; Srivastava, M. Wire Arc Additive Manufacturing through GMAW Route. In *Wire Arc Additive Manufacturing*; CRC Press: Boca Raton, FL, USA, 2024; pp. 54–70.
77. Derekar, K.S.; Addison, A.; Joshi, S.S.; Zhang, X.; Lawrence, J.; Xu, L.; Melton, G.; Griffiths, D. Effect of pulsed metal inert gas (pulsed-MIG) and cold metal transfer (CMT) techniques on hydrogen dissolution in wire arc additive manufacturing (WAAM) of aluminium. *Int. J. Adv. Manuf. Technol.* **2020**, *107*, 311–331. [CrossRef]
78. Sivakumar, M.; Balaji, N.; Kannan, G.R.; Karthikeyan, R. Directed Energy Deposition (DED) Process. In *Advances in Additive Manufacturing*; Scrivener Publishing LLC: Beverly, MS, USA, 2024; pp. 39–60.
79. Bhuvanesh Kumar, M.; Justus Panicker, C.; Arivazhagan, D. Technologies for Additive Manufacturing of Metals and Their Classification. In *Metal Additive Manufacturing: Principles, Techniques and Applications*; Scrivener Publishing LLC: Beverly, MS, USA, 2025; pp. 1–26.
80. Morshed-Behbahani, K.; Nasiri, A. Corrosion response of steels fabricated through arc directed energy deposition additive manufacturing: A review. *Mater. Horiz.* **2024**, *11*, 3011–3037. [CrossRef] [PubMed]
81. Chen, J.; Chen, B. Progress in additive manufacturing of magnesium alloys: A review. *Materials* **2024**, *17*, 3851. [CrossRef]
82. Mishra, S.K.; P. R, S.; Sajin Jose, S.S.; Upadhyay, R.K. Wire arc additive manufacturing: Materials, processes and its constraints. *Mater. Manuf. Process.* **2025**, *40*, 723–740. [CrossRef]
83. Kowshik, A.S. Influence of Welding Process on Geometry of WAAM Components. Master's Thesis, University West, Department of Engineering Science, Trollhättan, Sweden, 2025.
84. Lone, S.F.; Rathod, D.W.; Nazir Ahmad, S. Impact of Cold Metal Transfer and Pulse Multicontrol Heat Inputs on SS316L Wire Arc Additively Manufactured Built-Up Properties and Performance. *J. Eng. Mater. Technol.* **2026**, *148*, 011004. [CrossRef]
85. Li, X.; Liu, J.; Wu, H.; Miao, K.; Wu, H.; Li, R.; Liu, C.; Fang, W.; Fan, G. Research progress of residual stress measurement methods. *Heliyon* **2024**, *10*, e28348. [CrossRef]
86. Yang, Z.; Dong, S.; Zhang, Y. Particle packing optimization and pore structure assessment of ternary cementitious system based on X-ray computed tomography and mercury intrusion porosimetry. *Constr. Build. Mater.* **2024**, *413*, 134913. [CrossRef]
87. Omiyale, B.O.; Jack, T.A.; Ogedengbe, I.I.; Odeyemi, J.; Mishra, D.; Ogbeyemi, A.; Zhang, W.C. Impact of cold metal transfer variants on the mechanical and microstructural properties of aluminum alloys in wire arc additive manufacturing: A critical review. *Int. J. Adv. Manuf. Technol.* **2025**, *140*, 1183–1210. [CrossRef]

88. Cui, B.; Zhou, P.; Lv, Y. Research Progress in and Defect Improvement Measures for Laser Cladding. *Materials* **2025**, *18*, 3206. [CrossRef]
89. Valcarcel, A.F.; Stevens, C.L.; O'Callaghan, J.M.; Suanda, S.H. Overlapping turbulent boundary layers in an energetic coastal sea. *Ocean Sci.* **2025**, *21*, 965–987. [CrossRef]
90. Imran, M.M.; Che Idris, A.; De Silva, L.C.; Kim, Y.B.; Abas, P.E. Advancements in 3D printing: Directed energy deposition techniques, defect analysis, and quality monitoring. *Technologies* **2024**, *12*, 86. [CrossRef]
91. Prakash, V.J. *Automated Process Planning for Additive Manufacturing with Directed Energy Deposition*; Springer: Cham, Switzerland, 2025.
92. Chaurasia, P.K.; Fabry, Ç.; Pittner, A.; De, A.; Rethmeier, M. Automated in situ monitoring and analysis of process signatures and build profiles during wire arc directed energy deposition. *Prog. Addit. Manuf.* **2025**, *11*, 39–58. [CrossRef]
93. BÖHLER. BÖHLER, 2024. Available online: https://aipweldingsupplies.co.uk (accessed on 5 February 2026).
94. Omajene, J.E.; Martikainen, J.; Kah, P. Effect of welding parameters on weld bead shape for welds done underwater. *Int. J. Mech. Eng. Appl.* **2015**, *2*, 128–134.
95. Han, S.W.; Yoo, H.; Shin, S.; Kim, H.; Lee, G.; Jeon, J.; Han, S.; Cho, J. Parameter optimization of WAAM with pulsed GMAW for manufacturing propeller-shaped blade. *Int. J. Precis. Eng. Manuf.* **2023**, *24*, 1103–1110. [CrossRef]
96. Połaski, P.; Golański, D.; Kołodziejczak, P.; Pakuła, A. Effect of the Electrode Extension on the Geometry of Parts Made of 316LSi Steel by Wire Arc Additive Manufacturing Method. *Adv. Sci. Technol. Res. J.* **2024**, *18*, 343–359. [CrossRef]
97. Babu, N.K.; Talari, M.K.; Srirangam, P.; AlFaify, A.Y.; Rehman, A.U. Characterization of microstructure, weld heat input, and mechanical properties of Mg–Al–Zn alloy GTA weldments. *Appl. Sci.* **2022**, *12*, 4417. [CrossRef]
98. Hao, H.; Ni, D.; Huang, H.; Wang, D.; Xiao, B.; Nie, Z.; Ma, Z. Effect of welding parameters on microstructure and mechanical properties of friction stir welded Al–Mg–Er alloy. *Mater. Sci. Eng. A* **2013**, *559*, 889–896. [CrossRef]
99. Liu, J.; Nie, Y.; Feng, Q.; Liang, X.; Lei, H.; Niu, S.; Lou, M. Influence of Welding Speed on the Microstructure and Mechanical Properties of Laser-Welded Joints in 316L Stainless Steel Sheets. *Metals* **2025**, *15*, 624. [CrossRef]
100. Kshirsagar, R.; Jones, S.; Lawrence, J.; Tabor, J. Prediction of bead geometry using a two-stage SVM–ANN algorithm for automated tungsten inert gas (TIG) welds. *J. Manuf. Mater. Process.* **2019**, *3*, 39. [CrossRef]

Disclaimer/Publisher's Note: The statements, opinions and data contained in all publications are solely those of the individual author(s) and contributor(s) and not of MDPI and/or the editor(s). MDPI and/or the editor(s) disclaim responsibility for any injury to people or property resulting from any ideas, methods, instructions or products referred to in the content.

metrology

MDPI

Article

Uncertainty Evaluation of CMM and Optical 3D Scanning in Centrifugal Rotor Inspection

Ionuț-Alin Dumitrache [1,2,*], Andrei George Totu [1], Ana-Maria Dumitrache [3] and Mihai Vlăduț [1]

[1] Romanian Research and Development Institute for Gas Turbines—COMOTI, 061103 Bucharest, Romania; andrei.totu@comoti.ro (A.G.T.); mihai.vladut@comoti.ro (M.V.)
[2] Doctoral School of Industrial Engineering and Robotics, POLITEHNICA, 060042 Bucharest, Romania
[3] Automotive Engineering Department, Faculty of Transports, POLITEHNICA, 060042 Bucharest, Romania; ana_maria.manea1108@upb.ro
* Correspondence: alin.dumitrache@comoti.ro

Abstract

Dimensional verification of turbomachinery rotors requires traceable accuracy on functional data and dense coverage of freeform blades. This study quantifies the expanded measurement uncertainty (U95) for a centrifugal rotor inspected with a bridge-type CMM (Nikon Altera 10.10.8) and a structured-light scanner (ATOS Compact Scan 5M Rev.1), using repeated measurements in accordance with ISO 10360 and ISO 15530-3. The CMM achieved U95 ≈ 4–6 µm on bores, whereas optical scanning yielded U95 ≈ 12–18 µm on freeform blade regions. Cross-system results exhibited systematic offsets, indicating that the two methods are not directly interchangeable in absolute terms. Nevertheless, they are complementary: CMM ensures datum traceability, while optical scanning enables rapid full-field blade assessment, supporting uncertainty-aware hybrid inspection.

Keywords: CMM; structured-light scanning; measurement uncertainty; ISO 15530-3; ISO 10360; turbomachinery inspection; centrifugal rotor; freeform surfaces; hybrid metrology

1. Introduction

Dimensional verification of complex components is a must in order to ensure product quality, functional performance, and safety across sectors such as aerospace, energy, and micromechanics. With increasing demands for miniaturization and tighter tolerances, the ability to characterize both functional datums data and intricate freeform geometries has become a central challenge in quality control. Among the available technologies, coordinate measuring machines (CMMs) and optical 3D scanners represent two complementary approaches [1,2]. However, for parts featuring both datum-based functional features (e.g., planes and bores) and complex freeform blade surfaces, experimental evidence under controlled conditions remains limited with respect to expanded measurement uncertainty and cross-system agreement. This gap complicates uncertainty-aware selection and deployment of measurement systems in hybrid inspection workflows.

CMMs remain the benchmark for dimensional verification because they provide traceable, high-accuracy measurements of datums and functional features (e.g., planes, bores, and other primitives) that are directly relevant to assembly and performance [3]. However, for micro gas turbine rotors that combine datum-driven functional features with complex freeform blade surfaces, controlled and uncertainty-quantified comparisons between tactile CMM and structured-light inspection remain limited, which complicates the selection and validation of hybrid inspection strategies in practice. In operational settings, the

relatively low acquisition speed of CMMs and the typically sparse nature of tactile sampling can reduce efficiency and representativeness when characterizing freeform surfaces requiring dense spatial information [4]. Optical 3D scanners mitigate these constraints by rapidly capturing dense surface point clouds and enabling full-field assessment of freeform regions [5], but their metrological performance is more dependent on surface properties (reflectivity and texture), ambient conditions, and calibration and alignment strategies, which often leads to higher and less predictable uncertainty levels than tactile probing [6,7]. For this reason, the reliable determination of measurement uncertainty becomes a cornerstone of quality control when deciding how to verify different feature types and when reconciling datasets within hybrid workflows: for CMMs, uncertainty evaluation is commonly addressed through design-of-experiments approaches [8], Monte Carlo-based propagation and simulation frameworks [4], and ISO-compliant procedures [9], whereas for optical systems, uncertainty-related developments include improved calibration models [7], standardized performance assessment of portable scanners [8], and digital twin-enabled error mapping to capture spatially varying deviations [10]. Despite these methodological advances, like-for-like experimental evidence reporting expanded uncertainty and cross-system agreement on representative turbomachinery rotors remains scarce, motivating systematic evaluation under well-defined conditions.

Recent research has highlighted this complementarity. Altinisik and Bolova [11] compared laser scanning and CMMs, concluding that non-contact methods improve efficiency but require stricter calibration. Sato et al. [12] proposed robust experimental design methods to reduce CMM variability, while Chen et al. [13] demonstrated the advantages of multi-sensor fusion in surface geometry inspection. Kortaberria et al. [14] reinforced the importance of uncertainty-aware analysis for dense point clouds, aligning with ISO 15530-3 and ISO 15530-4 to ensure traceability. Collectively, these studies support hybrid inspection, yet they also indicate that feature-level, uncertainty-quantified comparisons on real rotors remain underrepresented, particularly when both datums (e.g., planes, bores) and freeform blades must be assessed within the same verification workflow.

Standards and guidelines play a decisive role in these efforts. The ISO 10360 series define acceptance and reverification tests for CMMs [15]. Beyond physical inspection, emerging paradigms such as digital twins [16] and the Guide to the Expression of Uncertainty in Measurement (GUM) [17] with its Monte Carlo supplement [18] establish an international consensus on evaluating and propagating uncertainty. Furthermore, virtual control strategies [19] aim to integrate predictive uncertainty with physical measurements, moving towards predictive quality management. Nonetheless, Vrba et al. [20] emphasize that estimating uncertainty for complex geometries remains practically challenging, with probe configuration, scanning strategy, and sampling density exerting significant influence.

In practice, implementing uncertainty-aware inspection on real turbomachinery parts remains challenging, particularly when datum verification and dense freeform assessment must be combined within the same workflow. While standards and advanced models provide robust frameworks, their application to real-world components (where tactile and optical data must be reconciled) is still limited. Addressing this gap, the present study experimentally evaluates the measurement uncertainty of a centrifugal micromotor rotor using a bridge-type CMM and a structured-light scanner. Following ISO 10360 [15] and ISO 15530-3 guidelines, repeated measurements are used to quantify expanded uncertainties and compare system performance across features. By clarifying the trade-offs between accuracy, coverage, and efficiency, this study contributes practical evidence for hybrid inspection strategies and supports uncertainty-aware sensor selection in turbomachinery and micromotor manufacturing.

https://doi.org/10.3390/metrology6010012

2. Materials and Methods

2.1. Test Component: Centrifugal Rotor

The test object is a single-stage centrifugal rotor from a micro-turbojet assembly. The rotor operates as the compact air-compression element, delivering an overall pressure ratio $\approx$ 5:1 at rotational speeds up to 80,000 rpm. The engine is configured as an interchangeable quick-change testbed, allowing rapid component swaps (including the rotor) so that the same core can serve both as a propulsion unit and as an instrumented validation platform for alternative designs and control strategies. Program activities encompass gas-dynamic computations, new-part conception and design, start/command/control software development and verification, and component evaluation with additive-manufacturing trials at engine-assembly level, supported by structured instrumentation for operating parameter acquisition and validation of Romanian Research and Development Institute for Gas Turbines COMOTI (www.comoti.ro) redesigns. The target propulsion unit addresses compact aviation (dry mass < 4 kg; thrust $\approx$ 40 daN) while maintaining straightforward rotor integration and enabling rapid, low-downtime iteration across design cycles (Figure 1).

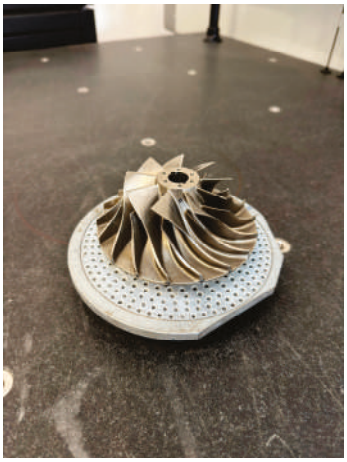


Figure 1. Centrifugal rotor used in this study.

Prior to measurement, the component was stabilized in a controlled laboratory environment (temperature 20 $\pm$ 0.5 °C; relative humidity <50%). The rotor and fixturing were conditioned on the granite for $\geq$2 h before any data acquisition to minimize thermal gradients. Environmental conditions were recorded immediately before and after each acquisition set using a calibrated laboratory thermometer–hygrometer, see Figure 2. In this work, repeatability refers to variability obtained under identical conditions (same system, program, operator, environment and fixturing), i.e., repeated acquisitions without intentionally changing the measurement setup. Reproducibility refers to additional variability introduced by controlled changes between runs (e.g., part removal and re-fixturing/realignment and, where applicable, sensor/probe configuration changes), representative of a realistic inspection workflow within the same laboratory.

All tactile measurements were performed using a Nikon Altera 10.10.8 bridge-type CMM (LK Metrology Ltd., Derby, UK).. The machine provides a measuring volume of 1000 $\times$ 1000 $\times$ 800 mm and a manufacturer-specified MPEE (maximum permissible error for length measurement) of (1.8 + L/350) µm according to ISO 10360-2:2009, where L is the measured length in mm [21]. The system was equipped with a Renishaw TP20 touch-trigger probe mounted on a PH10M PLUS motorized probe head, using a Ø 2 mm ruby stylus. Probe calibration was performed prior to measurement using a certified reference sphere.

https://doi.org/10.3390/metrology6010012



Figure 2. Measurement station environment parameters: calibrated thermometer–hygrometer display.

2.2. Measurement System

The CMM was operated with Camio software (version 2025 1.3.38478), which enabled parametric GD&T inspection and automated feature extraction. The machine underwent full verification according to ISO 10360 [15] procedures before experimentation, ensuring traceable accuracy. Geometric primitives (planes, axes, and cylinders) and datums were defined following standard GD&T practices.

Optical measurements were acquired using an ATOS Compact Scan Rev.1 structured-light scanner (GOM GmbH, Braunschweig, Germany). The scanner features a dual camera stereo configuration with interchangeable lenses and scalable measuring areas ranging from 45×35 mm^2 up to 1200×1000 mm^2, depending on the selected setup [22]. According to the manufacturer, the system achieves point accuracies of up to 0.01 mm, verified by calibration standards. The scanner uses Blue Light Technology to minimize ambient-light sensitivity and includes self-monitoring functions to compensate for environmental variations [22].

The system was calibrated immediately prior to measurement using the certified GOM calibration plate. Immediately after calibration, a verification procedure was performed, confirming that the achieved dimensional deviations and point errors were within the manufacturer-specified accuracy limits ($\leq$0.01 mm). This ensured that the structured-light scanner operated under nominal conditions at the start of the experimental campaign.

Scans were performed using a motorized rotary table to ensure complete surface coverage. Data acquisition and inspection were carried out in Zeiss Inspect (version 2025.3.1.6), which provided meshing, filtering, and GD&T evaluation of the resulting point clouds. Alignment to the CMM coordinate system was performed using a common datum scheme (primary plane A, cylindrical bore B, and secondary locating feature C).

2.3. Measurement Strategy

To ensure comparability between the two quality control systems, a common datum scheme and feature set were defined on the centrifugal micromotor rotor (Figure 3). The scheme was consistent with functional requirements and geometric dimensioning and tolerancing (GD&T) principles:

- Datum A (Primary datum axis): Cylindrical bore (Ø $\approx$ 14.5 mm) defining the shaft interface.
- Datum B (Primary plane): Rear mounting surface, providing the axial reference.
- Datum C (Secondary locating surface): Orthogonal pin bores intersecting datum B, constraining rotation.

https://doi.org/10.3390/metrology6010012

- Freeform blades: Main and splitter impeller airfoils, subdivided into hub, mid-span, and shroud sections, further separated into pressure and suction sides.

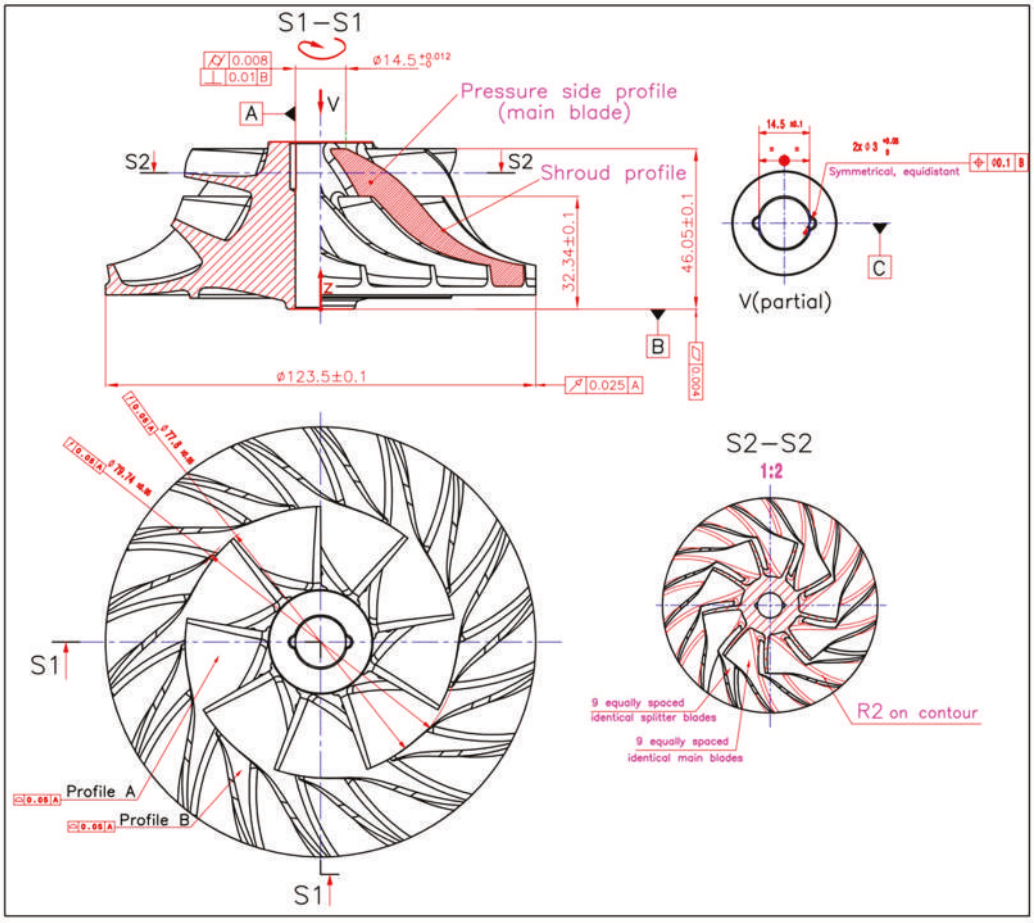


Figure 3. Technical drawing of the centrifugal micromotor rotor highlighting the functional datums (A, B, C) and controlled geometric features selected for measurement.

Measurements were conducted on the Nikon Altera 10.10.8 CMM [21], programmed in Camio software. For each feature, sampling strategies were optimized to balance accuracy and acquisition time:

- Datum A (cylinder): 6 points per cross-section at five axial levels (30 total points), ensuring coverage of diameter repeatability, cylindricity and perpendicularity with respect to datum A.
- Datum B (plane): 12 equidistant points distributed radially across the mounting surface.
- Datum C (Locking bores): Diameters of the two through-holes and their positional relationship to datum B.

Each feature was measured in 10 repeated runs to capture both repeatability and reproducibility contributions. Repeatability was estimated from repeated probing under unchanged conditions (same program and fixturing), whereas reproducibility (within-laboratory) was assessed across runs including part re-fixturing and datum re-establishment between measurements. Two calibrated styli were employed depending on feature accessibility, Ø1 mm × 20 mm and Ø5 mm × 21 mm ruby balls, each mounted with a Renishaw SH25-3 extension. The use of two calibrated styli reflects typical accessibility-driven probing configurations and was treated as a potential contributor to between-run variability when the stylus configuration had to be changed.

https://doi.org/10.3390/metrology6010012

Optical scans were acquired using the ATOS Compact Scan Rev.1 [22] in Zeiss Inspect software. A high-density mesh was generated, with resolution set to 60 points/mm^2 (point spacing $\approx$ 0.08 mm at 300 mm field of view). The scanning strategy involved:

- Full 360° coverage using a rotary table, with additional tilted scans to capture blade shroud edges and undercuts.
- Global alignment reconstructed via the datum scheme (A–B) from best-fit primitives (locking bores C were used only for fixturing, not for uncertainty evaluation).
- Analysis outputs:
  - **Datum A and B evaluation:** Plane flatness, bore diameter, cylindricity, and perpendicularity extracted by primitive fitting.
  - **Blade evaluation:** Global CAD-to-mesh comparison, with deviation flags across hub, mid-span, and shroud.
  - **Blade tip diameters:** Section planes at CAD-defined heights (main and splitter blades).

Unlike CMM, scanner measurements were repeated 10 times with complete re-orientation of the part and re-alignment to the datum scheme, thereby incorporating setup-driven variability into the reproducibility estimate. Repeatability was derived from repeated acquisitions under nominally identical scanner settings and calibration states, while reproducibility reflected the additional scatter introduced by re-positioning/re-alignment steps typical of shop-floor optical inspection (Table 1). This ensures direct comparability between CMM and optical results while maintaining the dense-coverage advantage of structured-light scanning.

Table 1. Measurement scope per system (CMM vs. optical scanner).

Feature/Characteristic	CMM	Optical Scanner	Notes
Datum B—Plane flatness	✓	✓	Repeated n = 10 on CMM and scanner
Datum A—Bore diameter (Ø14.5)	✓	✓	Two CMM strategies (circles vs. lines); scanner via best-fit primitive
Datum A—Cylindricity	✓	✓	Both extracted from fitted bore geometry
Datum B $\perp$ Datum A (perp.)	✓	✓	Relation of bore axis to plane, measurable both ways
Datum C—Locking bore position	✓	✓	Position of 2 auxiliary bores relative to datum A
Datum C—Bore diameter	✓	✓	Direct measurement of small bore diameters
Blade profile deviation	✗	✓	CAD-to-mesh comparison (main + splitter blades)
Blade tip diameters (hub/shroud)	✗	✓	Section planes at specified heights from drawing
Global GD&T alignment (A–B–C)	✓	✓	Common reference system applied for comparability

2.4. Uncertainty Evaluation Procedure

Uncertainty evaluation followed the GUM framework for Type A/Type B components and their combination into an expanded uncertainty, with the experimental design aligned to task-specific good practice from ISO 15530-3 (via recent, ISO-consistent literature) and instrument verification under ISO 10360 [15] for the CMM. The steps and formulas below reference GUM (JCGM 100) and its Monte Carlo supplement (JCGM 101) where applicable [17,18], together with instrument specifications and acceptance testing practices [22] and ISO-consistent task-specific guidance [14].

2.4.1. Measurand and Repeated Observations

Let the measurand **Y** be a scalar characteristic (e.g., diameter of the A datum bore, plane flatness B, or profile deviation on a freeform patch). For each system and feature,

https://doi.org/10.3390/metrology6010012

n = 10 repeated observations $\{y_j\}$ were acquired under the protocol in Section 2.3 (with re-fixturing).

The sample mean and sample standard deviation are:

$$\overline{y} = \frac{1}{n}\sum_{j=1}^{n} y_j,\ s = \sqrt{\frac{1}{n-1}\sum_{j=1}^{n}(y_j - \overline{y})^2} \tag{1}$$

The Type A standard uncertainty for repeatability is

$$u_{rep} = \frac{s}{\sqrt{n}} \tag{2}$$

If a certified reference value y_{ref} is available, the bias is $b = \overline{y} - y_{\text{ref}}$. For the bias-corrected result $yc = \overline{y} - b$, the associated uncertainty is

$$u_b = \sqrt{u_{ref}^2 + \left(\frac{s}{\sqrt{n}}\right)^2} \tag{3}$$

2.4.2. Repeatability vs. Reproducibility Components

Because repetitions include re-fixturing, we separate within-setup and between-setup effects using a random-effects ANOVA (two levels: setup $i = 1, \ldots, a$, replication $j = 1, \ldots, m$, with $n = am$). Denote:

$$\begin{aligned} s^2_{\text{within}} &= \frac{1}{a(m-1)}\sum_{i=1}^{a}\sum_{j=1}^{m}\left(y_{ij} - \overline{y_{i\cdot}}\right)^2, \\ s^2_{\text{between}} &= \frac{m}{a-1}\sum_{i=1}^{a}\left(\overline{y_{i\cdot}} - \overline{y_{\cdot\cdot}}\right)^2 \end{aligned} \tag{4}$$

Then the repeatability standard deviation $s_r = s_{within}$ and the reproducibility (setup) standard deviation is estimated as (non-negative):

$$u_{rep} = \frac{s_r}{\sqrt{n}},\ \ u_{repro} = \frac{s_r}{\sqrt{a}} \tag{5}$$

2.4.3. Type B Components (Systematic)

Type B components are evaluated from specifications, certificates and environmental bounds (GUM §4.3). We include at minimum instrument specification (CMM MPE_E/probing MPE_P): If the instrument's maximum permissible error bound is treated as a rectangular distribution over $[-MPE, +MPE]$, the standard uncertainty is:

$$u_{MPE} = \frac{MPE}{\sqrt{3}} \tag{6}$$

- For length-dependent forms (e.g., $\text{MPE}_E = A + B\,L$), evaluate at the task length L. Reference artifact/certification: Use the stated (expanded) uncertainty U_{ref} and convert to standard uncertainty via the coverage k_{ref}:$u_{\text{ref}} = U_{\text{ref}}/k_{\text{ref}}$ (GUM §6).

Environmental residuals (thermal): For a length L, residual temperature deviation ΔT, and coefficient of thermal expansion α, with rectangular modeling of ΔT over $[-\Delta T_{max}, +\Delta T_{max}]$:

$$u_T = \frac{|\alpha L|\,\Delta T_{max}}{\sqrt{3}} \tag{7}$$

- Alignment/modeling (freeform fitting): If best-fit/alignment steps are used, include a model contribution u_{fit} estimated from residuals on repeated registrations (or via

https://doi.org/10.3390/metrology6010012

leave-one-patch-out resampling); see task-specific ISO-aligned practice for dense point clouds [14].

When applicable, other bounded effects (vibration, residual form filtering, and lens calibration for the scanner) are analogously modeled with appropriate PDFs (rectangular/triangular/normal) per GUM §6 and JCGM 101 §6.

2.4.4. Combining Uncertainty

For uncorrelated input components u_i with sensitivity coefficients c_i (often $c_i = 1$ when the measurand is directly measured), the combined standard uncertainty is as follows (GUM §5):

$$u_c = \sqrt{u_{rep}^2 + u_{repro}^2 + u_{MPE}^2 + u_{ref}^2 + u_T^2 + u_{fit}^2 + \cdots} \tag{8}$$

If correlations exist (e.g., common alignment influences multiple features), include covariance terms:

$$u_c^2 = \sum_i \sum_k c_i c_k \, u_i u_k \, r_{ik} \tag{9}$$

2.4.5. Effective Degrees of Freedom and Coverage Factor

We compute the effective degrees of freedom using the Welch–Satterthwaite formula (GUM Annex G):

$$\nu_{\text{eff}} = \frac{u_c^4}{\sum_i \frac{(c_i u_i)^4}{\nu_i}} \tag{10}$$

where ν_i represents the degrees of freedom of each component (infinite for Type A unless otherwise justified; $n - 1$ or ANOVA-derived for Type B). The expanded uncertainty for approximately 95% coverage is

$$U_{95} = k \, u_c, \; k = t_{0.975,\nu_{\text{eff}}} \approx 2 \; (\nu_{\text{eff}} \gtrsim 30) \tag{11}$$

2.4.6. Cross-System Comparison Metrics

For each feature, we report: (i) bias relative to a reference (if available) or cross-sensor difference of means $\Delta = \overline{y}scan - \overline{y}CMM$, with comparison uncertainty

$$u_\Delta = \sqrt{u_{c,\text{scan}}^2 + u_{c,\text{CMM}}^2} \tag{12}$$

and (ii) agreement via whether $|\Delta| \leq U_{95,\Delta}$. This directly supports uncertainty-aware decisions on GD&T conformity and sensor selection (GUM §7; ISO-consistent practice for task-specific evaluation [14]).

3. Results

The results are presented in two parts: (i) tactile acquisitions performed on the CMM with repeated measurements to assess repeatability and reproducibility, and (ii) optical scanning acquisitions, providing dense point-cloud deviations relative to the CAD model. Both sets of results are structured according to the common datum scheme (A–B–C) and controlled geometric features defined in the technical drawing (Figure 3). In the following, agreement between systems is interpreted on a feature-by-feature basis, recognizing that tactile probing and structured-light scanning may rely on different surface sampling and fitting definitions; therefore, non-agreement for selected form-related characteristics does not imply inadequate scanner performance overall, but rather limited interchangeability for those measurands at the required tolerance level.

For CMM measurements, each feature was measured in 10 independent runs with full re-alignment of the rotor, thus enabling the separation of repeatability (within setup) and

https://doi.org/10.3390/metrology6010012

reproducibility (between setups). The results are summarized in Table 2, while representative measurement screenshots and deviation maps from Camio software are provided in Figures 4–7. This design allows the within-setup scatter (repeatability) to be distinguished from setup-induced variability (within-laboratory reproducibility) relevant to production-like inspection workflows.

Table 2. Raw CMM measurement results for datums A–C (n = 10 repetitions).

Repetition	B—r [mm]	O A l [1] [mm]	j A l [1] [mm]	A l [1]{ A [mm]	O A c [2] [mm]	j A c [2] [mm]	A c [2]{ B [mm]	C1 O [mm]	C2 O [mm]	C1 l [mm]	C2 l [mm]
1	0.0016	14.5062	0.0125	0.0080	14.5062	0.0129	0.0082				
2	0.0016	14.5063	0.0123	0.0080	14.5059	0.0127	0.0085				
3	0.0014	14.5062	0.0122	0.0081	14.5061	0.0126	0.0084				
4	0.0016	14.5063	0.0124	0.0085	14.5063	0.0122	0.0081				
5	0.0016	14.5065	0.0123	0.0083	14.5062	0.0125	0.0085	3.0054	2.9826	0.0261	0.0423
6	0.0016	14.5067	0.0124	0.0081	14.5063	0.0124	0.0082				
7	0.0015	14.5067	0.0122	0.081	14.5064	0.0124	0.0083				
8	0.0016	14.5065	0.0123	0.0033	14.5064	0.0124	0.0079				
9	0.0016	14.5071	0.0123	0.0081	14.5067	0.0125	0.0083				
10	0.0015	14.5066	0.0123	0.0081	14.5064	0.0125	0.0078				

[1] Line measuring method. [2] Circle measuring method.

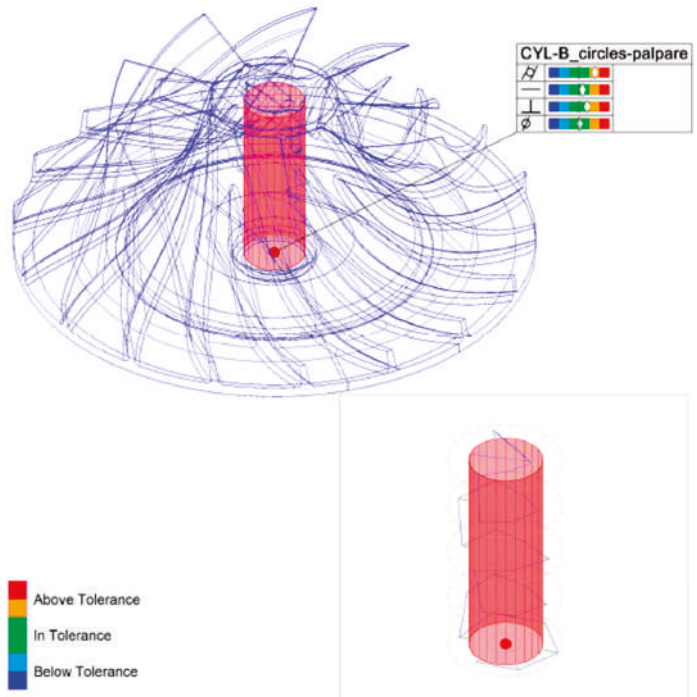


Figure 4. Cylinder datum A evaluation on the CMM using circle-based fitting method.

For optical scanner measurements, the rotor was acquired under identical environmental conditions. A high-density mesh (≈60 points/mm^2, spacing ≈ 0.08 mm) was generated for each acquisition. Unlike CMM, where feature probing can be repeated, the scanner workflow relies on full-surface coverage and best-fit extraction of primitives (planes, cylinders, and bores) and CAD-to-mesh deviation analysis for freeform geometries. Accordingly, for primitive/form characteristics the scanner result depends not only on acquisition but also on the data processing and feature extraction workflow (meshing, filtering, patch selection, and fitting), which may yield feature-dependent biases relative to discrete-point tactile probing. To enable direct comparability with tactile results, the mesh was re-aligned to the same datum scheme (A–B–C) and the entire scan procedure was

https://doi.org/10.3390/metrology6010012

repeated 10 times with complete re-orientation of the part, so that repeatability descriptors could be computed in analogy with CMM. In addition to primitives (data A, B), profile deviations were obtained through global CAD-to-mesh comparison, with local deviation flags placed across hub, mid-span, and shroud regions (Figures 8–11).

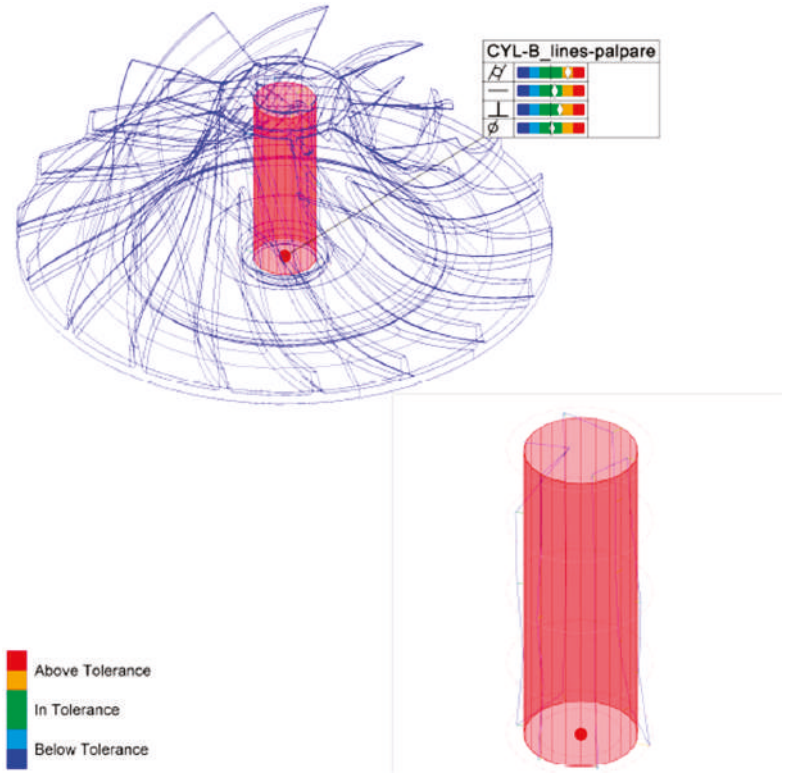


Figure 5. Cylinder datum A evaluation on the CMM using line-based fitting method.

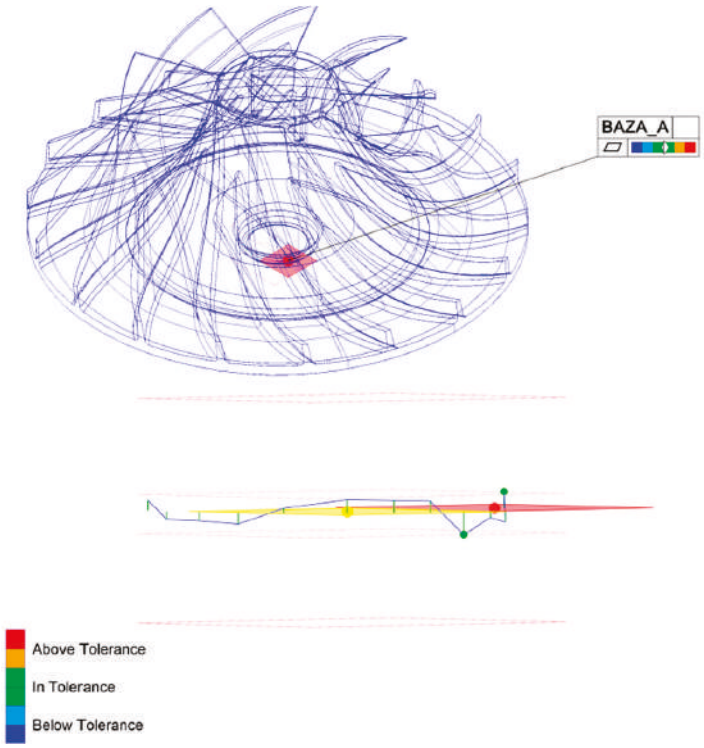


Figure 6. Flatness deviation map for datum B (mounting plane).

https://doi.org/10.3390/metrology6010012

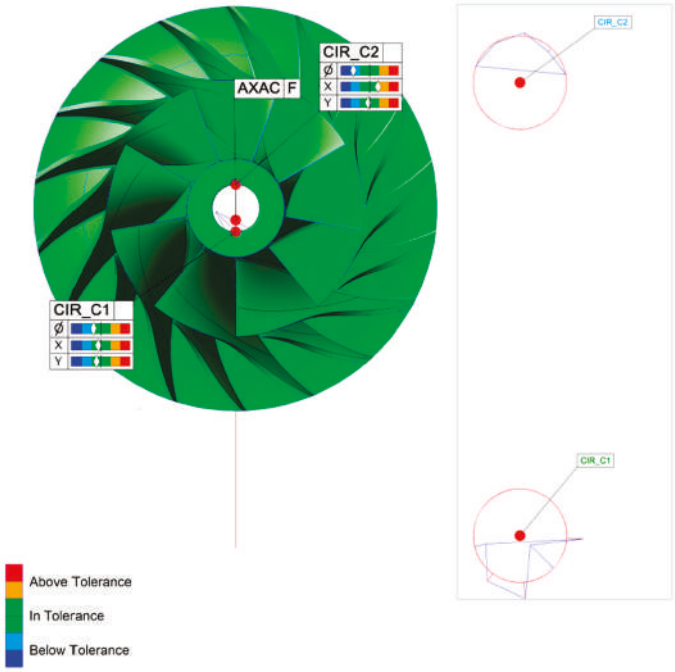


Figure 7. Locking bores (datum C) evaluation showing positional deviation relative to datum B.

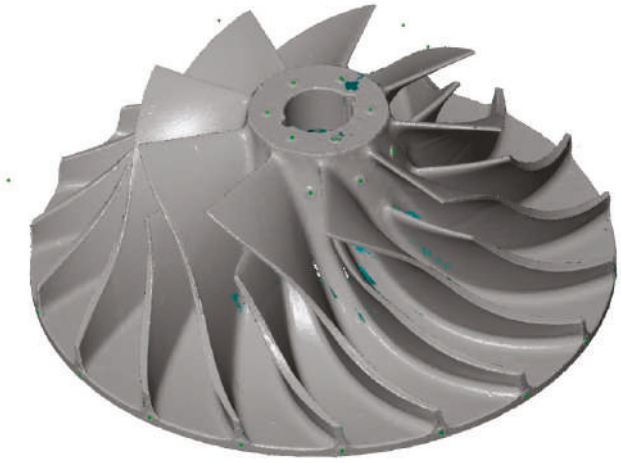


Figure 8. Raw optical scan of the centrifugal micromotor rotor prior to meshing and rendering.

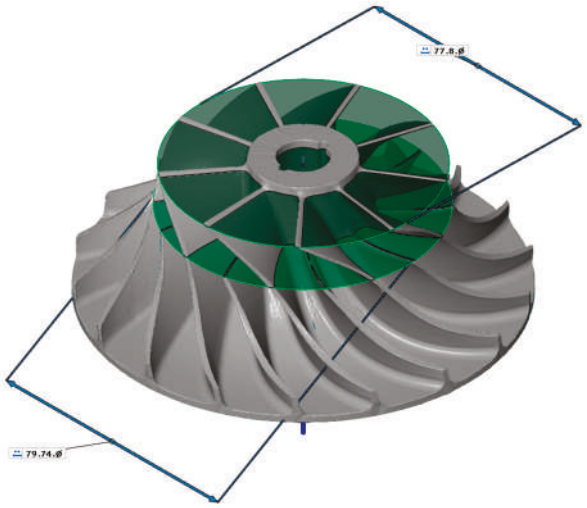


Figure 9. Section-plane evaluation of main and splitter blade tip diameters at CAD-defined heights.

https://doi.org/10.3390/metrology6010012

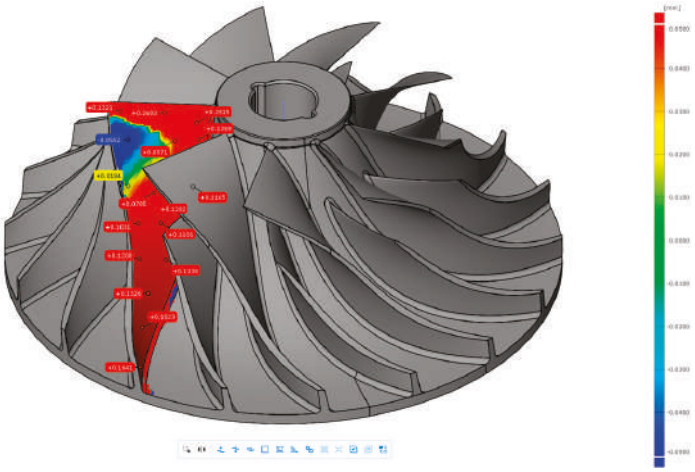


Figure 10. CAD-to-mesh deviation map of the main blade aerofoil.

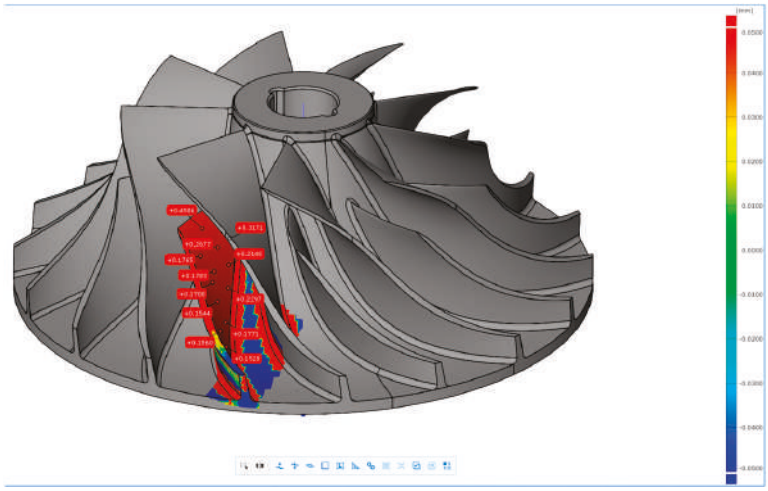


Figure 11. CAD-to-mesh deviation map of the splitter blade aerofoil.

3.1. CMM Measurement Results

The statistical analysis of the CMM acquisitions (Table 3) shows that datum B exhibits excellent stability, with a mean flatness of 1.6 µm and an expanded uncertainty below 0.05 µm, well within functional tolerances for mounting. The bore diameter of datum A (Ø14.5 mm) also proved highly consistent across repetitions, with a standard deviation below 0.3 µm and U95 ≈ 0.18 µm, confirming the high repeatability of the tactile probing strategy. Cylindricity and perpendicularity values, although stable, revealed slightly higher scatter, with expanded uncertainties approaching 0.15 µm, reflecting the sensitivity of these derived characteristics to alignment and probing path selection (line vs. circle method). For the locking bores (datum C), positional deviations were small but reproducibility effects were more pronounced, as expected due to their reduced diameter and deeper probing path. Overall, the tactile system demonstrated repeatability and reproducibility compatible with ISO 10360 [15] acceptance tests, ensuring that subsequent scanner comparisons can be interpreted relative to a traceable tactile baseline with substantially lower uncertainty for datum-related primitives.

https://doi.org/10.3390/metrology6010012

Table 3. Statistical summary of CMM measurements for datums A–B (mean, standard deviation, and uncertainty evaluation).

Feature	Mean [mm]	Std. dev. [mm]	U_{rep} [mm]	U_{95} [mm]
B—r	0.00156	0.0000699206	0.000022111	0.000044222
O A l	14.50651	0.000280674	0.000088757	0.00017751
j A l	0.01232	0.0000918937	0.000029059	0.000058119
A l{ B	0.01495	0.023258081	0.00735485	0.0147097
O A c	14.50629	0.000213177	0.000067412	0.00013482
j A c	0.01251	0.000191195	0.000060461	0.00012092
A c{ B	0.00822	0.000234758	0.000074237	0.00014847

3.2. Optical Scanner Results

The structured-light scanner provided dense point-cloud data, from which primitives corresponding to datums A–B were extracted and compared to the CAD reference. It is important to distinguish between freeform profile deviations, for which dense sampling is advantageous, and high-precision form characteristics on datums (e.g., micro-flatness, cylindricity in deep bores), for which visibility, surface response and fitting choices can dominate the result. Table 4 lists the raw results for 10 repeated acquisitions under full re-orientation of the rotor, while Table 5 summarizes the statistical descriptors (mean, standard deviation, and expanded uncertainty). The flatness of datum B was consistently larger than the CMM values, with a mean of ~48 μm reflecting the combined effect of surface sampling, mesh noise, and the limited suitability of full-field acquisition for micro-flatness evaluation at the few-micrometer level. The bore diameter (datum A) remained close to the nominal 14.5 mm, with sub-0.1 μm repeatability, although the cylindricity values were notably higher (0.14 mm), consistent with the limited visibility of the deep bore in optical acquisition. This behavior is feature-dependent: the diameter extracted from visible edge regions can remain stable, whereas form descriptors (e.g., cylindricity) become strongly sensitive to line-of-sight and partial data.

Table 4. Raw optical scanner measurement results for datums A–C and blade features (n = 10 repetitions).

Repetition	B—r [mm]	O A [mm]	j A [mm]	A { B [mm]	O 77.8 [mm]	^ | A [mm]	O79.74 [mm]	^ | A [mm]	Main Blade h [mm]	Splitter Blade h [mm]
1	0.0482	14.5033	0.1701	0.0107	77.7904	0.0158	79.7147	0.0085	0.2515	0.3527
2	0.0484	14.5032	0.1821	0.0102	77.7886	0.1436	79.7152	0.0091	0.2241	0.2986
3	0.0482	14.5033	0.1706	0.0104	77.7906	0.0986	79.7233	0.0163	0.1997	0.3542
4	0.0481	14.5033	0.1614	0.0105	77.7763	0.0263	79.7621	0.0883	0.2299	0.2886
5	0.0483	14.5033	0.1423	0.0106	77.8093	0.1324	79.7126	0.0860	0.2118	0.2942
6	0.0482	14.5031	0.1213	0.0108	77.7863	0.0322	79.7113	0.0934	0.1955	0.2699
7	0.0482	14.5033	0.0089	0.0107	77.7899	0.0149	79.7217	0.1169	0.2862	0.3122
8	0.0481	14.5032	0.1703	0.0106	77.7864	0.0162	79.7229	0.0899	0.2883	0.3221
9	0.0483	14.5032	0.1642	0.0107	77.7944	0.0122	79.7318	0.0713	0.2314	0.3228
10	0.0481	14.5033	0.1422	0.0109	77.7882	0.0861	79.7139	0.0093	0.2298	0.3125

Perpendicularity between datum A and B showed good stability, with uncertainties on the order of 0.1 μm. In addition to datum features, the scanner enabled the evaluation of functional blade geometries. Section-plane diameters at the main and splitter blade tips (Figure 9) were extracted at CAD-defined heights, while CAD-to-mesh deviation maps (Figures 10 and 11) revealed systematic trends across the pressure and suction sides of the airfoils. These global profile deviations highlight the added value of optical scanning,

https://doi.org/10.3390/metrology6010012

which can capture freeform surface errors beyond the reach of tactile probing. In addition to data A and B, locking bores (datum C) were also probed on both the CMM and the scanner. However, due to limited line of sight inside the deep bores, structured-light scanning did not yield sufficiently stable primitive fits. For this reason, the datum C results are reported descriptively but excluded from the cross-system comparison, where only reliably extractable features are considered.

Table 5. Statistical summary of optical scanner measurements (mean, standard deviation, and uncertainty evaluation).

Feature	Mean [mm]	Std. dev. [mm]	U_{rep} [mm]	U_{95} [mm]
B—r	0.04821	0.0000994429	0.000031447	0.000062893
O A	14.50325	0.0000707107	0.000022361	0.000044721
j A	0.14334	0.050565627	0.01599026	0.03198051
A { B	0.01061	0.000202485	0.000064031	0.00012806

3.3. Cross-System Comparison

Cross-system comparison focuses on datums A and B, where both CMM and the scanner provided consistent measurements. Locking bores (datum C), while measured, are excluded from the statistical comparison because of scanner visibility constraints and their primary role as fixturing aids rather than dimensional verification.

Table 6 summarizes the comparison between the CMM and optical scanner results for the common features (datums A, B). The differences Δ were evaluated against the combined expanded uncertainty U_{95}, Δ where the scanner systematically overestimated the flatness of datum B (+48 µm vs. 1.6 µm on CMM). Since $\mid \Delta \mid \gg U_{95}, \Delta$, agreement is rejected (✗). This indicates that, under the present mesh-based extraction settings, planar micro-flatness is a challenging measurand for structured-light inspection at this tolerance level, with mesh noise and filtering choices dominating the estimated flatness. A bias of -3.3 µm was observed on the diameter of datum A, beyond the uncertainty band, leading to non-agreement (✗). Non-agreement (✗) is interpreted as a lack of interchangeability for the specific measurand under the present acquisition/extraction settings, not as a general limitation of structured-light scanning. This deviation likely originates from the partial visibility of the bore and reliance on end-section fitting in the scanner. Large discrepancies were found while evaluating the cylindricity of datum A (+131 µm), far exceeding the uncertainty budget (✗). This confirms that scanner primitives are insufficiently sensitive for high-precision form errors compared to tactile probing. Agreement was obtained (✓) after perpendicularity evaluation A $\perp$ B, with $\Delta = -4.3$ µm within U_{95}, $\Delta = 14.7$µm. This shows that scanner-based axis-to-plane alignment is robust enough for orientation control features.

Table 6. Cross-system comparison for common features (CMM vs. optical scanner).

Feature	CMM Mean [mm]	Scanner Mean [mm]	Δ (Scan–CMM) [mm]	$U_{95}\Delta$ [mm]	Agreement
B—r	0.00156	0.0482	+0.04665	0.00008	✗
O A	14.50651	14.5033	−0.00326	0.00018	✗
j A	0.01232	0.14334	+0.13102	0.0320	✗
A { B	0.01495	0.01061	−0.00434	0.0147	✓

https://doi.org/10.3390/metrology6010012

Overall, the CMM provides a traceable baseline for datum-related primitives, whereas structured-light scanning adds high-value information for freeform blade assessment; the observed non-agreement is primarily feature-dependent (measurand definition, visibility, and data processing/feature extraction workflow), rather than an intrinsic shortcoming of the optical system.

4. Discussion

4.1. Agreement and Discrepancies Between Systems

The comparative analysis demonstrated that the tactile CMM and the optical scanner provide consistent results only for orientation-related features, while significant discrepancies remain for form and flatness evaluation. Datum B (plane flatness) showed the most pronounced divergence: the scanner overestimated flatness by approximately +46 μm compared to the CMM value of 1.6 μm. This result is consistent with prior findings that structured-light scanning is limited in detecting sub-10 μm planar deviations due to mesh noise and fitting artifacts [3,11]. For datum A (cylindrical bore), the mean diameter bias (−3.3 μm) and especially the large deviation in cylindricity (+131 μm) exceeded the combined expanded uncertainty. These discrepancies confirm that scanner-based primitive extraction is insufficient for high-precision form control, in line with Fei et al. [7] and Givi et al. [8], who reported systematic underperformance of non-contact systems in deep, line-of-sight-limited bores. Conversely, perpendicularity between datum B and A was within the acceptance band, showing that orientation features are less sensitive to the scanner's intrinsic resolution limits.

It should be noted that the CMM-based planarity evaluation relies on a functionally distributed probing strategy rather than dense surface sampling. In accordance with standard GD&T practice and ISO 10360-based methodologies, planarity was assessed using a limited number of strategically positioned points to ensure traceability and robustness of the form error evaluation. Increasing the probing density on the CMM was therefore not expected to significantly improve the planarity result, as the measured deviation is dominated by global form rather than localized surface features. In contrast, optical scanning inherently produces dense point clouds; however, the resulting planar form estimation remains constrained by point spacing, meshing residuals, and fitting algorithms, which limit its capability for sub-10 μm flatness evaluation.

4.2. Causes of Scanner Deviations

Two factors primarily account for the systematic deviations observed in scanner results. First, line-of-sight constraints limited the bore acquisition to edge regions, such that diameter and form descriptors were derived from partial sections rather than full generatrices. Second, meshing and best-fit fitting propagate residual noise (≈0.01–0.02 mm per patch) into the extracted primitives, particularly for form-related characteristics [1,3,9]. Consistently across the 10 full re-orientations, dispersion was higher for form metrics (cylindricity and flatness) than for size or orientation descriptors, supporting a feature-dependent interpretation of cross-system non-agreement. This behavior is consistent with the uncertainty-mapping work of Sepahi-Boroujeni and Khameneifar [9], who emphasize the role of digital twin-based error fields in quantifying scanner repeatability.

4.3. Industrial Implications and Complementarity of Systems

From an industrial perspective, the two systems play complementary roles. The CMM establishes traceable, high-precision data, indispensable for tolerances in the order of micrometers (e.g., bore cylindricity or rotor mounting flatness). This aligns with Kruth et al. [4], Feng et al. [6], and Sato et al. [12], who demonstrate that CMM-based experimental

https://doi.org/10.3390/metrology6010012

designs remain the benchmark for Type B and Type A uncertainty evaluation under ISO 10360 [15]. In contrast, the optical scanner provides added value for freeform surfaces, such as the impeller blades, where dense CAD-to-mesh deviation maps enable rapid identification of systematic airfoil deviations that tactile probing cannot access [5,13,14]. This duality reflects the current trend toward integrated metrology [5], where tactile and optical systems are combined to exploit their respective strengths—high-precision data and global freeform coverage.

4.4. Relation to Existing Literature

Our results reinforce and extend previous comparative studies. Altinisik and Bolova [11] observed similar scanner biases when measuring standard test parts against a CMM reference, while Bilušić and Olivari [3] highlighted the role of task-specific uncertainty factors in optical 3D metrology. The present study contributes by explicitly quantifying scanner repeatability under repeated reorientation—a protocol rarely applied in industrial practice, where single-pass scanning is the norm [1,3]. The observation that bore-related deviations are dominated by visibility constraints is consistent with the accessibility-driven uncertainty patterns reported by Vrba et al. [20] for complex surfaces. Moreover, the systematic overestimation of flatness echoes the mesh residual effects described in Kruth et al. [4] and Kortaberria et al. [14], who emphasize that ISO 15530-3 approaches must be adapted when transferring uncertainty models from tactile to optical data.

4.5. Limitations and Future Work

Two limitations of the present study deserve mention. First, locking bores (datum C) were measured with both systems but were excluded from the cross-system comparison due to restricted scanner visibility; this follows the practice of excluding features where geometry or access prevents reliable evaluation [7,8]. Second, while 10 repetitions enabled Type A evaluation for both systems, Type B contributors for the scanner (e.g., vibration, photogrammetric alignment stability, lens calibration) were not separately isolated; future work could address these via Monte Carlo propagation [4,16,18,19]. A promising avenue is the integration of digital twin-based error modeling [9,16,19] and hybrid CMM–scanner workflows [5,13], which could reduce biases in form-related features and support more robust uncertainty budgets. Future publications will extend the present work by including additional measurement techniques, enabling a broader multi-sensor comparison and a deeper investigation of uncertainty propagation in hybrid inspection workflows.

4.6. Overall Contribution

The study demonstrates that while structured-light scanners cannot yet replace tactile probing for micro-tolerance features, they provide unique capabilities for freeform geometry evaluation. By aligning both systems to a common datum scheme and repeating acquisitions under controlled conditions, this work contributes a traceable, uncertainty-aware framework for CMM–scanner comparison, consistent with ISO 15530 task-specific practice [14]. These findings are directly relevant to industries where rotors, blades, or other turbomachinery parts require both micrometric control of data and global airfoil inspection.

5. Conclusions

This work provides an uncertainty-driven comparison between CMM probing and structured-light scanning for a centrifugal rotor in micro gas turbine applications under a unified GD&T datum scheme. CMM probing delivered a traceable performance with sub-micrometer repeatability/reproducibility and expanded uncertainties (U95) below 0.2 μm for key size features, confirming its role as the reference method for functional

https://doi.org/10.3390/metrology6010012

datum verification. Structured-light scanning provided consistent full-field geometry and enabled dense assessment of freeform blade surfaces; however, cross-system agreement was feature-dependent, with systematic offsets observed for selected form-related characteristics where Δ exceeded the combined uncertainty band. Accordingly, optical results should be interpreted as non-interchangeable with tactile probing for these measurands under the present acquisition and feature-extraction workflow, rather than as a general limitation of the technology. Overall, the findings support hybrid inspection, combining tactile datum traceability with optical freeform mapping to balance accuracy, coverage, and throughput. Future work will target task-specific ISO-consistent uncertainty budgets and error-compensation/sensor-fusion strategies to reduce feature-dependent offsets.

6. Patents

The authors declare that no patents are associated with the work reported in this manuscript.

Author Contributions: Conceptualization, I.-A.D. and A.G.T. methodology, I.-A.D.; validation, I.-A.D., A.G.T. and A.-M.D.; formal analysis, I.-A.D.; investigation, I.-A.D.; resources, A.G.T. and M.V.; data curation, I.-A.D.; writing—original draft preparation, I.-A.D.; writing—review and editing, A.-M.D.; visualization, I.-A.D.; supervision, A.G.T.; project administration, I.-A.D. All authors have read and agreed to the published version of the manuscript.

Funding: This research was carried out under the "Nucleu" Program, Grant No. 31N/2023, funded by the Romanian Ministry of Research, Innovation and Digitization.

Data Availability Statement: Data supporting the reported results can be obtained from the corresponding author upon reasonable request. No publicly archived datasets were generated in this study due to laboratory confidentiality restrictions.

Acknowledgments: The author gratefully acknowledges the support of COMOTI—Romanian Research & Development Institute for Gas Turbines for providing access to the measurement infrastructure (CMM and optical scanning systems) and the technical staff involved in instrument setup and calibration. This work was carried out within the framework of the Nucleus Program of the National Plan for Research, Development and Innovation 2022–2027, conducted with the support of the Ministry of Research, Innovation and Digitalization (MCID), Project No. PN23.12.03.01. The author has reviewed and edited the output and takes full responsibility for the content of this publication.

Conflicts of Interest: The authors declare no conflicts of interest. The funders had no role in the design of the study; in the collection, analyses, or interpretation of data; in the writing of the manuscript; or in the decision to publish the results.

Abbreviations

The following abbreviations are used in this manuscript:

CMM	Coordinate Measuring Machine
GD&T	Geometric Dimensioning and Tolerancing
GUM	Guide to the Expression of Uncertainty in Measurement
MPEE	Maximum Permissible Error for Length Measurement
U95	Expanded Uncertainty at 95% Confidence Level
ANOVA	Analysis of Variance
CAD	Computer-Aided Design
PDF	Probability Density Function
ISO	International Organization for Standardization
JCGM	Joint Committee for Guides in Metrology

https://doi.org/10.3390/metrology6010012

References

1. Yin, S.; Ren, Y.; Guo, Y.; Zhu, J.; Yang, S.; Ye, S. Development and Calibration of an Integrated 3D Scanning System for High-Accuracy Large-Scale Metrology. *Measurement* **2014**, *54*, 65–76. [CrossRef]
2. Dumitrache, I.-A.; Manolache, D.S.; Nanu, S. Study on Geometric Advanced Control of Actual Machined Product Features. *U.P.B. Sci. Bull. Series D* **2025**, *87*, 186–194. Available online: https://www.scientificbulletin.upb.ro/static/pdfs/full361_921678.pdf (accessed on 11 February 2026).
3. Bilušić, M.; Olivari, L. Assessment of Process Chain Suitability of the Optical 3D Measuring System by Using Influencing Factors for Measurement Uncertainty. *J. Ind. Inf. Integr.* **2024**, *41*, 100654. [CrossRef]
4. Kruth, J.-P.; Van Gestel, N.; Bleys, P.; Welkenhuyzen, F. Uncertainty Determination for CMMs by Monte Carlo Simulation Integrating Feature Form Deviations. *CIRP Ann. Manuf. Technol.* **2009**, *58*, 463–466. [CrossRef]
5. Archenti, A.; Gao, W.; Donmez, A.; Savio, E.; Irino, N. Integrated Metrology for Advanced Manufacturing. *CIRP Ann. Manuf. Technol.* **2024**, *73*, 639–665. [CrossRef]
6. Feng, C.-X.J.; Saal, A.L.; Salsbury, J.G.; Ness, A.R.; Lin, G.C.S. Design and Analysis of Experiments in CMM Measurement Uncertainty Study. *Precis. Eng.* **2007**, *31*, 94–101. [CrossRef]
7. Fei, L.; Dantan, J.-Y.; Baudouin, C.; Du, S. Calibration and Uncertainty Estimation of Non-Contact Coordinate Measurement Systems Based on Kriging Models. *Precis. Eng.* **2019**, *57*, 16–29. [CrossRef]
8. Givi, M.; Cournoyer, L.; Reain, G.; Eves, B.J. Performance Evaluation of a Portable 3D Imaging System. *Precis. Eng.* **2019**, *59*, 156–165. [CrossRef]
9. Sepahi-Boroujeni, S.; Khameneifar, F. Digital Twin-Enabled Error and Uncertainty Mapping for 3D Scanning. *Precis. Eng.* **2024**, *88*, 527–539. [CrossRef]
10. Dhanish, P.B.; Mathew, J. Effect of CMM Point Coordinate Uncertainty on Uncertainties in Determination of Circular Features. *Measurement* **2006**, *39*, 522–531. [CrossRef]
11. Altinisik, A.; Bolova, E. A Comparison of Off-Line Laser Scanning Measurement Capability with Coordinate Measuring Machines. *Measurement* **2021**, *168*, 108228. [CrossRef]
12. Sato, O.; Takatsuji, T.; Matsuzaki, K.; Watanabe, M.; Kajima, M.; Miura, Y.; Nakanishi, S. Practical Experimental Design and Uncertainty Evaluation Method for Dimensional and Form Measurements Using Coordinate Measuring Machines. *Measurement* **2024**, *227*, 114224. [CrossRef]
13. Chen, G.; Li, Y.; Mehdi-Souzani, C.; Liu, X. Implicit Residual Approximation for Multi-Sensor Data Fusion in Surface Geometry Measurement. *J. Manuf. Syst.* **2024**, *75*, 246–256. [CrossRef]
14. Kortaberria, G.; Mutilba, U.; Gomez, S.; Ahmed, B. Three-Dimensional Point Cloud Task-Specific Uncertainty Assessment Based on ISO 15530-3 and ISO 15530-4 Technical Specifications and Model-Based Definition Strategy. *Metrology* **2022**, *2*, 394–413. [CrossRef]
15. The New Acceptance and Reverification Tests for Coordinate Measuring Machines. Beuth Verlag: Berlin, Germany, 2009. Available online: https://qualityforum.zeiss.com/migration/images/120_2230526f9bdb0832c207ec0e65c8986e.pdf (accessed on 11 February 2026).
16. Deantoni, J.; Muñoz, P.; Gomes, C.; Verbrugge, C.; Mittal, R.; Heinrich, R.; Bellis, S.; Vallecillo, A. Quantifying and Combining Uncertainty for Improving the Behavior of Digital Twin Systems. *arXiv* **2024**, arXiv:2402.10535. [CrossRef]
17. *JCGM 100:2008*; Evaluation of Measurement Data—Guide to the Expression of Uncertainty in Measurement (GUM 1995 with Minor Corrections). BIPM: Paris, France, 2008. [CrossRef]
18. *JCGM 101:2008*; Evaluation of Measurement Data—Supplement 1 to the Guide to the Expression of Uncertainty in Measurement—Propagation of Distributions Using a Monte Carlo Method. BIPM: Paris, France, 2008. [CrossRef]
19. Cramer, S.; Müller, T.; Schmitt, R.H. Measurement Uncertainty: Relating the Uncertainties of Physical and Virtual Measurements. *arXiv* **2024**, arXiv:2402.13666. [CrossRef]
20. Vrba, I.; Palencar, R.; Hadzistevic, M.; Strbac, B.; Spasic-Jokic, V.; Hodolic, J. Different Approaches in Uncertainty Evaluation for Measurement of Complex Surfaces Using Coordinate Measuring Machine. *Meas. Sci. Rev.* **2015**, *15*, 111–119. [CrossRef]
21. *ALTERA 15.7.6/10.10.8*; Nikon Metrology. Technical Datasheet. Nikon Metrology NV: Leuven, Belgium, 2013. Available online: https://loewener.dk/wp-content/uploads/2015/03/ALTERA-15.7.6-x.10.8.pdf (accessed on 11 February 2026).
22. GOM GmbH. *ATOS Compact Scan—Mobile 3D Scanner for a Wide Range of Applications*; ATOS Technical Datasheet; GOM GmbH: Braunschweig, Germany, 2020. Available online: https://www.zeiss.co.in/metrology/systems/optical-3d/3d-scanning/atos/atos-compact-scan.html (accessed on 11 February 2026).

Disclaimer/Publisher's Note: The statements, opinions and data contained in all publications are solely those of the individual author(s) and contributor(s) and not of MDPI and/or the editor(s). MDPI and/or the editor(s) disclaim responsibility for any injury to people or property resulting from any ideas, methods, instructions or products referred to in the content.

https://doi.org/10.3390/metrology6010012

metrology

MDPI

Article

A Flexible Wheel Alignment Measurement Method via APCS-SwinUnet and Point Cloud Registration

Bo Shi [1,2,*], Hongli Liu [3] and Emanuele Zappa [2]

[1] School of Artificial Intelligence, Changsha University of Science and Technology, Changsha 410114, China
[2] Department of Mechanical Engineering, Politecnico di Milano, 20156 Milan, Italy; emanuele.zappa@polimi.it
[3] College of Electrical and Information Engineering, Hunan University, Changsha 410082, China; honglliu@hnu.edu.cn
* Correspondence: boshi@hnu.edu.cn

Abstract

To achieve low-cost and flexible wheel angles measurement, we propose a novel strategy that integrates wheel segmentation network with 3D vision. In this framework, a semantic segmentation network is first employed to extract the wheel rim, followed by angle estimation through ICP-based point cloud registration. Since wheel rim extraction is closely tied to angle computation accuracy, we introduce APCS-SwinUnet, a segmentation network built on the SwinUnet architecture and enhanced with ASPP, CBAM, and a hybrid loss function. Compared with traditional image processing methods in wheel alignment, APCS-SwinUnet delivers more accurate and refined segmentation, especially at wheel boundaries. Moreover, it demonstrates strong adaptability across diverse tire types and lighting conditions. Based on the segmented mask, the wheel rim point cloud is extracted, and an iterative closest point algorithm is then employed to register the target point cloud with a reference one. Taking the zero-angle condition as the reference, the rotation and translation matrices are obtained through point cloud registration. These matrices are subsequently converted into toe and camber angles via matrix-to-angle transformation. Experimental results verify that the proposed solution enables accurate angle measurement in a cost-effective, simple, and flexible manner. Furthermore, repeated experiments further validate its robustness and stability.

Keywords: wheel alignment; angle measurement; semantic segmentation; point cloud registration; vision measurement

1. Introduction

Wheel alignment is a routine yet essential maintenance procedure that ensures the wheels are properly angled relative to the vehicle's frame and the road surface [1]. Manufacturers set the wheel alignment within a specified range before the vehicle leaves the factory [2]. However, factors such as suspension wear, heavy loads, poor road conditions, collisions, or chassis damage can cause wheel misalignment, which refers to a deviation from the manufacturer's specifications [3]. Wheel misalignment may involve numerous issues, including uneven tire wear, wheel shimmy, suspension damage, poor handing, increased fuel consumption, and safety risk. Therefore, regular wheel alignment inspections and adjustments are crucial. During maintenance, three primary angles, namely camber, caster and toe angles, are usually measured and adjusted. Toe and camber angles of the vehicle wheels are the two alignment parameters most commonly inspected and adjusted

during routine maintenance and post-repair operations, and they are also the primary focus of most existing research on vision-based wheel alignment. Therefore, at the current stage, this work primarily focuses on the estimation of toe and camber angles.

1.1. Challenges of 3D Vision-Based Methods

Compared to methods based on inertial measurement unit and 2D vision, the 3D vision-based measurement methods offer advantages such as low cost, high precision, and greater flexibility in application. However, 3D vision-based wheel alignment still faces several challenges, which are summarized below.

(1) Complicated calibration and limited flexibility: Most passive and active 3D measurement systems require a complex and rigorous calibration procedure to reconstruct the wheel shape. Once calibrated, cameras and light sources need to remain fixed, which limits its flexibility and application range. Moreover, the reflective surface of the wheel hub leads to low texture and feature information, which affects stereo matching accuracy and ultimately reduces the accuracy of 3D reconstruction.
(2) Additional target board and potential damage: Commercial scanner-based methods often require mounting a clamped target board with a special reflective film onto the wheel. This process is time-consuming, may cause secondary damage to the wheel, and incurs additional costs due to the consumable film, thereby reducing overall efficiency.
(3) Inefficient and noise-sensitive full-cloud registration: Directly using the entire 3D point cloud acquired by the sensor to estimate wheel angles not only increases computational cost and reduces measurement efficiency, but also introduces interference from background, noise, and points from the vehicle body during point-cloud registration. These irrelevant points can significantly degrade registration accuracy. Therefore, it is more effective to perform 3D registration and angle estimation using only a stable, wheel-related subset of the point cloud.
(4) Challenges in precise wheel segmentation: The reconstructed point cloud includes not only the wheel but also background elements, making accurate region-of-interest (ROI) extraction essential. Existing methods often rely on traditional image processing algorithms (e.g., Canny edge detection and Hough transforms), which are sensitive to background clutter and environmental changes. These methods often require manual parameter tuning and lack the precision needed for accurate wheel boundary and detail extraction.

1.2. Outline of Our Work

To address the challenges outlined above, this paper presents a low-cost and practical wheel alignment method that integrates semantic segmentation with point cloud registration. The proposed approach overcomes the limitations of using 2D or 3D single-modality data alone and fully leverages the rich texture information in 2D images together with the depth and pose information encoded in 3D point clouds, thereby improving both the efficiency and the accuracy of wheel angle measurement. The primary application context of this work is post-production wheel alignment in small and medium-sized garages and workshops, where vehicles are serviced after leaving the factory. The main contributions are summarized as follows.

(1) As a relatively stable region of the wheel, the wheel rim provides reliable geometric cues, so using only the rim point cloud to estimate wheel angles helps improve both measurement efficiency and angle accuracy. Building on this idea, the proposed method reformulates the wheel alignment task as a pipeline of wheel rim mask extraction, corresponding point cloud registration, and wheel angle calculation.

https://doi.org/10.3390/metrology6010004

Compared with existing approaches, it offers greater flexibility, lower cost, and higher efficiency, as it removes the need for complex calibration procedures, target boards, and additional auxiliary equipment or materials.

(2) Wheel rim extraction is critical for accurate angle estimation. To enhance the precision of wheel rim segmentation, we propose APCS-SwinUnet, a task-driven adaptation of Swin-Unet for wheel rim extraction. Atrous spatial pyramid pooling is embedded into the encoder to capture multi-scale contextual information for wheel rims of different sizes and viewpoints, while a channel-spatial attention mechanism in the decoder selectively enhances rim features and suppress background clutter. This design jointly improves the representation of global wheel contours and fine-grained rim structures, both essential for reliable angle estimation. Compared with traditional image processing pipelines and baseline deep networks, APCS-SwinUnet achieves higher accuracy and robustness in wheel rim segmentation.

(3) The segmented mask is used to isolate the wheel rim point cloud, effectively filtering out irrelevant background data. The iterative closest point algorithm is then employed to register the initial and target wheel rim point clouds. After registration, the corresponding rotation and translation matrices are obtained, and the rotation matrix is subsequently used to compute the wheel's toe and camber angles.

The rest of this paper is organized as follows. Section 2 reviews related work on wheel alignment. Section 3 presents the overview framework of this paper. Section 4 details the motivation for segmentation and the proposed network structure. Section 5 explains the principle of wheel angles calculated using the iterative closest point method. Section 6 describes the experimental setup and configuration. In Section 7, the segmentation and angle measurement results are presented. Section 8 summarizes the paper and discusses future development.

2. Related Work

In this section, we review related work from two complementary perspectives. First, we summarize existing wheel alignment techniques in terms of sensing and measurement strategies. Most conventional approaches can be broadly grouped into inertial-based methods and vision-based inspection methods, where the latter can be further divided into 2D and 3D vision-based measurement schemes. Second, since the proposed method formulates wheel alignment as a thin structure segmentation problem, we also review recent deep learning-based thin structure segmentation methods.

2.1. Wheel Alignment Sensing and Measurement Methods

2.1.1. Inertial-Based Wheel Alignment Methods

Inertial-based wheel alignment methods typically involve contact measurement. Specific sensors such as inertial measurement units (IMUs), accelerometers, gyroscopes, and angle sensors are mounted on the wheel or vehicle to collect acceleration and angular velocity data [4]. This data is preprocessed to reduce noise, correct sensors bias, and compensate for drift. Afterward, the data is transmitted to a processor (e.g., mobile phone, computer, or embedded device) via Bluetooth, WiFi, or RS232 for further analysis and computation of wheel alignment angles.

Numerous studies have explored the inertial-based methods. Young et al. [4] employed a microcontroller and triaxial accelerometer to measure the camber angle, introducing a calibration technique to correct axis misalignment between the sensor and the measurement system. Chatur et al. [5] proposed a wireless alignment method using accelerometers. D'Mello et al. [6] developed an internet of things (IoT) device consisting of a 6-axis microelectromechanical system (MEMS) sensor (MPU6050), an ESP32 microcon-

https://doi.org/10.3390/metrology6010004

troller, and battery to measure toe and camber angles. Similarly, Bohari et al. [7] designed a Bluetooth-enabled alignment system using the MPU6050 sensor. Lee et al. [8] presented an online toe angle measurement approach based on lateral tire force, which was validated through simulations in CarSim and Simulink. To reduce energy consumption, Tang et al. [9] introduced a dual wake-up and self-calibration strategy for long-term monitoring. Inertia-based offer methods offer advantages such as high sampling frequency, low latency, low power consumption, and resistance to environmental conditions. However, they face several challenges. Physical contact is often required, risking damage to the wheel hub. Furthermore, sensor drift may cause cumulative errors, and measurement accuracy is affected by electromagnetic interference, temperature, and sensor location.

2.1.2. Vision-Based Wheel Alignment Methods

Compared with inertial-based methods, vision-based wheel alignment methods offer the advantages of convenience, highly automation, and efficiency. Typically, vision-based measurement techniques are divided into 2D and 3D vision measurement methods.

2D Vision-Based Measurement Methods

A 2D vision inspection platform usually consists of target boards, infrared light emitting diodes (IR LEDs), image acquisition modules such as charged coupled device (CCD) or video cameras, and a computer [10]. Each target board, made of reflective material and featuring special patterns (e.g., chessboard or concentric circles), is mounted on the wheel rim using a four-legged clamp to represent the wheel attitude. During the measurement, IR LEDs illuminate the target boards, which are then captured by the CCDs. The technician turns the steering wheel in different directions and moves the vehicle back and forth to determine the axes of rotation and roll for each wheel. Finally, the wheel angles are calculated by analyzing the captured images based on projective geometry. Numerous 2D vision-based methods have been proposed. For instance, Xu et al. [11] proposed a toe and camber angles measurement method using a relevance vector machine and spatial clustering to classify the concentric circles on the target board. Xu et al. [12] proposed a global registration system combining multiple sensors with articulated arms and target boards, although this system is costly and complex. Ge et al. [13] introduced a multi-camera calibration technique using a transparent target board and image correlation. Jiang et al. [14] designed a calibration method for large cabin assembly with an improved homography matrix and combined large targets. Roshan et al. [15] developed a checkboard with augmented markers made of high-emissivity material and aluminum to expand its applicability. Xu et al. [16] proposed a kinpin inclination and caster measurement method using a 1D target with concentric circles.

Two-dimensional vision-based approaches are known for their high accuracy and efficiency, making them widely adopted in vehicle maintenance. However, they also have the following limitations. A complete 2D vision wheel alignment system is expensive, and installing clamps and the target boards is time-consuming and cumbersome, reducing measurement efficiency and increasing costs. Moreover, direct contact between the clamps and the wheels may cause potential.

3D Vision-Based Measurement Methods

Three-dimensional vision-based measurement methods are generally categorized into passive and active 3D vision methods. Passive vision does not project any light source onto the wheel but relies on two or more cameras to recover depth maps or point clouds using triangulation between the camera centers and the wheel. In contrast, active 3D vision involves projecting a structured light source, such as point, line or surface, onto the wheel to reconstruct the object's point cloud. Padegaonakar et al. [17] proposed a binocular

https://doi.org/10.3390/metrology6010004

passive vision method to measure wheel angles. Canny edge detection was applied to extract circular contours of the wheel, from which the outermost contour was selected as the region of interest (ROI). Wheel angles were then calculated using the depth map and trigonometry principles. While this method can reconstruct wheel point cloud, it has the following limitations. Passive stereo vision requires stereo rectification and stereo matching. Stereo rectification, based on intrinsic and extrinsic camera parameters, aligns corresponding points onto a common horizontal line. Stereo matching is then performed by exploiting surface textures and feature information. However, wheel hubs are highly reflective and often exhibit homogeneous textures, resulting in limited distinguishable features. This leads to low stereo matching accuracy, which in turn degrades the overall precision of 3D reconstruction. To address these issues, Xu et al. [2] proposed a method using a line laser and 1D target for large-scale onsite measurement. Furferi et al. [18] attached non-structured markers to the tire sidewall, combing image processing and stereo triangulation to associate 3D marker positions with the wheel plane. Senjalia et al. [19] developed a system using laser triangulation and camera calibration, where wheel regions were identified using OpenCV's blob detection. However, this approach requires frequent threshold adjustment due to varying wheel shape, which reduces flexibility and efficiency. Furthermore, lighting conditions, reflections, and surface contamination can significantly affect accuracy. Kim et al. [20] employed two orthogonally mounted laser modules on the wheel knuckle to measure toe and camber angles. Baek et al. [21] developed a surface light-based depth-sensing system that acquires the wheel's point cloud for geometric and posture analysis. Like 2D vision methods, this method requires a target board to be fixed on the wheel. Although no pattern is used, the board is used to represent the attitude of the wheel. To facilitate the ROI extraction, a thin (0.075 mm) adhesive film was applied. Wheel condition was assessed by comparing the current point cloud with a reference plane. While this method enables fast and stable point cloud acquisition, it still requires mounting a target board with a fixed relative position to the wheel. If the relative position changes, an error will be introduced. Moreover, additional matte adhesive film increases costs and reduce efficiency.

2.2. Deep Learning-Based Thin Structure Segmentation Methods

Current research on deep learning-based thin structure segmentation is still relatively limited, and most existing methods are built on convolutional neural networks (CNN) or Transformer-based architectures. Wang et al. [22] proposed a dual-path pavement crack segmentation network that combines a lightweight CNN encoder with a Transformer encoder incorporating attention and an efficient feedforward design to fuse local and global features for crack delineation. Gao et al. [23] proposed a multi-scale global attention network that integrates a densely connected attention U-Net backbone with a global context attention module for hierarchical context aggregation and top-down guidance, achieving consistently competitive retinal vessel segmentation and noticeably improved thin-vessel delineation. Geetha et al. [24] proposed an image-processing-assisted 1D frequency-domain CNN framework that extracts crack candidate regions via adaptive local binarization and then iteratively tracks missing single-pixel-wide propagating cracks. Siriborvornratanakul [25] evaluated Segment Anything Model (SAM) as a zero-shot solution for thin crack segmentation and reported that, although the SAM-Canny pipeline can delineate crack patterns reasonably well on multiple benchmark datasets, its numerical scores remain inferior to task-specific deep learning architectures, e.g., modified U-Net, when assessed under stringent 1-pixel crack annotation criteria. Li et al. [26] developed a dual-path progressive fusion network for retinal vessel segmentation, where a CNN branch is responsible for capturing fine local vessel details and a recurrent convolutional branch models richer contextual information. In addition, they introduced a progressive fusion mechanism

https://doi.org/10.3390/metrology6010004

composed of interactive fusion, cross-layer fusion, and scale feature fusion modules to integrate multi-scale features and mitigate the semantic gap between encoder and decoder.

Although these studies have advanced thin structure segmentation for targets such as vessels and pavement cracks, they do not fully address the wheel rim segmentation problem in our wheel alignment pipeline. The wheel rim in this work is not only a thin structure but also exhibits inner and outer boundaries with approximate symmetry, which differs significantly from tree-like or irregular thin patterns, and there is very limited work specifically targeting wheel-like thin structures. Moreover, rim segmentation here is only an intermediate step: our core objective is to estimate wheel angles from the segmented rim point cloud, so background and tire points can affect the robustness of subsequent point cloud matching, making accurate boundary segmentation particularly critical. In addition, practical wheel alignment requires a favorable trade-off between segmentation accuracy and efficiency, whereas many existing thin structure models are too computationally demanding for such scenarios.

In summary, inertial-based methods require physical sensor installation, which may damage the wheel and are sensitive to environmental factors such as electromagnetic interference and temperature. Although vision-based methods improve measurement efficiency, most of them still rely on target boards to estimate the wheel angle. To address these limitations from a technical perspective, this paper proposes a low-cost, non-contact, and practically feasible wheel alignment approach that integrates 3D vision and semantic segmentation techniques. Furthermore, to better handle the wheel rim, which is a thin, wheel-like structure with both inner and outer boundaries and approximate symmetry, we develop an APCS-SwinUNet architecture tailored for accurate rim segmentation.

3. Framework of Proposed Solution

The overall framework of the proposed method is shown in Figure 1. In the first stage, a wheel rim segmentation network based on APCS-SwinUnet is used to extract the wheel rim region from the RGB image. To achieve accurate and fine-grained segmentation, the network incorporates an ASPP module, an attention fusion module, and a hybrid Dice–Focal loss. The resulting segmentation mask is then mapped to the point cloud to obtain the wheel rim point cloud. In the second stage, the initial and target wheel rim point clouds are registered using the ICP algorithm, yielding the rotation and translation matrices that describe the wheel pose. The toe and camber angles are subsequently derived from the rotation matrix and converted to degrees, providing the final wheel angle measurements. Thus, the segmentation network and the point cloud registration are the two core components of the framework, bridging image-level processing and 3D geometric estimation.

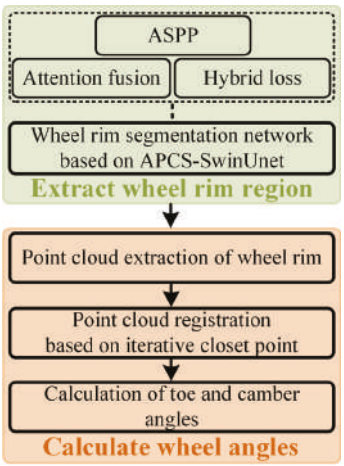


Figure 1. Overall framework of the proposed solution.

https://doi.org/10.3390/metrology6010004

4. Wheel Rim Segmentation Based on APCS-SwinUnet

This section presents the network architecture for wheel rim segmentation. We first introduce the motivation and objective of employing a segmentation network for wheel rim extraction. Next, we outline the overall structure of the proposed APCS-SwinUnet, followed by a detailed description of the key components, including atrous spatial pyramid pooling, convolutional block attention module, and hybrid loss function.

4.1. Motivation for Using Segmentation Network

As mentioned in the introduction, most existing wheel alignment methods require mounting a target board on the wheel and involve complex calibration procedures. Although some emerging approaches offer simplified setups, they still rely on target boards or matte adhesive films, which reduce measurement efficiency and increase system cost. To address these limitations, we propose a target-free alignment method by leveraging the point cloud of the wheel rim, eliminating the need for additional auxiliary materials. Traditionally, the target board is used to capture changes in the wheel's attitude and angle due to the non-planar surface of the wheel hub. However, a closer examination reveals that the area between the wheel and the tire contains a circular smooth surface, which naturally spans a range of angles and can effectively reflect the wheel's attitude changes, thereby making it a viable alternative for alignment purposes. The 3D scanner can capture the RGB image and point cloud of the entire scene, whereas our task focuses specifically on extracting the wheel rim's point cloud.

Wheel rim extraction is critical for accurate angle estimation. As shown in Figure 2, the wheel rim is a narrow annular structure that occupies only a small portion of the wheel, making its extraction particularly challenging for the following reasons: (1) The wheel rim has both inner and outer boundaries, and its thin, curved geometry complicates accurate localization. (2) Although there is a noticeable reflectance difference between the wheel rim and the tire, the wheel rim and hub often share similar reflectivity, leading to weak grayscale contrast and ambiguous edges. (3) Since the point cloud of the wheel rim is used to estimate the overall wheel posture, background and tire regions need to be excluded, requiring precise segmentation of the rim contours. Traditional image processing methods can, in principle, perform this task, but they typically involve multiple steps and require manual tuning for different wheel types, resulting in limited flexibility and poor generalization. Deep learning-based segmentation offers a more robust and adaptive alternative.



Figure 2. Schematic illustration of the wheel rim.

Prior studies on thin or narrow structures (such as vessels, roads, or cracks) often leverage multi-scale context and attention mechanisms to improve boundary delineation, and are predominantly implemented within U-Net-like or transformer-based encoder–decoder architectures. However, these methods are generally designed for tree-like or line-like topologies, rather than for closed, narrow annular rims with dual inner-outer boundaries and weak contrast between the rim and the hub, and they are not specifically

https://doi.org/10.3390/metrology6010004

optimized for downstream wheel alignment tasks. As a result, existing architectures still struggle to accurately delineate the thin boundary regions of the wheel rim and to provide sufficiently stable contours for subsequent 3D point cloud registration and angle estimation. To address these issues, we design APCS-SwinUnet as a task-specific adaptation of established segmentation modules, tailored to the geometric and photometric characteristics of the wheel rim and its role in wheel alignment measurement.

4.2. Network Architecture of APCS-SwinUnet

The architecture of APCS-SwinUnet is illustrated in Figure 3. It is built upon the Swin Transformer and U-Net frameworks and achieves high segmentation accuracy while maintaining efficiency. First, an atrous spatial pyramid pooling (ASPP) module is added after the third encoder layer to capture multi-scale features relevant to wheel rims. Second, a convolutional block attention module (CBAM) is integrated into the third decoder layer to strengthen the network's focus on the rim contour and suppress background clutter. Finally, a hybrid loss function combining Dice and Focal losses is employed to better handle class imbalance and stabilize training. In this way, APCS-SwinUnet is not a completely novel architecture, but a carefully engineered combination and adaptation of known modules tailored to the challenges of wheel rim segmentation.

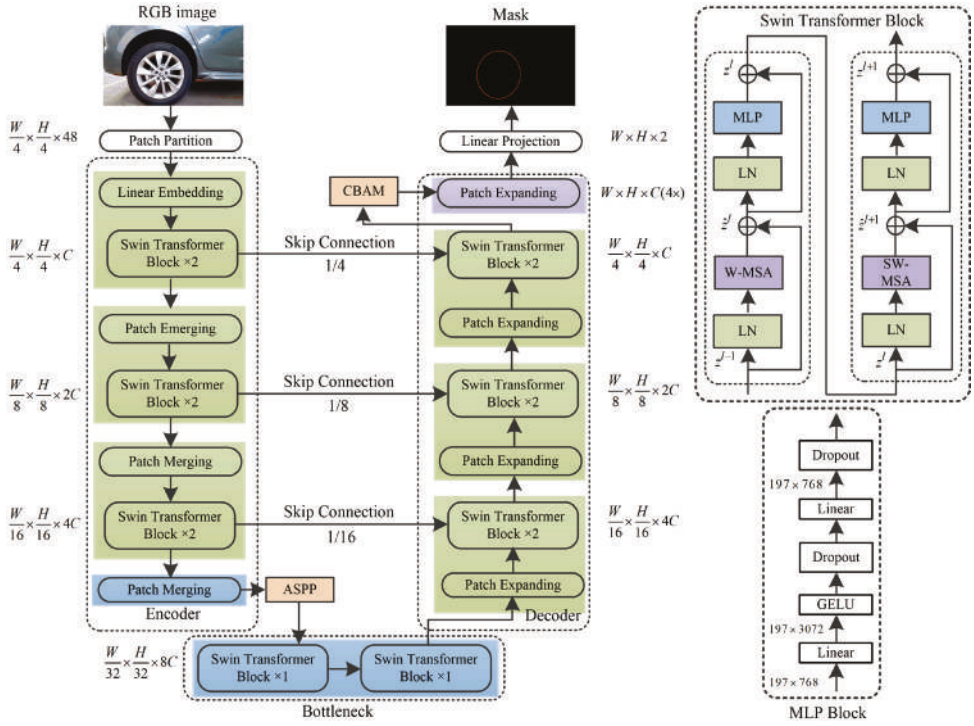


Figure 3. The network architecture of APCS-SwinUnet.

These design choices are particularly effective for wheel rim segmentation for several reasons. The ASPP module provides annulus-aware multi-scale context, enabling the network to capture both the thin rim band and the full circular structure, which helps maintain a closed, consistent rim contour while suppressing spurious responses from the tire and background. CBAM is especially beneficial under weak rim-hub contrast: by refining channel and spatial attention at decoder stages where rim and hub features are mixed, it enhances subtle structural cues along the rim boundary and reduces confusion between these two regions. The Swin-Transformer backbone contributes by modeling long-range dependencies along the rim circumference and across the whole wheel, which promotes global

https://doi.org/10.3390/metrology6010004

shape consistency while preserving local boundary details that are crucial for producing stable contours for subsequent 3D point cloud registration and angle estimation.

4.2.1. Atrous Spatial Pyramid Pooling

The segmentation task in this study aims to accurately localize the global contour of the wheel rim while capturing fine-grained boundary details. To enhance segmentation performance, we incorporate the ASPP module, as illustrated in Figure 4. ASPP strengthens the network's ability to capture multi-scale contextual information by combing atrous convolution with image-level features at varying sampling rates. The ASPP structure [27] consists of multiple convolution layers, atrous convolution layers with different dilation rates, pooling layers, ReLU activations, and an upsampling layer. Its core component is a set of parallel atrous convolutions, which enable the network to extract features across multiple receptive fields without increasing the size or computational cost. Specifically, we employ three parallel atrous convolutions with dilation rates of 4, 6 and 8. Since the proposed segmentation network is based on a Transformer architecture, the input sequence needs to be converted into a 2D convolutional format before entering the ASPP. After processing, the ASPP output is then reshaped back into sequence form for subsequent Transformer-based operations.

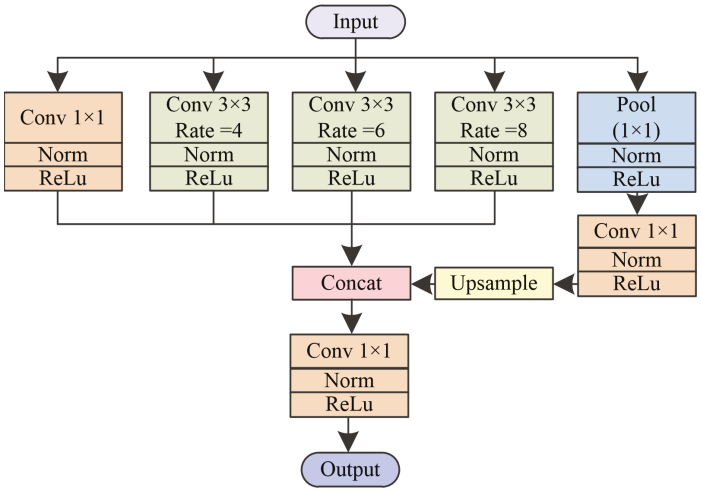


Figure 4. The network architecture of ASPP.

4.2.2. Attention Fusion Module

To enhance the network's ability to recognize wheel contour, we add a convolutional block attention module after the last Swin-transformer block of the decoder. The structure of the CBAM is shown in Figure 5. The CBAM [28] consists of a channel attention module and a spatial attention module. The channel attention focuses on identifying what features are important, and comprises an average pooling layer, a max pooling layer, a multilayer perceptron (MLP), and a Sigmoid activation. This process is formulated in Equation (1). In contrast, the spatial attention module emphasizes where the important features are located. It includes average and max pooling operations followed by a convolution layer, as described in Equation (2). The final feature map is obtained by sequentially applying both attention mechanisms, as shown in Equation (3).

$$F_c = \sigma\left\{W_1\left[W_0\left(F_{aveg_pool}\right)\right]\right\} + W_1\left[W_0\left(F_{\max_pool}\right)\right] \quad (1)$$

$$F_s = \sigma\left[f^{7\times7}\left(F_{aveg_pool}, F_{\max_pool}\right)\right], F_s \in \mathbb{R}^{1\times H\times W} \quad (2)$$

https://doi.org/10.3390/metrology6010004

$$F' = F_c \otimes F, F'' = F_s \otimes F' \tag{3}$$

where F_{avg_pool} and $F_{\max_pool}$ denote the average pooling and maximum pooling, respectively. W_0 and W_1 denote the weights of the MLP. $f^{7\times7}$ denotes the convolutional operation with a convolutional kernel size 7×7. σ denotes the sigmoid function. $\otimes$ represents the element-wise multiplication operation. F' and F'' denote the temporary output and the refined output, respectively. F, F_c and F_s denote the original feature map, output of channel attention module and output of spatial attention module, respectively.

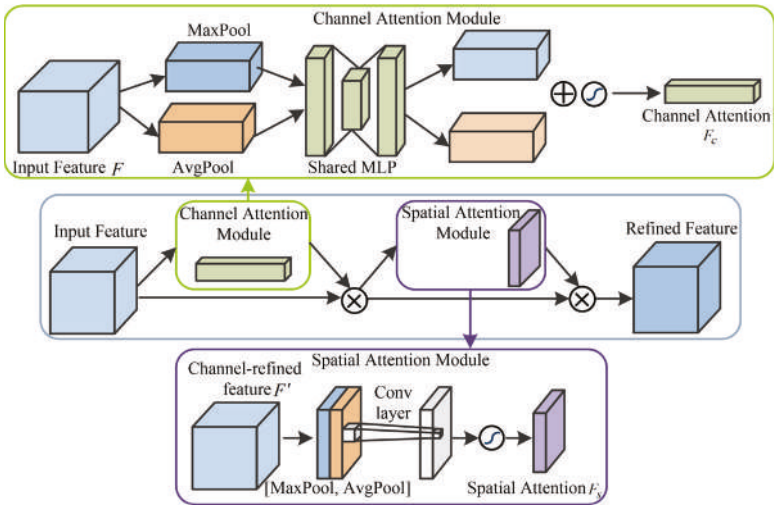


Figure 5. The architecture of the CBAM.

4.2.3. Hybrid Loss Function

To enhance the network's ability to capture fine details of wheel boundaries and improve training stability, we employed a hybrid loss function that combines Dice loss and Focal loss, as defined in Equations (4)–(7).

$$L_{loss} = (1-\tau)L_{dice} + \tau L_{focal} \tag{4}$$

$$L_{dice} = \frac{1}{N_D}\sum_{t=1}^{N_D}\left(1 - \frac{2\times\sum_k p_t^k g_t^k}{\sum_k p_t^k + \sum_k g_t^k}\right) \tag{5}$$

$$L_{focal} = \frac{1}{N_D}\sum_{t=1}^{N_D}\sum_{k=1}^{N_P} -\alpha_t\left(1-c_t^k\right)^{\beta_t}\log\left(c_t^k\right) \tag{6}$$

$$c_t^k = \begin{cases} p_t^k, & if\ g_t^k = 1 \\ 1-p_t^k, & if\ g_t^k = 0 \end{cases} \tag{7}$$

where L, L_{dice} and L_{focal} denote the total Dice, Dice loss and Focal loss, respectively. τ in Equation (4) is used to balance the contributions of L_{dice} and L_{focal}. p_t^k and g_t^k denote the predicted and ground-truth probabilities for pixel k in category t, respectively. N_D and N_P denote the number of classes and the total number of pixels, respectively. α_t and β_t are introduced to adjust the weighting for each class t, helping to mitigate the class imbalance between foreground and background.

https://doi.org/10.3390/metrology6010004

5. Toe and Camber Angles Calculation Based on Iterative Closest Point

This section is about how to combine the segmented mask and the acquired point cloud to calculate the wheel angles. It is organized in three main parts: point cloud extraction of wheel rim, point cloud registration of wheel rim based on iterative closest point and wheel angle calculation.

5.1. Point Cloud Extraction of Wheel Rim

Based on the mask generated by the APCS-SwinUnet, the wheel rim needs to be extracted from the 3D point cloud. As illustrated in Figure 6, the 3D scanner stores point cloud data in a row-wise sequence. Let the point cloud sequence be denoted by $P_i\ (X_i,\ Y_i,\ Z_i)$, where i denotes the index of the point cloud, and X, Y and Z have the same index. The point cloud corresponding to the point (x_w, y_h) on the mask can be calculated using the following equation.

$$\begin{cases} P_i' = P_i,\ if\ mask(x_w, y_h) > 0 \\ P_i' = 0,\ if\ mask(x_w, y_h) \le 0 \end{cases}, i = (y_h - 1) \times W + x_w \tag{8}$$

where P and P' denote the original point cloud and the extracted point cloud, respectively. (x_w, y_h) denotes a point on the segmented mask. W and H refer to the width and height of the image, respectively.

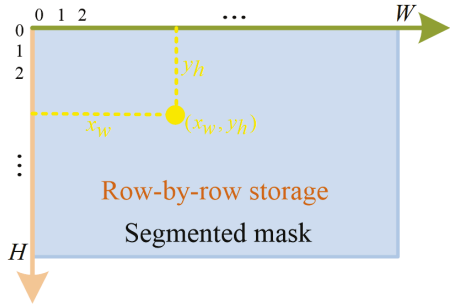


Figure 6. Schematic diagram of point cloud storage.

5.2. Point Cloud Registration of Wheel Rim Based on Iterative Closest Point

This section is about how to combine the segmented mask and the acquired point cloud to calculate the wheel angles. It is organized in three main parts: point cloud extraction of wheel rim, point cloud registration of wheel rim based on iterative closest point and wheel angle calculation. Suppose that the initial and target point cloud sequences are $P\{p_1, p_2, p_3, \ldots p_i\},\ i \le N$ and $Q\{q_1, q_2, q_3, \ldots q_j\},\ j \le N$, respectively, where N denotes the total number of points. Since P and Q are acquired from different viewpoints by the same 3D scanner, each point j in the set P can find a corresponding point in Q by the rigid transformation, including rotation matrix $\mathbf{R}$ and translation matrix $\mathbf{t}$, such that

$$\forall_j,\ q_j = \mathbf{R}p_j + \mathbf{t} \tag{9}$$

Then, we use the iterative closest point (ICP) algorithm [29] to find $\mathbf{R}$ and $\mathbf{t}$ that minimize the alignment error defined by the following objective function.

$$F = \sum_{j=1}^{N} \left\| q_j - (\mathbf{R}p_j + \mathbf{t}) \right\|^2 \tag{10}$$

To ensure robustness, a least-squares optimization is performed based on all point correspondences and the singular value decomposition (SVD) algorithm is used to solve for $\mathbf{R}$ and $\mathbf{t}$. This approach guarantees a stable and optimal solution under the rigid

https://doi.org/10.3390/metrology6010004

transformation assumption, while ensuring that the resulting **R** and **t** satisfy orthogonality constraints. Such a formulation not only minimizes the geometric alignment error but also ensures the reliability of rotation matrix **R** and translation matrix **t** for subsequent angular measurements or geometric analyses.

5.3. Toe and Camber Angles Calculation

After applying the ICP algorithm, the rotation matrix **R** is obtained, which describes the rotational relationship between the initial and target point clouds with respect to each axis. The rotation matrix can be expressed as follows:

$$\mathbf{R} = \begin{pmatrix} r_{11} & r_{12} & r_{13} \\ r_{21} & r_{21} & r_{23} \\ r_{31} & r_{32} & r_{33} \end{pmatrix} = \begin{pmatrix} \cos\psi\cos\theta & \cos\psi\sin\theta\sin\phi - \sin\psi\cos\phi & \cos\psi\sin\theta\cos\phi + \sin\psi\sin\phi \\ \sin\psi\cos\theta & \sin\psi\sin\theta\sin\phi + \cos\psi\cos\phi & \sin\psi\sin\theta\cos\phi - \cos\psi\sin\phi \\ -\sin\theta & \cos\theta\sin\phi & \cos\theta\cos\phi \end{pmatrix} \quad (11)$$

where $r_{11} \sim r_{33}$ denote the elements of the rotation matrix **R**. ψ, θ and ϕ represent the Euler angles around the z, y and x axes, respectively, which are commonly referred to as the yaw, pitch, and roll angles. Since the rotation matrix **R** is obtained through the ICP algorithm, the Euler angle can be calculated using Equations (12)–(14).

$$\psi = \tan^{-1}\left(\frac{r_{21}}{r_{11}}\right) \quad (12)$$

$$\theta = -\sin^{-1}(r_{31}) \quad (13)$$

$$\phi = \tan^{-1}\left(\frac{r_{32}}{r_{33}}\right) \quad (14)$$

Then, the Euler angle can be converted from radians to degrees using Equation (15).

$$\psi' = \psi \times \frac{180}{\pi},\ \theta' = \theta \times \frac{180}{\pi},\ \phi' = \phi \times \frac{180}{\pi} \quad (15)$$

where ψ', θ' and ϕ' denote the Euler angles in degrees corresponding to ψ, θ and ϕ respectively. In this paper, ϕ' and θ' represent the toe angle and camber angle, respectively.

6. Experimental Setup and Configuration

This section presents the detailed parameters of the measurement system, including the overall system architecture, detailed parameters of the 3-D scanner, clinometer and server.

6.1. Measurement System

As shown in Figure 7, the measurement system consists of an Azure Kinect, a clinometer, a tripod, and a computer. The Azure Kinect was positioned approximately 70 cm from the measured wheel and 29.3 cm above the ground. The intrinsic parameters (focal length, principal point, and lens distortion) and the extrinsic transformation between the RGB and depth cameras are taken from the factory calibration provided by the Azure Kinect SDK. Since the wheel-angle estimation is performed directly in the depth coordinate frame, the relevant extrinsic relationship is the pose of the Azure Kinect with respect to the wheel, defined by the measured distance, height, and the rotation angle given by the clinometer.

Since a commercial wheel alignment system is very expensive, we do not yet have sufficient budget to purchase such equipment. As a result, we adopt a feasibility-oriented experimental setup in which the Azure Kinect sensor is mounted on a tripod with a lockable pan-tilt head, and its pose is adjusted manually via the handle. In this setup, the camber and toe angles are simulated by rotating the Azure Kinect vertically and horizontally,

https://doi.org/10.3390/metrology6010004

respectively, while keeping the wheel itself stationary. Because the sensor is adjusted manually, it is only approximately, but not perfectly, parallel to the wheel plane. The corresponding camber and toe angles are measured using a clinometer, and these readings are treated as ground-truth values in our experiments. In the implemented system, the initial scan is taken as the geometric reference configuration of the wheel rim, and all subsequent measurements are obtained by registering the new rim point clouds to this reference using ICP. Consequently, the proposed method relies on relative pose estimation between the reference and current rim configurations, rather than on any absolute pose of the sensor. This design makes the approach inherently robust to non-parallelism between the camera plane and the wheel surface, as long as the relative motion between the sensor and the wheel is accurately captured.

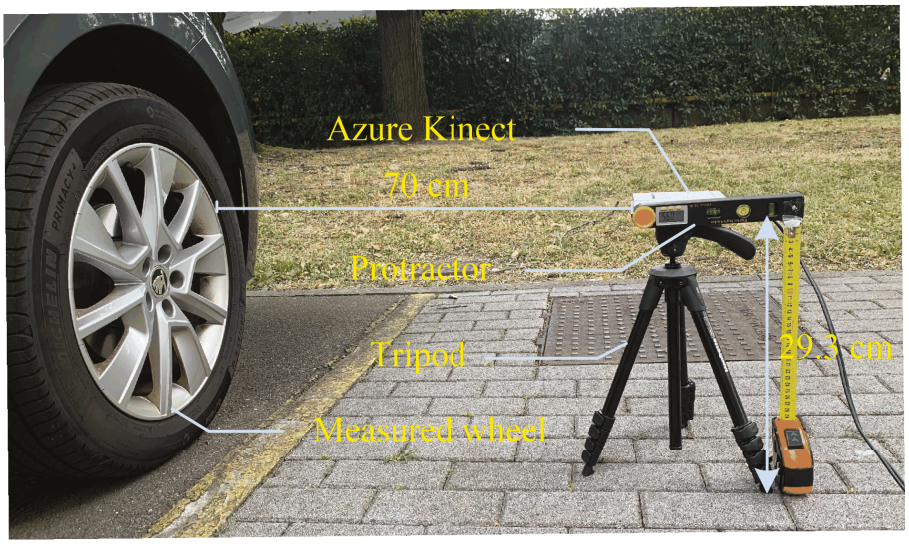


Figure 7. Schematic diagram of the measurement platform.

The main uncertainty sources in this feasibility setup include depth-measurement noise, the limited resolution and alignment accuracy of the clinometer, manual sensor positioning, and segmentation errors in the wheel-rim boundary that propagate to the estimated angles. A complete uncertainty budget and a more detailed repeatability analysis based on higher-precision fixtures and encoders are left for future work.

6.2. Three-Dimensional Scanner Description

The 3D scanner used in this study is the Azure Kinect, as shown in Figure 8. The Kinect is a low-cost 3D scanner that integrates three main imaging components: an RGB camera, a depth camera, and infrared (IR) emitters. It recovers the depth map and 3D point cloud based on the time-of-flight (ToF) principle. Specifically, the device emits IR light pulses onto the object, and the depth is calculated based on the time taken for the reflected light to return to the sensor. The key parameters used in this study are as follows: the RGB camera acquires images at a resolution of 1920 $\times$ 1080 pixels, with a frame rate of 30 fps and a 16:9 aspect ratio. The depth camera operates in Wide Field of View (WFOV) mode. The IR settings include 9 pulses, 125 µs pulse width, 8 idle periods, 1450 µs idle time, and 12.8 ms exposure time. Data acquisition was implemented using the Azure Kinect SDK in Visual Studio 2019. A custom program was developed to capture both RGB images and the corresponding 3D point clouds of the measured wheel.

https://doi.org/10.3390/metrology6010004



Figure 8. Schematic diagram of the Azure Kinect.

6.3. Description of Clinometer

The clinometer is used to measure the rotation angles of the Azure Kinect. As shown in Figure 7, it is fixed to the Kinect and rotates together with it either horizontally or vertically. The clinometer used in this study has a measurement range from 0° to 360° degrees, with a resolution of 0.05°.

6.4. Server Configuration

The APCS-SwinUnet network was trained on a server equipped with an NVIDIA GeForce RTX 3090Ti graphics card (24 GB; NVIDIA Corporation, Santa Clara, CA, USA), an Intel Core i9 CPU (4.3 GHz; Intel Corporation, Santa Clara, CA, USA), and 64 GB of RAM (Samsung Electronics Co., Ltd., Suwon, Republic of Korea). The system runs on Ubuntu 20.04. The software environment includes Python 3.8, Pytorch 1.13, and CUDA 11.6.

7. Experimental Results and Analysis

This section aims to verify and evaluate the feasibility of the proposed solution, focusing on the segmentation results and the calculated wheel angles. The experimental details and corresponding results are presented below.

7.1. Wheel Segmentation Experiments

We first provide details of the network training process, including the dataset composition and parameter settings of the proposed APCS-SwinUnet. Subsequently, the segmentation performance is evaluated under normal conditions through both quantitative analysis based on defined evaluation metrics and quantitative assessment of the segmentation results. Next, we evaluate the segmentation performance of the proposed method on our wheel dataset under varying illumination conditions. Then, feature maps from both the encoder and decoder are visualized. Finally, the performance of different segmentation methods is compared on a public wheel dataset.

7.1.1. Datasets for Training and Testing

In this study, 535 different wheel types were collected. These wheel types come from different vehicles, most of which are passenger vehicles, and were captured primarily under sunny and overcast outdoor conditions. Among these 535 wheel types, 423 types were assigned to the training set and the remaining 112 types to the test set. This split is performed at the wheel-type level, so that images (original or augmented) belonging to the same wheel type never appear in both the training and test sets. To enhance the diversity and robustness of the training data, we applied a series of data augmentation techniques to the initial training set, including brightness and contrast adjustment, noise injection, rotation, and other geometric and photometric transformations. As a result, the training set contains 5499 images in total. The test set comprises 112 original, unaltered images and is not augmented, in order to preserve the integrity and validity of the evaluation.

https://doi.org/10.3390/metrology6010004

7.1.2. Parameter Settings of APCS-SwinUnet

The network was trained for 30 epochs with a batch size of 6. Input images were resized to 512 × 512 pixels after being fed into the network. The Adam optimizer was used, with an initial learning rate 0.2 and a drop path rate of 0.001, respectively. The window size and embedding dimension were set to 32 and 96, respectively. The numbers of multi-head attention modules in each stage were 3, 6, 12, and 24. The dilation rates in the ASPP module were set to 4, 6 and 8, respectively.

7.1.3. Evaluation Criteria for Segmentation Network

We first use the Dice similarity coefficient (Dice) to evaluate the overlap and similarity between the predicted mask (P) and the ground truth mask (G), as illustrated in the schematic diagram in Figure 9a. The Dice coefficient can be calculated by Equation (16).

$$Dice = \frac{2|P \cap G|}{|P| \cup |G|} \tag{16}$$

where $|P \cap G|$ and $|P| \cup |G|$ denote the number of intersecting pixels and the total number of pixels of the predicted and ground truth regions, respectively. In addition, we introduce the Hausdorff distance (HD) metric, whose schematic diagram is shown in Figure 9b. While Dice coefficient is more sensitive to the interior of the mask, HD focuses on boundary differences. The HD is defined by the following equation.

$$\begin{cases} D(G,P) = \max(d(G,P), d(G,P)) \\ d(G,P) = \max\limits_{g \in G}\left\{\min\limits_{p \in P}\|g-p\|\right\} \\ d(P,G) = \max\limits_{p \in P}\left\{\min\limits_{g \in G}\|p-g\|\right\} \end{cases} \tag{17}$$

where $\|\cdot\|$ represents a distance paradigm operation (e.g., Euclidean distance). The Hausdorff Distance is a bidirectional metric composed of two one-way distances, $d(G,P)$ and $d(P,G)$. Specifically, $D(G,P)$ computes the distance $\|g-p\|$ between each point g_i in the set of G to the point p_i that is closest to this point g_i. Then, the maximum value of these distances is the value of this distance as the value of $d(G,P)$. Similarly, $d(P,G)$ is computed by the same way. Finally, the bidirectional HD is the largest of the two unidirectional distances $d(G,P)$ and $d(P,G)$, which denotes the maximum degree of mismatch between G and P. In this study, we adopt HD95, which represents the 95% of all point-to-set distances between H and G. HD95 can reduce the effect of outliers and enhance the stability of the evaluation.

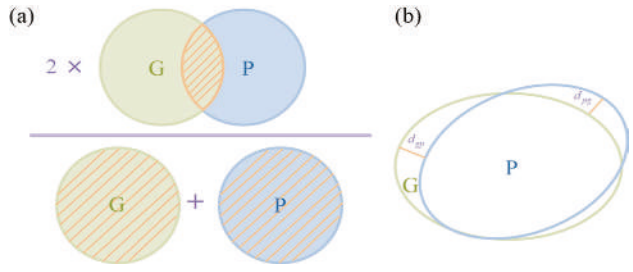


Figure 9. Schematic diagram of metrics. (**a**) Schematic diagram of Dice. (**b**) Schematic diagram of HD95.

7.1.4. Comparisons with Different Segmentation Networks

To evaluate the performance of the proposed APCS-SwinUnet network, we conducted comparisons with several representative segmentation networks, including FCN [30], DeepLabV3 [27], OcUnet [31], U-Net [32], Att-Unet [33], U-Net 2+ [34], U-Net 3+ [35], Tran-

https://doi.org/10.3390/metrology6010004

sUnet [36], and SwinUnet [37] networks. Both quantitative and qualitative segmentation results are provided for comprehensive analysis.

(1) Quantitative Analysis:

The Dice scores achieved by different methods are summarized in Table 1. As shown in Table 1, there are significant differences among the methods. The proposed method achieves a relatively high Dice score and a comparatively low HD95 value. A higher Dice score indicates better overall contour of the wheel, while a lower HD95 indicates improved accuracy in delineating fine boundary details. Empirically, APCS-SwinUnet outperforms strong baselines, including SwinUnet and TransUnet, in both Dice and HD95. In particular, SwinUnet achieves a Dice of 90.23% and an HD95 of 2.47, whereas APCS-SwinUnet achieves a Dice of 90.66% and an HD95 of 2.11. The 0.43% improvement in Dice reflects better overall rim contour segmentation, while the reduction in HD95 directly indicates more accurate localization of fine boundary regions, which is precisely the aspect targeted in thin-structure segmentation. In practice, these improvements translate into measurable gains in toe and camber angle estimation, confirming that the adapted architecture is effective for the real-world wheel alignment scenario.

Table 1. Comparisons with different networks.

Methods	Dice (%)	HD95
FCN	84.12	8.62
DeepLabV3	86.67	8.18
OcNet	88.11	8.06
U-Net	85.76	11.90
Att-Unet	88.65	9.65
U-Net 2+	89.10	3.00
U-Net 3+	89.49	3.43
TransUnet	89.85	2.56
SwinUnet	90.23	2.47
APCS-SwinUnet	90.66	2.11

These improvements mainly stem from three factors: the strong feature extraction of Swin Transformer blocks, the ASPP module's ability to capture multi-scale rim boundaries, and the CBAM attention mechanism, which focuses on rim regions while suppressing background clutter.

(2) Qualitative Analysis:

To more intuitively compare the strengths and weakness of each method, we conducted a qualitative analysis on typical segmentation results. Specifically, five types of wheels (T1~T5), shown in the first row of Figure 10, were segmented using different network in Table 1. For wheel type T1, all listed methods achieve satisfactory segmented results. However, when the wheel rotates, as in the T2 column, the segmentation becomes more challenging. As shown in the T2 column of Figure 10, U-Net and Att-Unet networks not only miss part of the wheel region but also mistakenly classify background regions as wheel areas. In contrast, the other methods demonstrate better performance on T2 type of wheel. For the T3 type, methods including FCN, DeepLabV3, U-Net and U-Net2+ tend to misclassify the wheel fender as part of the wheel region, likely due to the fender's circular shape resembling the upper portion of the wheel. In type T4, the wheel's lower edge is very close to the ground, making it difficult to distinguish from the background. As a result, methods such as U-Net, Att-UNet, U-Net2+, U-Net3+, and SwinUnet misclassify parts of the ground as the wheel. Type T5 presents a different challenge: the wheel edges are particularly narrow, which leads to partial omission of the wheel region by U-Net,

https://doi.org/10.3390/metrology6010004

Att-UNet, U-Net2+, U-Net3+, TransUnet, and SwinUnet. In contrast, the proposed method consistently delivers accurate segmentation across all wheel types (T1~T5), producing results that are visually closer to the ground truth (GT), as seen in Figure 10. It is worth noting that although some methods may not show obvious omissions or misclassifications, their segmentation masks may still be slightly larger or smaller than the ground truth, particularly around the boundaries. This discrepancy is reflected in the quantitative results presented in Table 1. In summary, from both quantitative and qualitative perspectives, the proposed method demonstrates superior and more stable segmentation performance compared to other mainstream networks. Although the Dice score of our method is 0.43% higher than that of SwinUnet, it achieves better boundary precision and segmentation stability, which is beneficial for subsequent point cloud registration and angle computation.

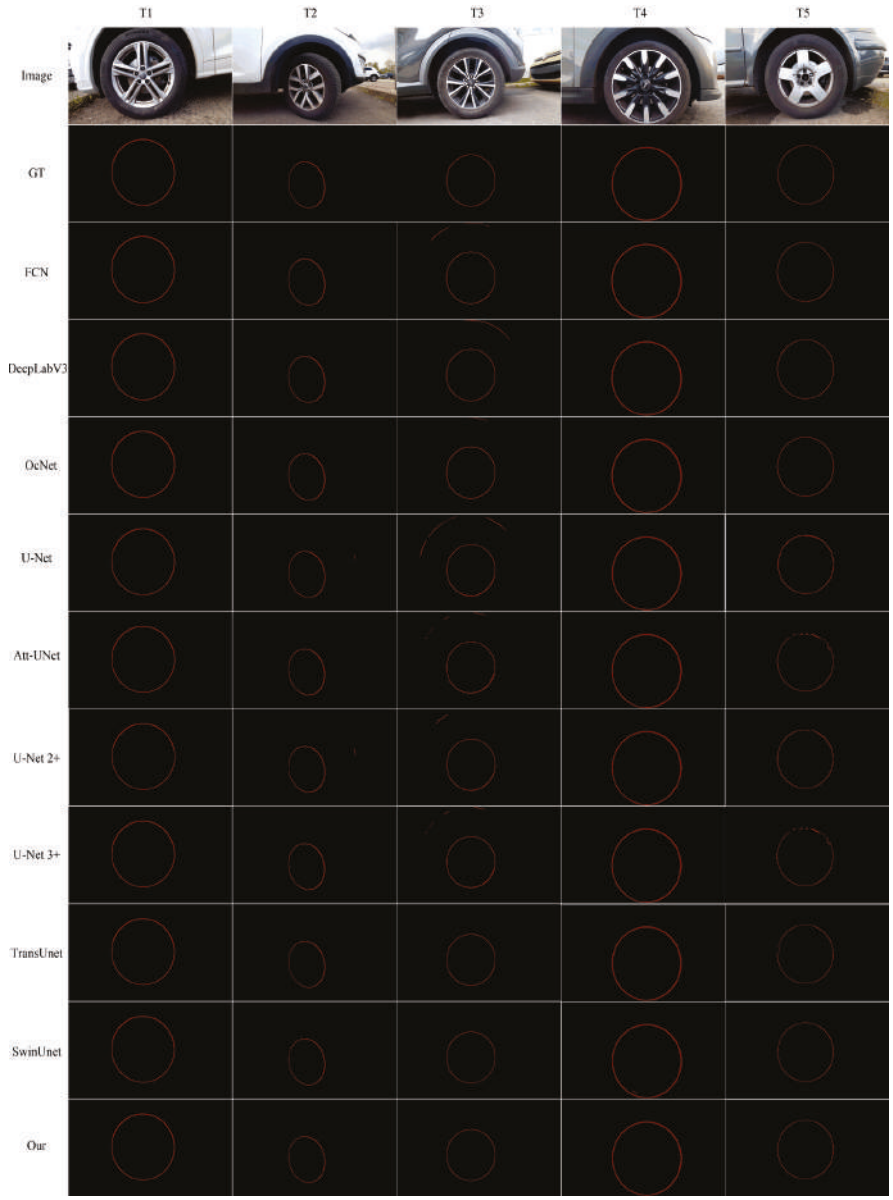


Figure 10. The segmented results produced by different networks.

7.1.5. Comparison Results Under Inconsistent Illuminations

To evaluate the impact of illumination changes, we collected 106 wheels under diverse lighting conditions, including cloudy weather, direct sunlight, and shadow occlusion, with examples shown in Figure 11. The previously trained models were applied to this

https://doi.org/10.3390/metrology6010004

dataset, and the segmentation results are summarized in Table 2. A comparison between Tables 1 and 2 reveals that most methods suffer from performance degradation to varying degrees under inconsistent illumination, particularly in accurately delineating the edges of the wheel rims, as reflected by the HD95 metrics. In contrast, the proposed method exhibits a smaller performance drop, indicating greater stability and robustness under different lighting conditions.

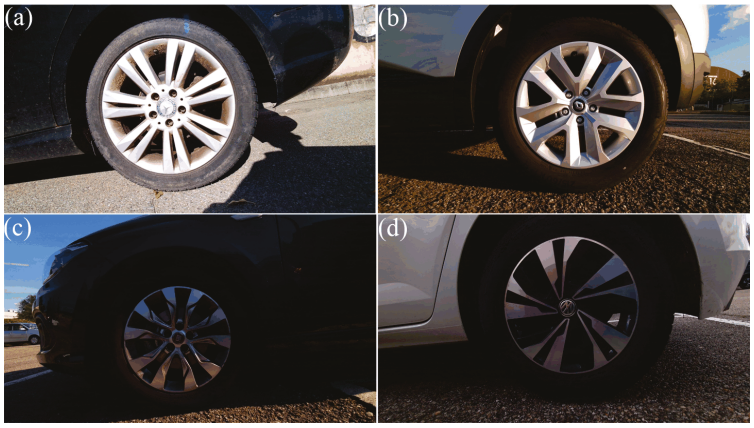


Figure 11. Wheel images under various illumination conditions. (**a**) Sunlight at noon. (**b**) Afternoon. sunlight. (**c**) Backlit with shadow. (**d**) Partial shadow.

Table 2. Comparisons under inconsistent illumination.

Methods	Dice (%)	HD95
FCN	84.35	16.95
DeepLabV3	86.57	10.51
OcNet	87.74	17.48
U-Net	84.10	21.48
Att-Unet	86.97	31.55
U-Net 2+	86.89	25.86
U-Net 3+	88.60	12.46
TransUnet	90.19	2.80
SwinUnet	90.16	2.71
APCS-SwinUnet	90.46	2.51

7.1.6. Feature Visualization of Encoder and Decoder

To provide a clearer and more intuitive understanding of the proposed network's internal representations, we use the wheel image in Figure 11b as an example and visualize the feature maps of each stage of the encoder and decoder. The feature maps of the four transformer modules in the encoder are shown in Figure 12a–d, while those in the decode are shown in Figure 12e–h, respectively. For consistency, all feature maps in Figure 12a–h are displayed at the same size. Figure 12a–d illustrate the progressive abstraction from low-level to high-level semantic features, whereas Figure 12e–h demonstrate the gradual restoration of spatial resolution via upsampling. As observed in Figure 12, the APCS-SwinUnet network consistently focuses on regions near the wheel rim in both encoder and decoder stages, while background and vehicle body regions are significantly suppressed. This facilitates accurate segmentation of the wheel rim region, particularly its contour.

https://doi.org/10.3390/metrology6010004

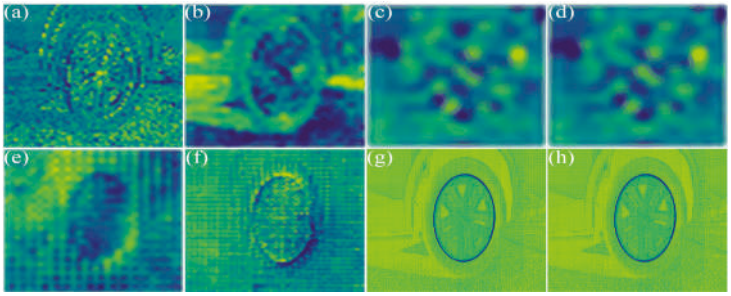


Figure 12. Visualization of feature maps at different stages of the network. (**a**–**d**) Encoder stages 1~4 (left side of Figure 3). (**e**–**h**) Decoder stage 5~8 (right side of Figure 3).

7.1.7. Comparison Results on the Public Wheel Dataset

To evaluate the performance of the proposed method on public wheel datasets, we selected a publicly available dataset named CAWDEC [38]. Representative sample images are shown in Figure 13. As this dataset does not provide ground-truth masks for wheel hub contours, we manually annotated 101 images to support evaluation. Given the time-consuming labeling process, we annotated only 101 images from the CAWDEC dataset. These annotated images were then used to compare the proposed method with several mainstream segmentation approaches. Thus, this experiment mainly serves as a complementary 2D rim-segmentation benchmark and is inherently constrained by the limited number of manually annotated samples and the practical cost of dense wheel-rim labeling. To better assess the generalization ability of the proposed method, we did not retrain the model on the CAWDEC dataset. Instead, the model trained on our own dataset was directly applied to perform segmentation. The segmentation results of different methods are summarized in Table 3.

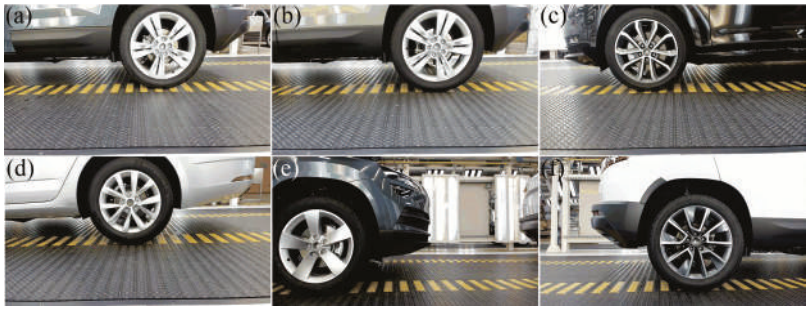


Figure 13. Examples from the public wheel dataset. (**a**–**f**) Sample illustrations from various, publicly available wheel datasets.

Table 3. Comparisons of wheel public dataset.

Methods	Dice (%)	HD95
FCN	70.38	28.79
DeepLabV3	72.47	4.37
OcNet	72.24	4.58
U-Net	72.87	16.68
Att-Unet	74.31	6.13
U-Net 2+	74.49	5.53
U-Net 3+	75.50	9.51
TransUnet	75.35	4.00
SwinUnet	75.27	9.92
APCS-SwinUnet	75.88	3.84

https://doi.org/10.3390/metrology6010004

As observed, most methods exhibit a notable drop in accuracy, likely due to inconsistencies in acquisition devices, shooting angles, and environmental conditions. Despite these challenges, the proposed method achieves comparatively better segmentation performance. It is worth noting that segmentation serves only as an intermediate step in the proposed framework, with the resulting segmentation masks used to extract the point cloud of the wheel rim. Therefore, all subsequent evaluations are conducted on images captured by the developed platform. As shown in Table 1, the proposed method also achieves strong segmentation performance on the developed platform. Accurate wheel-rim annotation requires fine-grained, pixel-level masks and is therefore extremely time-consuming. Nevertheless, since this research is still in the early stages, we plan to further expand the dataset in both size and diversity in future work.

7.2. Point Cloud Extraction Result of Wheel Rim

After obtaining the wheel rim mask using APCS-SwinUnet, the corresponding point cloud can be extracted from the full point cloud. To illustrate this process, we take the wheel in Figure 14a as an example. Its point cloud, acquired by the Azure Kinect, is shown in Figure 14b. The wheel image is then fed into the APCS-SwinUnet for inference, producing a mask containing only the wheel rim, as shown in Figure 14c. Finally, the point cloud of the wheel rim is extracted using the segmented mask and the method described in Section 5.1, which is shown in Figure 14d.

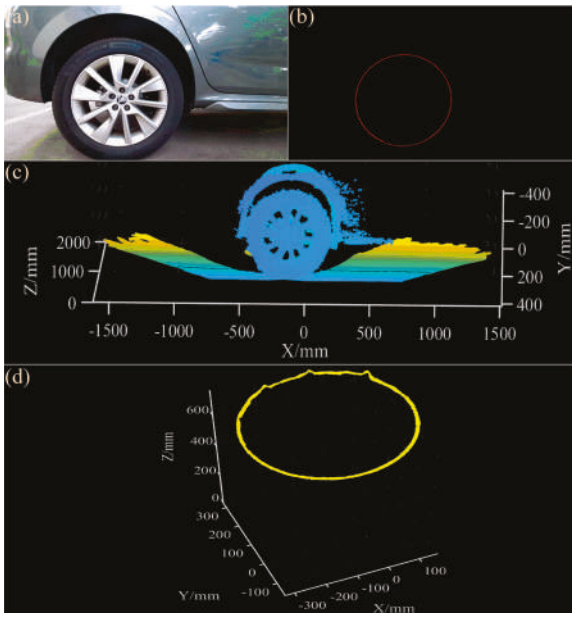


Figure 14. Point cloud extraction results of the wheel rim. (**a**) RGB image of the wheel. (**b**) Segmented mask of the wheel rim. (**c**) Original point cloud. (**d**) Extracted point cloud corresponding to the wheel rim.

7.3. Wheel Angle Measurement and Evaluation

7.3.1. Point Cloud Registration Result

The initial point cloud and registered point cloud are shown in Figure 15a and 15d, respectively. Figure 15b,c displays the initial point clouds from two additional positions, with their corresponding registration results presented in Figure 15e,f. This study uses the reference and target point clouds shown in Figure 15a as an example to illustrate the process of point cloud registration and wheel angle calculation. The registration between the reference and target point clouds, as shown in Figure 15b, is performed using the

https://doi.org/10.3390/metrology6010004

ICP algorithm described in Section 5.2. The corresponding rotation matrix is provided in Equation (18).

$$\mathbf{R} = \begin{pmatrix} r_{11} & r_{12} & r_{13} \\ r_{21} & r_{21} & r_{23} \\ r_{31} & r_{32} & r_{33} \end{pmatrix} = \begin{pmatrix} 0.9988 & 0.0001 & 0.0495 \\ -0.0002 & 1.0000 & 0.0034 \\ -0.0495 & -0.0034 & 0.9988 \end{pmatrix} \tag{18}$$

The rotation matrix **R** is an orthogonal matrix used to align the reference point cloud with the target point cloud. The rotation matrix **R** contains nine elements, denoted as $r_{11} \sim r_{33}$. The specific definition of $r_{11} \sim r_{33}$ is provided in Equation (11). $\hat{X}(0.9988, -0.0002, -0.0495)^T$, $\hat{Y}(0.0001,\ 1.0000, -0.0034)^T$ and $\hat{Z}(0.00495,\ 0.0034,\ 0.9988)^T$ in matrix **R** represent the projections of X', Y' and Z' axes of the target coordinate system onto the reference coordinate system, respectively. Next, the rotation matrix can be decomposed into radian angles $(\psi,\ \theta,\ \phi)$ representing rotation rotated around Z, Y, X axes. $(\psi,\ \theta,\ \phi)$ in radian values are then converted into their corresponding degrees angles $(\psi',\ \theta',\ \phi')$. Both the radian and degree values are summarized in Table 4. Since the Kinect is currently moving along the horizontal direction, this simulated a camber angle, with the resulting angle θ'_y representing the target camber angle.

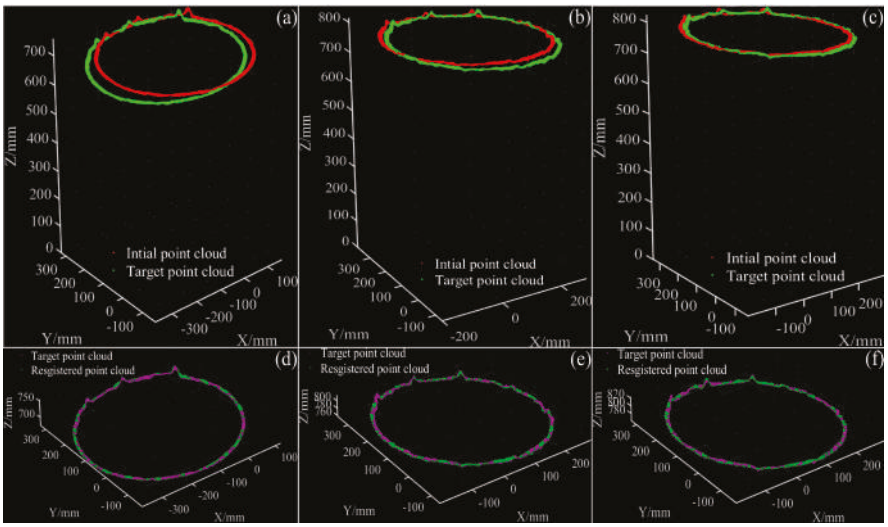


Figure 15. Point cloud registration results between the initial point clouds and target point clouds. (**a**–**c**) Initial and target point clouds. (**d**–**f**) Corresponding point cloud registration results.

Table 4. Angle measurement results.

ψ (rad)	θ (rad)	ϕ (rad)	$\psi'(^\circ)$	$\theta'(^\circ)$	$\phi'(^\circ)$
−0.00020	0.04952	−0.00340	−0.01146	2.83729	−0.19481

To evaluate the reliability and robustness of point cloud registration process, Gaussian noise with a standard deviation σ ranging from 0.01 to 0.10 was added to both the original reference point cloud and target point cloud shown in Figure 15a. The ICP algorithm was then applied to perform point cloud registration and compute the corresponding rotation matrices, which were subsequently used to calculate the wheel angles. To more intuitively assess the impact of segmentation on angle estimation accuracy, a relative error metric is introduced, as defined in Equation (19).

$$R_e = \frac{|y_i - \hat{y}_i|}{|y_i|} \tag{19}$$

https://doi.org/10.3390/metrology6010004

where y_i and $\hat{y}_i$ denote the real angle and the measured angle of i, respectively.

The measured angles, absolute errors and relative errors under different noise levels are summarized in Table 5. As shown in Table 5, the estimated wheel angles remain relatively stable despite increasing noise levels, with both absolute and relative errors being small. These results demonstrate the obtained rotation matrices and the point cloud registration process are stable and robust.

Table 5. Angle measurement results under noisy point clouds.

Noise Level	Real (°)	Meas (°)	Error (°)	R_e (%)
0.01	2.8500	2.8373	−0.0127	0.45
0.02	2.8500	2.8341	−0.0159	0.56
0.03	2.8500	2.8333	−0.0167	0.59
0.04	2.8500	2.8334	−0.0166	0.58
0.05	2.8500	2.8339	−0.0161	0.56
0.06	2.8500	2.8348	−0.0152	0.53
0.07	2.8500	2.8340	−0.0160	0.56
0.08	2.8500	2.8333	−0.0167	0.59
0.09	2.8500	2.8339	−0.0161	0.56
0.10	2.8500	2.8336	−0.0164	0.58

7.3.2. Measurement Results of Toe and Camber Angles

In this section, we give the results of angle measurements at different positions and directions. In addition, in order to evaluate the effect of the measurement distance on angle measurement, the measurement platform was placed at different distances from the wheel. The measured results are shown in Tables 6 and 7, respectively. D_s and D_e in Tables 6 and 7 denote the distance of the innermost and outermost sides of the wheel from the platform, respectively. We can see from Tables 6 and 7 that the maximum measurement errors of the toe and camber angles are and -0.105° and 0.158°, respectively. Most of the measured angles are very close to the real angle, which proves that the proposed method has a strong stability with the change in the measurement distance.

Table 6. Measurement results of toe angles.

No	D_s (mm)	D_e (mm)	Real (°)	Meas (°)	Error (°)	R_e (%)
1	687	743	−1.450	−1.457	−0.007	0.48
2	677	754	2.850	2.837	−0.013	0.46
3	691	733	−1.650	−1.755	−0.105	6.36

Table 7. Measurement results of camber angles.

No	D_s (mm)	D_e (mm)	Real (°)	Meas (°)	Error (°)	R_e (%)
1	751	802	−0.750	−0.807	−0.057	7.60
2	778	821	−0.650	−0.685	−0.035	5.38
3	750	808	3.200	3.358	0.158	4.94

https://doi.org/10.3390/metrology6010004

7.4. Extended Experiments

7.4.1. Angle Measurement Results of the Raw Point Couds

To verify the necessity of the proposed segmentation-guided registration scheme, we first attempted direct registration using the raw wheel point clouds, each containing up 2,073,000 points. However, due to the high point density, point cloud registration was extremely time-consuming and often exhibited poor convergence. To address this issue, we applied downsampling to the raw wheel point clouds at various rates (ranging from 10% to 80%) and performed point cloud registration on the sampled data. The experimental results shown in Table 8 indicate that increasing the sampling rate leads to longer registration times, while the angle estimation accuracy remains limited and does not improve with more point data. This is primarily due to the presence of unstable points from the car body, tire, and background in the raw data, which negatively affect the registration process and ultimately introduce angle estimation errors. In addition to poor accuracy, when the sampling rate reaches 80%, the point cloud registration takes nearly seven hours, rendering the registration process time-consuming and less viable. In contrast, the proposed solution first segments the wheel rim using a dedicated network before point cloud registration, enabling faster and more accurate angle estimation. This proposed solution not only improves the measurement efficiency but also enhances the angle estimation accuracy. The experimental results in Table 8 validate the above conclusions.

Table 8. Registration time and angle estimation across sampling rates.

Sampling Rate	Time (s)	Real (°)	Meas (°)	R_e (%)
10%	260.105	1.766	−1.084	38.04
20%	1006.079	1.747	−1.103	38.70
30%	2461.575	1.732	−1.118	39.23
40%	5875.771	1.728	−1.122	39.37
50%	8530.951	1.728	−1.122	39.37
60%	10,223.756	1.721	−1.129	39.61
70%	16,907.151	1.720	−1.130	39.65
80%	24,226.577	1.723	−1.127	39.54

7.4.2. Impact of Pixel Shifts on Angle Measurement

To evaluate the impact of wheel rim segmentation on wheel angle estimation, this section uses the wheel mask shown in Figure 16a as an example. The masks are then horizontally shifted by several pixels to the left and right, as shown in Figure 16b,c, respectively. These shifted masks are subsequently used for point cloud registration, and the corresponding wheel angles are calculated. The experimental results are presented in Table 9, where S_L, M_L, S_R, M_R, A_e, and R_e denote the leftward pixel shift, leftward angular measurement, rightward pixel shift, rightward angular measurement, absolute angular error, and relative angular error, respectively. As observed from Table 9, the angle estimation error increases with the magnitude of the pixel shift, regardless of whether the masks are shifted to the left or right. This growing error is primarily attributed to the inclusion of non-wheel-rim point cloud regions in the registration process as the shift increases. These extraneous regions lie outside the actual wheel rim and do not form a consistent planar surface. Their varying distances from the measurement platform introduce inaccuracies in point cloud registration, ultimately leading to deviations from the true wheel angle. These findings highlight the importance of accurate wheel rim segmentation for precise wheel angle estimation.

https://doi.org/10.3390/metrology6010004

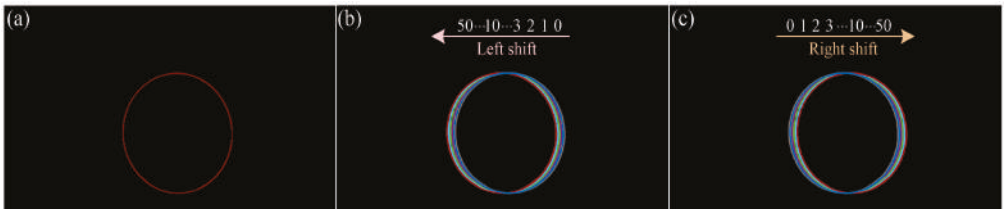


Figure 16. Illustration of pixel-wise mask shifting. (**a**) Original mask. (**b**) Left shift in the mask. (**c**) Right shift in the mask.

Table 9. Angle measurement results under different mask pixel shifts.

S_L	M_L (°)	A_e (°)	R_e (%)	S_R	M_R (°)	A_e (°)	R_e (%)
0	−1.457	0.011	0.48	0	−1.457	0.011	0.48
−1	−1.439	0.011	0.76	1	−1.469	−0.019	1.31
−2	−1.424	0.026	1.79	2	−1.481	−0.031	2.14
−3	−1.416	0.034	2.34	3	−1.498	−0.048	3.31
−4	−1.405	0.045	3.10	4	−1.510	−0.060	4.14

Table 9. *Cont.*

S_L	M_L (°)	A_e (°)	R_e (%)	S_R	M_R (°)	A_e (°)	R_e (%)
−5	−1.394	0.056	3.86	5	−1.528	−0.078	5.38
−6	−1.357	0.093	6.41	6	−1.543	−0.093	6.41
−7	−1.321	0.129	8.90	7	−1.560	−0.110	7.59
−8	−1.291	0.159	10.97	8	−1.594	−0.144	9.93
−9	−1.257	0.193	13.31	9	−1.612	−0.162	11.17
−10	−1.202	0.248	17.10	10	−1.666	−0.216	14.90
−15	−0.840	0.610	42.07	15	−2.019	−0.569	39.24
−20	−0.480	0.970	66.90	20	−2.431	−0.981	67.66
−30	0.207	1.657	114.28	30	−3.101	−1.651	113.86
−40	0.963	2.413	166.41	40	−3.833	−2.383	164.34
−50	1.850	3.300	227.59	50	−4.892	−3.442	237.38

7.4.3. Impact of Segmentation Methods on Angle Measurement

To evaluate the impact of different segmentation methods on wheel angle measurement, a wheel with a ground-truth angle of 3.200° is selected as an example for analysis. Segmentation masks generated by various methods are used to estimate the wheel angle, and the results are summarized in Table 10. As shown in Table 10, the accuracy of angle estimation varies significantly across different segmentation methods, primarily due to significant differences in the Dice coefficients and HD95 values. Compared with the other methods, the proposed approach achieves more accurate segmentation of the wheel rim, particularly around the boundaries, which results in higher precision in the final angle estimation. The experimental results presented in this section demonstrate a strong correlation between the accuracy of wheel rim segmentation and the accuracy of angle estimation. Moreover, compared with other methods, the proposed approach yields smaller angle estimation errors, further validate its effectiveness.

https://doi.org/10.3390/metrology6010004

Table 10. Angle measurement results of different segmentation methods.

Methods	Dice (%)	HD95	Meas (°)	Error (°)	R_e(%)
FCN	83.29	2.24	3.425	0.225	7.03
DeepLabV3	85.12	3.00	3.530	0.330	10.31
OcNet	86.36	2.24	3.515	0.315	9.84
U-Net	87.94	4.47	3.769	0.569	17.78
Att-Unet	89.67	3.61	3.646	0.446	13.94
U-Net 2+	89.13	4.00	2.741	−0.459	14.34
U-Net 3+	89.27	2.00	2.980	−0.220	6.88
TransUnet	89.72	2.83	2.874	−0.326	10.19
SwinUnet	90.09	2.24	3.404	0.204	6.38
APCS-SwinUnet	90.55	2.00	3.358	0.158	4.94

7.4.4. Runtime and Computational Efficiency

To quantify the computational efficiency of the proposed solution, we evaluated the end-to-end runtime of the complete pipeline, which consists of three main stages: wheel rim edge segmentation, point cloud registration, and angle estimation. On our test platform, the segmentation network requires approximately 0.463 s per image to generate the wheel rim mask. The subsequent point cloud registration and angle estimation take about 4.476 s per sample, resulting in a total processing time of roughly 4.939 s per wheel. For comparison, when point cloud matching is performed directly on the raw point cloud without prior segmentation, the computational burden increases drastically. At a sampling rate of 80%, the point cloud registration alone requires nearly 7 h to complete, and the resulting accuracy is significantly lower. These results demonstrate that the proposed method offers a favorable trade-off between computational efficiency and practical applicability in wheel-alignment scenarios.

7.4.5. Repeatability Experiments at Different Distances and Illuminations

To evaluate the stability and robustness of the proposed method under varying distances and illuminations, a series of repeated experiments were conducted. Four alignment cases were considered in this section: toe-in, toe-out, negative camber, and positive camber. The experiments were carried out on a sunny and breezy day, with the ambient temperature around 31 degrees Celsius. To account for illumination variations, wheel measurements were taken at 11:39 a.m., 12:45 p.m., 18:01 p.m., and 19:08 p.m. The corresponding wheel images captured at these different times are shown in Figure 17.



Figure 17. Wheel images under different illumination conditions and distances. (**a**–**d**) Wheel images captured at 12:45 p.m., 11:39 a.m., 18:01 p.m. and 19:08 p.m., respectively.

Taking the toe-in case as an example, five RGB images and corresponding point clouds were acquired at the initial wheel position using the Azure Kinect, with a two-minute

https://doi.org/10.3390/metrology6010004

interval between each capture. After repositioning the sensor, another five sets of RGB images and point clouds were collected at the target position using the same procedure. Including the time required for data storage, each angular repeatability experiments took approximately twenty minutes. Given the extended acquisition period, several random factors were considered, including sensor noise, illumination variation, wind disturbances, and the inherent measurement uncertainty of the Azure Kinect. The repeatability results for toe-in, toe-out, negative camber, and positive camber angles are summarized in Table 11. For each alignment case, five data groups were collected at both the initial and target positions. These were paired to compute five corresponding angular values per case. As shown in Table 11, the angular measurement errors under varying distances and lighting conditions remain within a narrow range. To quantitatively assess the accuracy, mean absolute error (MAE) and root mean square error (RMSE) were calculated according to Equation (20).

$$\begin{cases} MAE = \dfrac{1}{n}\sum_{i=1}^{n}(y_i - \hat{y}_i) \\ RMSE = \sqrt{\dfrac{1}{n}\sum_{i=1}^{n}(y_i - \hat{y}_i)^2} \end{cases} \tag{20}$$

where MAE and $RMSE$ denote the mean absolute error and root mean square error. y_i and $\hat{y}_i$ denote the real value and the measured value of i, while N denotes the total number of samples. The MAE and RMSE for the toe angle are -0.045° and 0.078°, respectively, while those for the camber angle are 0.010° and 0.066°, respectively. These repeated experiments show that the proposed method exhibits good stability and robustness against environmental variations. It is worth noting that direct sunlight should be avoided during measurement. A distance ranging from 670 mm to 850 mm between the wheel and the measurement platform is considered acceptable. Furthermore, since wheel alignment tasks are typically performed indoors in vehicle maintenance facilities, the measurement environment is generally well-controlled and stable.

Table 11. Repeated experiments under different distances and illuminations.

No	Toe−In			Toe−Out			Negative−Camber			Positive−Camber		
	12:45 p.m.~12.59 p.m.			11:39 a.m.~11:57 a.m.			18:01 p.m.~18:19 p.m.			19:08 p.m.~19:25 p.m.		
	D_s = 698 mm		D_e = 744 mm	D_s = 704 mm		D_e = 742 mm	D_s = 769 mm		D_e = 831 mm	D_s = 698 mm		D_e = 745 mm
	Real (°)	Meas (°)	Error (°)	Real (°)	Meas (°)	Error (°)	Real (°)	Meas (°)	Real (°)	Meas (°)	Error (°)	Real (°)
1	−0.900	−0.902	−0.002	1.400	1.307	−0.093	−0.900	−1.014	−0.114	1.250	1.323	0.073
2	−0.900	−0.946	−0.046	1.400	1.292	−0.108	−0.900	−0.932	−0.032	1.250	1.260	0.010
3	−0.900	−0.933	−0.033	1.400	1.227	−0.173	−0.900	−0.954	−0.054	1.250	1.224	−0.026
4	−0.900	−0.877	0.023	1.400	1.283	−0.117	−0.900	−1.000	−0.100	1.250	1.228	−0.022
5	−0.900	−0.912	−0.012	1.400	1.281	−0.119	−0.900	−0.997	−0.097	1.250	1.315	0.065
6	−0.900	−0.873	0.027	1.400	1.348	−0.052	−0.900	−0.935	−0.035	1.250	1.401	0.151
7	−0.900	−0.904	−0.004	1.400	1.311	−0.089	−0.900	−0.887	0.013	1.250	1.325	0.075
8	−0.900	−0.873	0.027	1.400	1.259	−0.141	−0.900	−0.888	0.012	1.250	1.289	0.039
9	−0.900	−0.838	0.062	1.400	1.314	−0.086	−0.900	−0.924	−0.024	1.250	1.287	0.037
10	−0.900	−0.863	0.037	1.400	1.318	−0.082	−0.900	−0.938	−0.038	1.250	1.389	0.139
11	−0.900	−0.906	−0.006	1.400	1.380	−0.020	−0.900	−0.997	−0.097	1.250	1.346	0.096
12	−0.900	−0.959	−0.059	1.400	1.355	−0.045	−0.900	−0.925	−0.025	1.250	1.274	0.024
13	−0.900	−0.927	−0.027	1.400	1.313	−0.087	−0.900	−0.926	−0.026	1.250	1.251	0.001
14	−0.900	−0.870	0.030	1.400	1.358	−0.042	−0.900	−0.958	−0.058	1.250	1.235	−0.015
15	−0.900	−0.906	−0.006	1.400	1.368	−0.032	−0.900	−0.974	−0.074	1.250	1.342	0.092
16	−0.900	−0.873	0.027	1.400	1.258	−0.142	−0.900	−0.958	−0.058	1.250	1.392	0.142
17	−0.900	−0.924	−0.024	1.400	1.256	−0.144	−0.900	−0.891	0.009	1.250	1.316	0.066
18	−0.900	−0.909	−0.009	1.400	1.214	−0.186	−0.900	−0.907	−0.007	1.250	1.304	0.054
19	−0.900	−0.850	0.050	1.400	1.266	−0.134	−0.900	−0.944	−0.044	1.250	1.283	0.033
20	−0.900	−0.899	0.001	1.400	1.279	−0.121	−0.900	−0.948	−0.048	1.250	1.381	0.131
21	−0.900	−0.889	0.011	1.400	1.342	−0.058	−0.900	−0.922	−0.022	1.250	1.343	0.093
22	−0.900	−0.918	−0.018	1.400	1.326	−0.074	−0.900	−0.851	0.049	1.250	1.275	0.025
23	−0.900	−0.902	−0.002	1.400	1.272	−0.128	−0.900	−0.868	0.032	1.250	1.248	−0.002
24	−0.900	−0.842	0.058	1.400	1.331	−0.069	−0.900	−0.907	−0.007	1.250	1.236	−0.014
25	−0.900	−0.877	0.023	1.400	1.342	−0.058	−0.900	−0.909	−0.009	1.250	1.343	0.093
MAE	−0.045						0.010					
RMSE	0.078						0.066					

https://doi.org/10.3390/metrology6010004

8. Conclusions and Future Development

To enable low-cost and flexible wheel alignment, this paper proposes a novel strategy that integrates semantic segmentation and 3D vision. We develop an APCS-SwinUnet segmentation network that incorporates ASPP, CBAM, and a hybrid loss function to achieve accurate wheel rim extraction. Using the segmented rim as the region of interest, we apply the ICP algorithm to register the reference and target point clouds, and then convert the resulting rotation matrix into toe and camber angles. Experimental results show that high-quality segmentation is crucial for reliable point-cloud registration and precise angle estimation. Overall, the proposed solution provides accurate, stable, and robust wheel-angle measurements while remaining cost-effective and flexible compared with conventional wheel alignment methods.

Quantitatively, APCS-SwinUnet achieves a Dice score of 90.66% and an HD95 of 2.11 for rim segmentation, representing a 0.43% increase in Dice and a 0.36 reduction in HD95 compared with the baseline model. Repeated experiments further show that the MAE and RMSE are -0.045° and 0.078° for the toe angle, and 0.010° and 0.066° for the camber angle, respectively, confirming that the proposed system can deliver accurate and reliable wheel-angle measurements. In the revised manuscript, we also relate these errors to the accuracy requirements specified in standards for four-wheel alignment instruments. Specifically, the allowable indication errors for total toe and single-wheel toe are within $\pm 4'$, and that for camber is within $\pm 2'$, corresponding to approximately 0.03–0.07°. Although some of our current measurements yield absolute toe and camber errors that are slightly larger, the errors remain well below 0.1° and are close to the target accuracy range.

The primary purpose of this study is to validate the feasibility of combining semantic segmentation with point-cloud registration for wheel-angle measurement. Accordingly, the current experiments focus on a single wheel in a controlled environment, and the proposed system should be regarded as a feasibility prototype rather than an industrial-grade product. For applications requiring higher angle-measurement accuracy, the proposed algorithmic framework can, in principle, be integrated with industrial-grade 3D sensors. We also explicitly acknowledge that the RGB images and associated 3D point-cloud data in our self-collected dataset have limited diversity in wheel types and acquisition conditions. This limitation constrains the current assessment of generalization and motivates future extensions to larger and more diverse datasets. In particular, we have outlined a future plan to enlarge the 3D dataset with additional wheel designs, environmental conditions, and viewpoints so as to more comprehensively assess and improve the generalization ability of the proposed model. Due to current resource constraints, a direct quantitative comparison with a commercial wheel-alignment system is not yet feasible. However, we recognize that such a benchmark would be technically sound and highly valuable, and we plan to allocate future resources to acquire a commercial system for more rigorous, industry-relevant validation. Future work will first extend the system to simultaneously measure the angles of all four wheels by integrating four such subsystems. We also plan to further narrow the gap to industrial standards by (i) adopting industrial-grade 3D scanners with higher stability and smaller systematic errors, (ii) performing rigorous comparisons against certified commercial alignment systems, and (iii) conducting a quantitative uncertainty analysis in accordance with metrological standards (e.g., ISO-GUM [39]), including a complete measurement model, an uncertainty budget, and traceability to SI units. Additional research will address robustness under more challenging conditions, such as dirty or partially occluded wheels and diverse rim geometries, and will investigate dedicated mechanical fixtures to improve stability and repeatability. Finally, we envision leveraging advanced machine-learning techniques not only for segmentation but also for data-driven uncertainty

https://doi.org/10.3390/metrology6010004

estimation, thereby strengthening the connection between this work and broader topics in three-dimensional metrology and machine learning for metrology.

Author Contributions: Conceptualization, B.S. and E.Z.; methodology, B.S. and E.Z.; software, B.S.; validation, B.S., E.Z. and H.L.; formal analysis, B.S., E.Z. and H.L.; investigation, B.S. and E.Z.; resources, E.Z.; data curation, B.S.; writing—original draft preparation, B.S.; writing—review and editing, B.S., E.Z. and H.L.; visualization, B.S.; supervision, E.Z.; project administration, E.Z.; funding acquisition, E.Z. All authors have read and agreed to the published version of the manuscript.

Funding: This work was supported in part by the National Nature Science Foundation of China under Grant 62173133, in part by the Postgraduate Study Abroad Program by China Scholarship Council under Grant 202306130094, and in part by the Postgraduate Scientific Research Innovation Project of Hunan Province CX20220398.

Data Availability Statement: The datasets used for the examples described outside Section 7.1.7 are not readily available, because the data are part of an ongoing study. The publicly available dataset [38] was used for the example described in Section 7.1.7.

Conflicts of Interest: The authors declare no conflicts of interest.

References

1. Yunta, J.; Garcia-Pozuelo, D.; Diaz, V.; Olatunbosun, O. Influence of camber angle on tire tread behavior by an on-board strain-based system for intelligent tires. *Measurement* **2019**, *145*, 631–639. [CrossRef]
2. Xu, G.; Wang, Y.; He, W.; Shen, H.; Chen, F.; Li, X.T.; Zhao, X.X. Large-scale all-wheel alignment globally registered by laser line family and verified by global benchmark. *IEEE Trans. Instrum. Meas.* **2024**, *73*, 5013510. [CrossRef]
3. Young, J.S.; Hsu, H.Y.; Chuang, C.Y. Camber angle inspection for vehicle wheel alignments. *Sensors* **2017**, *17*, 285. [CrossRef]
4. Feng, L.H.; Chen, W.; Cheng, M.; Zhang, W.G. The gravity-based approach for online recalibration of wheel force sensors. *IEEE/ASME Trans. Mechatron.* **2019**, *24*, 1686–1697. [CrossRef]
5. Chatur, S. Computer based wireless automobile wheel alignment system using accelerometer. *Inter. J. Eng. Sci.* **2015**, *4*, 62–69.
6. D'Mello, G.; Gomes, R.; Mascarenhas, R.; Ballal, S.; Kamath, V.S.; Lobo, V.J. Wheel alignment detection with IoT embedded system. *Mater. Today Proc.* **2022**, *52*, 1924–1929. [CrossRef]
7. Bohari, A.A.; Hafiz, M.F.H.M.; Yi, S.S.; Jamal, N.; Talib, M.N.M.; Safuan, S.N.M. Development of automobile wheel smart alignment monitoring system. *PaperASIA* **2024**, *40*, 28–35. [CrossRef]
8. Lee, H.; Choi, S.B. Online detection of toe angle misalignment based on lateral tire force and tire aligning moment. *Int. J. Automot. Technol.* **2023**, *24*, 623–632. [CrossRef]
9. Tang, X.L.; Shi, Y.; Chen, B.; Longden, M.; Farooq, R.; Lees, H.; Jia, Y. A miniature and intelligent low-power in situ wireless monitoring system for automotive wheel alignment. *Measurement* **2023**, *211*, 112578. [CrossRef]
10. Song, L.M.; Wang, R.H.; Chen, E.Z.; Yang, Y.G.; Zhu, X.J.; Liu, M.Y. Research on global calibration method of large-scene multi-vision sensors in wheel alignment. *Meas. Sci. Technol.* **2022**, *32*, 105023. [CrossRef]
11. Xu, G.; Wei, H.; Fang, C.; Hui, S.; Li, X.T. Automatic and accurate vision-based measurement of camber and toe-in alignment of vehicle wheel. *IEEE Trans. Instrum. Meas.* **2022**, *71*, 5024613. [CrossRef]
12. Xu, G.; Shen, H.; Li, X.T.; Chen, F.; He, W. Large-range reconstruction with non-pre-calibrated camera via MBM of laser referenced by radial-collinear-features. *IEEE Trans. Instrum. Meas.* **2022**, *71*, 5013510. [CrossRef]
13. Ge, P.X.; Wang, H.Q.; Wang, Y.H.; Wang, B. Calibration of ring multicamera system with transparent target for panoramic measurement. *IEEE Sens. J.* **2022**, *22*, 23154–23164. [CrossRef]
14. Jiang, T.; Cui, H.; Cheng, X.S. A calibration strategy for vision-guided robot assembly system of large cabin. *Measurement* **2020**, *163*, 107991. [CrossRef]
15. Roshan, M.C.; Isaksson, M.; Pranata, A. A geometric calibration method for thermal cameras using a ChArUco board. *Infrared Phys. Technol.* **2024**, *138*, 105219. [CrossRef]
16. Xu, G.; He, W.; Chen, F.; Shen, H.; Li, X.T. One-dimension orientation method of caster and kingpin inclination of vehicle wheel alignment. *Measurement* **2022**, *198*, 111371. [CrossRef]
17. Padegaonkar, A.; Brahme, M.; Bangale, M.; Raj, A.N.J. Implementation of machine vision system for finding defects in wheel alignment. *Int. J. Comput. Inf. Technol.* **2014**, *1*, 339–344.
18. Furferi, R.; Governi, L.; Volpe, Y.; Carfagni, M. Design and assessment of a machine vision system for automatic vehicle wheel alignment. *Int. J. Adv. Robot. Syst.* **2013**, *10*, 242. [CrossRef]

https://doi.org/10.3390/metrology6010004

19. Senjalia, J.; Pandya, P.; Kapadia, H. Measurement of wheel alignment using camera calibration and laser triangulation. In Proceedings of the 2013 Nirma University International Conference on Engineering (NUiCONE), Ahmedabad, India, 28–30 November 2013; pp. 1–5.
20. Kim, S.H.; Lee, K.I. Wheel alignment of a suspension module unit using a laser module. *Sensors* **2020**, *20*, 1648. [CrossRef] [PubMed]
21. Baek, D.; Cho, S.; Bang, H. Wheel alignment inspection by 3D point cloud monitoring. *Mech. Sci. Technol.* **2014**, *28*, 1465–1471. [CrossRef]
22. Wang, J.; Zeng, Z.; Sharma, P.K.; Alfarraj, O.; Tolba, A.; Zhang, J.; Wang, L. Dual-path network combining CNN and transformer for pavement crack segmentation. *Autom. Constr.* **2024**, *158*, 105217. [CrossRef]
23. Gao, G.; Li, J.Y.; Yang, L.; Liu, Y.H. A multi-scale global attention network for blood vessel segmentation from fundus images. *Measurement* **2023**, *222*, 113553. [CrossRef]
24. Geetha, G.K.; Yang, H.J.; Sim, S.H. Fast detection of missing thin propagating cracks during deep-learning-based concrete crack/non-crack classification. *Sensors* **2023**, *23*, 1419.
25. Siriborvornratanakul1, T. Image segmentation for thin structures using a zero-shot learner. *Int. J. Inf. Technol.* **2025**, *17*, 721–726. [CrossRef]
26. Li, J.Y.; Gao, G.; Yang, L.; Bian, G.B.; Liu, Y.H. DPF-Net: A dual-path progressive fusion network for retinal vessel segmentation. *IEEE Trans. Instrum. Meas.* **2023**, *72*, 2517817. [CrossRef]
27. Chen, L.; Papandreou, G.; Schroff, F.; Adam, H. Rethinking atrous convolution for semantic image segmentation. *arXiv* **2017**, arXiv:1706.05587. [CrossRef]
28. Woo, S.; Park, J.; Lee, J.; Kweon, I.S. CBAM: Convolutional Block Attention Module. In Proceedings of the European Conference on Computer Vision (ECCV), Munich, Germany, 8–14 September 2018; pp. 3–19.
29. Xu, M.B.; Han, Y.M.; Zhong, X.T.; Sang, F.Y.; Zhang, Y.A. A precise registration method for large-scale urban point clouds based on phased and spatial geometric features. *Meas. Sci. Technol.* **2025**, *36*, 015202. [CrossRef]
30. Long, J.; Shelhamer, E.; Darrell, T. Fully convolutional networks for semantic segmentation. In Proceedings of the IEEE Conference on Computer Vision and Pattern Recognition (CVPR), Boston, MA, USA, 7–12 June 2015; pp. 3431–3440.
31. Yuan, Y.H.; Huang, L.; Guo, J.Y.; Zhang, C.; Chen, X.L.; Wang, J.D. OCNet: Object context for semantic segmentation. *Int. J. Comput. Vis.* **2021**, *129*, 2375–2398. [CrossRef]
32. Zunair, H.; Hamza, A.B. Sharp U-Net: Depthwise convolutional network for biomedical image segmentation. *Comput. Biol. Med.* **2021**, *136*, 104699. [CrossRef] [PubMed]
33. Oktay, O.; Schlemper, J.; Folgoc, L.L.; Lee, M.; Heinrich, M.; Misawa, K.; Mori, K.; McDonagh, S.; Hammerla, N.Y.; Kainz, B.; et al. Attention U-Net: Learning where to look for the pancreas. *arXiv* **2018**, arXiv:1804.0399. [CrossRef]
34. Zhou, Z.W.; Siddiquee, M.M.R.; Tajbakhsh, N.; Liang, J. UNet++: A nested U-Net architecture for medical image segmentation. In *Deep Learning in Medical Image Analysis and Multimodal Learning for Clinical Decision Support: 4th International Workshop*; Springer: Berlin/Heidelberg, Germany, 2018; pp. 3–11.
35. Huang, H.M.; Lin, L.F.; Tong, R.F.; Hu, H.J.; Zhang, Q.W.; Iwamoto, Y.; Han, X.; Chen, Y.-W.; Wu, J. Unet 3+: A full-scale connected unet for medical image segmentation. In Proceedings of the ICASSP 2020—2020 IEEE International Conference on Acoustics, Speech and Signal Processing (ICASSP), Barcelona, Spain, 4–8 May 2020; pp. 1055–1059.
36. Chen, J.N.; Lu, Y.Y.; Yu, Q.H.; Luo, X.D.; Adeli, E.; Wang, Y.; Lu, L.; Yuille, A.L.; Zhou, Y. TransUNet: Transformers make strong encoders for medical image segmentation. *arXiv* **2021**, arXiv:2102.04306. [CrossRef]
37. Cao, H.; Wang, Y.Y.; Chen, J.; Jiang, D.S.; Zhang, X.P.; Tian, Q.; Wang, M.N. Swin-Unet: Unet-like pure Transformer for medical image segmentation. In Proceedings of the European Conference on Computer Vision (ECCV), Tel Aviv, Israel, 23–27 October 2022; pp. 205–218.
38. Available online: https://www.kaggle.com/datasets/adamnovozmsk/cawdec?resource=download (accessed on 31 May 2019).
39. ISO/IEC. *ISO/IEC Guide 98-6:2021(en), Uncertainty of Measurement—Part 6: Developing and Using Measurement Models*; International Organization for Standardization: Geneva, Switzerland, 2021.

Disclaimer/Publisher's Note: The statements, opinions and data contained in all publications are solely those of the individual author(s) and contributor(s) and not of MDPI and/or the editor(s). MDPI and/or the editor(s) disclaim responsibility for any injury to people or property resulting from any ideas, methods, instructions or products referred to in the content.

https://doi.org/10.3390/metrology6010004

metrology

MDPI

Review

The Critical Role of International Comparisons in Global Metrology System: An Overview

Patrice Salzenstein [1,*], Thomas Y. Wu [2,*] and Ekaterina Pavlyuchenko [3]

[1] Centre National de la Recherche Scientifique (CNRS), Franche-Comté Electronique Optique Sciences et Technologies (FEMTO-ST) Institute, Université Marie et Louis Pasteur (UMLP), 15B Avenue des Montboucons, F-25030 Besançon, France
[2] National Metrology Centre (NMC), Agency for Science, Technology and Research (A*STAR), 8 CleanTech Loop, #01-20, Singapore 637145, Singapore
[3] Centre National de la Recherche Scientifique (CNRS), Avenue de la Terrasse, F-91190 Gif-sur-Yvette, France; ekaterina.pavlyuchenko@cnrs.fr
* Correspondence: patrice.salzenstein@cnrs.fr (P.S.); askskyy@163.com (T.Y.W.)

Abstract: International comparisons play a critical role in ensuring precision, accuracy, consistency, and trust in the global metrology system. The Comité International des Poids et Mesures (CIPM) established the Mutual Recognition Arrangement (MRA) in 1999 to facilitate global trade. This paper gives an overview of the critical role of international comparisons to National Metrology Institutes (NMIs), industrial calibration laboratories, and research laboratories in fostering global measurement equivalence and the CIPM MRA. NMIs rely on Key and Supplementary Comparisons to ensure the mutual recognition of calibration and reference material certificates, vital for global trade and regulatory compliance. Industrial calibration laboratories participate in inter-laboratory or international comparisons to validate their calibration and measurement capability (CMC) and balance their risk management. Research laboratories push the frontiers of measurement science and validate their measurement result via international comparisons. Through some examples of comparisons, the paper illustrates how measurement result discrepancies uncovered in comparisons drive technical improvements, uncertainty component identification, and measurement technique refinement. International comparisons enhance scientific credibility, build public trust, support industrial innovation, and drive evolution in measurement science. As technological demands grow, fostering broader participation in international comparisons by various metrology and research laboratories remains crucial to maintain a robust and reliable global metrology system.

Keywords: international comparisons; global metrology system; measurement uncertainty; measurement science; National Metrology Institutes; industrial calibration laboratories; research laboratories; calibration and measurement capability

1. Introduction

The global metrology system can be viewed as a top-down pyramid: at the top, the Comité International des Poids et Mesures (CIPM) and the Bureau International des Poids et Mesures (BIPM) maintain the International System of Units (SI) and coordinate international comparisons [1–3]. Below them, the Regional Metrology Organizations (RMOs) coordinate regional comparisons and peer reviews among the National Metrology Institutes (NMIs) and Designated Institutes (DIs).

CIPM and BIPM work in close cooperation with organizations like the Organisation Internationale de Métrologie Légale (OIML) and the International Laboratory Accredi-

tation Cooperation (ILAC), among others, to support the global metrology system. The OIML plays an important role in the global metrology system by focusing on the legal metrology and regulatory aspects of measurement. It complements the scientific metrology work coordinated by the BIPM and the CIPM. The role of ILAC in the global metrology system is to ensure that measurement, testing, and calibration results from industrial accredited laboratories are technically reliable, internationally recognized, and traceable to the SI [4]. ILAC harmonizes the practices of national accreditation bodies to promote a harmonized assessment of laboratories [5], reference material producers [6], proficiency test (PT) providers [7], etc.

The CIPM has gradually established ten Consultative Committees (CCs) in various technical areas from the 1920s to the 1990s. These CCs play an instrumental role in maintaining the integrity of the global metrology system. There are eight CCs in physical metrology areas which provide technical guidance and coordinate the work of NMIs in areas such as length, mass, force, pressure, flow, temperature, humidity, electricity, magnetism, time and frequency, photometry, radiometry, acoustics and vibration, ionizing radiation, etc. The Consultative Committee for Amount of Substance: Metrology in Chemistry and Biology (CCQM) coordinates the work of NMIs in organic analysis, inorganic analysis, gas analysis, electrochemical analysis, surface analysis, isotope ratios, nucleic acid analysis, protein analysis and cell analysis [8–11]. The Consultative Committee for Units (CCU) was set up to advise the CIPM on matters concerning units of measurement, to develop and improve the SI, and to prepare and update the SI Brochure [12]. These CCs ensure that metrology standards of each country are continually updated to reflect the latest advancements in science and technology.

Each country or economy has an NMI and/or one or more DIs that realize SI units, participates in international comparisons, and provides traceability. These NMIs and DIs provide a link to industrial calibration laboratories that serve industry under ISO/IEC 17025 accreditation [5]. Research laboratories support technology innovation by developing new measurement methods or sensors with higher accuracy and precision, while industry and society form the base of the global metrology system, benefiting from reliable, globally comparable measurements and calibrations [2,3,13–15].

In the global metrology system, where metrological traceability and measurement uncertainty of measurement results are fundamental, international comparisons serve as a cornerstone for validating and harmonizing measurement standards across the globe. International comparisons have a long history of development, spanning nearly 140 years. In the 1st General Conference on Weights and Measures (CGPM) held in 1889 in Paris, the International Prototype of the Kilogram (IPK) and the International Prototype of the Metre (IPM) were adopted. BIPM compared each national copy of the metre bar and kilogram (standards of many countries) against the IPK and IPM and reported their differences in the 1st CGPM [16]. This can be considered the first formal international comparison for mass and length standards.

The first international comparison of electrical resistance standards (mercury–ohm standard) and voltage standards (Weston cells) was conducted in 1910 between the NMI of the United Kingdom, Germany, France, and the United States of America [17–19]. The first metrological international comparison of time and frequency standards (clocks) was coordinated by the BIPM and reported at the 7th CGPM in 1927 [20]. In the 1920s–1960s, international comparisons in other areas, such as temperature, photometry, pressure, and ionizing radiation, were also organized by the BIPM [2].

By the 1950s–1960s, the BIPM had broadened international comparisons into most base and derived SI quantities, providing the foundation for the establishment of the SI in 1960. This ultimately led to the CIPM Mutual Recognition Arrangement (MRA) in 1999 [21],

which formalized the structure for international key comparisons (KCs) between NMIs and created the key comparison database (KCDB) as a central record of equivalence and calibration capabilities. Since then, KCs have been organized by CIPM's CCs, and cover all SI quantities (mass, length, time, temperature, electricity, acoustics, vibration, ionizing radiation, photometry, radiometry, chemistry, biology, etc.).

RMOs also run supplementary comparisons (SC) and regional key comparisons, which are linked back to the CIPM KCs for equivalence. Pilot studies organized by each CC and the SCs run by RMO are designed to allow research laboratories to participate, gain experience, and compare their measurement result to the respective international KC. These activities enhance global measurement capability while maintaining traceability through linking NMIs.

The CIPM established the MRA in 1999 to ensure that measurement standards maintained by different countries are comparable and equivalent [21]. The MRA relies on KCs and SCs among NMIs to support the international trust in national metrology systems [22–26]. International comparisons are used to verify that measurement results from different countries are traceable to equivalent national reference standards, and ultimately to the SI. This builds confidence in the accuracy and equivalence of measurements worldwide. Such comparisons help NMIs align their national metrology standards, ensuring mutual recognition of measurement capabilities across borders.

By participating in international comparisons, an individual country or economy demonstrates its measurement competence to satisfy trade partners and reduce technical barriers to trade. Demonstration of a quality management system (QMS) that has been reviewed and accepted through peer review or accreditation is an essential component of the CIPM MRA. The QMS of an NMI should comply with ISO/IEC 17025 for calibration and measurement services [5], and, where applicable, ISO 17034 for NMIs producing reference materials [6]. Based on the successful peer review of both their technical capabilities and their QMS, NMIs may submit their Calibration and Measurement Capabilities (CMCs) to the KCDB. These submitted CMCs will be reviewed first by the NMI's own RMO (intra-RMO review), then by other RMOs (inter-RMO review). After the CMCs are approved, they are published in the KCDB.

Certified Reference Materials (CRMs) are widely regarded as the preferred means for disseminating metrological traceability in chemistry, biological, and materials measurements where direct calibration against physical standards is not feasible. CRMs from NMIs or DIs must be produced in accordance with ISO 17034. Their certified values are traceable to SI units via measurements covered by the CIPM MRA if their CMCs are published in the KCDB. Such CRMs provide well-characterized reference values with stated uncertainties and traceability to SI units, enabling reliable dissemination of traceable measurements to industry. CRMs form a robust and internationally recognized route to establishing traceability, thereby complementing the traditional calibration-based dissemination used in physical metrology.

In a broader sense, international comparisons or inter-laboratory comparisons involve a wider network of participating laboratories—NMIs, industrial calibration laboratories, and research laboratories—all of which have contributed to the global consistency of measurements. Many bilateral/multi-lateral comparisons (not registered with the BIPM), hybrid comparisons [27] and informal comparisons between these laboratories are conducted to validate their measurement results. The importance of international comparisons extends beyond scientific rigour; it has practical implications for industry, trade, regulation, and research.

An important reason for NMIs and DIs to participate in KCs is to meet the requirements of clause 7.7 in ISO/IEC 17025 (to ensure the validity of their measurement results).

International comparisons serve as performance benchmarks for participating laboratories to identify gaps, support training, and drive continuous improvement in measurement technologies. High-precision measurements are essential for cutting-edge research in various research laboratories. International comparisons ensure that research conducted across countries is comparable and reproducible.

This paper begins with an introduction to the measurement uncertainty estimation and description of the methodology and process of international KC. Section 4 discusses how NMIs ensure global measurement consistency via international comparisons. We then discuss how industrial calibration laboratories validate their CMCs and balance their risk management. Section 6 addresses how research laboratories push the frontiers of measurement science and validate their measurement result via international comparisons. In Section 7, we underline the technical value of international comparisons with two case studies. A summary of the main findings is presented in Section 8, followed by the conclusions drawn from this review paper.

2. Uncertainty in Measurement

Measurement results must be assigned an estimated uncertainty when they are reported; otherwise, they have no meaning. Without measurement uncertainty, you do not know the 95% confidence interval of the measured result, or whether it can meet a specification or tolerance. The measurement uncertainties are also important to compare measurement results made by various laboratories and for assessing a product's compliance with limits and specifications [28–30]. One of the central purposes of international comparisons is to validate the measurement uncertainties claimed by metrology laboratories. By demonstrating that results from different laboratories agree within their stated uncertainties, these comparisons confirm the credibility of each laboratory's measurement capability.

Measurement uncertainties are estimated following the Guide to the Expression of Uncertainty in Measurement (GUM) [28]. The GUM was originally published in 1993 and republished with minor corrections in 1995. In GUM, measurement uncertainty is divided into Type A and Type B evaluations. Type A uncertainty comes from statistical analysis of repeated measurements. Type B uncertainty includes components evaluated using non-statistical methods, such as calibration certificate information, manufacturer specifications, reference data, instrument limits, previous measurement data, physical constants, environmental effects, uncertainty in bias correction, instrument resolution, long-term stability, drift, noise, modelling errors, etc. All Type A and Type B uncertainty components are first expressed as standard uncertainties and then combined using the law of uncertainty propagation (LUP) to derive the expanded uncertainty at a 95% confidence level.

For non-linear models or non-normal probability distributions, the classical GUM approach for propagation of uncertainty can be inadequate. In 2008, GUM Supplement 1 was published to introduce the Monte Carlo method for propagating uncertainty in non-linear models and non-normal input distributions. The GUM is under ongoing revision to accommodate modern measurement methods, complex models, and digital metrology [31,32].

Measurement uncertainty analysis in diverse metrology standards has been well described in the literature [33–49]. Careful analysis of all possible uncertainty contributions is needed to derive reliable measurement uncertainties of a measurement system. Rigorous uncertainty analysis can also help to improve the accuracy of such systems. Uncertainty analysis can provide valuable insights into instruments' performance and support the development of instruments with higher precision [50,51]. A detailed uncertainty analysis of Liquified Natural Gas (LNG) flow measurement [52,53] has revealed theoretically the best accuracy that can be achieved for LNG bunkering and cryogenic liquid flow measurement.

Measurement uncertainty is essential for interpreting results reported in international or inter-laboratory comparisons. Without quantifying uncertainty, it becomes difficult to assess the significance of differences in measurement results between laboratories. Reliable uncertainty assessments are needed so that a laboratory can demonstrate the equivalence of its metrology standards and maintain traceability to the SI.

For each KC, one or more key comparison reference values (KCRV) can be derived. The KCRV is a reference value representing the best estimate of the "true" measurand in the comparison, based on all valid results reported by participating laboratories. KCRV is used as a common reference point to compare all results of participating laboratories and derive each laboratory's degree of equivalence (DoE), which is the deviation of their measured result from the KCRV. The uncertainty of the KCRV and DoE must also be estimated in the KC report. Many statistical methods for the evaluation of key comparison data to identify outliers and derive KCRV with uncertainty estimation have been proposed [54–69].

For RMO comparisons or pilot studies, measurement results from participating laboratories need to be combined using statistical methods, considering their respective measurement uncertainties to derive a comparison reference value (CRV) and to evaluate its associated uncertainty. Methods for data analysis and linking the CRV in RMO comparisons to KCRV have been proposed [58,70–74].

3. Methodology and Process of International Key Comparisons

In this section, we briefly describe how a typical KC is conducted. An international KC begins with planning by a CC or the BIPM, which appoints a pilot laboratory responsible for preparing the comparison protocol. This technical protocol specifies the comparison's scope, measurands, travelling standard, participating laboratories, circulation scheme (e.g., sequential loop or star configuration), measurement procedures, principal components of the uncertainty budget, environmental conditions, results and uncertainty reporting format, schedule, data submission deadlines, etc. [75]. The comparison protocol needs to be reviewed and approved by the CC.

Before travelling standard circulation, the pilot laboratory verifies its suitability—ensuring stability, transportability, and traceability to primary standards—and performs initial characterization measurements. During the circulation phase, each participating NMI receives the travelling standard, performs measurements, and reports the results with complete measurement uncertainty budgets. The stability of the travelling standard is monitored using the pilot laboratory's repeated measurements during the circulation phase. Data validation is performed to identify inconsistencies or drift for the travelling standard.

After measurements are completed by all participating laboratories, the pilot laboratory analyses all submitted data using statistical methods to identify outliers and determine the KCRV with its expanded uncertainty [55–57,62,63]. The DoE between each laboratory's result and the KCRV are then calculated. Pairwise DoE among all participating laboratories is also derived.

The KC report prepared by the pilot laboratory will go through the Draft A and Draft B stages. In the Draft A report stage, all participating laboratories will review their own submitted results and uncertainties, outlier identification, proposed KCRV and DoE, statistical processing method, etc., in the report. When the final version of Draft A report has been agreed upon by all participants, it becomes the Draft B report. In this stage, the Draft B report will be sent to CC for technical review and formal approval. Once approved, the KC final report is published in the BIPM KCDB.

4. National Metrology Institutes: Ensuring Global Measurement Consistency and Traceability

NMIs play a crucial role in ensuring the accuracy and consistency of measurements within their respective countries, but their responsibilities extend far beyond national borders. Participation in international comparisons is essential for NMIs to uphold their status as custodians of national metrology standards. These standards and CMCs are validated against other NMIs through international comparisons, ensuring a robust traceability chain for calibration laboratories and industry. Successful comparison results can confirm that an NMI's measurement standards are comparable to those of other countries. NMIs demonstrate the international equivalence of their measurement capabilities through KCs and SCs coordinated by the BIPM and its associated CCs.

The international comparisons support the mutual recognition of calibration certificates, which are recognized by all MRA signatory countries. This mutual recognition is vital for industries and businesses that operate internationally. The calibration of their products can meet internationally accepted standards. Many products benefit from the MRA through appropriate testing and conformity assessment. This can eliminate disputes over measurement discrepancies, facilitating smooth international trade.

Accurate measurements are crucial for safety, quality, and compliance with regulations. Nowadays, industries rely on standardized measurements to ensure that their products meet international specifications. Satisfactory results in comparisons reinforce the credibility and international standing of NMIs. For industries such as aerospace, automotive, electronics, and pharmaceuticals, the reliable standards of NMIs can ensure smooth trade globally.

NMIs participate in various comparisons to ensure their measurement standards and CMCs evolve with scientific progress [76–89]. Such standards also need to maintain their relevance in a rapidly changing world. We give some examples of international key comparisons between NMIs in this section.

- The Consultative Committee for Length (CCL) has conducted key comparisons of optical frequency and wavelength standards, such as CCL-K11 [79,90,91]. These comparisons are used to ensure uniformity in laser wavelength measurements across different NMIs. The comparisons CCL-K1 focus on the calibration of gauge blocks by optical interferometry, to maintain length measurement equivalence and traceability [83,92]. These CCL key comparisons have supported length metrology development and the realization of the metre.
- The Consultative Committee for Mass and Related Quantities (CCM) organized the first key comparison CCM.M-K8.2019 for realizations of the kilogram definition based on the Planck constant, with a final report published in 2020 [93]. This comparison is used to determine agreement between realizations of the kilogram using Kibble balances, joule balances, and the X-ray Crystal Density (XRCD) method. The KCRV has a deviation of -0.0188 mg (with a standard uncertainty of 0.0075 mg) from the mass unit maintained by the BIPM working standards (nominal mass is 1 kg). The second CCM key comparison CCM.M-K8.2021 for realizations of the kilogram definition was conducted in 2021–2022 [94]. Its KCRV has a standard uncertainty of 0.0074 mg and a deviation of -0.0152 mg from the 1 kg mass unit maintained by the BIPM working standards.
- BIPM has carried out an ongoing on-site key comparison of Josephson voltage standards among NMIs under the denomination BIPM.EM-K10.a (1 V) and BIPM.EM-K10.b (10 V) under the auspices of the Consultative Committee for Electricity and Magnetism (CCEM) [95]. A recent comparison between the NMI of Finland and BIPM was reported in 2021 [96]. Their final results were in good agreement within the

combined relative standard uncertainty of 2.5 parts in 10^{10} for the nominal voltage of 10 V.

- CCT-K7.2021 key comparison of water-triple-point (TPW) cells was conducted between 19 NMIs, with its final report approved by the Consultative Committee for Thermometry (CCT) in 2023 [97]. The maximum difference between two transfer cells was 92 μK, with a standard deviation of 26 μK, which shows an almost factor-of-two improvement compared to CCT-K7 results. Compared to the previous comparison, CCT-K7 [98], this recent comparison has shown major improvements in the quality of TPW cells, definition of national references, and quality of uncertainty assessments.
- The Consultative Committee for Photometry and Radiometry (CCPR) has organized a key comparison CCPR-K1.a.2017 for Spectral Irradiance in the wavelength range of 250 to 2500 nm using Tungsten quartz halogen lamps (1000 W) as artifacts [99]. The relative standard uncertainties of the KCRV were estimated to be 0.08% to 0.28%. The measurement uncertainties reported by the participants in CCPR-K1.a.2017 were, in general, less than those claimed in the previous comparison for Spectral Irradiance (CCPR-K1.a). The final report shows that ~80% of all results (at all wavelengths) agree with the KCRV within 1% at 250 to 2500 nm, which is similar to the results of the previous CCPR-K1.a comparison (published in 2006) [100].
- The Consultative Committee for Acoustics, Ultrasound and Vibration (CCAUV) organized the first key comparison CCAUV.A-K4 for free-field microphone sensitivity derived using the reciprocity technique [101]. The travelling standards were two $\frac{1}{2}$ inch laboratory-standard microphones (Brüel & Kjær 4180), which were calibrated at 1 kHz to 40 kHz under free-field conditions in an anechoic chamber. The submitted results of all seven NMIs were included in the estimation of the KCRVs. The final report shows that ~94% of all results (for all frequencies) agree with the KCRV within the uncertainties.
- The CCQM has organized three KCs on natural gas mixtures, namely CCQM-K1, CCQM-K16 and CCQM-K23, to ensure comparability in natural gas composition reference standards among the NMIs [80,102–105]. The final report for a more recent KC for natural gas (CCQM-K118) was published in 2022 [106]. In this comparison, the KCRVs have been derived using a weighted mean computed from the largest consistent subset (LCS) of the submitted results. Some of the participants reported one or a few discrepant results, partly due to the heterogeneity and heteroscedasticity of the datasets. Overall, the results in CCQM-K118 have shown good comparability of the metrology standards for natural gas composition in the 14 participating institutes.

As illustrated in Figure 1, the role of NMIs is essential for maintaining the traceability and credibility of the global metrology system. The equivalence of measurement standards across borders, verified through international comparisons, also fosters scientific innovation. Researchers working with international partners can trust that the measurement data they exchange is consistent, which supports collaborative research work.

To publish a CMC in the BIPM KCDB, an NMI must demonstrate its technical competence and QMS by peer review or accreditation before the CMCs can be submitted to the KCDB. The QMS of an NMI should comply with ISO/IEC 17025 [5] for calibration and measurement services and ISO 17034 if the NMI produces reference materials [6]. The QMS ensures that an NMI implements systematic controls and proper documentation over measurement processes and traceability to the SI [1,107–110]. The QMS, CMCs, and MRA form an integrated framework to ensure global confidence in measurement results. The audited QMS practices build mutual confidence among NMIs, which form the basis for global equivalence in measurement standards.

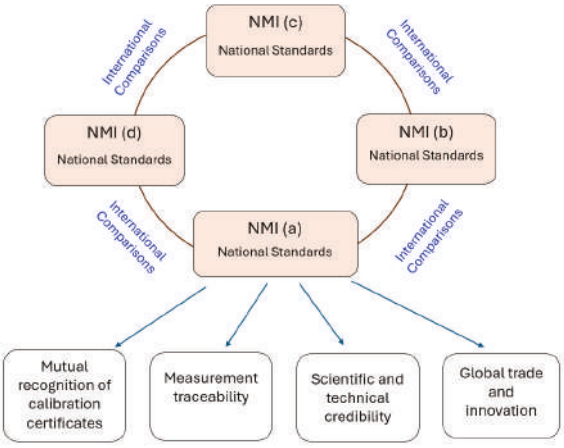


Figure 1. Roles of NMIs in ensuring the global measurement consistency and traceability.

5. Industrial Calibration Laboratories: CMC Validation and Risk Management

5.1. Validation of CMC

Industrial calibration laboratories need to demonstrate their competence through ISO/IEC 17025 accreditation. Their calibration standards must be traceable to SI units, usually through calibration services provided by NMIs or other accredited calibration laboratories. For these laboratories, participation in international comparisons, inter-laboratory comparisons or PT plays a crucial role in validating their claimed CMCs and meeting the requirements of accreditation assessment [111–117].

Accreditation bodies request accredited calibration laboratories to regularly participate in PT or inter-laboratory comparison (when PT is not available) to show their competence in calibration [7]. Such PT can be conducted by an NMI or a commercial organization which offers PT services with ISO/IEC 17043 accreditation [7]. PT provides an external, unbiased check of a laboratory's ability to perform accurate calibrations. Successful PT results enable the calibration laboratory to be recognized internationally under the ILAC MRA [118].

5.2. Financial and Legal Binding of Measurements

These calibration laboratories often provide calibration services or develop products where precise measurements are legally or financially binding. Thus, their reported measurement uncertainties and CMCs carry significant weight. To mitigate potential legal and financial risks, industrial laboratories may need to declare uncertainties with a conservative margin. Liability and financial risk management influence the measurement uncertainty declared by industrial calibration laboratories.

In many industries, the calibration reports directly impact product quality, safety and regulatory compliance. The uncertainty affects how reliable and trustworthy their measurements are perceived to be. For example, any deviation in measurement in pharmaceutical products could lead to a batch being rejected. In the aerospace industry, even minor calibration discrepancies can result in catastrophic outcomes. As a result, industrial calibration laboratories are under pressure to provide measurements with a high level of reliability, as reflected in the reported measurement uncertainty.

Overly optimistic uncertainty in calibration certificates means the laboratory could have underestimated the true measurement uncertainty, resulting in a reported uncertainty that is too small to be realistic. This could expose the laboratory to liability in legal disputes or claims for damages. The measurement uncertainty also often has regulatory implications; in many jurisdictions, products and processes need to conform to standards and such con-

formance decisions are influenced by the uncertainty values. In this context, measurement uncertainty becomes part of a risk management strategy. Calibration laboratories must ensure their uncertainty values have an adequate cushion against potential errors.

5.3. Risk Management and Decision Rule

Industrial laboratories have to consider the potentially unknown uncertainty factors in the calibration process. This is to protect themselves from potential legal claims or financial repercussions. Thus, a conservative approach is often adopted in estimating the measurement uncertainty. A safety margin, or uncertainty guard-banding, is included to account for any unforeseen errors during calibration [119,120]. This decision rule can mitigate the risk of underestimating uncertainty. This conservative approach also helps to ensure that their calibration reports comply with industry standards and regulations. Measurement uncertainty with guard banding means adding a safety margin to the estimated measurement uncertainty. Their final reported uncertainty (or CMC) includes a margin factor to ensure their calibration results can comply with contractual obligations.

The priority of industrial laboratories is to ensure that their measurement results are reliable with acceptable uncertainty. They need to focus on risk and responsibility. In the automotive or pharmaceutical sectors, precise instrument calibration can affect product performance or patient safety. In these cases, a measurement result with a reliable uncertainty estimation is most important.

In industrial laboratories, uncertainty estimation and decision rules are tools for managing legal and financial risk [119–121]. A conservative approach in declaring uncertainty helps safeguard against disputes and legal challenges. This becomes an essential part of the laboratory's overall risk management strategy. ISO/IEC 17025 emphasizes that calibration laboratories should identify, evaluate, and control risks that could affect the validity of calibration results or the reliability of decisions [5]. ILAC has published a guideline ILAC G8:09/2019 on the use of decision rules when issuing statements of conformity to specifications or standards [122].

Participation in inter-laboratory comparisons or PTs enables a calibration laboratory to compare its measurement results with peers or comparison reference values and to validate its claimed uncertainties (with guard banding). The deviations detected in such comparisons can reveal sources of error which are not captured in the uncertainty budget. Thus, participation in such comparisons is also a risk management tool for industrial laboratories.

6. Research Laboratories: Pushing the Frontiers of Measurement Science

Research laboratories in academia and industry operate under a distinctive paradigm compared to NMIs and industrial calibration laboratories. While the calibration laboratories typically focus on providing calibration services with legal liability, research laboratories primarily concentrate on advancing scientific understanding and technology. Their role is to explore the limits of measurement science and develop cutting-edge methodologies for high-precision measurement [123–133].

Many NMIs also have research laboratories or R&D groups with a role distinct from other groups that focus on routine metrology functions (e.g., performing calibration service, maintaining national standards and supporting traceability chains). Instead, their role is to advance measurement science, conduct cutting-edge research, and develop new metrology standards using novel methods.

Research laboratories focus on the pursuit of knowledge and technological innovation. In this context, their core objective is often to reduce measurement uncertainty to its lowest possible levels, exploring new ways to push the boundaries of measurement precision

and accuracy. Such research works are often highly experimental, leading to innovations that could eventually revolutionize measurement techniques. Some of these research findings have been used by NMIs to develop new metrology standards (e.g., quantum time standards [134–141], graphene electrical resistance standards [142–146], quantum voltage standards [147,148], primary realization of the kilogram using a Kibble balance and XRCD [149–161], etc.).

6.1. Pushing the Frontiers of Measurement Science

Research laboratories focus on achieving the lowest possible measurement uncertainty by developing novel measurement methods that outperform traditional approaches. This drive for superiority aimed to prove the scientific robustness of their work, for instance, by achieving high measurement precision in fields like quantum technology, nanotechnology, or space science.

Research laboratories have contributed to the development of metrology and pushed the boundaries of measurement precision and accuracy. Research laboratories innovate new measurement techniques to achieve smaller uncertainties. Their research findings may ultimately lead to new instruments and methodologies with higher precision.

6.2. Benchmarking via International Comparisons

Many research laboratories have participated in international comparisons, including those pilot studies organized by the BIPM, SCs organized by RMO and inter-laboratory comparisons [77,78,81,162–165]. These comparisons allow research laboratories to benchmark their measurement performance against NMIs and other leading metrology laboratories. They validate their measurement capabilities and identify areas for improvement via the comparisons. Contributions from many research laboratories help drive new developments in metrology. A few examples are given below to show significant developments in these areas:

- The Consultative Committee for Time and Frequency (CCTF) has initiated a roadmap for redefining the SI second to enhance precision, accuracy, and long-term stability of timekeeping. This initiative is driven by advancements in optical frequency standards, such as those based on ^{171}Yb and ^{87}Sr, which are intrinsically accurate at the level of parts in 10^{18}, two orders of magnitude lower than that of traditional ^{133}Cs microwave atomic clocks [166–170]. The redefinition aims to improve the accuracy and stability of International Atomic Time (TAI) and Coordinated Universal Time (UTC) [12,164,167,170–173]. An international comparison of optical frequencies via a transportable optical lattice clock and another comparison of optical clocks through very long baseline interferometry (VLBI) have been conducted to check the consistency of optical clocks at the fractional uncertainty of 10^{-18} level on an intercontinental scale [81,162].
- NPL and the University of Cambridge had reported their work to develop a quantum current standard using single-electron pumps [174]. They compared the electron pump current with a reference current generated outside the pump cryostat, with an uncertainty on the order of 1 ppm. This is an important work in Quantum Metrology Triangle (QMT) experiments to check the self-consistency of the three fundamental quantum electrical standards [163,175,176].
- A pilot study on AC voltage comparisons was conducted in 2024 by the National Institute of Standards and Technology (NIST) and BIPM [147,148]. The aim of this comparison is to harmonize quantum voltage standards globally. This pilot study focuses on quantum-based Josephson voltage standards to ensure consistency in AC voltage measurements. The BIPM's transportable Programmable Josephson Voltage

Standards (PJVSs) were compared to NIST's Josephson Arbitrary Waveforms Synthesizer (JAWS). They have achieved a type A uncertainty of a few parts in 10^9 for a 10 Hz sine wave at 2 V rms in this comparison.

- Comparison between NIST and National Institute for Advanced Industrial Science and Technology (AIST) has been conducted using Graphene and GaAs Quantized Hall resistance (QHR) Devices [82]. In this work, several graphene QHR devices from NIST were compared to GaAs QHR devices and a 100 Ω standard resistor from AIST. Comparisons between the QHR devices have been reported with uncertainties of less than 5 nΩ/Ω.
- An inter-laboratory comparison on quantum resistance (memristor) between 3 NMIs and 3 research laboratories has been reported [165]. The results show the consensus values of this comparison have deviations of −3.8% and 0.6% from the agreed SI values for the fundamental quantum of conductance, G_0 and $2G_0$, respectively. The consensus values' deviations from the SI values are well covered by their expanded measurement uncertainty.
- A comparison was conducted by four laboratories for measuring the detection efficiency of free-running InGaAs/InP single-photon avalanche detectors (SPAD) at the wavelength of 1550 nm [177]. The detection efficiency for the mean photon number per pulse was between 0.01 and 2.4. The measured efficiency values by the participants are all consistent within the claimed uncertainties. This study is a good preparation for organizing future international comparisons of the detection efficiency of single-photon detectors at telecom wavelengths.

Over time, research laboratories have been responsible for many breakthroughs that form the backbone of modern measurement systems, such as the development of new metrology standards for time (microwave atomic clocks and optical clocks) [178], the invention of laser interferometry for precision dimensional measurement [179,180], etc. Together with NMIs, research laboratories play a vital role in the advancement of precision measurement technologies. Their work ensures that measurement science continues to evolve and improve, benefiting industries and government agencies in the long run.

7. The Technical Value of International Comparisons

International comparisons also provide a unique opportunity for all participating laboratories to validate their measurement setups. When the same standard or artefact is circulated among multiple laboratories, it allows each participant to confirm the consistency of their measurements. If a laboratory obtains a result that significantly deviates from the consensus, it prompts an internal review. This discrepancy can lead to improvements in the measurement system. Thus, comparisons are a powerful method of external validation.

Discrepancies in comparison results will trigger an investigation of the source of the error. This could involve re-examining calibration procedures, identifying potential systematic errors, or revisiting the uncertainty analysis framework. Additionally, when a laboratory's results diverge notably from others, it may prompt a re-evaluation of measurement protocols or equipment maintenance schedules to ensure alignment with established standards. Two case studies are given below to show this technical value.

7.1. Case Study: Phase Noise Inter-Laboratory Comparison

The first international comparison in the area of phase noise was held in 1993 [181]. More than 10 years later, another important international comparison for phase noise was conducted and reported by Salzenstein et al. in 2006 [111]. This study involved various industrial calibration laboratories and research laboratories across Europe and aimed to assess the consistency and reliability of multiple phase noise measurement systems. The

preliminary results, published in the proceedings of the 20th European Frequency and Time Forum, revealed disparities among participants that sparked valuable technical discussions.

As an illustration, we provide some results of this comparison in Figure 2. At 5 MHz, one of the participating laboratories (B) shows a big deviation from the other participants. After some investigation, this laboratory (B) found it was due to a technical issue. Three other laboratories did not report their measurement uncertainties. The reported phase noise levels appear to be quite similar across most participating laboratories.

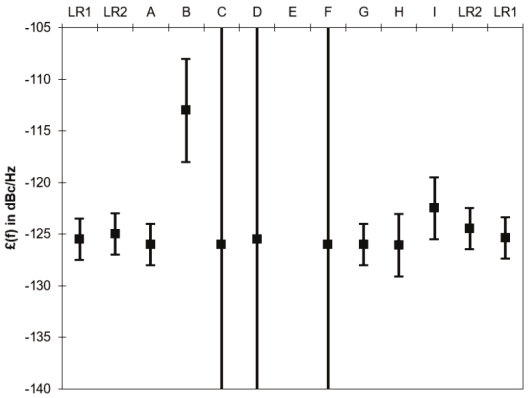


Figure 2. Single sideband (SSB) phase noise at 1 Hz offset from the 5 MHz carrier, in a phase noise inter-laboratory comparison conducted in 2006 [111]. LR1 and LR2 represent the measurements carried out on the two benches of the reference laboratory. One participant (B) identified an issue after the comparison, which can explain the observed big deviation during the comparison. Three participants (C, D, and F) did not report the uncertainty of their measurements, although their results were consistent with the overall average. Participant E was unable to provide a result.

Technical discussions were sparked due to these differences in the results. These differences also led to modifications in some participants' measurement setups and a deeper understanding of the measurement process itself. The comparison facilitated not only performance benchmarking but also the identification of best practices for phase noise characterization. Such inter-laboratory comparisons are vital in niche areas like phase noise metrology, where measurement complexity and system sensitivity make standardization particularly challenging.

7.2. Case Study: Comparison of Particle Charge Concentration and Particle Number Concentration

The European Association of National Metrology Institutes (EURAMET) organized a pilot study for comparison of aerosol electrometers (EuRAMET comparison #1244) in 2013 [182]. This is the first comprehensive international comparison of particle charge concentration measured by aerosol electrometers for particle sizes from 6 nm to 200 nm. This pilot study shows that some laboratories may have underestimated their uncertainties at certain particle number concentrations, and that their relative deviations from the CRVs exceeded their claimed uncertainty. The result of this comparison has led to a review of uncertainty budgets and to the identification of other possible sources of measurement errors (noise floor of electrometer, port bias error, sample flow rate error, etc.) to derive reliable measurement uncertainty.

After this EuRAMET pilot study, the CCQM organized the first and second KC for particle number concentration and particle charge concentration in 2017 and 2024, respectively (CCQM-K150, CCQM-K185) [85,183,184]. The results of CCQM-K150 and CCQM-K185 show that many NMIs have improved their measurement accuracy, and the estimated uncertainties are more realistic, which ensures that their results agree with the KCRVs within the uncertainties.

7.3. Discussion

International comparisons have helped to support continuous improvement in the metrology laboratory. The deviation from the CRV can highlight potential bias errors in their system or insufficient measurement uncertainty. Laboratories may need to develop new calibration techniques to enhance their measurement system.

Such comparisons act as a catalyst for sustained improvement in measurement technique. This process of comparison, review, and improvement can enhance the quality of metrology standards. NMIs can identify needs for better reference materials, more accurate instruments, or improved calibration methods via such international comparisons. This ensures that metrology can keep pace with scientific innovations.

8. Summary

We have given an overview of the critical role of international comparisons in the global metrology system. Since the first international comparison of mass and length standards in 1889, we have seen the impact of such comparisons on the development of metrology standards. International comparisons ensure the precision, accuracy, consistency, and mutual trust within the global metrology system. Measurement uncertainty analysis is essential for interpreting the results of each participating laboratory in international comparisons. Reliable uncertainty assessments and analysis ensure that various laboratories can demonstrate the equivalence of their metrology standards with CRVs and validate their traceability to the SI. The data from each comparison needs to be analyzed using appropriate statistical methods to identify outliers and derive a CRV with reliable uncertainty.

This paper has discussed the challenges faced by NMIs, industrial calibration laboratories, and research laboratories. NMIs have relied on KCs, SCs and pilot studies coordinated by the BIPM and CCs to ensure the mutual recognition of metrology standards and traceability to the SI, which are vital for global trade and regulatory compliance. NMIs have been developing quantum metrology standards and have organized many international comparisons to validate the measurement uncertainties and precision.

Industrial calibration laboratories regularly participate in inter-laboratory or international comparisons to validate their CMCs and meet ISO/IEC 17025 accreditation requirements. They also need to balance the claimed uncertainties with their risk management, as their calibration reports would be subject to legal liability for compliance with regulatory standards.

The focus of research laboratories is to push the frontiers of measurement science and develop cutting-edge measurement techniques with breakthroughs in measurement precision. Research laboratories have participated in international comparisons to validate their measurement result and benchmark their capabilities with other NMIs or research laboratories.

We have given some examples of international comparisons to illustrate their technical value. Measurement result discrepancies uncovered during these comparisons have driven technical improvements, the identification of uncertainty components, and the refinement of measurement techniques. This helps NMIs to improve their metrology standards, leading to higher accuracy and more reliable uncertainty assessment.

It is known that large discrepancies have appeared in some international comparisons, which could be due to travelling standard drift, differences in measurement methods, environmental conditions, differences in traceability, etc. Sometimes these issues can lead to large uncertainty of KCRV or CRV, arguments over the identification of outliers, or a suitable statistical method for processing comparison data. In the future, it will require more

mature measurement techniques, more stable artifacts, or more accurate reference standards to improve the results of international comparisons for those more challenging areas.

9. Conclusions

International comparisons are more than just technical exercises—they are foundational to the integrity, coherence, and advancement of measurement science. They have played a critical role in validating measurement capabilities, building public trust, supporting international trade, enhancing scientific credibility, and fostering continuous technology innovation. Each stakeholder—be it an NMI ensuring global measurement consistency, an industrial calibration laboratory providing calibration services, or a research laboratory striving for scientific excellence—derives distinct yet equally vital benefits from these international comparisons.

KC and SC protocols and final reports are all published to foster public trust in the global metrology system. Comparison reports with satisfactory results reassure the public that measurements are accurate and traceable. Regulatory bodies and industrial stakeholders can benefit from this transparency and trust. Ultimately, this will support more collaboration between nations to develop globally accepted metrology standards.

As science and technology continue to evolve, the role of international comparisons in ensuring measurement traceability and validating measurement uncertainties will remain central. To build a robust global metrology system, we need to encourage international comparisons with broader coverage of measurands, greater participation by more laboratories, and deeper integration into scientific and industrial practices.

Author Contributions: Conceptualization, P.S.; methodology, P.S., T.Y.W. and E.P.; figures, P.S. and T.Y.W.; validation, P.S. and T.Y.W.; formal analysis, P.S., T.Y.W. and E.P.; investigation, P.S. and T.Y.W.; resources, P.S.; writing—original draft preparation, P.S. and T.Y.W.; writing—review and editing, P.S. and T.Y.W.; supervision, P.S.; project administration, P.S. All authors have read and agreed to the published version of the manuscript.

Funding: This research received no external funding.

Data Availability Statement: Data is available upon reasonable request.

Conflicts of Interest: The authors declare no conflicts of interest.

Abbreviations

The following abbreviations are used in this manuscript:

BIPM	Bureau International des Poids et Mesures
CC	Consultative Committees
CGPM	General Conference on Weights and Measures
CIPM	Comité International des Poids et Mesures
CMC	Calibration and measurement capability
ILAC	International Laboratory Accreditation Cooperation
IPK	International Prototype of the Kilogram
IPM	International Prototype of the Metre
KC	Key comparison
KCDB	Key comparison database
MRA	Mutual Recognition Arrangement
NMI	National Metrology Institute
OIML	International Organization of Legal Metrology
RMO	Regional Metrology Organization

SC	supplementary comparison
SI	International System of Units
AIST	Advanced Industrial Science and Technology
CCL	Consultative Committee for Length
CCQM	Consultative Committee for Amount of Substance: Metrology in Chemistry and Biology
CCTF	Consultative Committee for Time and Frequency
CRV	Comparison reference value
DoE	Degree of equivalence
EURAMET	European Association of National Metrology Institutes
GUM	Guide to the Expression of Uncertainty in Measurement
JAWS	Josephson Arbitrary Waveforms Synthesizer
KCRV	key comparison reference value
LNG	Liquefied Natural Gas
NIST	National Institute of Standards and Technology
PJVS	Programmable Josephson Voltage Standard
PT	Proficiency testing
QHR	Quantized Hall resistance
QMT	Quantum Metrology Triangle
SSB	Single sideband
TAI	International Atomic Time
TFPI	Tandem Fabry–Pérot interferometer
UTC	Coordinated Universal Time
VLBI	Very long baseline interferometry
ISO	International Organisation for Standardization
QMS	Quality management system
LCS	Largest consistent subset
CCU	Consultative Committee for Units
CCEM	Consultative Committee for Electricity and Magnetism
CCT	Consultative Committee for Thermometry
CCAUV	Consultative Committee for Acoustics, Ultrasound and Vibration
CCPR	Consultative Committee for Photometry and Radiometry
CCM	Consultative Committee for Mass and Related Quantities
SPAD	Single-photon avalanche detector
XRCD	X-ray crystal density
CRM	Certified Reference Material

References

1. Wallard, A.J. The Organization of Metrology. In *Proceedings of the International School of Physics "Enrico Fermi"*; IOS Press: Amsterdam, The Netherlands, 2007; Volume 166, pp. 21–33. [CrossRef]
2. Quinn, T. *From Artefacts to Atoms: The BIPM and the Search for Ultimate Measurement Standards*; Oxford University Press: Oxford, UK, 2012.
3. Quinn, T. The Metre Convention and World-Wide Comparability of Measurement Results. In *Proceedings of the Accreditation and Quality Assurance*; Springer: Berlin/Heidelberg, Germany, 2004; Volume 9, pp. 533–538.
4. Placko, D. *Metrology in Industry: The Key for Quality*; Wiley: Hoboken, NJ, USA, 2010; ISBN 9781905209514.
5. *ISO/IEC 17025:2017*; ISO/IEC General Requirements for the Competence of Testing and Calibration Laboratories. International Organization for Standardization: Geneva, Switzerland, 2017.
6. *ISO/IEC 17034*; ISO/IEC General Requirements for the Competence of Reference Material Producers. International Organization for Standardization: Geneva, Switzerland, 2016.
7. *ISO/IEC 17043*; ISO/IEC Conformity Assessment—General Requirements for Proficiency Testing. International Organization for Standardization: Geneva, Switzerland, 2010.
8. Richter, W. Comparability and Recognition of Chemical Measurement Results—An International Goal. *Fresenius J. Anal. Chem.* **1999**, *365*, 569–573. [CrossRef]

9. Konopelko, L.A.; Kustikov, Y.A.; Okrepilov, M.V.; Kolobova, A.V.; Migal, P.V.; Krylov, A.I.; Vonskiy, M.S.; Chubchenko, I.K.; Efremova, O.V.; Kulyabina, E.V.; et al. Development of International Key Comparisons in the Field of Chemico-Analytical Measurements. *Meas. Tech.* **2021**, *64*, 598–605. [CrossRef]
10. Wielgosz, R.I. International Comparability of Chemical Measurement Results. *Anal. Bioanal. Chem.* **2002**, *374*, 767–771. [CrossRef]
11. Richter, W. How to Achieve International Comparability for Chemical Measurements. *Accredit. Qual. Assur.* **2000**, *5*, 418–422. [CrossRef]
12. BIPM. *The International System of Units (SI)*, 9th ed.; The Bureau International Des Poids et Mesures: Sèvres, France, 2019.
13. Semerjian, H.G.; Watters, R.L. Impact of Measurement and Standards Infrastucture on the National Economy and International Trade. *Measurement* **2000**, *27*, 179–196. [CrossRef]
14. Seiler, E. From the International System of Units to a Global Metrology System. In Proceedings of the XVII IMEKO World Congress Metrology in the 3rd Millennium, Dubrovnik, Croatia, 22–27 June 2003.
15. Kumar, A.; Bangal, P.R.; Panja, S.; Sharma, S.K. Metrological Innovations for Science, Technology and Global Trade. *Mapan J. Metrol. Soc. India* **2023**, *38*, 557–559. [CrossRef]
16. BIPM. *Compte Rendu Des Séances de La 1re Conférence Générale Des Poids et Mesures (CGPM)*; The Bureau International Des Poids et Mesures: Sèvres, France, 1889.
17. Rosa, E.B. Report to the International Committee on Electrical Units and Standards. Available online: https://www.google.com.sg/books/edition/Report_to_the_International_Committee_on/ccRGAQAAMAAJ?hl=en&gbpv=0 (accessed on 19 September 2025).
18. Rosa, E.B.; Wolff, F.A. Work of the International Technical Committee on Electrical Units. *J. Wash. Acad. Sci.* **1912**, *2*, 259–267.
19. Elmquist, R.E.; Cage, M.E.; Tang, Y.H.; Jeffery, A.M.; Kinard, J.; Dziuba, R.F.; Oldham, N.M.; Williams, E.R. The Ampere and Electrical Standards. *J. Res. Natl. Inst. Stand. Technol.* **2001**, *106*, 65. [CrossRef]
20. BIPM. *Compte Rendu Des Séances de La 7th Conférence Générale Des Poids et Mesures (CGPM)*; The Bureau International Des Poids et Mesures: Sèvres, France, 1927.
21. CIPM. *Mutual Recognition of National Measurement Standards and of Calibration and Measurement Certificates Issued by National Metrology Institutes (CIPM MRA)*; The Bureau International Des Poids et Mesures: Sèvres, France, 1999.
22. Werhahn, O.; Olson, D.A.; Kuanbayev, C.; Henson, A. The CIPM MRA—Success and Performance. *Metrologia* **2023**, *60*, 042001. [CrossRef]
23. Henson, A. The CIPM MRA: Past, Present and Future. *Rev. Esp. Metrol.* **2015**, *24*. Available online: https://www.e-medida.es/numero-8/the-cipm-mra-past-present-and-future/ (accessed on 19 September 2025).
24. Krietsch, A.; Werhahn, O. CIPM MRA Support for Hydrogen Metrology—A Case Study. *Measurement* **2024**, *235*, 115041. [CrossRef]
25. Schwitz, W.; Hetherington, P. The CIPM MRA in Its 3rd Year of Implementation in Europe. In Proceedings of the CPEM Digest (Conference on Precision Electromagnetic Measurements), Ottawa, ON, Canada, 16–21 June 2002; pp. 270–271. [CrossRef]
26. Quinn, T. World-Wide Recognition of National Measurement Standards: Ten Years of the CIPM MRA: Recalibration. *IEEE Instrum. Meas. Mag.* **2010**, *13*, 42–46. [CrossRef]
27. APMP. APMP Guideline for Using Hybrid Comparisons as CMC Evidence. Available online: https://www.apmpweb.org/upload/portal/20231205/44023c95738e28e3f93e9a394feb8327.pdf (accessed on 19 October 2025).
28. *JCGM 100:2008*; Evaluation of Measurement Data—Guide to the Expression of Uncertainty in Measurement. The Bureau International Des Poids et Mesures: Sèvres, France, 2008.
29. *JCGM GUM-1:2023*; Guide to the Expression of Uncertainty in Measurement—Part 1: Introduction. The Bureau International Des Poids et Mesures: Sèvres, France, 2023.
30. *JCGM 106:2012*; Evaluation of Measurement Data-The Role of Measurement Uncertainty in Conformity Assessment. The Bureau International Des Poids et Mesures: Sèvres, France, 2012.
31. Bich, W.; Cox, M.; Michotte, C. Towards a New GUM—An Update. *Metrologia* **2016**, *53*, S149. [CrossRef]
32. Bich, W.; Cox, M.G.; Dybkaer, R.; Elster, C.; Estler, W.T.; Hibbert, B.; Imai, H.; Kool, W.; Michotte, C.; Nielsen, L.; et al. Revision of the 'Guide to the Expression of Uncertainty in Measurement'. *Metrologia* **2012**, *49*, 702. [CrossRef]
33. Hamilton, C.A.; Tang, Y.H. Evaluating the Uncertainty of Josephson Voltage Standards. *Metrologia* **1999**, *36*, 53. [CrossRef]
34. Wu, T.Y.; Lu, Y.L. Error Analysis and Uncertainty Estimation for a Millimeter-Wave Phase-Shift Measurement System at 325 GHz. *Measurement* **2015**, *59*, 198–204. [CrossRef]
35. Haloua, F.; Foulon, E.; Allard, A.; Hay, B.; Filtz, J.R. Traceable Measurement and Uncertainty Analysis of the Gross Calorific Value of Methane Determined by Isoperibolic Calorimetry. *Metrologia* **2015**, *52*, 741. [CrossRef]
36. Coquelin, L.; Le Brusquet, L.; Fischer, N.; Gensdarmes, F.; Motzkus, C.; Mace, T.; Fleury, G. Uncertainty Propagation Using the Monte Carlo Method in the Measurement of Airborne Particle Size Distribution with a Scanning Mobility Particle Sizer. *Meas. Sci. Technol.* **2018**, *29*, 055801. [CrossRef]
37. Wu, T.Y.; Horender, S.; Tancev, G.; Vasilatou, K. Evaluation of Aerosol-Spectrometer Based PM2.5 and PM10 Mass Concentration Measurement Using Ambient-like Model Aerosols in the Laboratory. *Measurement* **2022**, *201*, 111761. [CrossRef]

38. Siegwarth, J.D. *Estimated Uncertainty of Calibrations of Freestanding Prismatic Liquefied Natural Gas Cargo Tanks*; NBSIR 81-1655; National Bureau of Standards: Washington, DC, USA, 1981.
39. Siegwarth, J.D. Volume Uncertainty of a Large Tank Calibrated by Photogrammetry. *Photogramm. Eng. Remote Sens.* **1984**, *50*, 1127–1134.
40. Scott, J.; Lewis, M. Uncertainty Analysis of the NIST Nitrogen Flow Facility. *NIST Tech. Note* **1994**, 1364. Available online: https://www.nist.gov/system/files/documents/calibrations/tn1364.pdf (accessed on 19 October 2025).
41. van der Beek, M.; Lucas, P.; Kerkhof, O.; Mirzaei, M.; Blom, G. Results of the Evaluation and Preliminary Validation of a Primary LNG Mass Flow Standard. *Metrologia* **2014**, *51*, 539–551. [CrossRef]
42. Von Martens, H.J. Investigations into the Uncertainties of Interferometric Measurements of Linear and Circular Vibrations. *Shock. Vib.* **1997**, *4*, 327–340. [CrossRef]
43. Guenther, F.R.; Possolo, A. Calibration and Uncertainty Assessment for Certified Reference Gas Mixtures. *Anal. Bioanal. Chem.* **2011**, *399*, 489–500. [CrossRef]
44. Milton, M.J.T.; Vargha, G.M.; Brown, A.S. Gravimetric Methods for the Preparation of Standard Gas Mixtures. *Metrologia* **2011**, *48*, R1. [CrossRef]
45. Schley, P.; Beck, M.; Uhrig, M.; Sarge, S.M.; Rauch, J.; Haloua, F.; Filtz, J.R.; Hay, B.; Yakoubi, M.; Escande, J.; et al. Measurements of the Calorific Value of Methane with the New GERG Reference Calorimeter. *Int. J. Thermophys.* **2010**, *31*, 665–679. [CrossRef]
46. Wu, T.Y.; Chua, S.W.; Lu, Y.L. Noise Floor and Dynamic Range Analysis of a Microwave Attenuation Measurement Receiver from 50 MHz to 26.5 GHz. *Measurement* **2011**, *44*, 1516–1525. [CrossRef]
47. Wu, T.Y. Accurate Measurement of Millimeter-Wave Attenuation from 75 GHz to 110 GHz Using a Dual-Channel Heterodyne Receiver. *Measurement* **2012**, *45*, 1105–1110. [CrossRef]
48. Salzenstein, P.; Pavlyuchenko, E.; Hmima, A.; Cholley, N.; Zarubin, M.; Galliou, S.; Chembo, Y.K.; Larger, L. Estimation of the Uncertainty for a Phase Noise Optoelectronic Metrology System. *Phys. Scr.* **2012**, *T149*, 14025. [CrossRef]
49. Wu, T.Y.; Kenbar, A. Investigation of Measurement Uncertainties in LNG Density and Energy for Custody Transfer. *Meas. Sci. Technol.* **2021**, *32*, 45005. [CrossRef]
50. Salzenstein, P.; Wu, T.Y. Uncertainty Analysis for a Phase-Detector Based Phase Noise Measurement System. *Measurement* **2016**, *85*, 118–123. [CrossRef]
51. Salzenstein, P.; Pavlyuchenko, E. Uncertainty Evaluation on a 10.52 Ghz (5 Dbm) Optoelectronic Oscillator Phase Noise Performance. *Micromachines* **2021**, *12*, 474. [CrossRef]
52. Wu, T.Y.; Kenbar, A.; Pruysen, A. LNG Mass Flowrate Measurement Using Coriolis Flowmeters: Analysis of the Measurement Uncertainties. *Measurement* **2021**, *177*, 109258. [CrossRef]
53. Wu, T.Y.; Kenbar, A. LNG Mass Flow Measurement Uncertainty Reduction Using Calculated Young's Modulus and Poisson's Ratio for Coriolis Flowmeters. *Measurement* **2022**, *188*, 110413. [CrossRef]
54. Cox, M.G.; Eiø, C.; Mana, G.; Pennecchi, F. The Generalized Weighted Mean of Correlated Quantities. *Metrologia* **2006**, *43*, S268. [CrossRef]
55. Cox, M.G. The Evaluation of Key Comparison Data. *Metrologia* **2002**, *39*, 589. [CrossRef]
56. Cox, M.G.; Harris, P.M. The Evaluation of Key Comparison Data Using Key Comparison Reference Curves. *Metrologia* **2012**, *49*, 437–445. [CrossRef]
57. Cox, M.G. The Evaluation of Key Comparison Data: Determining the Largest Consistent Subset. *Metrologia* **2007**, *44*, 187–200. [CrossRef]
58. Cox, M.; Shirono, K. Analysis of a Regional Metrology Organization Key Comparison: Model-Based Unilateral Degrees of Equivalence. *Metrologia* **2023**, *60*, 055014. [CrossRef]
59. Milton, M.J.T.; Cox, M.G. Evaluating Degrees of Equivalence Using "exclusive" Statistics. *Metrologia* **2003**, *40*, L1. [CrossRef]
60. Cox, M.G.; Harris, P.M. Technical Aspects of Guidelines for the Evaluation of Key Comparison Data. *Meas. Tech.* **2004**, *47*, 102–111. [CrossRef]
61. Kacker, R.; Datla, R.; Parr, A. Combined Result and Associated Uncertainty from Interlaboratory Evaluations Based on the ISO Guide. *Metrologia* **2002**, *39*, 279–293. [CrossRef]
62. Kacker, R.N.; Datla, R.U.; Parr, A.C. Statistical Analysis of CIPM Key Comparisons Based on the ISO Guide. *Metrologia* **2004**, *41*, 340–352. [CrossRef]
63. Kacker, R.N.; Datla, R.U.; Parr, A.C. Statistical Interpretation of Key Comparison Reference Value and Degrees of Equivalence. *J. Res. Natl. Inst. Stand. Technol.* **2003**, *108*, 439–446. [CrossRef] [PubMed]
64. Willink, R. Forming a Comparison Reference Value from Different Distributions of Belief. *Metrologia* **2005**, *43*, 12. [CrossRef]
65. Koepke, A.; Lafarge, T.; Possolo, A.; Toman, B. Consensus Building for Interlaboratory Studies, Key Comparisons, and Meta-Analysis. *Metrologia* **2017**, *54*, S34. [CrossRef]
66. van der Veen, A.M.H. Dark Uncertainty in Key Comparisons in the Gas Analysis Area. *Metrologia* **2023**, *60*, 064002. [CrossRef]

67. Cecelski, C.E.; Toman, B.; Liu, F.H.; Meija, J.; Possolo, A. Errors-in-Variables Calibration with Dark Uncertainty. *Metrologia* **2022**, *59*, 045002. [CrossRef]
68. Randa, J. Proposal for KCRV & Degree of Equivalence for GTRF Key Comparisons. In *Document of the CCEM Working Group on Radiofrequency Quantities, GT-RF/2000-12*; 2000.
69. CCQM. *CCQM Guidance Note: Estimation of a Concensus KCRV and Associated Degrees of Equivalence*; The Bureau International Des Poids et Mesures: Sèvres, France, 2013.
70. Sutton, C.M. Analysis and Linking of International Measurement Comparisons. *Metrologia* **2004**, *41*, 272. [CrossRef]
71. Elster, C.; Chunovkina, A.G.; Wöger, W. Linking of a RMO Key Comparison to a Related CIPM Key Comparison Using the Degrees of Equivalence of the Linking Laboratories. *Metrologia* **2010**, *47*, 96–102. [CrossRef]
72. Elster, C.; Link, A.; Wöger, W. Proposal for Linking the Results of CIPM and RMO Key Comparisons. *Metrologia* **2003**, *40*, 189. [CrossRef]
73. Delahaye, F.; Witt, T.J. Linking the Results of 10 PF Capacitance Key Comparisons CCEM-K4 and Euromet 345. In Proceedings of the CPEM Digest (Conference on Precision Electromagnetic Measurements), Ottawa, ON, Canada, 16–21 June 2002; pp. 526–527. [CrossRef]
74. Frahm, E.; Wright, J. Evaluation of Inter-Laboratory Comparison Results: Representative Examples. *Measurement* **2023**, *223*, 113723. [CrossRef]
75. *CIPM MRA-D-05*; CIPM Measurement Comparisons in the CIPM MRA. The Bureau International Des Poids et Mesures: Sèvres, France, 2016.
76. Shang, X.; Naftaly, M.; Skinner, J.; Ausden, L.; Gregory, A.; Ridler, N.M.; Arz, U.; Phung, G.N.; Ulm, D.; Kleine-Ostmann, T.; et al. Interlaboratory Comparison of Dielectric Measurements from Microwave to Terahertz Frequencies Using VNA-Based and Optical-Based Methods. *IEEE Trans. Microw. Theory Technol.* **2024**, *72*, 6473–6484. [CrossRef]
77. Mubarak, F.; Phung, G.N.; Arz, U. An Interlaboratory Comparison of On-Wafer S-Parameter Measurements up to 1.1 THz. *IEEE Trans. Terahertz Sci. Technol.* **2025**, *15*, 2025. [CrossRef]
78. Celep, M.; Stokes, D.; Danacı, E.; Ziadé, F.; Zagrajek, P.; Wojciechowski, M.; Phung, G.N.; Kuhlmann, K.; Kazemipour, A.; Durant, S.; et al. Interlaboratory Comparison of Power Measurements at Millimetre- and Sub-Millimetre-Wave Frequencies. *Metrology* **2024**, *4*, 279–294. [CrossRef]
79. Matus, M.; Margolis, H.S.; Seppä, J.; Karlsson, H.; Hanquist, C.-H.; Lancaster, A.J.; Lewis, A.J.; Brawer, M.; Pérez, M.d.M.; Bisi, M.; et al. The CCL-K11 Ongoing Key Comparison. Final Report for 2023. *Metrologia* **2024**, *61*, 04002. [CrossRef]
80. Alink, A. First Key Comparison of Primary Standard Gas Mixtures. *Metrologia* **2000**, *37*, 35–49. [CrossRef]
81. Amy-Klein, A.; Benkler, E.; Blondé, P.; Bongs, K.; Cantin, E.; Chardonnet, C.; Denker, H.; Dörscher, S.; Feng, C.-H.; Gaudron, J.-O.; et al. International Comparison of Optical Frequencies with Transportable Optical Lattice Clocks. *arXiv* **2024**, arXiv:2410.22973. [CrossRef]
82. Oe, T.; Rigosi, A.F.; Kruskopf, M.; Wu, B.Y.; Lee, H.Y.; Yang, Y.; Elmquist, R.E.; Kaneko, N.H.; Jarrett, D.G. Comparison between NIST Graphene and AIST GaAs Quantized Hall Devices. *IEEE Trans. Instrum. Meas.* **2019**, *69*, 3103–3108. [CrossRef]
83. Viliesid, M.; Colin, C.; Dube, P. Calibration of Gauge Blocks by Optical Interferometry Comparison—Final Report. *Metrologia* **2022**, *59*, 04005. [CrossRef]
84. Kuramoto, N.; Chang, K.H.; Fujii, K.; Lee, Y.J. International Comparison of Volume Measurement for a 1 kg Silicon Sphere between KRISS and NMIJ. *Measurement* **2014**, *49*, 187–195. [CrossRef]
85. Brown, A.S.; Quincey, P.; Ebert, V.; Nowak, A.; Tompkins, J.T.; Hessey, I.; Ciupek, K.; Schaefer, C.; Werhahn, O.; Vasilatou, K.; et al. International Comparison CCQM-K150: Particle Number Concentration (100 to 20,000 cm^{-3}) and Particle Charge Concentration (0.15 to 3 fC cm^{-3}). *Metrologia* **2023**, *60*, 08014. [CrossRef]
86. Vasilatou, K.; Dirscherl, K.; Iida, K.; Sakurai, H.; Horender, S.; Auderset, K. Calibration of Optical Particle Counters: First Comprehensive Inter-Comparison for Particle Sizes up to 5 μm and Number Concentrations up to 2 cm^{-3}. *Metrologia* **2020**, *57*, 25005. [CrossRef]
87. Wu, T.Y.; Murashima, Y.; Sakurai, H.; Iida, K. A Bilateral Comparison of Particle Number Concentration Standards via Calibration of an Optical Particle Counter for Number Concentration up to ∼1000 cm^{-3}. *Measurement* **2022**, *189*, 110446. [CrossRef]
88. Broda, R.; Bonková, I.; Capogni, M.; Carconi, P.; Cassette, P.; Coulon, R.; Courte, S.; De Felice, P.; Dziel, T.; Fazio, A.; et al. The CCRI(II)-K2.Fe-55.2019 Key Comparison of Activity Concentration Measurements of a 55Fe Solution. *Metrologia* **2021**, *58*, 06010. [CrossRef]
89. Vykydal, Z.; Park, H.; Kim, J.; Pereira, W.W.; da Fonseca, E.S.; Thiam, C.; Hui, Z.; Dewey, M.S.; Mumm, H.P.; Harano, H.; et al. International Comparison of Measurements of Neutron Source Emission Rate (2016–2021)—CCRI(III)-K9.Cf.2016. *Metrologia* **2024**, *61*, 06001. [CrossRef]
90. Colín, C.; Viliesid, M.; Chaudhary, K.P.; Decker, J.; Dvorácek, F.; Franca, R.; Ilieff, S.; Rodríguez, J.; Stoup, J. Final Report on SIM Regional Key Comparison SIM.L-K1.2007: Calibration of Gauge Blocks by Optical Interferometry. *Metrologia* **2012**, *49*, 04010. [CrossRef]

91. BIPM Comparison of Optical Frequency and Wavelength Standards, CCL-K11. Available online: https://www.bipm.org/kcdb/comparison?id=978 (accessed on 16 September 2025).
92. Thalmann, R. CCL Key Comparison: Calibration of Gauge Blocks by Interferometry. *Metrologia* **2002**, *39*, 165. [CrossRef]
93. Stock, M.; Conceição, P.; Fang, H.; Bielsa, F.; Kiss, A.; Nielsen, L.; Kim, D.; Kim, M.; Lee, K.C.; Lee, S.; et al. Report on the CCM Key Comparison of Kilogram Realizations CCM.M-K8.2019. *Metrologia* **2020**, *57*, 07030. [CrossRef]
94. Stock, M.; Conceição, P.; Fang, H.; Bielsa, F.; Kiss, A.; Nielsen, L.; Beaudoux, F.; Espel, P.; Thomas, M.; Ziane, D.; et al. Final Report on the CCM Key Comparison of Kilogram Realizations CCM.M-K8.2021. *Metrologia* **2023**, *60*, 07003. [CrossRef]
95. Solve, S.; Stock, M. BIPM Direct On-Site Josephson Voltage Standard Comparisons: 20 Years of Results. *Meas. Sci. Technol.* **2012**, *23*, 124001. [CrossRef]
96. Solve, S.; Chayramy, R.; Stock, M.; Immonen, P.; Nissilä, J.; Manninen, A. Comparison of the Josephson Voltage Standards of the MIKES and the BIPM. *Metrologia* **2021**, *58*, 01007. [CrossRef]
97. Peruzzi, A.; Dedyulin, S.; Levesque, M.; Del Campo, D.; Izquierdo, B.C.G.; Gomez, M.E.; Quelhas, K.N.; Neto, M.A.P.; Lozano, B.M.; Eusebio, L.; et al. CCT-K7.2021: CIPM Key Comparison of Water-Triple-Point Cells. *Metrologia* **2023**, *60*, 03002. [CrossRef]
98. Stock, M.; Solve, S.; del Campo, D.; Chimenti, V.; Méndez-Lango, E.; Liedberg, H.; Steur, P.P.M.; Marcarino, P.; Dematteis, R.; Filipe, E.; et al. Final Report on CCT-K7: Key Comparison of Water Triple Point Cells. *Metrologia* **2006**, *43*, 03001. [CrossRef]
99. Khlevnoy, B.B.; Solodilov, M.V.; Kolesnikova, S.S.; Otryaskin, D.A.; Pons, A.; Campos, J.; Shin, D.J.; Park, S.; Obein, G.; Valin, M.H.; et al. CIPM Key Comparison CCPR-K1.a.2017 for Spectral Irradiance 250 nm to 2500 nm. Final Report. *Metrologia* **2023**, *60*, 02002. [CrossRef]
100. Woolliams, E.R.; Fox, N.P.; Cox, M.G.; Harris, P.M.; Harrison, N.J. Final Report on CCPR K1-a: Spectral Irradiance from 250 nm to 2500 nm. *Metrologia* **2006**, *43*, 02003. [CrossRef]
101. Barrera-Figueroa, S.; Nielsen, L.; Rasmussen, K.; Matzumoto, A.E.P.; Razo, J.N.R. Final Report on the Key Comparison CCAUV.A-K4. *Metrologia* **2010**, *47*, 09003. [CrossRef]
102. van der Veen, A.M.H.; Heine, H.J.; Brinkmann, F.N.C.; Ziel, P.R.; De Leer, E.W.B.; Zhen, W.L.; Kato, K.; Konopelko, L.A.; Popova, T.A.; Alexandrov, Y.I.; et al. International Comparison CCQM-K16: Composition of Natural Gas Types IV and V. *Metrologia* **2005**, *42*, 8003. [CrossRef]
103. van der Veen, A.M.H.; Chander, H.; Ziel, P.R.; de Leer, E.W.B.; Smeulders, D.; Besley, L.; da Cunha, V.S.; Zhou, Z.; Qiao, H.; Heine, H.-J.; et al. International Comparison CCQM K23b: Natural Gas Type II. *Metrologia* **2010**, *47*, 08013. [CrossRef]
104. van der Veen, A.M.H.; Ziel, P.R.; de Leer, E.W.B.; Smeulders, D.; Besley, L.; da Cunha, V.S.; Zhou, Z.; Qiao, H.; Heine, H.-J.; Tichy, J.; et al. Final Report on International Comparison CCQM K23ac: Natural Gas Types I and III. *Metrologia* **2007**, *44*, 08001. [CrossRef]
105. Alink, A.; Milton, M.; Guenther, F.; de Leer, E.; Heine, H.; Marschal, A.; Suk Heo, G.; Takahashi, C.; Wang, L.; Kustikov, Y.; et al. *Final Report of Key Comparison CCQM-K1*; Technical report; Nederlands Meetinstituut, Van Swinden Laboratory: Delft, The Netherlands, 1999; Corrected version, September 2001. Available online: https://www.bipm.org/documents/20126/44595999/CCQM-K1.pdf/f8a8b735-2530-5bf3-1cfa-d924475e52dd?version=1.3&t=1643120279736 (accessed on 19 September 2025).
106. van der Veen, A.M.H.; Zalewska, E.T.; Kipphardt, H.; Beelen, R.R.; Tuma, D.; Maiwald, M.; Füko, J.; Büki, T.; Szilágyi, Z.N.; Beránek, J.; et al. International Comparison CCQM-K118 Natural Gas. *Metrologia* **2022**, *59*, 08017. [CrossRef]
107. CIPM. *Quality Management Systems in the CIPM MRA: Guidelines for Monitoring and Reporting, MRA-G-12*; The Bureau International Des Poids et Mesures: Sèvres, France, 2021.
108. Mandal, G.; Ansari, M.A.; Aswal, D.K. Quality Management System at NPLI: Transition of ISO/IEC 17025 From 2005 to 2017 and Implementation of ISO 17034: 2016. *Mapan J. Metrol. Soc. India* **2021**, *36*, 657–668. [CrossRef]
109. Kumar, V.; Al-Bashrawi, S.A. Quality Infrastructure: Metrology, Accreditation, and Standards. In *Handbook of Quality System, Accreditation and Conformity Assessment*; Springer: Berlin/Heidelberg, Germany, 2024; pp. 753–802. [CrossRef]
110. Brandi, H.S.; De Souza, T.L. Metrology Infrastructure for Sustainable Development of the Americas: The Role of SIM. *Accredit. Qual. Assur.* **2009**, *14*, 567–573. [CrossRef]
111. Salzenstein, P.; Lefebvre, F.; Barillet, R.; Čermak, J.; Schaefer, W.; Cibiel, G.; Sauvage, G.; Franquet, O.; Llopis, O.; Meyer, F.; et al. Phase Noise Inter-Laboratory Comparison Preliminary Results. In Proceedings of the 20th European Frequency and Time Forum, EFTF 2006, Braunschweig, Germany, 27–30 March 2006; pp. 147–151.
112. Patan Alper, M. Inter-Laboratory Comparison of a Digital Multimeter Measurement in Turkey. *Sci. Rep.* **2023**, *13*, 19406. [CrossRef]
113. Furuichi, N.; Terao, Y.; Ogawa, S.; Cordova, L.; Shimada, T. Inter-Laboratory Comparison of Small Water Flow Calibration Facilities with Extremely Low Uncertainty. *Measurement* **2016**, *91*, 548–556. [CrossRef]
114. Mittal, M.K.; Biswas, J.C.; Yadav, A.S. Proficiency Testing in AC Power and Energy. *Mapan J. Metrol. Soc. India* **2009**, *24*, 41–66. [CrossRef]
115. Guimarães, J.V.; Dias, M.H.C.; Dos Santos, J.C.A. Proficiency Testing of Electromagnetic Compatibility (EMC) Labs in Brazil by Measurement Comparisons. *Meas. Sci. Technol.* **2009**, *20*, 115107. [CrossRef]

116. Yadav, S.; Prakash, O.; Gupta, V.K.; Kumaraswamy, B.V.; Bandyopadhyay, A.K. Evaluation of Interlaboratory Performance through Proficiency Testing Using Pressure Dial Gauge in the Hydraulic Pressure Measurement up to 70 MPa. *Mapan J. Metrol. Soc. India* **2008**, *23*, 79–99.
117. Salzenstein, P. Rapport de Comparaison Internationale Interlaboratoire N° EM 03-99 (Haute Fréquence—Facteur de Réflexion). In *Comité Français d'accréditation (COFRAC) Report*; COFRAC: Paris, France, 1999.
118. *ILAC B7:10/2015*; ILAC The ILAC Mutual Recognition Arrangement. International Laboratory Accreditation Cooperation: Newton, Australia, 2015.
119. Salsbury, J. Uncertainty Management versus Risk Management in Calibration. *NCSLI Meas.* **2010**, *5*, 60–67. [CrossRef]
120. Dobbert, M. A Guard-Band Strategy for Managing False-Accept Risk. *NCSLI Meas.* **2008**, *3*, 44–48. [CrossRef]
121. NASA. Estimation and Evaluation of Measurement Decision Risk. In *NASA Measurement Quality Assurance Handbook*; National Aeronautics and Space Administration: Washington, DC, USA, 2010; p. 227.
122. *ILAC-G8:09*; ILAC Guidelines on Decision Rules and Statements of Conformity. International Laboratory Accreditation Cooperation: Newton, Australia, 2019.
123. Casacio, C.A.; Madsen, L.S.; Terrasson, A.; Waleed, M.; Barnscheidt, K.; Hage, B.; Taylor, M.A.; Bowen, W.P. Quantum-Enhanced Nonlinear Microscopy. *Nature* **2021**, *594*, 201–206. [CrossRef] [PubMed]
124. Giovannetti, V.; Lloyd, S.; Maccone, L. Quantum-Enhanced Measurements: Beating the Standard Quantum Limit. *Science* **2004**, *306*, 1330–1336. [CrossRef]
125. Ho, L.B. Squeezing-Induced Quantum-Enhanced Multiphase Estimation. *Phys. Rev. Res.* **2024**, *6*, 033292. [CrossRef]
126. Li, T.; Li, F.; Liu, X.; Yakovlev, V.V.; Agarwal, G.S. Quantum-Enhanced Stimulated Brillouin Scattering Spectroscopy and Imaging. *Optica* **2022**, *9*, 959. [CrossRef]
127. Tse, M.; Yu, H.; Kijbunchoo, N.; Fernandez-Galiana, A.; Dupej, P.; Barsotti, L.; Blair, C.D.; Brown, D.D.; Dwyer, S.E.; Effler, A.; et al. Quantum-Enhanced Advanced LIGO Detectors in the Era of Gravitational-Wave Astronomy. *Phys. Rev. Lett.* **2019**, *123*, 231107. [CrossRef]
128. Tóth, G.; Apellaniz, I. Quantum Metrology from a Quantum Information Science Perspective. *J. Phys. A Math.* **2014**, *47*, 39. [CrossRef]
129. Xiang, G.; Guo, G. Quantum Metrology. *Chin. Phys. B* **2013**, *22*, 110601. [CrossRef]
130. Degen, C.L.; Reinhard, F.; Cappellaro, P. Quantum Sensing. *Rev. Mod. Phys.* **2017**, *89*, 035002. [CrossRef]
131. Giovannetti, V.; Lloyd, S.; MacCone, L. Advances in Quantum Metrology. *Nat. Photonics* **2011**, *5*, 222–229. [CrossRef]
132. Jarzyna, M.; Demkowicz-Dobrzański, R. True Precision Limits in Quantum Metrology. *New J. Phys.* **2015**, *17*, 13010. [CrossRef]
133. Carlton, M. Caves Quantum Mechanical Radiation-Pressure Fluctuations in an Interferometer. *Phys. Rev. Lett.* **1980**, *45*, 75–79.
134. Zheng, X.; Dolde, J.; Lochab, V.; Merriman, B.N.; Li, H.; Kolkowitz, S. Differential Clock Comparisons with a Multiplexed Optical Lattice Clock. *Nature* **2022**, *602*, 425–430. [CrossRef]
135. Ludlow, A.D.; Zelevinsky, T.; Campbell, G.K.; Blatt, S.; Boyd, M.M.; De Miranda, M.H.G.; Martin, M.J.; Thomsen, J.W.; Foreman, S.M.; Ye, J.; et al. Sr Lattice Clock at 1×10^{-16} Fractional Uncertainty by Remote Optical Evaluation with a Ca Clock. *Science* **2008**, *319*, 1805–1808. [CrossRef]
136. Rosenband, T.; Hume, D.B.; Schmidt, P.O.; Chou, C.W.; Brusch, A.; Lorini, L.; Oskay, W.H.; Drullinger, R.E.; Fortier, T.M.; Stalnaker, J.E.; et al. Frequency Ratio of Al+ and Hg+ Single-Ion Optical Clocks; Metrology at the 17th Decimal Place. *Science* **2008**, *319*, 1808–1812. [CrossRef]
137. Beloy, K.; Bodine, M.I.; Bothwell, T.; Brewer, S.M.; Bromley, S.L.; Chen, J.S.; Deschênes, J.D.; Diddams, S.A.; Fasano, R.J.; Fortier, T.M.; et al. Frequency Ratio Measurements at 18-Digit Accuracy Using an Optical Clock Network. *Nature* **2021**, *591*, 564–569. [CrossRef] [PubMed]
138. Brewer, S.M.; Chen, J.S.; Hankin, A.M.; Clements, E.R.; Chou, C.W.; Wineland, D.J.; Hume, D.B.; Leibrandt, D.R. Al^+ 27 Quantum-Logic Clock with a Systematic Uncertainty below 10–18. *Phys. Rev. Lett.* **2019**, *123*, 033201. [CrossRef] [PubMed]
139. Robinson, J.M.; Miklos, M.; Tso, Y.M.; Kennedy, C.J.; Bothwell, T.; Kedar, D.; Thompson, J.K.; Ye, J. Direct Comparison of Two Spin-Squeezed Optical Clock Ensembles at the 10–17 Level. *Nat. Phys.* **2024**, *20*, 208–213. [CrossRef]
140. Ye, J.; Yoon, T.H.; Hall, J.L.; Madej, A.A.; Bernard, J.E.; Siemsen, K.J.; Marmet, L.; Chartier, J.M.; Chartier, A. Accuracy Comparison of Absolute Optical Frequency Measurement between Harmonic-Generation Synthesis and a Frequency-Division Femtosecond Comb. *Phys. Rev. Lett.* **2000**, *85*, 3797–3800. [CrossRef]
141. Udem, T.; Holzwarth, R.; Hänsch, T.W. Optical Frequency Metrology. *Nature* **2002**, *416*, 233–237. [CrossRef] [PubMed]
142. He, H.; Cedergren, K.; Shetty, N.; Lara-Avila, S.; Kubatkin, S.; Bergsten, T.; Eklund, G. Accurate Graphene Quantum Hall Arrays for the New International System of Units. *Nat. Commun.* **2022**, *13*, 6933. [CrossRef]
143. Lafont, F.; Ribeiro-Palau, R.; Kazazis, D.; Michon, A.; Couturaud, O.; Consejo, C.; Chassagne, T.; Zielinski, M.; Portail, M.; Jouault, B.; et al. Quantum Hall Resistance Standards from Graphene Grown by Chemical Vapour Deposition on Silicon Carbide. *Nat. Commun.* **2015**, *6*, 6806. [CrossRef]

144. Yin, Y.; Kruskopf, M.; Gournay, P.; Rolland, B.; Götz, M.; Pesel, E.; Tschirner, T.; Momeni, D.; Chatterjee, A.; Hohls, F.; et al. Graphene Quantum Hall Resistance Standard for Realizing the Unit of Electrical Resistance under Relaxed Experimental Conditions. *Phys. Rev. Appl.* **2025**, *23*, 014025. [CrossRef]
145. Giesbers, A.J.M.; Rietveld, G.; Houtzager, E.; Zeitler, U.; Yang, R.; Novoselov, K.S.; Geim, A.K.; Maan, J.C. Quantum Resistance Metrology in Graphene. *Appl. Phys. Lett.* **2008**, *93*, 222109. [CrossRef]
146. Schopfer, F.; Poirier, W. Graphene-Based Quantum Hall Effect Metrology. *MRS Bull.* **2012**, *37*, 1255–1264. [CrossRef]
147. NIST. NIST Broadens Collaboration with BIPM to Enhance Voltage Standards. Available online: https://www.nist.gov/news-events/news/2024/10/nist-broadens-collaboration-bipm-enhance-voltage-standards (accessed on 16 September 2025).
148. BIPM New Pilot Study Enhances Accuracy of AC Voltage Comparisons. Available online: https://www.bipm.org/en/-/2024-10-24-pilot-study-ac-voltage (accessed on 22 September 2025).
149. Fujii, K.; Massa, E.; Bettin, H.; Kuramoto, N.; Mana, G. Avogadro Constant Measurements Using Enriched 28Si Monocrystals. *Metrologia* **2018**, *55*, L1–L4. [CrossRef]
150. Bartl, G.; Becker, P.; Beckhoff, B.; Bettin, H.; Beyer, E.; Borys, M.; Busch, I.; Cibik, L.; D'Agostino, G.; Darlatt, E.; et al. A New 28Si Single Crystal: Counting the Atoms for the New Kilogram Definition. *Metrologia* **2017**, *54*, 693–715. [CrossRef]
151. Eppers, D.; Knopf, D.; Nicolaus, A.; Kuhn, E.; Borys, M.; Müller, M.; Bettin, H. Status of the Kilogram Realisation Using the XRCD Method at PTB. *Meas. Sens.* **2025**, *38*, 101353. [CrossRef]
152. Eppers, D.; Müller, M.; Kuhn, E.; Borys, M.; Rodiek, B.; Knopf, D.; Schrader, T. Realisation of the Kilogram with the XRCD Method—Improved XRF Evaluation and Its Impact. *Metrologia* **2025**, *62*, 065001. [CrossRef]
153. Kuramoto, N.; Mizushima, S.; Zhang, L.; Fujita, K.; Okubo, S.; Inaba, H.; Azuma, Y.; Kurokawa, A.; Ota, Y.; Fujii, K. Reproducibility of the Realization of the Kilogram Based on the Planck Constant by the XRCD Method at NMIJ. *IEEE Trans. Instrum. Meas.* **2021**, *70*, 1005609. [CrossRef]
154. Fujii, K.; Bettin, H.; Becker, P.; Massa, E.; Rienitz, O.; Pramann, A.; Nicolaus, A.; Kuramoto, N.; Busch, I.; Borys, M. Realization of the Kilogram by the XRCD Method. *Metrologia* **2016**, *53*, A19–A45. [CrossRef]
155. Robinson, I.A.; Schlamminger, S. The Watt or Kibble Balance: A Technique for Implementing the New SI Definition of the Unit of Mass. *Metrologia* **2016**, *53*, A46–A74. [CrossRef]
156. Fang, H.; Bielsa, F.; Li, S.; Kiss, A.; Stock, M. The BIPM Kibble Balance for Realizing the Kilogram Definition. *Metrologia* **2020**, *57*, 045009. [CrossRef]
157. Stock, M. The Watt Balance: Determination of the Planck Constant and Redefinition of the Kilogram. In *Proceedings of the Philosophical Transactions of the Royal Society A: Mathematical, Physical and Engineering Sciences*; The Royal Society Publishing: London, UK, 2011; Volume 369, pp. 3936–3953.
158. Konrad, J.; Rothleitner, C.; Vasilyan, S.; Rogge, N.; Behr, R.; Götz, M.; Kruskopf, M.; Fröhlich, T. Small Mass Value Realization Equivalent to Accuracy Class E1 Using the Planck-Balance at PTB. *Metrologia* **2025**, *62*, 025014. [CrossRef]
159. Chao, L.; Seifert, F.; Haddad, D.; Pratt, J.; Newell, D.; Schlamminger, S. The Performance of the KIBB-G1 Tabletop Kibble Balance at NIST. *Metrologia* **2020**, *57*, 035014. [CrossRef]
160. Keck, L.; Seifert, F.; Newell, D.; Schlamminger, S.; Theska, R.; Haddad, D. Design of an Enhanced Mechanism for a New Kibble Balance Directly Traceable to the Quantum SI. *EPJ Technol. Instrum.* **2022**, *9*, 7. [CrossRef]
161. Robinson, I.A. Watt and Joule Balances. *Metrologia* **2014**, *51*, S1. [CrossRef]
162. Pizzocaro, M.; Sekido, M.; Takefuji, K.; Ujihara, H.; Hachisu, H.; Nemitz, N.; Tsutsumi, M.; Kondo, T.; Kawai, E.; Ichikawa, R.; et al. Intercontinental Comparison of Optical Atomic Clocks through Very Long Baseline Interferometry. *Nat. Phys.* **2021**, *17*, 223–227. [CrossRef]
163. Giblin, S.P.; Yamahata, G.; Fujiwara, A.; Kataoka, M. Precision Measurement of an Electron Pump at 2 GHz; the Frontier of Small DC Current Metrology. *Metrologia* **2023**, *60*, 055001. [CrossRef]
164. Stock, M.; Davis, R.; De Mirandés, E.; Milton, M.J.T. The Revision of the SI—The Result of Three Decades of Progress in Metrology. *Metrologia* **2019**, *56*, 022001. [CrossRef]
165. Milano, G.; Zheng, X.; Michieletti, F.; Leonetti, G.; Caballero, G.; Oztoprak, I.; Boarino, L.; Bozat, Ö.; Callegaro, L.; De Leo, N.; et al. A Quantum Resistance Memristor for an Intrinsically Traceable International System of Units Standard. *Nat. Nanotechnol.* **2025**, 1–7. [CrossRef]
166. Riehle, F.; Gill, P.; Arias, F.; Robertsson, L. The CIPM List of Recommended Frequency Standard Values: Guidelines and Procedures. *Metrologia* **2018**, *55*, 188. [CrossRef]
167. BIPM. Mise En Pratique for the Definition of the Second in the SI. In *SI Brochure*; The Bureau International Des Poids et Mesures: Sèvres, France, 2019.
168. Lindvall, T.; Pizzocaro, M.; Godun, R.M.; Abgrall, M.; Akamatsu, D.; Amy-Klein, A.; Benkler, E.; Bhatt, N.M.; Calonico, D.; Cantin, E.; et al. Coordinated International Comparisons between Optical Clocks Connected via Fiber and Satellite Links. *Optica* **2025**, *12*, 843. [CrossRef]

169. Sanner, C.; Huntemann, N.; Lange, R.; Tamm, C.; Peik, E.; Safronova, M.S.; Porsev, S.G. Optical Clock Comparison for Lorentz Symmetry Testing. *Nature* **2019**, *567*, 204–208. [CrossRef]
170. Margolis, H.S.; Panfilo, G.; Petit, G.; Oates, C.; Ido, T.; Bize, S. The CIPM List 'Recommended Values of Standard Frequencies': 2021 Update. *Metrologia* **2024**, *61*, 035005. [CrossRef]
171. BIPM Vers La Redéfinition de La Seconde. Available online: https://www.bipm.org/fr/-/2024-02-20-redefinition-second (accessed on 16 September 2025).
172. BIPM. SI Base Unit: Second (s). Available online: https://www.bipm.org/en/si-base-units/second (accessed on 16 September 2025).
173. Dimarcq, N.; Gertsvolf, M.; Mileti, G.; Bize, S.; Oates, C.W.; Peik, E.; Calonico, D.; Ido, T.; Tavella, P.; Meynadier, F.; et al. Roadmap towards the Redefinition of the Second. *Metrologia* **2024**, *61*, 012001. [CrossRef]
174. Giblin, S.P.; Kataoka, M.; Fletcher, J.D.; See, P.; Janssen, T.J.B.M.; Griffiths, J.P.; Jones, G.A.C.; Farrer, I.; Ritchie, D.A. Towards a Quantum Representation of the Ampere Using Single Electron Pumps. *Nat. Commun.* **2012**, *3*, 930. [CrossRef]
175. Bae, M.H.; Chae, D.H.; Kim, M.S.; Kim, B.K.; Park, S.I.; Song, J.; Oe, T.; Kaneko, N.H.; Kim, N.; Kim, W.S. Precision Measurement of Single-Electron Current with Quantized Hall Array Resistance and Josephson Voltage. *Metrologia* **2020**, *57*, 065025. [CrossRef]
176. Scherer, H.; Camarota, B. Quantum Metrology Triangle Experiments: A Status Review. *Meas. Sci. Technol.* **2012**, *23*, 124010. [CrossRef]
177. López, M.; Meda, A.; Porrovecchio, G.; Starkwood (Kirkwood), R.A.; Genovese, M.; Brida, G.; Šmid, M.; Chunnilall, C.J.; Degiovanni, I.P.; Kück, S. A Study to Develop a Robust Method for Measuring the Detection Efficiency of Free-Running InGaAs/InP Single-Photon Detectors. *EPJ Quantum Technol.* **2020**, *7*, 14. [CrossRef]
178. Quinn, T.J. The BIPM and the Accurate Measurement of Time. *Proc. IEEE* **1991**, *79*, 894–905. [CrossRef]
179. McNish, A.G. Lasers for Length Measurement. *Science* **1964**, *146*, 177–182. [CrossRef] [PubMed]
180. Beers, J.S.; Penzes, W.B. The NIST Length Scale Interferometer. *J. Res. Natl. Inst. Stand. Technol.* **1999**, *104*, 225. [CrossRef]
181. Walls, F.L.; Barillet, R.; Besson, R.J.; Groslambert, J.; Schumacher, P.; Rufenacht, J.; Hilty, K. International Comparison of Phase Noise. In Proceedings of the 8th European Frequency and Time Forum (EFTF), Weihenstephan, Germany, 25–27 June 1994; pp. 439–456.
182. Quincey, P.; Sarantaridis, D.; Yli-Ojanperä, J.; Keskinen, J.; Högström, R.; Heinonen, M.; Lüönd, F.; Nowak, A.; Riccobono, F.; Tuch, T.; et al. EURAMET Comparison 1244 Comparison of Aerosol Electrometers, Issue 2: EURAMET REPORT. In *NPL REPORT AS 85*; The National Physical Laboratory: London, UK, 2014.
183. Brown, A.; Nowak, A.; Tompkins, J.; Tomson, M.; Waheed, A.; Godau, D.; Jung, J.; Kim, H.; Wu, T.; Auderset, K.; et al. Ensuring the Worldwide Equivalence of Measurements of Nanoparticle Number Concentration and Charge Concentration: An International Comparison. In Proceedings of the European Aerosol Conference (EAC 2025), Lecce, Italy, 31 August–5 September 2025.
184. Brown, A.; Nowak, A.; Tipler, J.; Tompkins, J.; Tomson, M.; Waheed, A.; Godau, D.; Jung, J.; Kim, H.; Wu, T.; et al. International Comparison CCQM-K185: Particle Number Concentration 1000 to 500,000 cm^{-3}) and Particle Charge Concentration 0.16 fC to 16 fC cm^{-3}). Final report for International Comparison CCQM-K185, to be published in BIPM website.

Disclaimer/Publisher's Note: The statements, opinions and data contained in all publications are solely those of the individual author(s) and contributor(s) and not of MDPI and/or the editor(s). MDPI and/or the editor(s) disclaim responsibility for any injury to people or property resulting from any ideas, methods, instructions or products referred to in the content.

MDPI AG
Grosspeteranlage 5
4052 Basel
Switzerland
Tel.: +41 61 683 77 34

Metrology Editorial Office
E-mail: metrology@mdpi.com
www.mdpi.com/journal/metrology



Disclaimer/Publisher's Note: The title and front matter of this reprint are at the discretion of the Guest Editor. The publisher is not responsible for their content or any associated concerns. The statements, opinions and data contained in all individual articles are solely those of the individual Editor and contributors and not of MDPI. MDPI disclaims responsibility for any injury to people or property resulting from any ideas, methods, instructions or products referred to in the content.





Academic Open
Access Publishing

mdpi.com

ISBN 978-3-7258-9118-4